



**NOVA**

NOVA SCHOOL OF  
SCIENCE & TECHNOLOGY

DEPARTAMENTO DE FÍSICA

# SOLAR-PUMPED LASER TECHNOLOGY

DISSERTAÇÃO PARA OBTENÇÃO DO GRAU DE DOUTORAMENTO

BRUNO DIOGO RODRIGUES MATOS TIBÚRCIO

Mestre em Engenharia Física

DOUTORAMENTO EM ENGENHARIA FÍSICA

Universidade NOVA de Lisboa

MARÇO, 2022



# SOLAR-PUMPED LASER TECHNOLOGY

DISSERTAÇÃO PARA OBTENÇÃO DO GRAU DE DOUTORAMENTO

**BRUNO DIOGO RODRIGUES MATOS TIBÚRCIO**

**Mestre em Engenharia Física**

**Orientador:** Doutor Dawei Liang, Professor Associado, Faculdade de Ciências e Tecnologia da Universidade Nova de Lisboa

**Co-orientador:** Doutor Paulo Morais, Investigador Sénior, Instituto de Soldadura e Qualidade

**Júri:**

**Presidente:** Doutor Orlando Manuel Neves Duarte Teodoro, Professor Catedrático, Faculdade de Ciências e Tecnologia da Universidade Nova de Lisboa

**Arguentes:** Doutor Luís Manuel Guerra da Silva Rosa, Professor Associado com Agregação, Instituto Superior Técnico da Universidade de Lisboa

Doutor Gonçalo Nuno Marmelo Foito Figueira, Professor Auxiliar, Instituto Superior Técnico da Universidade de Lisboa

**Orientador:** Doutor Dawei Liang, Professor Associado, Faculdade de Ciências e Tecnologia da Universidade Nova de Lisboa

**Membros:** Doutor João Miguel Pinto Coelho, Investigador Associado, Faculdade de Ciências da Universidade de Lisboa

Doutora Joana Isabel Lázaro Almeida, Investigadora Auxiliar, Faculdade de Ciências e Tecnologia da Universidade Nova de Lisboa

DOUTORAMENTO EM ENGENHARIA FÍSICA

Universidade NOVA de Lisboa

Março, 2022





### **Solar-pumped laser technology**

Copyright ©Buno Diogo Rodrigues Matos Tibúrcio, NOVA School of Science and Technology | FCT NOVA.

NOVA School of Science and Technology | FCT NOVA have the right, perpetual and without geographical boundaries, to file and publish this dissertation through printed copies reproduced on paper or on digital form, or by any other means known or that may be invented, and to disseminate through scientific repositories and admits its copying and distribution for non-commercial, educational or research purposes, as long as credit is given to the author and editor.



# Acknowledgements

I would like to express my sincere gratitude to:

Firstly, to my advisor Prof. Dawei Liang, a mentor to me in so many ways, a friend. His inspiration and orientation was fundamental in this long journey, with constant exchanging of ideas that enriched my work and made me grow and believe.

My colleagues Cláudia, Dário, Miguel and Hugo of the Solar Laser Laboratory, for all their friendship and support, and in particular to Joana, my partner of many profitable discussions and useful points of view.

Dr. Emmanuel Guillot as the coordinator of SFERA II and SFERA III European project PROMES-CNRS, for the opportunity to access the solar facilities.

My thesis commission Prof. Adelaide de Jesus and Prof. Gonçalo Figueira, for the insightful comments and orientation.

Science and Technology Foundation of Portuguese Ministry of Science, Technology and Higher Education, for the attribution of the PhD fellowship in the Doctoral Program in Applied and Engineering Physics (DAEPHYS).

NOVA School of Science and Technology of NOVA University of Lisbon, it was a pleasure and an honor to be part of this prestigious institution.

My mother and my father, for their support and sacrifices made on my behalf, all the love and comprehension I needed to be what I am. To my sister Edla and all my family, for the dedication and trust, and for a life history in common.

To Anna Lina, my lifemate, always with love and passion, for her patience, sharing so many moments of comprehension and beauty.



# Abstract

In this dissertation are reported technological advancements in solar-pumped lasers and solar energy collection and concentration systems. New insights to improve the overall efficiency and the tracking error stability of solar lasers are presented, demonstrating new possibilities towards a sustainable energy generation and a low carbon industry as a solution for new segments of technology innovation.

Significant progresses in solar laser efficiency and tracking error stability were obtained with numerical analysis. ZEMAX<sup>®</sup> non-sequential ray-tracing and LASCAD<sup>®</sup> resonant cavity analysis were used to optimize the optical designs and the laser cavity parameters. 38.2 W/m<sup>2</sup> multimode solar laser in end-side-pumping configuration was achieved by using a ring-array concentrator (RAC). Dual-rod side-pumping scheme increased the multimode collection efficiency and the solar-to-laser power conversion efficiency to 24.18 W/m<sup>2</sup> and 2.88%, respectively. Through the RAC primary concentrator and the dual-rod scheme, 29.06 W/m<sup>2</sup> in multimode collection efficiency and 3.06% solar-to-laser power conversion efficiency were obtained. Also, TEM<sub>00</sub>-mode solar laser was improved with the novel three-folding-mirror laser beam merging technique, reaching 16.10 W/m<sup>2</sup> of collection efficiency. Finally, a Nd:YAG dual-rod solar laser prototype was designed and built based on the numerical calculations. Experimental advancements were achieved regarding the solar tracking stability of the solar laser emission, reducing the eventual costs of future solar laser systems. The improvement in solar tracking error width at 10% laser power loss was 3.5 times and 1.5 times in its vertical and horizontal solar laser setups, respectively. Compared with the most efficient experimental single-rod solar laser, tracking error enhancement attained with the dual-rod in its vertical and horizontal setups was 23.3 and 10.0 times, respectively. The solar laser beam merging technique is also presented.

The research work performed along this thesis and its results are discussed and future perspectives are finally proposed.

**Keywords:** Solar-pumped laser; Dual-rod scheme; Solar tracking error; Solar laser efficiency; Laser beam merging.



# Resumo

Nesta dissertação são reportados os avanços tecnológicos em lasers de bombeamento solar e coleção e concentração de energia solar. Novos conhecimentos para melhorar a eficiência geral e a estabilidade de seguimento solar de lasers solares são apresentados, demonstrando novas possibilidades em direção à uma geração de energia sustentável e a uma indústria de baixo carbono como uma solução para novos segmentos de inovação tecnológica.

Progressos significantes em eficiência de laser solar e estabilidade de seguimento solar foram obtidos com análise numérica. ZEMAX® em modo não-sequencial para o traçado de raios e LASCAD® para análise da cavidade ressonante foram usados para otimizar o design ótico e os parâmetros da cavidade ressonante. 38.2 W/m<sup>2</sup> de laser solar multimodo com configuração de bombeamento longitudinal-lateral foi conseguido utilizando um concentrador de anéis (CA). O esquema de dois-cristais com bombeamento lateral aumentou a eficiência de coleção e a eficiência de conversão de potência solar-para-laser multimodo para 24.18 W/m<sup>2</sup> e 2.88%, respectivamente. Através do CA como concentrador primário e do esquema de dois-cristais, 29.06 W/m<sup>2</sup> em eficiência de coleção em multimodo e 3.06% de eficiência de conversão de potência solar-para-laser foram obtidos. Também o laser solar em modo fundamental foi melhorado com a nova técnica de fusão de feixes laser com três-espelhos, atingindo 16.10 W/m<sup>2</sup> de eficiência de coleção. Finalmente, um protótipo de laser solar Nd:YAG de dois-cristais foi desenhado e construído baseado nas simulações numéricas.

Avanços experimentais foram atingidos em relação à estabilidade de seguimento solar da emissão de laser solar, reduzindo os eventuais custos de futuros sistemas de laser solar. O melhoramento na largura de erro de seguimento solar a 10% de perda de potência laser foi 3.5 vezes e 1.5 vezes nos seus esquemas vertical e horizontal, respectivamente. Comparado com o mais eficiente laser solar experimental de um cristal, a melhoria conseguida no erro de seguimento com o dois-cristais nos seus esquemas vertical e horizontal foi de 23.3 e 10.0 vezes, respectivamente. A técnica de fusão de feixes laser com três espelhos também é apresentada.

O trabalho de pesquisa feito ao longo desta tese e os seus resultados são discutidos e futuras perspectivas são finalmente propostas.

**Palavras-chave:** Laser de bombeamento solar; Esquema de dois-cristais; Erro de seguimento solar; Eficiência de laser solar; Fusão de feixes lasers.





# Contents

|  |             |
|--|-------------|
| <b>Acknowledgements .....</b>  | <b>V</b>    |
| <b>Abstract.....</b>   | <b>VII</b>  |
| <b>Resumo.....</b>   | <b>IX</b>   |
| <b>List of Figures.....</b>  | <b>XIII</b> |
| <b>List of Tables .....</b>  | <b>XXI</b>  |
| <b>Chapter 1 Introduction.....</b>   | <b>1</b>    |
| <b>Chapter 2 Solid-state lasers.....</b>   | <b>5</b>    |
| 2.1 Light-matter interaction .....   | 5           |
| 2.2 Population Inversion .....   | 7           |
| 2.3 Creation of a Population Inversion .....   | 8           |
| 2.4 Laser oscillator.....  | 10          |
| <b>Chapter 3 Solar-pumped lasers .....</b>   | <b>19</b>   |
| 3.1 Laser materials .....  | 19          |
| 3.2 State-of-the-art of solar-pumped lasers.....   | 21          |
| <b>Chapter 4 Solar energy collection and concentration systems for solar–pumped lasers .....</b> | <b>27</b>   |
| 4.1 Parabolic mirrors.....   | 27          |
| 4.2 NOVA Heliostat-parabolic mirrors system.....   | 28          |
| 4.3 PROMES Heliostat-parabolic mirror system.....  | 29          |
| 4.4 Numerical ring-array concentrator.....   | 30          |
| 4.5 Aspheric lens secondary concentrator.....  | 32          |
| <b>Chapter 5 Modeling tools for solar pumped lasers .....</b>                                    | <b>35</b>   |
| 5.1 ZEMAX® software for modeling and analysis of solar laser systems .....                       | 35          |
| 5.2 LASCAD® software for modeling of the solar laser resonant cavity.....                        | 40          |
| <b>Chapter 6 Recent advancements in solar-pumped laser technology .....</b>                      | <b>45</b>   |
| 6.1 Solar-pumped lasers in multimode regime .....  | 45          |
| 6.1.1 Improving solar-pumped laser efficiency by a ring-array concentrator.....                  | 45          |
| 6.1.2 Single-rod side-pumped solar laser.....  | 50          |
| 6.1.3 Highly efficient and stable dual-rod side-pumped solar laser.....                          | 52          |
| 6.1.4 Simultaneous solar laser emissions from three Nd:YAG rods.....                             | 59          |
| 6.1.5 Ce:Nd:YAG side-pumped solar laser.....   | 60          |

|   |            |
|---|------------|
| 6.2 Solar-pumped lasers in TEM <sub>00</sub> -mode regime.....  | 61         |
| 6.2.1 Dual-rod pumping concept for TEM <sub>00</sub> -mode solar lasers .....                                       | 61         |
| 6.2.2 Seven-rod pumping approach for TEM <sub>00</sub> -mode solar laser .....                                      | 68         |
| 6.2.3 Doughnut-shaped solar laser beams numerical analysis .....  | 69         |
| 6.2.4 A doughnut-shaped Nd:YAG solar laser beam.....  | 71         |
| 6.2.5 Solar laser TEM <sub>11</sub> , TEM <sub>01</sub> *, TEM <sub>10</sub> , TEM <sub>00</sub> mode profiles..... | 72         |
| 6.3 Laser beam merging technique .....  | 73         |
| 6.3.1 Dual-rod multimode solar laser beam merging technique .....   | 74         |
| 6.3.2 Multi-rod for TEM <sub>00</sub> -mode solar laser from a megawatt solar furnace and its beam merging ..       | 82         |
| 6.3.3 TEM <sub>00</sub> -mode solar laser with beam merging and ring-array concentrator.....                        | 84         |
| <b>Chapter 7 Tracking error in solar energy collection and concentration systems .....</b>                          | <b>91</b>  |
| 7.1 Sun-Earth relationship .....  | 91         |
| 7.2 Solar tracking error in parabolic mirrors.....  | 94         |
| 7.3 Solar tracking error in ring-array concentrators.....   | 106        |
| <b>Chapter 8 Dual-rod solar laser with tracking error compensation capacity.....</b>                                | <b>111</b> |
| 8.1 Dual-rod side-pumping solar-laser.....  | 111        |
| 8.2 Experimental tests at PROMES-CNRS heliostat-parabolic mirror system .....                                       | 115        |
| 8.3 Experimental tests at NOVA heliostat-parabolic mirror system.....   | 117        |
| 8.3.1 Improvement of the solar laser prototype .....  | 117        |
| 8.3.2 Dual-rod solar laser emission with one rod.....   | 119        |
| 8.3.3 Dual-rod side-pumping solar laser simultaneous emission.....  | 124        |
| 8.3.4 Tracking error compensation capacity measurements of the dual-rod solar laser .....                           | 126        |
| <b>Chapter 9 Conclusions and future perspectives.....</b>   | <b>133</b> |
| <b>Annexes .....</b>  | <b>135</b> |
| Publications during the PhD thesis .....  | 135        |
| Conferences.....  | 137        |
| Highlights.....   | 137        |

# List of Figures

|   |    |
|---|----|
| Figure 2.1 Schematic energy level diagram of a three level system. ....   | 8  |
| Figure 2.2 Schematic energy level diagram of a four level system. ....  | 9  |
| Figure 2.3 Major components of a light pumped solid-state laser oscillator. ....  | 11 |
| Figure 2.4 Energy conversion process in a solid-state laser system. ....  | 11 |
| Figure 2.5 Standard solar emission spectrum in space (AM0) and on the Earth (AM1.5), and the Nd:YAG absorption bands [39]. ....   | 13 |
| Figure 2.6 Schematic diagram of the TEM <sub>00</sub> -mode beam propagation along the symmetric laser resonator with large RoC (radius of curvature) mirrors. ....   | 16 |
| Figure 3.1 Energy level diagram of Nd:YAG [40]. ....  | 19 |
| Figure 3.2 Standard solar emission spectrum (in orange), Nd:YAG [39](in blue) and Ce:Nd:YAG (in black) absorption spectra (adapted from [54]). ....   | 20 |
| Figure 3.3 Energy-level diagram illustrating the energy transfer mechanism between Ce <sup>3+</sup> and Nd <sup>3+</sup> ions in the Ce:Nd:YAG ceramic (adapted from [49]). Solid arrows indicate the excitation and the emission processes, and dotted and dashed arrows represent the energy transfer and the nonradiative transition processes, respectively. .... | 21 |
| Figure 3.4 The 61 cm diameter, sun-tracking, equatorial mount solar collector. The water-cooled laser is mounted forward of the bucket. ....  | 22 |
| Figure 3.5 (a) The Astigmatic Corrected Target Aligned solar concentrator. The segmented primary mirror fixed axis is tilted southwards to the direction of the folding mirror center. (b) Safety construction made of inverse cut pyramid and a cubic structure. (c) A cube-like structure containing the filter beamsplitter. ....                                  | 22 |
| Figure 3.6 The Nd:YAG solar-pumped laser system with a 0.9 m diameter Fresnel lens and a laser head positioned in its focal zone. ....  | 23 |
| Figure 3.7 a) cone-shaped hybrid pumping cavity and b) liquid light-guide lens configuration. c) the focusing effect of the liquid light-guide lens. ....   | 23 |
| Figure 3.8 (a) The solar-pumped TEM <sub>00</sub> -mode Nd:YAG laser system (b) The laser head. ....  | 24 |
| Figure 3.9 The solar laser head is composed of the ellipsoid-shaped fused silica concentrator and a 2V-shaped pumping cavity within which the grooved Nd:YAG rod is efficiently pumped. (b) The grooved laser rod is cooled by water along 26 mm of its longitudinal surface. ....  | 25 |
| Figure 3.10 (a) Laser head and output coupler were separated by 11 mm for producing the maximum multimode laser power (b) Laser head and output coupler were separated by 430 mm for the generation of TEM <sub>00</sub> -mode laser power. ....  | 26 |
| Figure 4.1 Solar concentration by a parabolic mirror. ....  | 27 |
| Figure 4.2 NOVA parabolic-heliostat mirror solar energy collection and concentration system. ....   | 29 |
| Figure 4.3 PROMES parabolic-heliostat mirror solar energy collection and concentration system. ....   | 29 |
| Figure 4.4 Schematics of the RAC solar energy collection and concentration system. Inset picture with the pump light distribution at its focal zone. ....   | 30 |
| Figure 4.5 Concentration properties and the: a) spherical lens with spherical aberration and b) aspheric lens (adapted from Shanghai Optics); c) the aspherical lens used for the solar laser experiments fixed by the lens supporter. ....   | 32 |

|   |    |
|---|----|
| Figure 5.1 Non-sequential objects of ZEMAX <sup>®</sup> software to model and analyze a parabolic concentrator solar system.....  | 36 |
| Figure 5.2 Selection of the source ellipse in the source objects of ZEMAX <sup>®</sup> .....  | 36 |
| Figure 5.3 List of parameters of the source ellipse used for solar-pumped lasers in the Non-sequential component editor.....  | 37 |
| Figure 5.4 Solar source wavelength data, for solar-pumping of a Nd:YAG laser.....   | 37 |
| Figure 5.5 Geometrical objects in ZEMAX <sup>®</sup> . <i>Aspheric Surface</i> represent the object selected to model the Parabolic mirror system.....  | 38 |
| Figure 5.6 Transmission data of the Nd:YAG laser material.....  | 39 |
| Figure 5.7 a) Active medium and pump configuration models of LASCAD <sup>®</sup> ; b) importation of data files from ZEMAX <sup>®</sup> .....   | 40 |
| Figure 5.8 a) The cooling parameters of a side-pumping scheme solar laser; b) Nd:YAG laser material parameter.....  | 41 |
| Figure 5.9 The resonant cavity and the laser beam represented in the propagation planes of X-Z and Y-Z for the TEM <sub>00</sub> -mode solar laser emission.....  | 42 |
| Figure 5.10 Calculated laser output power as a function of a) the absorbed pump power and b) the reflectivity of the output coupler used.....   | 43 |
| Figure 5.11 Laser beam waist at the output mirror calculation by BPM cavity iterations function of LASCAD <sup>®</sup> software.....  | 44 |
| Figure 6.1 Design of the Nd:YAG rod solar laser head, composed of a large fused silica aspheric lens, conical pump cavity and the Nd:YAG rod.....   | 45 |
| Figure 6.2 Absorbed pump flux distributions along the 5 mm diameter, 20 mm length Nd:YAG rod, at the focal distance of 410 mm.....  | 46 |
| Figure 6.3 Numerically calculated laser output power as function of the RAC focal length. The laser resonator cavity has 11 mm length.....  | 47 |
| Figure 6.4 Numerically calculated laser output power as function of the Nd:YAG rod diameter, for 20 mm length.....  | 47 |
| Figure 6.5 Laser output power as function of the incoming solar power for 5.0 mm diameter, 20 mm length rod, with three different reflectivities: 90%, 94% and 98%.....   | 48 |
| Figure 6.6 Numerically calculated heat load, temperature and stress intensity distributions for the 5 mm diameter 20 mm length Nd:YAG rod.....  | 48 |
| Figure 6.7 Numerically calculated laser output power and stress intensity as function of the shift of the 5 mm diameter, 20 mm length rod.....  | 49 |
| Figure 6.8 Numerically calculated heat load, temperature and stress intensity distributions for the 5 mm diameter, 20 mm length Nd:YAG rod, shifted 1.5 mm upward.....  | 50 |
| Figure 6.9 Front and side views of the solar laser head, showing water cooling scheme for the laser rod through the space between the fused silica aspheric lens and the two-dimensional semi-cylindrical pump cavity. Inset photos on the left show the mechanical design details of the solar laser head. Inset photo on the right shows the external resonant laser cavity and solar laser head being pumped at the focus of the parabolic mirror..... | 51 |
| Figure 6.10 Solar laser output power versus incoming solar power.....   | 52 |
| Figure 6.11 Nd:YAG rod solar laser head design in its traditional side-pumped single-rod scheme: a) 3-D view and b) front view. It is composed of the fused silica aspherical lens, the 2D-shaped-semicylindrical pump cavity and the Nd:YAG rod, fixed by two holders.....   | 53 |

|  |    |
|--|----|
| Figure 6.12 Solar laser head design with two Nd:YAG laser rods: a) 3-D view and b) front view. It is composed of the fused silica aspherical lens, the two 2D-shaped-semicylindrical pump cavities and the two thick Nd:YAG rods, fixed by holders. The HR 1064 nm mirrors and the PR 1064 nm mirrors form the laser resonant cavities, along with the two laser rods. ....  | 53 |
| Figure 6.13 Absorbed pump flux distributions along a) the 5.5 mm diameter, 25 mm length Nd:YAG rod of the single-rod scheme and b) the 4.0 mm diameter, 25 mm length rod of the dual-rod scheme. ....  | 54 |
| Figure 6.14 Numerically calculated multimode laser output power as a function of both rod diameter and length for the single-rod scheme. ....  | 55 |
| Figure 6.15 Numerically calculated multimode laser output power as a function of both rod diameter and length for the dual-rod scheme with combined laser power. ....  | 55 |
| Figure 6.16 Proposed design of the solar laser head with two Nd:YAG rods to obtain one single laser beam from the two rods. Two HR 1064 nm folding mirrors, one HR 1064 nm mirror and one PR 1064 nm mirror compose the U-shaped laser resonant cavity, along with the two laser rods. ....  | 56 |
| Figure 6.17 Numerically calculated multimode laser output power as a function of the incoming solar power, for both the single-rod and the dual-rod schemes. The latter in two configurations, two laser beams and one laser beam schemes. The solar laser slope efficiencies are also represented. ....   | 56 |
| Figure 6.18 Numerically calculated heat load, temperature and stress intensity distributions of the 5.5 mm diameter 25 mm length Nd:YAG rod from the single-rod scheme, and the 4.0 mm diameter 25 mm length Nd:YAG rod from the dual-rod scheme. ....   | 58 |
| Figure 6.19 (a) Front image showing the three-rod solar laser head actively cooled by water. (b) Back image of the solar laser head with three positioners for accurate adjustments of the three small output couplers in relation to the three rods. ....   | 59 |
| Figure 6.20 Total solar laser output power from the three rods versus incoming solar power for $R = 95\%$ , $RoC = \infty$ and $L_1 = L_2 = L_3 = 50$ mm. ....   | 60 |
| Figure 6.21 (a) Front view; (b), (c) side view of the Ce:Nd:YAG solar laser head. PR, partial reflection; HR, high reflection. ....  | 60 |
| Figure 6.22 Design of the Nd:YAG rod solar laser head in its traditional side-pumped single-rod scheme, composed of a fused silica semicylindrical lens, CPC-semicylindrical pump cavity and the Nd:YAG rod, fixed by two holders. ....  | 62 |
| Figure 6.23 Design of the solar laser head with two Nd:YAG laser rods, composed of a fused silica semicylindrical lens, CPC-semicylindrical pump cavities and the two thin rods, fixed by holders. The HR 1064 nm mirrors and the PR 1064 nm mirrors form the laser resonant cavity, along with the two laser rods. ....   | 62 |
| Figure 6.24 a) Absorbed pump flux distributions along the 4.0 mm diameter, 25 mm length Nd:YAG rod single-rod scheme. b) Absorbed pump flux distributions along the 3.3 mm diameter, 25 mm length Nd:YAG dual-rod scheme. ....   | 63 |
| Figure 6.25 Asymmetric laser resonant cavity for the efficient production of fundamental $TEM_{00}$ -mode solar laser power. $L_1$ and $L_2$ represent the separation length of the high reflection (HR) mirror and partial (PR) mirror, respectively, to the end face of the laser rod with length $L_R$ . For the dual-rod scheme were used $L_1=563$ mm and $L_2=70$ mm. For the single-rod scheme were used $L_1=477$ mm and $L_2=70$ mm. .... | 63 |
| Figure 6.26 Numerically simulated 3-D $TEM_{00}$ -mode laser output beam pattern on the output mirror of the asymmetric laser resonant cavity for a) 3.3 mm diameter 25 mm length Nd:YAG rod and b) 4.0 mm diameter 25 mm length Nd:YAG rod. The spot size $1/e^2$ width is approximately $\omega = 1.1$ mm for the former and 2.1 mm for the latter. ....   | 64 |

|  |    |
|--|----|
| Figure 6.27 Numerically calculated TEM <sub>00</sub> -mode laser output power as a function of the rod diameter with 20, 25 and 30 mm length for combined dual-rod and single-rod schemes. ....  | 64 |
| Figure 6.28 Numerically calculated brightness figure of merit as a function of the rod diameter and length, for both the dual-rod and the single-rod schemes. ....   | 65 |
| Figure 6.29 Numerical TEM <sub>00</sub> -mode laser output power as a function of the incoming solar power for the dual-rod scheme with 3.3 mm diameter and 25 mm length rod, and the single-rod scheme with 4.0 mm diameter and 25 mm length rod. ....  | 65 |
| Figure 6.30 (a) 3D and (b) 2D view of the single large laser head near the focal zone, with their respective resonators. $\alpha$ represents the spatial angle between the optical axes of the external CPCs and the optical axis of the parabolic mirror. ....  | 68 |
| Figure 6.31 Total TEM <sub>00</sub> -mode-to-multimode (M-M) laser power ratio as a function of the laser rod diameter (DROD) from the seven-rod scheme. ....  | 69 |
| Figure 6.32 Six Fresnel lens solar laser side-pumping concept with 4.0 m <sup>2</sup> total collection area. F <sub>1</sub> – F <sub>6</sub> and M <sub>1</sub> – M <sub>6</sub> indicates the six Fresnel lenses and the six folding mirrors, respectively. ....  | 70 |
| Figure 6.33 3D view of the six secondary aspheric lenses, the six twisted light guides, the cylindrical pump cavity and the Nd:YAG rod, and the HR end mirror and the PR output coupler, which compose the resonant cavity. ....   | 70 |
| Figure 6.34 Numerically simulated 3D laser beam profile for (a) the 5.5 mm diameter and (b) the 5.8 mm diameter laser rods. ....   | 71 |
| Figure 6.35 (a, b) Photographs and (c) mechanical design of the Nd:YAG solar laser head. ....  | 71 |
| Figure 6.36 Doughnut-shape solar laser beam profiles at a resonant cavity length of 600 mm. Influenced by the slight angular adjustment of the output mirror. ....   | 72 |
| Figure 6.37 Alternative dual-rod laser cavity design to extract one single laser beam from the two Nd:YAG rods. One HR 1064 nm end mirror, two HR 1064 nm folding mirrors, one PR 1064 nm output mirror and two laser rods form the laser resonant cavity in the dual-rod single laser beam approach. ....   | 74 |
| Figure 6.38 Multimode laser output power as a function of the incoming solar power for the single-rod scheme with the 4.5 mm diameter, 25 mm length rod and the dual-rod scheme, with two 3.5 mm diameter, 25 mm length rods. ....   | 74 |
| Figure 6.39 Solar laser head design for the Nd:YAG side-pumped single-rod scheme: a) top view, b) cross-sectional view with the key dimensions indicated and c) 3D view. It consisted of the fused silica aspherical lens, the 2D-shaped-semicylindrical pump cavity and the Nd:YAG laser rod, fixed by two holders. The resonant laser cavity is also represented in a). .... | 76 |
| Figure 6.40 Solar laser head design for the Nd:YAG side-pumped dual-rod scheme: a) top view, b) cross-sectional view with the key dimensions indicated, c) 3D view and d) laser head built for future solar laser experiments. ....  | 77 |
| Figure 6.41 Numerically calculated multimode solar laser output power as a function of the rod diameter and length (L), for the single-rod and the dual-rod side-pumping schemes. ....   | 77 |
| Figure 6.42 Design of the solar laser head with two Nd:YAG crystals in order to obtain one single laser beam from the two rods. Two HR 1064 nm folding end-mirrors, one HR 1064 nm end-mirror and one PR 1064 nm output-mirror compose the folding laser resonant cavity, along with the two laser rods. ....  | 78 |
| Figure 6.43 Multimode solar laser output power as a function of the incoming solar power, for both the single-rod and the dual-rod side-pumping-schemes: the latter in two configurations, two laser beams with its total power and single laser beam. The laser slope efficiencies are also represented. ....   | 79 |
| Figure 6.44 Designs of the dual-rod solar laser heads with longer resonant cavities in order to obtain one single laser beam from the two Nd:YAG rods: a) dual-rod single laser beam with quasi-symmetric beam   |    |

|   |    |
|---|----|
| profile, b) the dual-rod single laser beam, with only two HR 1064 nm folding end-mirrors to compose the folding resonant cavity, along with the PR 1064 nm output mirror.....   | 80 |
| Figure 6.45 (a) Photograph and (b) simplified schematic of the MWSF facility in Odeillo, France. (c) Top-view of the solar energy collection and concentration system (based on [47]). The dimensions of a heliostat are presented in the inset of (c).....   | 83 |
| Figure 6.46 (a) 3D and (b) top view of the solar flux homogenizer, 1657 laser rods and the hexagonal reflector. The concentrated light distribution at the input and output faces of the homogenizer is also presented in (a). (c) Top view of a core-doped Nd:YAG rod. ....  | 83 |
| Figure 6.47 Illustration of the zigzag laser beam merging technique and TEM <sub>00</sub> -mode laser performance for arrays of different N rods. ....  | 84 |
| Figure 6.48 Design for the side-pumped single-rod configuration. It was composed of the fused silica aspherical lens, the semi-cylindrical pump cavity and the Nd:YAG rod.....  | 85 |
| Figure 6.49 Design for the side-pumped dual-rod configuration, consisting in an aspherical lens, two semi-cylindrical pump cavities and two Nd:YAG rods. ....   | 85 |
| Figure 6.50 The absorbed pump flux distributions along five transversal and the longitudinal central cross-sections. a) the single-rod and b) one of the rods of the dual-rod configuration. ....   | 86 |
| Figure 6.51 3D laser beam pattern on the output mirror of the laser resonator for a) 4.0 mm, 25 mm length laser rod of the single-rod configuration and b) the 3.5 mm diameter, 25 mm length laser rods of the dual-rod configuration.....  | 87 |
| Figure 6.52 TEM <sub>00</sub> -mode laser output power as a function of the rod diameter and length for a) the single-rod and b) the dual-rod configurations.....   | 87 |
| Figure 6.53 Schematics of the dual-rod single laser beam from the two Nd:YAG crystals. A compensation of the laser beam profile was achieved, by using the arrangement of three HR 1064 nm folding mirrors (M <sub>1</sub> , M <sub>2</sub> and M <sub>3</sub> ) to compose the folding resonant cavity, along with the mirrors of the laser cavities. .... | 88 |
| Figure 7.1 Sun-Earth relationship. ....   | 91 |
| Figure 7.2 Representative drawing of latitude, solar declination and hour angle, adapted from [93]. ....  | 92 |
| Figure 7.3 Solar declination angle of the Sun [91]. ....  | 93 |
| Figure 7.4 Designed compact solar-pumped laser (μSPL). ....   | 95 |
| Figure 7.5 The Influence of the solar tracking error in the focal spot to pump the dual-rod scheme at a) ΔY, moving upwards from the lower rod to the upper rod; b) ΔX, moving in azimuthal direction; c) ΔY and ΔX simultaneously, moving the focal spot upwards to the upper rod and also to the right in azimuthal direction. ....                       | 96 |
| Figure 7.6 Numerically calculated multimode laser output power as a function of both rod diameter and length for a) the single-rod scheme and b) the dual-rod scheme. ....  | 97 |
| Figure 7.7 The absorbed pump flux distribution along the longitudinal cross-section of the Nd:YAG crystal rods, for the dual-rod and the single-rod schemes, pumped with solar tracking error at a) ΔY and b) ΔX. The laser output powers numerically obtained are also indicated.....  | 97 |
| Figure 7.8 The normalized total multimode laser output power, from the optimal alignment (0.0°) of the solar laser head, as a function of the ΔY and ΔX solar tracking errors, for the dual and the single-rod schemes. ....  | 98 |
| Figure 7.9 The absorbed pump flux distribution along the longitudinal cross-section of the Nd:YAG crystal rods, pumped with solar tracking error at a) ΔY and b) ΔX, for the dual-rod and the end-pumped scheme [17], with the same collection area of NOVA solar system.....   | 99 |

|  |     |
|--|-----|
| Figure 7.10 The normalized total multimode laser output power, from the optimal alignment ( $0.0^\circ$ ) of the solar laser head, as a function of the right and left shift of the $\Delta Y$ and $\Delta X$ solar tracking error, for the dual-rod scheme and the end-pumped scheme [17], pumped with the same collection area of NOVA solar system. It is also shown the tracking error width at 10% laser power loss ( $TEW_{10\%}$ )..... | 99  |
| Figure 7.11 The absorbed pump flux distribution along the longitudinal cross-section of the Nd:YAG crystal rods, pumped with solar tracking error at $\Delta Y$ and $\Delta X$ simultaneously, for the dual-rod and the end-side-pumped scheme [17], pumped with the same collection area of NOVA solar system. The laser output powers numerically obtained are also indicated. ....  | 100 |
| Figure 7.12 The normalized total multimode laser output power, from the optimal alignment ( $0.0^\circ$ ) of the solar laser head, as a function of the simultaneous variation in $\Delta Y$ and $\Delta X$ solar tracking errors, for the dual-rod and the single-rod schemes and the end-side pumped scheme [17], pumped with the same collection area of NOVA solar system. ....  | 100 |
| Figure 7.13 Solar tracking error and its influence in the focal spot to pump the dual-rod scheme at a) altitude direction ( $\Delta Y$ ), b) azimuth direction ( $\Delta X$ ) and c) $\Delta Y$ and $\Delta X$ simultaneously. ....  | 102 |
| Figure 7.14 Absorbed pump flux distribution along the longitudinal cross-section of the Nd:YAG crystal rods, for the dual-rod and the single-rod schemes, pumped with solar tracking error at a) $\Delta X$ and b) $\Delta Y$ . The laser output powers numerically calculated are also shown. ....  | 103 |
| Figure 7.15 Normalized total multimode laser output power, from the optimal alignment ( $0.0^\circ$ ) of the solar laser head, as a function of the $\Delta Y$ and $\Delta X$ solar tracking errors, for the single and the dual-rod schemes and also for the previous dual-rod scheme [28]. ....  | 104 |
| Figure 7.16 Absorbed pump flux distribution along the longitudinal cross-section of both the single and the dual Nd:YAG crystal rods, pumped with solar tracking error at $\Delta Y$ and $\Delta X$ simultaneously. The laser output powers numerically calculated are also shown. ....  | 105 |
| Figure 7.17 The ring-array concentrator is composed of 13 rings and a small Fresnel lens. Inset picture with the pump light distribution at its focal point. ....  | 106 |
| Figure 7.18 Influence of tracking error on output laser power for the 5 mm diameter, 20 mm length Nd:YAG rod. The solar laser power loss is represented in percentage. Altitude and azimuthal tracking error are represented in degrees. ....  | 107 |
| Figure 7.19 Numerically calculated tracking errors for (A) the ring-array assembly and (B) the Fresnel lens pumping scheme with the same diameter. ....  | 107 |
| Figure 7.20 3D RAC solar furnace composed of five seven-ring RACs and four folding mirrors. ....   | 108 |
| Figure 7.21 (a) The absorbed energy by black body detector with the tracking error in altitude and azimuth directions. (b) The heat load distributions of the 3D RAC (1)(2)(3)(4)(5) and the MSSF parabolic mirror (1')(2')(3')(4')(5').....   | 108 |
| Figure 7.22 Normalized total solar laser output power for the single and the dual-rod side-pumping schemes and the end-side pumping scheme [32], as a function of the altitude and azimuth solar tracking errors, ranging from the optimal alignment ( $0.0^\circ$ ) to $0.3^\circ$ using the same RAC solar energy collection and concentration system. ....  | 109 |
| Figure 7.23 The normalized total solar laser output power in percentage, for both the single and the dual-rod side-pumping schemes, and the end-side pumping scheme [32], as a function of the simultaneous variation in altitude and azimuth solar tracking errors, ranging from the optimal alignment ( $0.0^\circ$ ) to $0.3^\circ$ , using the same RAC solar energy collection and concentration system. ....                             | 110 |
| Figure 8.1 Dual-rod side-pumping solar laser head design with the key dimensions indicated: a) front view, b) top view; 3D view with solar rays from the simulation model. The solar laser head consisted in   |     |



|   |     |
|---|-----|
| the fused silica aspherical lens, the semicylindrical pump cavity and two Nd:YAG laser rods, fixed by two rod-holders. ....   | 111 |
| Figure 8.2 The solar laser head project: a) front view; b) side view; c) top view.....  | 112 |
| Figure 8.3 The solar laser head and the pump cavity for the dual-rod solar laser experiments.....   | 113 |
| Figure 8.4 Different views of the pump cavity produced and covered with the reflective surface.....   | 113 |
| Figure 8.5 The Nd:YAG rods mounting into the laser head: a) the special tool built by us to carefully insert the rods and the o’rings into the rod-hole of the laser head; b) Nd:YAG rods mounted inside the laser head. ....   | 114 |
| Figure 8.6 Photographs of the laser head: a) and b) top view of the laser head, with the inserted pump cavity.....  | 114 |
| Figure 8.7 Mini output mirrors fabrication from the large standard commercial output coupler: a) the production of two mini-mirrors for the solar laser experiments; b) The supporting structure for the solar laser head, output couplers and other accessories, where is visible the positioners and the mini-mirrors mounted. ....   | 115 |
| Figure 8.8 The water-leakage tests: a) and b) show the water test in order to avoid any water leakage; .  | 115 |
| Figure 8.9 Solar laser head prepared for the experimental tests at the CNRS-PROMES solar furnace, showing the power meter, the supporting structure for the laser head and its accessories. ....  | 116 |
| Figure 8.10 Experimental test at the solar furnace in France: a) the full set up seen from the back of the parabolic mirror, through the hole in its center, from where the shutter is visible behind the solar laser head; b) alignment testing with the focal spot and a piece of paper; c) open shutter for solar pumping, where it can be seen the heliostat outside the laboratory. .... | 117 |
| Figure 8.11 Experimental model for the solar laser head, consisting in the larger fused silica aspherical lens, the same pump cavity as before and the two Nd:YAG laser rods, fixed by two rod-holders: a) side view and the key dimensions; b) top view.....   | 117 |
| Figure 8.12 New supporting structures for the mini-output mirrors and their X-Y-Z positioners, bolted in the aluminum casing; a) top view; b) side-view. ....   | 118 |
| Figure 8.13 Alignment tests made to form and study the focal spot. It starts in a) and finishes in d), with the formed spherical solar light focus. ....  | 118 |
| Figure 8.14 New supporting structures for the mini-mirrors and their X-Y-Z positioners, bolted in the aluminum casing; a) top view; b) side-view; c) perspective d) attached to the laser head and a metal stick for the installation at the solar furnace.....   | 119 |
| Figure 8.15 a) The schematics for the solar laser head: a) the output mirrors configuration and the vertical set up for the 35 mm length rod; b) Photograph of the solar laser head showing the aspherical lens, the water cooling system, the output mirror and the power detector. ....   | 120 |
| Figure 8.16 Solar laser output power in its vertical setup in the one rod experiments: solar laser output power as a function of the solar power at the focus.....  | 120 |
| Figure 8.17 a) The schematics for the solar laser head: a) the output mirrors configuration and the vertical setup for the 30 mm length rod; b) Photograph of the solar laser head showing the aspherical lens illuminated by the solar light, the water cooling system, output mirrors configuration and the power detector.....   | 121 |
| Figure 8.18 Solar laser output power in its vertical setup in the one rod experiments with the 30 mm length rod: solar laser output power as a function of the solar power at the focus. ....   | 121 |

|   |     |
|---|-----|
| Figure 8.19 a) The schematics for the solar laser head: a) output mirrors configuration and the horizontal setup for the 35 mm length rod; b) Photograph of the solar laser head showing the aspherical lens illuminated by the solar light, the water cooling system and the power detector. ....  | 122 |
| Figure 8.20 Solar laser in its horizontal setup in the one rod experiments with the 35 mm length rod: solar laser output power as a function of the solar power at the focus. ....  | 122 |
| Figure 8.21 a) The schematics for the solar laser head: a) output mirrors configuration and the horizontal setup for the 30 mm length rod; b) Photograph of the solar laser head showing the aspherical lens illuminated by the solar light, the water cooling system and the power detector. ....  | 123 |
| Figure 8.22 Solar laser output power in its horizontal setup in the one rod experiments with the 30 mm length rod: solar laser output power as a function of the incoming solar power. ....   | 123 |
| Figure 8.23 Different solar laser emissions obtained with one rod during the experiments: a) 12.96 W; c) 15.73 W.....   | 124 |
| Figure 8.24 Dual-rod side-pumping solar laser head for the solar laser experiment: The solar laser head consisted in the fused silica aspherical lens, the semicylindrical pump cavity and two Nd:YAG laser rods, fixed by two rod-holders. Both the solar laser emissions were detected by one power meter.....  | 125 |
| Figure 8.25 Dual-rod solar laser output power versus incoming solar power. ....   | 125 |
| Figure 8.26 a) Solar laser head design for the Nd:YAG dual-rod side-pumping and its output couplers configuration; b) Photograph of the solar laser head showing the aspherical lens, the water cooling scheme and the power detectors 1 and 2; c) the two rods illuminated by solar light.....   | 126 |
| Figure 8.27 The solar laser head and the schematics for a), c) two maximum displacements of the focal spot due to the solar tracking error in both altitude and azimuth directions in the vertical setup, corresponding to the positions 1 and 3; b) optimal alignment of the focal spot, corresponding to the position 2; d) normalized total solar laser power for the left and the right laser rods.....   | 127 |
| Figure 8.28 The horizontal setup with two detectors for the solar laser measurements of each one of the rods; in b) the two rods illuminated by solar light during the alignment procedure; in c) The size and the shape of the obtained solar laser beam in a piece of paper, where around 2.0 mm was obtained. ....   | 128 |
| Figure 8.29 The solar laser head and the schematics for a), c) two maximum displacements of the focal spot due to the solar tracking error in both altitude and azimuth directions in the horizontal setup, corresponding to the positions 1 and 3; b) optimal alignment, corresponding to the position 2; d) normalized total solar laser power for the upper and the lower laser rods, as well as the normalized laser power from each laser rod..... | 129 |
| Figure 8.30 Normalized solar laser output power from the vertical and horizontal setups with no Sun tracking, compared to the previous numerical results of the single-rod and the dual-rod side-pumping using a small aspherical lens as secondary concentrator [30].....  | 130 |
| Figure 8.31 Normalized solar laser output power with vertical and horizontal setups with no Sun tracking, compared to the previous numerical results of the solar laser approach using cylindrical lens as secondary concentrator [28], and that of the most efficient end-side-pumping solar laser [17, 28]. ....  | 130 |

# List of Tables

|   |    |
|---|----|
| Table 4.1. Key parameters of the reflective rings and the Fresnel lens of the RAC. ....   | 31 |
| Table 4.2 Conic constants and the conic surfaces for aspherical surfaces. ....  | 33 |
| Table 6.1 Analytically calculated laser output power, slope efficiency and threshold pump power for R = 90%, 94% and 98%. ....  | 46 |
| Table 6.2 Thermal performances of 5.0 and 5.5 mm Nd:YAG rod. ....   | 49 |
| Table 6.3 The numerical results in this work compared with the experimental results of Dinh <i>et al</i> [16] and Liang <i>et al</i> [17]. ....   | 50 |
| Table 6.4 Numerically calculated multimode laser output power, collection efficiency, solar-to-laser power conversion efficiency, slope efficiency, threshold pump power, $M^2$ factors and brightness figure of merit for the single-rod scheme, the dual-rod two laser beams and the dual-rod one laser beam schemes. ....                            | 57 |
| Table 6.5 Numerically and analytically calculated laser output power, slope efficiency and threshold pump power, for the single-rod scheme and the dual-rod scheme with two laser beams and one laser beam. ....  | 57 |
| Table 6.6 Numerically calculated laser output power, collection efficiency and solar-to-laser power conversion efficiency for the single-rod and the dual-rod schemes, and its comparison with the most efficient experimental side-pumped solar laser of Liang <i>et al</i> [76]. It is also shown the collection areas and the solar irradiance. .... | 58 |
| Table 6.7 Solar-to-TEM <sub>00</sub> -mode laser power efficiencies comparison between the single-rod and dual-rod schemes. ....  | 66 |
| Table 6.8 Numerical thermal performances of 4.0 mm diameter 25 mm length of the single-rod scheme and 3.3 mm diameter 25 mm length of the dual-rod scheme. ....   | 66 |
| Table 6.9 Comparison between the LASCAD <sup>®</sup> numerical results and the experimental results of the most recent solar laser experiment [18]. ....  | 67 |
| Table 6.10 The numerical results in this work compared with the experimental results in side-pumped TEM <sub>00</sub> -mode laser production of Vistas <i>et al</i> [45], Liang <i>et al</i> [46] and Liang <i>et al</i> [17]. ....   | 67 |
| Table 6.11 Summary of TEM <sub>11</sub> , TEM <sub>01</sub> <sup>*</sup> , TEM <sub>10</sub> and TEM <sub>00</sub> -mode laser beam profiles by side-pumping the 3mm diameter 30mm length rod with the two-dimensional semi-cylindrical pump cavity. ....   | 73 |
| Table 6.12 Numerically calculated multimode laser output power, slope efficiency, threshold pump power, $M^2$ factors and brightness figure of merit for the single-rod scheme and the dual-rod two laser beams and one laser beam schemes. ....  | 75 |
| Table 6.13 Multimode solar laser output power, collection efficiency, threshold pump power, laser slope efficiency, solar-to-laser power conversion efficiency, $M^2$ factors and brightness figure of merit for the single-rod scheme, the dual-rod two laser beams and the dual-rod single laser beam schemes. ....                                   | 79 |
| Table 6.14 Numerically calculated solar laser $M^2$ factors and resonant cavity lengths for the single-rod scheme and the dual-rod scheme for two laser beams, single laser beam and single laser beam with quasi-symmetric beam profile. ....  | 81 |
| Table 6.15 Numerically calculated laser output power, collection efficiency and solar-to-laser power conversion efficiency for the single-rod and the dual-rod schemes presented in this work, and their comparison with the most efficient experimental side-pumped solar laser of Liang <i>et al</i> [76] and the most efficient numerical            |    |

|   |     |
|---|-----|
| single-rod and dual-rod solar laser [30]. It is also shown the collection areas and the solar irradiance. The collection areas of the solar concentrators are also shown. ....  | 81  |
| Table 6.16 Laser output power, collection efficiency, solar-to-laser power conversion efficiency, brightness figure-of-merit and brightness conversion efficiency for the single-rod and the dual-rod configurations, and its comparison with the most efficient numerical side-pumped TEM <sub>00</sub> -mode solar laser [29]. The respective collection areas are also shown. .... | 89  |
| Table 7.1 Numerically calculated tracking error width at 10% laser power loss, for the single-rod and the end-pumped [17] schemes, and the numerically calculated improvement, using the dual-rod pumping scheme. ....  | 101 |
| Table 7.2 Numerically calculated tracking error width at 10% laser power loss, for the single-rod and the dual-rod schemes and the previous dual-rod scheme [28]. The numerically calculated improvement in tracking error capacity using the dual-rod pumping scheme of the present work is also indicated. ....   | 105 |
| Table 8.1 Tracking error width at 10% laser power loss comparison for dual-rod scheme experimentally tested in vertical and horizontal setups from this work and the numerically calculated single-rod and dual-rod schemes from [30], and the dual-rod and the end-side-pumped schemes from [17, 28]. ....   | 131 |

# Chapter 1 Introduction

The development of renewable energy technology is now widely considered of paramount importance to move towards a sustainable energy generation and climate change mitigation [1, 2]. Problems with energy and its use are related not only to global warming, but also to such environmental concerns as air pollution, ozone depletion forest destruction and emission of radioactive substances. The low energy density and seasonal variations with geographical dependence makes the development of high concentration systems in solar energy an important and challenging investigation [3].

The production of laser radiation from the conversion of solar light has the potential to enable laser applications in a carbon-free way. Solar-pumped lasers have demonstrated their feasibility for space and earth technologies [4-7], and have attracted significant interest in recent years, adding value to solar energy applications [8]. Compared to electrical lasers, solar laser is much simpler and reliable due to the elimination of the electrical power generation and conditioning equipments, offering the prospect of a drastic reduction in the cost of coherent optical radiation for high-average-power applications, leading to numerous environmental and economical benefits. The solar laser is a future emerging technology for space borne applications, where extended run times are required and where compactness, reliability, and efficiency are critical. As solar energy is the main continuous energy source in space, it can be used to pump solid-state lasers either directly or indirectly. Since the strength of the sunlight in space is about twice that on Earth, and there are four or five times the hours of sunlight due to the absence of clouds or night, space - based solar power generation would be a major step forward in terms of fulfilling energy needs. Among the potential space applications of solar lasers are remote sensing from space [4], deep space communications, wireless space power laser beaming [9], asteroid deflection [10].

Solar laser performance has been continuously improved since the first report of 1 W sun-pumped continuous wave (cw) laser in 1966 [11]. Several advances have been made by other researchers using parabolic mirrors to highly concentrate incoming sunlight into a laser medium [12-15]. In 2012, 30 W/m<sup>2</sup> was reported using 4.0 m<sup>2</sup> area Fresnel lens [16]. Multi-rod or single-rod concepts have been experimentally investigated in the last years in order to enhance the overall efficiency and stability [17-20]. Different configurations like end-side-pumping [17, 21-24] or side-pumping [13, 14, 25-27] have been studied through the years. Regarding to tracking error compensation capacity, the side-pumping solar laser approach demonstrated the capability to compensate the inherent solar tracking errors in comparison to the end-side-pumping approaches [28, 29]. Numerical studies have been carried out to improve tracking error tolerance and overall emission stability of solar-pumped lasers [30, 31].

A solar tracking system (STS) enable solar collectors to accurately point towards the sun and compensate for day and season changes observed in altitude and azimuth angles of the sun.

In this thesis, side-pumping approaches were chosen to ensue the enhancing of solar laser efficiency. These configurations are very attractive for several reasons. Side-pumping configuration is more suitable

for laser power scaling and may achieve higher laser beam brightness, since they can provide more uniform energy absorption distribution along the laser crystal. The solar laser beam quality and the extraction of solar laser power can also be improved by the optimization of more laser resonator parameters through the free access to both rod ends. More importantly, the solar tracking error compensation capacity, as compared to that of the end-side-pumping configuration, is another advantage of the side-pumping approach. The solar tracking error in azimuth axis only influences the displacement of the focal spot along the laser rod, usually mounted in azimuth direction. The absorbed solar pump power within the laser rod is therefore not significantly affected by the tracking errors in azimuth axis. Also, the variation of solar tracking error in altitude axis is not significant, especially at noon; thus, it is possible to attain more stable solar laser emission by side-pumping configuration. For the end-side pumping configuration, however, the concentrated solar power at the focus is directly focused onto the end face of the laser rod, and any slight solar tracking error in either azimuth or altitude axis can prevent its stable emission, causing a significant reduction or even the extinction of solar laser output. Besides, the dual-rod side-pumping configuration is also very adequate in order to decrease the thermal prejudicial effects such as heat load, temperature and stress intensity comparatively to the single-rod schemes.

This thesis will show the most recent advancements in solar laser technology, where different approaches and strategies have been developed for solar energy harvesting. The implementation of new materials under solar concentration conditions, innovative solar concentrators, numerical and experimental advancements and strategies aiming to enhance the efficiency and the stability of solar pumped lasers.

Although the most commonly used solar concentrators are the heliostat-parabolic mirror systems and the Fresnel lenses, the former has shadowing areas between the incoming solar radiation and the laser head, while the latter has chromatic aberration, both reducing the overall efficiency. Therefore, the study of other solar energy collection and concentration systems is very important to circumvent the limitations of heliostat-parabolic mirror and Fresnel lens solar laser systems. Numerical studies of innovative solar energy collection and concentration system were performed in order to improve the solar laser efficiency [31, 32]. The easy technical and production accessibility of the ring-array concentrator (RAC) has attracted interest from many solar laser and solar PV researchers around the world. The RAC concentrator is light in weight, can be easily integrated to a solar tracker and prevents the shadow areas caused by both the solar laser head and its associated mechanical structure. More importantly, the RAC concentrator has a significantly reduced construction cost as compared to that of the classical parabolic mirrors of the same diameter. To the best of our knowledge, only a few countries in Europe have high quality primary parabolic mirrors of large diameters. These parabolic mirrors are usually very heavy and the inclusion of a heliostat system is also an expensive issue for the successful operation of a heliostat-parabolic mirror solar energy collection and concentration system. Fresnel lens has even lower production cost, as compared to that of RAC concentrator, but its low transmission efficiency and inherent chromatic aberration properties decrease its performance in the competition for the most efficient production of solar laser power.

A three-folding-mirror laser beam merging technique was developed for the emission of only one single  $TEM_{00}$ -mode solar laser beam from the dual-rod configuration. The arrangement of three HR 1064 nm folding mirrors allowed to significantly enhance the laser beam quality factors so that the merged laser beam profile as described in the previous publication [29] could now be successfully improved. This technique was already successfully investigated for multimode and  $TEM_{00}$ -mode solar laser. Other laser materials can also be pumped by these concepts, such as alexandrite crystal media [5], Ce:Nd:YAG [33,

34], composite laser rods such as YAG–Nd:YAG–YAG undoped–doped–undoped, and Nd:YAG grooved rods [35], Cr:Nd:YAG ceramic medium[36] and Cr: LiCAF [37]. During this thesis I could access the PROMES-CNRS, in France, through the participation in R&D projects supported by SFERA II and SFERA III projects (Solar Facilities for the European Research Area, 7th Framework Program of the EU).

Large numerical advances in side-pumped solar laser collection efficiency, solar-to-laser conversion efficiency and tracking error compensation capacity were developed in this thesis, using the NOVA heliostat-parabolic mirror solar energy collection and concentration system. Two side-pumped configurations, a single rod and a dual-rod pumping schemes, were extensively numerically investigated for TEM<sub>00</sub>-mode and multimode output laser power. The former pumped a thick laser rod, commonly implemented in today's solar pumped lasers, and the latter pumped two thin laser rods simultaneously. Both configurations used a fused silica aspheric lens and a 2D-semicylindrical pump cavity, within which the laser rods were mounted, enabling a tight focusing of the concentrated solar radiation from the focal spot of the parabolic mirror onto the laser rods. Also, for the dual-rod scheme, a solar laser head was built for solar laser experiments, and all its key dimensions and technical concerns such as water cooling and the mechanical fixation of the two Nd:YAG rods were considered in the numerical simulations. Finally, in the experimental work it was achieved promising results with the simultaneous solar laser emission from two laser rods in terms of efficiency and tracking error compensation capacity.

This thesis is divided in nine chapters, as follows:

**Chapter 2** describes the fundamental ideas and concepts about solid-state lasers, from the basic light-matter interaction to the laser oscillator.

**Chapter 3** gives more detail on the most suitable and used laser materials for solar-pumped lasers and the state-of-the-art of this technology.

**Chapter 4** presents the solar energy collection and concentration systems and secondary concentrators used along this thesis.

**Chapter 5** describes the modeling tools used for the numerical simulations of the solar lasers.

**Chapter 6** is dedicated to give a report about the most recent advancements developed along this thesis on solar-pumped lasers, divided in three parts: multimode regime solar laser, TEM<sub>00</sub>-mode solar laser regime and the laser beam merging technique.

**Chapter 7** gives a short review about tracking error systems and studies carried out along this work in order to achieve high tracking error compensation capacity in solar-pumped lasers.

**Chapter 8** describes in detail the experimental work and its results developed in the frame of this thesis to implement the dual-rod side-pumping solar laser.

**Chapter 9** presents the conclusions of the work and addresses future perspectives about the solar-pumped lasers.





# Chapter 2 Solid-state lasers

The first solid-state laser was built by T. Maiman, in 1960. It was a ruby crystal, pumped by a helical flashlamp that surrounded the cylindrical laser rod. The parallel end-faces of the ruby crystal were silvered, with a small hole at one end for observing and measuring the radiation output. The output wavelength was 694 nm. It was T. Maiman who defined the name “laser”, in analogy to maser, as an abbreviation for Light Amplification by Stimulated Emission of Radiation.

In 1964 the host for neodymium ions, namely yttrium aluminum garnet (YAG), was discovered by J. Geusic. Since that time, Nd:YAG remains the most versatile and largely used active material for solid-state lasers. Nd:YAG has a low threshold which permits continuous operation, and the host crystal has good thermal, mechanical, and optical properties. The system efficiency was about a factor of 10 higher with Nd:YAG as compared to ruby. At the end of the 1960s, continuously pumped Nd:YAG lasers with multi-hundred watts output power became commercially available.

The typical linewidth of an Nd:YAG laser is on the order of 10 GHz or 40 pm. Compared to the wavelength, lasers are very narrow-bandwidth radiation sources. A narrow linewidth is important in laser applications in coherent radar systems or in interferometric devices. Single mode operation of solid-state lasers is most readily achieved with small monolithic devices, having resonators which are so short as to allow only one longitudinal mode to oscillate.

In this introductory chapter of solid-state lasers it will be outlined the basic ideas underlying the operation of solid-state lasers.

## 2.1 Light-matter interaction

### Optical amplification

Aiming to understand the operation of the laser, we start know some principles governing the interaction of radiation and matter.

Atomic systems such as atoms, ions, and molecules can exist only in discrete energy states. A change from one energy state to another, called a transition, is associated with either the emission or the absorption of a photon. The wavelength of the absorbed or emitted radiation is given by Bohr’s frequency relation:

$$E_2 - E_1 = h\nu_{21} \quad (2.1)$$

where  $E_2$  and  $E_1$  are two discrete energy levels,  $\nu_{21}$  is the frequency, and  $h$  is the Planck’s constant. An electromagnetic wave whose frequency  $\nu_{21}$  corresponds to an energy gap of such an atomic system can interact with it. A solid-state material can be considered an ensemble of many identical atomic systems. At thermal equilibrium, the lower energy states in the material are more populated than the higher energy

states. A wave interacting with the substance will raise the atoms or molecules from lower to higher energy levels and thereby experience absorption. This is achieved by an external pump source which transfers electrons from a lower energy level to a higher one. The pump radiation causes a “population inversion.”

### **Boltzmann’s Statistics**

According to the statistical mechanics, when a large collection of similar atoms is in thermal equilibrium at temperature T, the relative populations of any two energy levels  $E_1$  and  $E_2$ , must be related by the Boltzmann ratio:

$$\frac{N_2}{N_1} = \frac{g_2}{g_1} \frac{N'_2}{N'_1} = \frac{g_2}{g_1} \exp\left(\frac{-(E_2 - E_1)}{kT}\right) \quad (2.2)$$

where  $N_1$  e  $N_2$  are the number of atoms of the relative energy levels,  $E_1$  e  $E_2$ ; when two or more states have the same energy, the respective level is called degenerate - represented by g; the states of the same energy level, for example  $E_1$ , will be equally populated, therefore  $N_1 = g_1 N'_1$ .

### **Absorption**

At thermal equilibrium, the lower energy states ( $E_1$ ) in the medium are more heavily populated than the higher energy states ( $E_2$  or  $E_3$ ). An electromagnetic wave interacting with the laser system will raise the atoms from lower to higher energy levels and it will produce absorption. In this case, the population of the lower level,  $N_1$ , will be depleted at a rate proportional both to the radiation density  $\rho(\nu)$  and to the population of that level:

$$\frac{\partial N_1}{\partial t} = -B_{12} \rho(\nu) N_1 \quad (2.3)$$

$B_{12}$  is a constant of proportionality with dimensions  $\text{cm}^3/\text{s}^2 \cdot \text{J}$ , related to the probability per unit frequency that transitions are induced by the effect of the field.

### **Spontaneous Emission**

After an atom has been raised to the upper level by absorption, the population of the upper level decays spontaneously to the lower level at a rate proportional to the upper level population:

$$\frac{\partial N_2}{\partial t} = -A_{21} N_2 \quad (2.4)$$

where  $A_{21}$  is a constant of proportionality with dimensions  $\text{s}^{-1}$ . The quantity  $A_{21}$  is called the spontaneous transition probability, because this coefficient gives the probability that an atom in level 2

will spontaneously change to a lower level 1 within a unit of time. Spontaneous emission is a statistical function of space and time. With a large number of spontaneously emitting atoms, there will be no phase relationship between the individual emission processes; the light emitted will be incoherent. Spontaneous emission is characterized by the lifetime of the electron in the excited state, after which it will spontaneously return to the lower state and radiate away the energy.

### Stimulated Emission

There is emission not only spontaneously but also under stimulation by an electromagnetic radiation of appropriate frequency. In this case, the atom gives up a quantum to the radiation field by “induced emission” according to:

$$\frac{\partial N_2}{\partial t} = -B_{21} \rho(\nu_{21}) N_2 \quad (2.5)$$

where  $B_{21}$  is a constant of proportionality with the same conditions as  $B_{12}$  from eq. (2.3). The Einstein coefficients for stimulated emission and absorption are equal ( $B_{21} = B_{12}$ ) when there is no degeneracy or if the levels have unequal degeneracy.

## 2.2 Population Inversion

According to the Boltzmann distribution, in a collection of atoms at thermal equilibrium there are always fewer atoms in a higher level  $E_2$  than in a lower level  $E_1$ . Introducing the absorption coefficient  $\alpha(\nu_S)$ :

$$\alpha(\nu_S) = \left( \frac{g_2}{g_1} n_1 - n_2 \right) \sigma_{21}(\nu_S) \quad (2.6)$$

where

$$\sigma_{21}(\nu_S) = \frac{h\nu_S g(\nu_S, \nu_0) B_{21}}{c} \quad (2.7)$$

Therefore the population difference  $N_1 - N_2$  is always positive, which means that the absorption coefficient  $\alpha(\nu_S)$  in (2.6) is positive and the incident radiation is absorbed. The essential condition for amplification is that there are more atoms in an upper energy level than in a lower energy level, i.e., for amplification:

$$N_2 > N_1 \text{ if } E_2 > E_1 \quad (2.8)$$

Stimulated absorption and emission processes always occur side by side independent of the population distribution among the levels. As far as the population of the higher energy level is smaller than that of the lower energy level, the number of absorption transitions is larger than that of the emission transitions, so that there is an overall attenuation of the radiation. When the numbers of atoms in both states are equal,

the number of emissions becomes equal to the number of absorptions; the material becomes transparent to the incident radiation. As soon as the population of the higher level becomes larger than that of the lower level, emission processes predominate and the radiation is enhanced collectively during passage through the material. To produce an inversion requires a source of energy to populate a specified energy level; this energy can be called the pump energy. The total amount of energy which is supplied by the atoms to the light wave is

$$E = \Delta N h \nu \quad (2.9)$$

where  $N$  is the total number of atoms dropping from the upper to the lower energy level during the time the signal or the pump energy is applied. If laser action is to be maintained, the pumping process must continually supply upper state atoms.

## 2.3 Creation of a Population Inversion

The operation of an actual laser material is properly described only by a many-level energy diagram. The main features can be understood, however, through the three-level or four-level idealizations.

### The Three-Level System

Figure 2.1 depicts a diagram to explain the operation of an optically pumped three-level laser, such as ruby. At the beginning, all ions of the laser medium are in the lowest level 1. The excitation is supplied to the material by radiation of frequencies to produce absorption into the broadband 3. The pump light raises ions from the ground state to the pump band, level 3. The “pumping” band, level 3, is made up of a number of bands, so that the optical pumping can be accomplished over a broad spectral range.

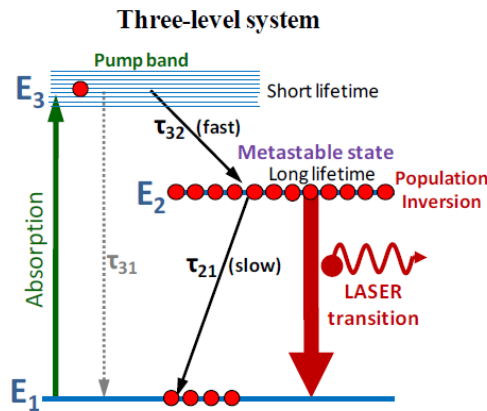


**Figure 2.1** Schematic energy level diagram of a three level system.

In this process, the energy lost by an electron is transferred to the lattice. Finally, the electron returns to the ground level by the emission of a photon. It is this last transition that is responsible for the laser emission. If pumping intensity is below laser threshold, ions in level 2 predominantly return to the ground state by spontaneous emission. Ordinary fluorescence acts as a drain on the population of level 2. It is necessary, in general, that the rate of radiationless transfer from the uppermost level to the level at which the laser action begins to be fast compared with the other spontaneous transition rates in a three-level

laser. Therefore, the lifetime of the  $E_2$  state should be large in comparison with the relaxation time of the  $3 \rightarrow 2$  transition, i.e.,

$$\tau_{21} \gg \tau_{32} \quad (2.10)$$

An important aspect of the three-level system is that the ions are in effect pumped directly from level 1 into the metastable level 2 with only a momentary pause as they pass through level 3. With these conditions, it can be calculated as if only two levels were present. In order that an equal population is achieved between  $E_2$  and  $E_1$  levels, one-half of all atoms must be excited to the  $E_2$  level:

$$N_2 = N_1 = \frac{N_{\text{total}}}{2} \quad (2.11)$$

The disadvantage of a three-level system is that more than half of the ions in the ground state must be raised to the metastable level  $E_2$ . There are thus many ions present to contribute to the spontaneous emission. Moreover, each one of the ions which participates in the pump cycle transfers energy into the lattice from the  $E_3 \rightarrow E_2$  transition. This transition is normally radiationless, the energy being carried into the lattice by phonons.

### The Four-Level System

The four-level laser system, which is characteristic of the rare earth ions in glass or crystalline host materials, is illustrated in Fig. 2.2. Note that a characteristic of the three-level laser material is that the laser transition takes place between the excited laser level 2 and the final ground state 1, the lowest energy level of the system. This leads to low efficiency. The four-level system avoids this disadvantage.

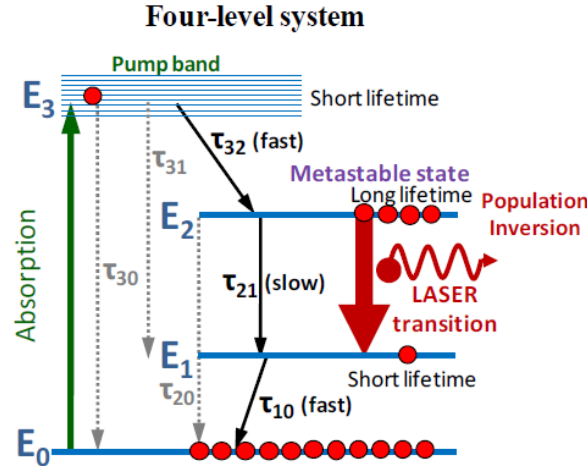


**Figure 2.2** Schematic energy level diagram of a four level system.

The pump transition extends again from the ground state (now level  $E_0$ ) to a wide absorption band  $E_3$ . As in the case of the three-level system, the ions so excited will proceed rapidly to the sharply defined level  $E_2$ . The laser transition, however, proceeds now to a fourth, terminal level  $E_1$ , which is situated above the ground state  $E_0$ . In a four-level system, the terminal laser level  $E_1$  will be empty. To qualify as a four-level system a material must possess a relaxation time between the terminal laser level and the ground

level, which is fast compared to the fluorescent lifetime ( $\tau_{10} \ll \tau_{21}$ ). In addition the terminal laser level must be far above the ground state so that its thermal population is small. The equilibrium population of the terminal laser level 1 is determined by the relation

$$\frac{N_1}{N_0} = \exp\left(\frac{-\Delta E}{kT}\right) \quad (2.12)$$

where  $E$  is the energy separation between level 1 and the ground state, and  $T$  is the operating temperature of the laser material. In a four-level system an inversion of the  $2 \rightarrow 1$  transition can occur even with vanishingly small pump power, and the high pump rate, necessary to maintain equilibrium population in the aforementioned three-level system, is no longer needed. In the most favorable case, the relaxation times of the  $3 \rightarrow 2$  and  $1 \rightarrow 0$  transitions in the four-level system are short compared with the spontaneous emission lifetime of the laser transition  $\tau_{21}$ . The existence of a metastable level is of paramount importance for laser action to occur. The relatively long lifetime of the metastable level provides a mechanism by which inverted population can be achieved.

The mechanism by which energy exchange takes place between the atom and the electromagnetic fields is the dipole radiation. As a consequence of quantum mechanical considerations and the ensuing selection rules, transfer between certain states cannot occur due to forbidden transitions. The term “forbidden” means that a transition among the states concerned does not take place as a result of the interaction of the electric dipole moment of the ion with the radiation field. As a result of the selection rules, an ion may get into an excited state from which it will have difficulty returning to the ground state. A state from which all dipole transitions to lower energy states are forbidden is metastable; an ion entering such a state will generally remain in that state much longer than it would in an ordinary excited state from which escape is comparatively easy. In the absence of a metastable level, the ions which become excited by pump radiation and are transferred to a higher energy level will return either directly to the ground state by spontaneous radiation or by cascading down on intermediate levels, or they may release energy by phonon interaction with the lattice. Thus, population inversion cannot be produced in this case.

## 2.4 Laser oscillator

The laser oscillator is a combination of two components: an optical amplifier and an optical resonator. Besides the pump energy maintaining the non-equilibrium state, it is also mandatory to have a feedback mechanism for the radiation to form the amplified optical field. This requirement can be called by the laser resonator. The optical resonator, comprising two opposing plane-parallel or curved mirrors perpendicular to the active material, acts as a highly selective feedback component by coupling back in phase a portion of the radiation emerging from the amplifying medium. Figure 2.3 shows the basic elements of a laser oscillator. The system starts to oscillate if the feedback is sufficiently large to compensate for the internal losses of the system. The amount of feedback is determined by the reflectivity of the mirrors. Lowering the reflectivity of the mirrors is equivalent to decreasing the feedback factor. The mirror at the output end of the laser must be partially transparent for a fraction of the radiation to “leak out” or emerge from the oscillator, forming the laser output beam.

The arrangement of flashlamp and laser rod shown below is referred to as side-pumped because the pump radiation strikes the laser rod from the side with respect to the direction of propagation of the laser radiation.

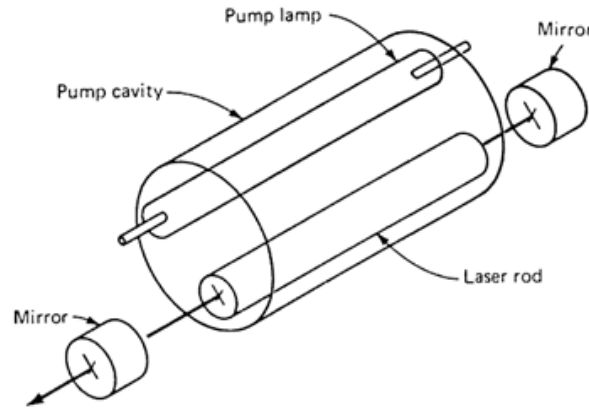


**Figure 2.3** Major components of a light pumped solid-state laser oscillator.

### Oscillator Performance Model

In this section it will be developed a model for the laser oscillation. To achieve a desired output performance with the maximum system efficiency it is of paramount importance to understand the dependency of the laser system design parameters and design issues which may help in the optimization of the overall laser efficiency. This can be represented by the energy diagram schematically illustrated in Fig. 2.4.

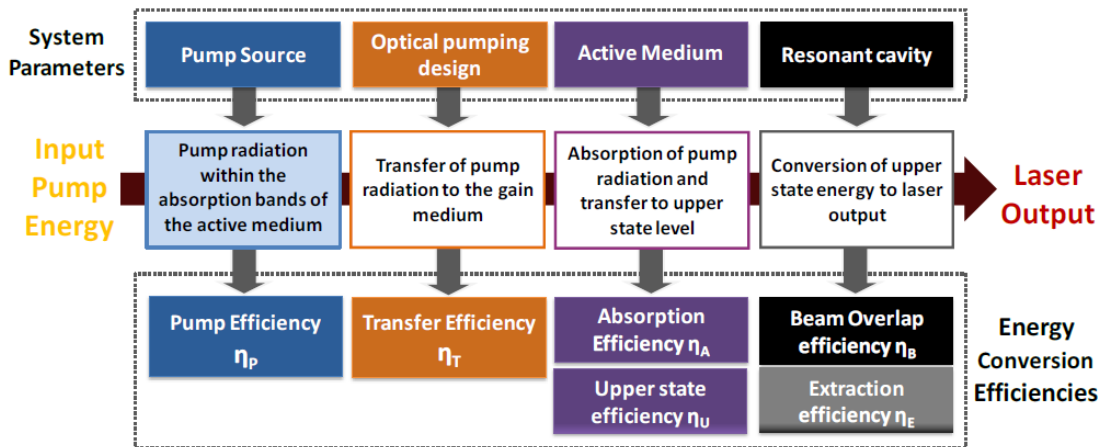


**Figure 2.4** Energy conversion process in a solid-state laser system.

Firstly, it will be discussed the various steps involved in the conversion process of electrical input to laser output. After that, we will relate these energy transfer mechanisms to parameters which are accessible to external measurements of the laser oscillator, explaining the flow of energy from electrical-optical input to laser output radiation, as shown in Fig. 2.4. Also listed are the principal factors and design issues that influence the energy conversion process. There are different ways of partitioning this chain of transfer processes. This approach was chosen from an engineering point of view, which divides the conversion process into steps related to individual system components. As shown in Fig. 2.4, the energy transfer from electrical input to laser output can conveniently be expressed as a four-step process:

### Conversion of Electrical Input Delivered to the Pump Source to Useful Pump Radiation

We define as useful radiation the emission from the pump source that falls within the absorption bands of the laser medium. The pump source efficiency  $\eta_p$  is therefore the fraction of electrical input power that is emitted as optical radiation within the absorption region of the gain medium. The output of a laser diode or a diode array represents all useful pump radiation, provided the spectral output is matched to the absorption band of the gain medium. Typical values of  $\eta_p$  for commercially available cw and quasi-cw diode arrays are 0.3–0.5.

For flashlamp or cw arc lamp-pumped systems, the pump source efficiency may be defined as:

$$\eta_p = \frac{P_\lambda}{P_{in}} = \int_{\lambda_1}^{\lambda_2} \frac{P'_\lambda d\lambda}{P_{in}} \quad (2.23)$$

where  $P_\lambda$  is the spectral output power of the lamp within the absorption bands of the gain material,  $P_{in}$  is the electrical power input, and  $P'_\lambda$  is the radiative power per unit wavelength emitted by the lamp, and the integral is taken over the wavelength range  $\lambda_1$  to  $\lambda_2$ , which is useful for pumping the upper laser level.

Typical values are  $\eta_p = 0.04 - 0.08$ . These numbers are typical for a 5- to 10-mm-thick laser material. The magnitude of  $\eta_p$  is dependent on the thickness of the active material because as the thickness increases, radiation at the wings of the absorption band will start to contribute more to the pumping action. In the case of electrical-pumped lasers the spectral output power of the pump source can be also defined as the product of the electrical-to-optical power efficiency,  $\eta_{EO}$ , and the fraction of the emitted radiation which matches the absorption bands of the active medium,  $\eta_{OVP}$ , also designated as overlap efficiency:

$$\eta_{Pel} = \eta_{EO} \eta_{OVP} \quad (2.24)$$

However, since the pump source of solar-pumped lasers is the Sun, they don't rely on electrical power. Therefore, the pump power efficiency is only affected by the overlap efficiency as follows:

$$\eta_{PSL} = \eta_{ovp} = \frac{\int_{\lambda_1}^{\lambda_2} g\lambda d\lambda}{\int_0^\infty g\lambda d\lambda} \quad (2.25)$$

where  $g\lambda$  is spectral irradiance of the pumping source and  $\lambda_1$  to  $\lambda_2$  is the wavelength range within the absorption bands of the active medium. For Nd:YAG solid-state laser material, which is the most widely used laser material for solar-pumped laser, the overlap between the absorption spectrum of Nd:YAG and the emission spectrum of solar radiation is only  $\eta_{OVP} = 0.16$  [38]. In Fig. 2.5 is given the extraterrestrial and terrestrial irradiances as a function of the wavelength.



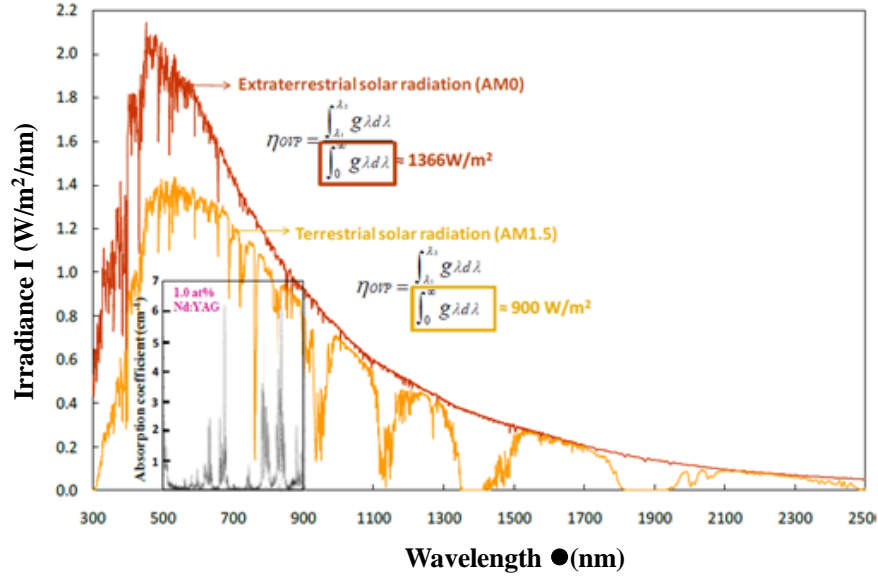


**Figure 2.5** Standard solar emission spectrum in space (AM0) and on the Earth (AM1.5), and the Nd:YAG absorption bands [39].

## TRANSFER OF THE USEFUL PUMP RADIATION EMITTED BY THE PUMP SOURCE TO THE ACTIVE MEDIUM

The energy transfer efficiency,  $\eta_T$ , from the useful pump radiation,  $P_p$ , to the active medium is defined as:

$$\eta_T = \frac{P_T}{P_p} \quad (2.26)$$

where  $P_T$  is the fraction of the radiation transferred into the laser material. This process is influenced by geometrical shape of the concentrating optics and pump cavity, diameter of the pump source and laser rod, as well as the separation distance between them, reflectivity of pump walls, absorption losses in the optical components and coolant fluid, radiation losses through spaces in the pump cavity.

## ABSORPTION OF PUMP RADIATION BY THE ACTIVE MEDIUM AND TRANSFER OF ENERGY TO THE UPPER LASER LEVEL

The absorption efficiency,  $\eta_A$ , can be defined as the ratio of absorbed power,  $P_A$ , to the useful pump power incident on the active medium,  $P_T$ , being a function of the absorption coefficient and the path length of the active medium.

$$\eta_A = \frac{P_A}{P_T} \quad (2.27)$$

The upper state efficiency,  $\eta_U$ , is defined as the fraction of the absorbed pump power,  $P_A$ , which is emitted at the laser transition,  $P_U$ . This efficiency is the product of two contributing factors, the quantum efficiency,  $\eta_Q$ , and the quantum defect efficiency,  $\eta_S$ , also referred as Stokes factor.

$$\eta_U = \frac{P_U}{P_A} = \eta_Q \eta_S \quad (2.28)$$

The quantum efficiency is the ratio between the number of photons contributing to laser emission and the number of pump photons ( $\eta_Q = 0.9$  for Nd:YAG [40]). The Stokes factor is the ratio of the photon energy emitted at the laser transition,  $h\nu_L$ , to the energy of a pump photon,  $h\nu_P$

$$\eta_S = \left( \frac{h\nu_L}{h\nu_P} \right) = \frac{\lambda_P}{\lambda_L} \quad (2.29)$$

where  $\lambda_P$  and  $\lambda_L$  are the pump transition and laser wavelengths, respectively. In solar-pumped lasers, the pump wavelength is defined as the mean absorbed and intensity-weighted solar radiation wavelength:

$$\lambda_P = \frac{\int_a^b I(\lambda) \lambda d\lambda}{\int_a^b I(\lambda) d\lambda} \quad (2.30)$$

where a and b indicates that the integration is performed over the laser absorption bands only. Since the laser wavelength of Nd:YAG laser material is  $\lambda_L = 1064$  nm, for solar-pumped Nd:YAG laser,  $\eta_S = 0.62$  is found based on  $\lambda_P = 660$  nm [26]. In most lasers, the laser wavelength is longer than the pump wavelength (except in upconversion lasers), which means that the energy of the laser photons is smaller than that of the pump photons. As a consequence, the upper state efficiency could not be 100% even if every pump photon could be converted into a laser photon. The difference in the photon energies is the quantum defect,  $q$

$$q = h\nu_P - h\nu_L = h\nu_P \left( 1 - \frac{h\nu_L}{h\nu_P} \right) = \left( 1 - \frac{\lambda_P}{\lambda_L} \right) = 1 - \eta_S \quad (2.31)$$

Both quantum defect and Stokes factor are not related to the quantum efficiency, since the latter refers to the average number of output photons, contributing to the laser emission, per pump photon, rather than to the photon energies.

## CONVERSION OF THE UPPER STATE ENERGY TO LASER OUTPUT

The efficiency of this process can be divided into beam overlap efficiency,  $\eta_B$ , and the extraction efficiency,  $\eta_E$ . The first one expresses the spatial overlap between the resonator modes and the pumped region of the laser medium, which can be given by an overlap integral

$$\eta_B = \frac{\int I_{PM}(r)I_{RM}(r)2\pi r dr}{\int I_{RM}^2(r)2\pi r dr} \quad (2.32)$$

where  $I_{PM}$  represents the absorbed pump intensity distribution and  $I_{RM}$  the resonator mode intensity distribution. The beam overlap efficiency is strongly dependent on the resonator parameters (radius of curvature of the mirrors, cavity length), rod diameter and pumping configuration.

After the pump source in a laser oscillator is turned on, the radiation flux in the resonator that builds up from noise will increase rapidly. A fraction of the intracavity power is coupled out of the resonator and appears as useful laser output. The laser output takes the form:

$$P_{out} = A \left( \frac{1-R}{1+R} \right) I_s \left( \frac{2g_0 l}{\delta - \ln(R)} - 1 \right) \quad (2.33)$$

In this equation,  $I_s$  is a materials parameter,  $A$  and  $l$  are the cross section and length of the laser rod, respectively, and  $R$  is the reflectivity of the output coupler. These quantities are usually known, whereas the unsaturated gain coefficient  $g_0$  and the resonator losses  $\delta$  are not known.  $g_0$  can be related to the system parameters, and describe methods for the measurement of  $g_0$  and the losses  $\delta$  in an oscillator.

In solid-state lasers, optical pumping leads to a radial temperature gradient in the laser rod. As a result, in high-average laser power systems, the laser rod acts like a positive thick lens with an effective focal length, which is inversely proportional to pump power [40, 41]. Pump induced fluctuations on the rod focal length will hence exert strong influence on resonator modes configuration and stability, giving rise to thermally stable zones [40, 41]. Conventionally, lasers are designed to operate at the middle of thermally stable zones, where the fundamental mode size is insensitive to thermal perturbation [40]. Since the TEM<sub>00</sub>-mode Gaussian beam has the smallest beam radius and divergence in a resonator, if the transverse dimension of the gain region is much larger than the TEM<sub>00</sub>-mode size, laser oscillates at several modes [40]. Thus, in case of a uniformly pumped gain medium operated in a highly multimode resonator a beam overlap efficiency equal to unit ( $\eta_B = 1$ ) can be reached. However, to achieve laser operation in fundamental mode, classically a pinhole with similar diameter to the fundamental mode size is inserted inside the laser resonant cavity to prevent higher-order modes from oscillating, considerably reducing the laser extraction efficiency because of poor utilization of the stored energy in the active medium. Thus, a suitable resonator design for efficient energy conversion to the TEM<sub>00</sub>-mode must maximize the overlap integral of the resonator TEM<sub>00</sub>-mode and the pump profile while simultaneously utilizing only the rod to apodize higher-order spatial modes [42]. In side-pumped solar lasers, the adoption of an asymmetric resonator configuration with concave end mirrors of large radius of curvature (RoC) has shown to provide a large spatial overlap between the fundamental mode and pump mode

volumes, as shown in Fig. 2.6. The use of small diameter laser rods played a crucial role. Since the laser rod acts as an aperture, high-order resonator modes can be easily suppressed with small diameter rod due to large diffraction losses, improving thus the beam quality and contributing largely on the efficient extraction of TEM<sub>00</sub>-mode laser power [17, 27, 43-46].



**Figure 2.6** Schematic diagram of the TEM<sub>00</sub>-mode beam propagation along the symmetric laser resonator with large RoC (radius of curvature) mirrors.

The ratio  $L_1/L_2$  is a key parameter for achieving the optimum mode overlap. High multimode, low TEM<sub>00</sub>-mode laser output power levels can be achieved with relatively small  $L_1/L_2$  ratio, as for  $L_1/L_2 = 1$ , where TEM<sub>00</sub>-mode radius,  $\omega_0$ , poorly matches the laser rod radius. However, this comes at the expense of high  $M^2$  beam quality values and thus poor laser beam quality. As  $L_1/L_2$  increases, the TEM<sub>00</sub>-mode size within the rod enhances and higher order modes are suppressed by large diffraction losses. Consequently, spatial overlap between TEM<sub>00</sub>-mode and pump mode volumes becomes larger and fewer higher-order modes oscillate. As pump power increases towards the resonator stability limit,  $\omega_0$  increases further until laser oscillation is only possible for the lowest-order mode.

A strong dependence of the beam overlap efficiency on the radius of curvature (RoC) of end mirrors has been also observed in solar-pumped laser designs [47]. In solar lasers, small laser oscillation mode occurs along the central region of the laser rod when using small RoC mirrors, which causes a large mismatch with the pumped volume. Thus, for the maximum extraction of TEM<sub>00</sub>-mode solar laser power from all the available absorbed solar pump power within the rod, it is preferable to adopt large RoC mirrors. The extraction efficiency,  $\eta_E$ , describes the fraction of total available upper state power,  $P_{U \text{ available}}$ , which appears at the output of the laser,  $P_{out}$ .

$$\eta_E = \frac{P_{out}}{P_{U \text{ available}}} \quad (2.34)$$

Summing up of absorption, scattering and diffraction losses inside the active medium constitutes an important part of round-trip losses. Any imperfection on the optical surfaces or in the optical coatings of the high reflection (HR), anti reflection (AR) or partial reflection (PR) of both laser rod or the resonator cavity mirrors are important constituents of the round-trip loss

The sum of absorption, scattering, and diffraction losses for laser emission wavelength within the active medium constitutes the most important part of round-trip resonant cavity losses. Imperfect high reflection (HR) and anti reflection (AR) coating losses of both laser medium and resonator cavity mirrors are also an important portion of the round-trip losses. The diffraction losses depend on rod diameter, resonator

length and radius of curvature of the resonator mirrors. Usually the diffraction losses of a large diameter rod within a short resonator are very small, even with large concave RoC end mirrors [47].

### The overall system efficiency

The overall laser system efficiency,  $\eta_{\text{system}}$ , of a solid-state laser is given by the product of the individual efficiency factors above mentioned:  $\eta_P$  - pump efficiency,  $\eta_T$  - transfer efficiency,  $\eta_A$  - absorption efficiency,  $\eta_Q$  - quantum efficiency and  $\eta_S$  - Stokes efficiency,  $\eta_B$  - beam overlap efficiency and  $\eta_E$  - extraction efficiency.

$$\eta_{\text{system}} = \eta_P \eta_T \eta_A \eta_Q \eta_S \eta_B \eta_E = \frac{P_{\text{out}}}{P_{\text{in}}} \quad (2.35)$$

### Slope efficiency

The reduction of the output power due to the losses in the resonator can be expressed by the coupling efficiency,  $\eta_C$ :

$$\eta_C = \frac{T}{\delta + T} \approx \frac{-\ln(R)}{\delta + \ln(R)} \quad (2.36)$$

where  $T$  is the transmission of the output end mirror, and  $R$  the reflectivity of the output mirror.  $\delta$  defines the round-trip losses, which reduces the available output power.

$$\delta = 2\alpha l + \delta_D + \delta_M \quad (2.37)$$

$2\alpha l$  represents the two-way loss within the laser medium,  $\delta_D$  represents the diffraction losses and  $\delta_M$  the absorption and scattering losses at the mirrors. The slope of the output versus input curve of a laser,  $\eta_{\text{slope}}$ , is directly proportional to the coupling efficiency, whereas the overall system efficiency of a laser is directly proportional to the extraction efficiency:

$$\eta_{\text{slope}} = \eta_P \eta_T \eta_A \eta_Q \eta_S \eta_B \eta_C = \eta_P \eta_T \eta_A \eta_Q \eta_S \eta_B \left( \frac{-\ln(R)}{\delta - \ln(R)} \right) \quad (2.38)$$

The slope efficiency can also be given as:

$$\eta_{\text{slope}} = \frac{P_{\text{out}}}{P_{\text{in}} - P_{\text{TH}}} \quad (2.39)$$

where  $P_{TH}$  is the pump power required to achieve laser emission threshold.

### Laser output power

The laser output power,  $P_{out}$ , can be expressed in terms of input pump power and measurable quantities by the equation below:

$$P_{out} = (-\ln(R)) \left( \frac{\eta_P \eta_T \eta_A \eta_Q \eta_S \eta_B}{\delta - \ln(R)} P_{in} - A I_S \right) \quad (2.40)$$

where  $I_S$  is the saturation intensity ( $I_S \approx 2.2 \text{ kW/cm}^2$  for a lamp-pumped cw Nd:YAG laser [40] and  $A$  the cross-section area of the laser rod. For solar-pumped lasers the laser output power can be defined by eq. (2.41), where the pump efficiency,  $\eta_P$ , is replaced by the overlap efficiency,  $\eta_{ovp}$ :

$$P_{out} = (-\ln(R)) \left( \frac{\eta_{ovp} \eta_T \eta_A \eta_Q \eta_S \eta_B}{\delta - \ln(R)} P_{focus} - A I_S \right) \quad (2.41)$$

In this case,  $P_{focus}$  represents the collected solar power at the focus or at the input face of the primary solar collector, which has been widely used in both the variants for defining the slope efficiency in many publications on solar-pumped lasers [12, 13, 48]. The respective threshold pump power at the focus, or as the incoming solar power reaching the primary solar collector  $P_{TH}$ , can also be found using the equation below:

$$P_{TH} = \left( \frac{\delta - \ln(R)}{\eta_P \eta_T \eta_A \eta_Q \eta_S \eta_B} A I_S \right) \quad (2.42)$$

# Chapter 3 Solar-pumped lasers

The solar-pumped laser has already a long history. Nearly 60 years of continuous research and development by several groups around the world. Today solar-pumped lasers can be considered a future emerging technology for both renewable energy and laser technology, providing cost-effective solutions for the delivering of laser radiation in a carbon-free way. The direct production of a narrow-band radiation from the conversion of broad-band solar light, with the highest efficiency possible has the potential to enable a wide range of laser applications, adding value to solar energy applications [8]. Sun-powered lasers have demonstrated their feasibility for space and earth technologies [4, 6, 7, 9]. We start this chapter introducing in more detail the most used laser materials in solar-pumped lasers.

## 3.1 Laser materials

### Nd:YAG

The Nd:YAG laser is the most widely used and accessible solid-state laser. It can be pumped by means of flashlamps, cw arc lamps, or laser diodes, and the laser can be operated in cw or pulsed regimes. Its properties are suitable for solar-pumped laser, demonstrates a good thermal performance and thus it is adequate to be under very high light pumping and extreme temperature and stress conditions. Despite the small overlap between the Nd:YAG absorption spectrum and the solar emission spectrum [40], around 16%, Nd:YAG crystal offers advantages over other laser materials, such as good thermal conductivity ( $K = 14 \text{ W m}^{-1} \text{ K}^{-1}$  [40]), high quantum efficiency and tensile strength ( $\sigma = 180\text{-}200 \text{ N/mm}^2$  [40]). It has a stimulated emission cross-section of  $2.8 \times 10^{-19} \text{ cm}^2$  and a fluorescence life time of  $230 \mu\text{s}$  [40].

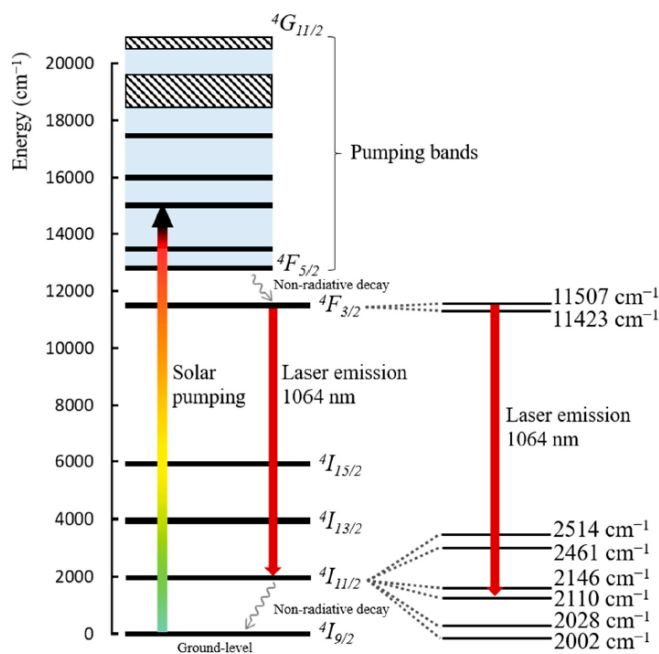


Figure 3.1 Energy level diagram of Nd:YAG [40].

The Nd:YAG is a four-level laser system, as depicted in Fig. 3.1, except for the 946 nm transition, offering substantial laser gain even for moderate excitation levels and pump intensities. Furthermore, the cubic structure of YAG favors a narrow fluorescent linewidth, which results in high gain and low threshold for laser operation. Also, due to the broadband pump absorption of Nd:YAG laser mediums and four-level characteristics, they can be lamp-pumped or solar-pumped [40].

The most used Nd:YAG laser emission wavelength is 1064 nm, because of its high gain compared to other laser emission wavelengths, and corresponds to the transition from  $^4F_{3/2}$  to the  $^4I_{11/2}$  level. Other emission lines are at 946, 1123, and 1319 nm, where Nd:YAG is a quasi-three-level laser system at the 946-nm transition. In a quasi-three-level laser system the lower laser level is so close to the ground state that an appreciable population in that level occurs in thermal equilibrium at the operating temperature, requiring significantly higher pump intensities, compared to four-level laser systems. All other emission lines of Nd:YAG are four-level transitions. Some of these, such as the one at 1123 nm, are very weak, so that efficient laser operation on these wavelengths is difficult to obtain [40].

### Ce:Nd:YAG

Ce:Nd:YAG ceramics have shown to improve diode/lamp-pumped laser efficiency, compared with the Nd:YAG crystal [49-51] because of its strong absorption in visible spectral region at broadband light pumping and efficient energy transfer from  $Ce^{3+}$  to  $Nd^{3+}$ .

The solar irradiance spectrum and the difference between the Nd:YAG and Ce:Nd:YAG absorption spectra are shown in Fig. 3.2. The Nd:YAG absorption spectrum contains various narrow bands extending to visible that match with the solar emission spectrum. However, these sharp absorption bands result in a relatively low overall efficiency when pumped with a broadband pump source. The Ce:Nd:YAG absorption spectrum has two broad absorption bands centered at 340 and 460 nm, which are characteristic of the  $Ce^{3+}$  ion in YAG lattice, [52] and other bands that correspond to the absorption spectrum by  $Nd^{3+}$  ions in YAG structure. [53] The broad, strong absorption band of the  $Ce^{3+}$  ion in the visible range overlaps well with the incident solar spectrum. Therefore, the  $Ce^{3+}$  sensitizer can be used to enhance the overall laser efficiency of Nd:YAG by increasing the pumping efficiency.

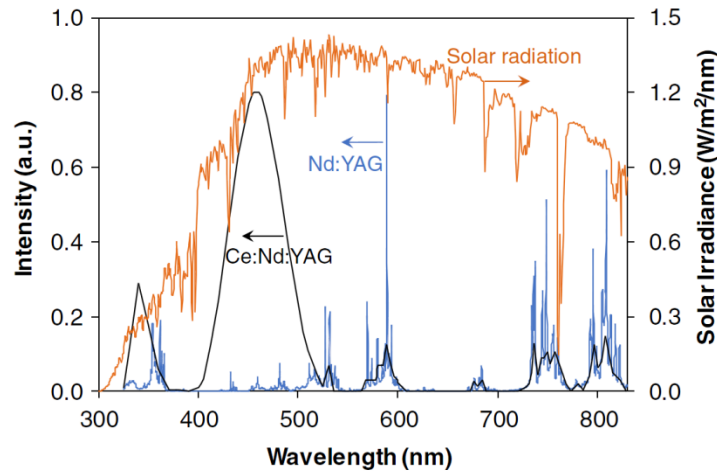


**Figure 3.2** Standard solar emission spectrum (in orange), Nd:YAG [39](in blue) and Ce:Nd:YAG (in black) absorption spectra (adapted from [54]).



An energy transfer mechanism between these two ions, depicted in an energy level diagram, is shown in Fig. 3.3 [49]. When the pump photons are absorbed, the electrons are excited to the d shell of  $\text{Ce}^{3+}$  ion. A small amount of electrons decays to the 4f ground state, producing broadband luminescence in the visible range. However, most of the energy of excited ions is transferred from the 5d state  $\text{Ce}^{3+}$  to the  $^2\text{G}_{7/2}$  level of  $\text{Nd}^{3+}$ , exciting thus  $\text{Nd}^{3+}$  ion.

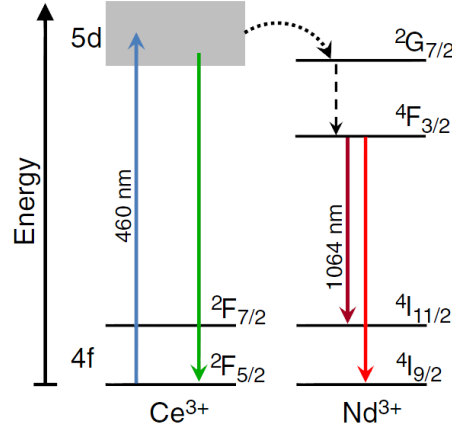


**Figure 3.3** Energy-level diagram illustrating the energy transfer mechanism between  $\text{Ce}^{3+}$  and  $\text{Nd}^{3+}$  ions in the Ce:Nd:YAG ceramic (adapted from [49]). Solid arrows indicate the excitation and the emission processes, and dotted and dashed arrows represent the energy transfer and the nonradiative transition processes, respectively.

Subsequently, the transferred electrons relax to  $^4\text{F}_{3/2}$  levels and finally transit to the ground state of  $\text{Nd}^{3+}$ , leading to the NIR emission, especially at 1064 nm.

The Ce:Nd:YAG ceramic can be a potential gain medium for solar-pumped lasers, particularly because of its strong absorption cross-section in the visible spectral region, which matches with the sunlight spectrum. Payziyev et al. demonstrated, by a simulation model, that the output laser power and the slope efficiency of a Ce:Nd:YAG solar laser could be doubled, compared with that of a Nd:YAG solar laser [55].

## 3.2 State-of-the-art of solar-pumped lasers

The first report of solar-pumped laser occurred shortly after the invention of laser, in 1963 by Kiss et al. [56], although it was called MASER, acronym for Microwave Amplification by stimulated emission of radiation. In 1966 Young succeeded implementing the first solar-pumped laser using Nd:YAG laser material [11]. Fig. 3.4 shows the telescope used by Young for the first solar laser emission. After that date, long time has passed without other experiments or developments in the field until 1984, when Arashi et al. reported a solar laser by pumping a Nd:YAG rod and attaining 18 W cw laser output power [13]. Other materials were also tested with solar pumping radiation, such as liquids, gasses [57], [58] or other materials [59], but the great majority of solar lasers were developed with bulk solid-state media.

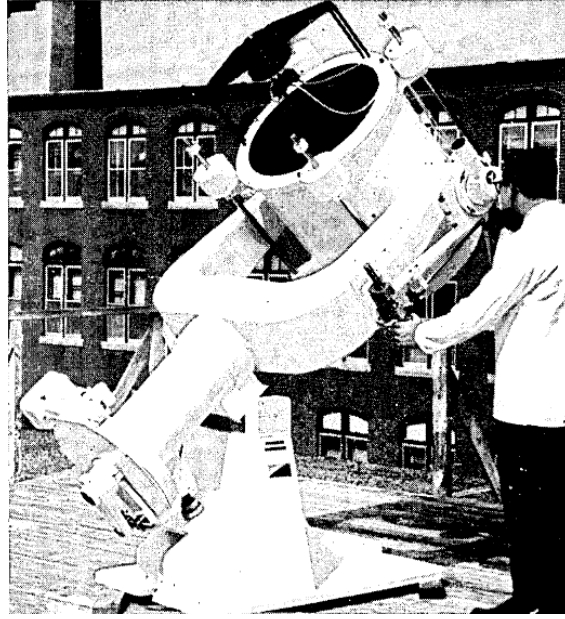


**Figure 3.4** The 61 cm diameter, sun-tracking, equatorial mount solar collector. The water-cooled laser is mounted forward of the bucket.

In 1988, Weksler achieved 60 W and since then, the research on solar laser have increased and added many advances to the field by many researchers [9, 14], [15, 60]. The definition collection efficiency for the solar laser output power has been created, as the laser output power per unit of collection area, or the reflective surface of the primary concentrator used to pump the laser material.

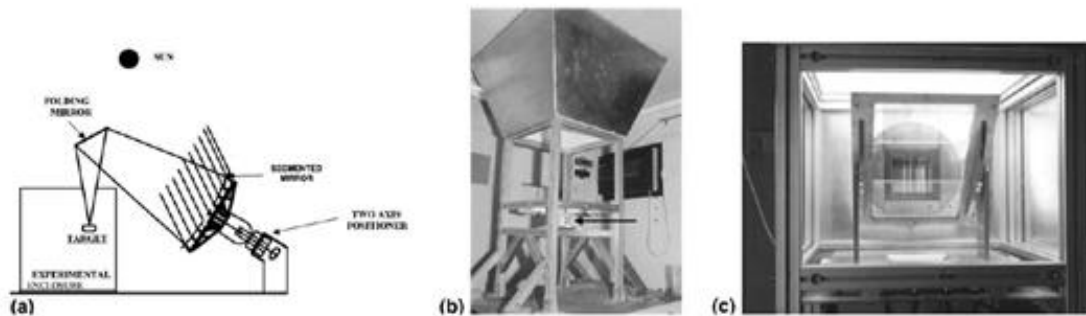


**Figure 3.5** (a) The Astigmatic Corrected Target Aligned solar concentrator. The segmented primary mirror fixed axis is tilted southwards to the direction of the folding mirror center. (b) Safety construction made of inverse cut pyramid and a cubic structure. (c) A cube-like structure containing the filter beamsplitter.

Also, in that prolific year of 2007, Yabe et al. obtained  $18.7 \text{ W/m}^2$  adopting a Fresnel lens as a primary concentrator and Cr:Nd:YAG as the active medium. This has revitalized the solar laser researchers, and in 2011 the Nd:YAG solar collection efficiency reached  $19.3 \text{ W/m}^2$  by Liang et al. [23]. In Fig. 3.6 is shown the solar laser system used.



**Figure 3.6** The Nd:YAG solar-pumped laser system with a 0.9 m diameter Fresnel lens and a laser head positioned in its focal zone.

Questions have been raised about what material could be the most efficient and more suitable to be pumped with solar radiation, Nd:YAG and Cr:Nd:YAG [25].

In 2012, 30 W/m<sup>2</sup> Nd:YAG solar laser collection efficiency was further achieved with 4.0 m<sup>2</sup> of Fresnel lens as a primary concentrator by Dinh et al, being better than that with Cr:Nd:YAG. Slope efficiency of 8.6% was also achieved [16]. Fresnel lenses have attractive advantages for solar laser research because of its reduced weight and cost, but with some practical inconveniences such as chromatic aberration, which is the dispersion of the full spectrum of the solar radiation along its focal zone.

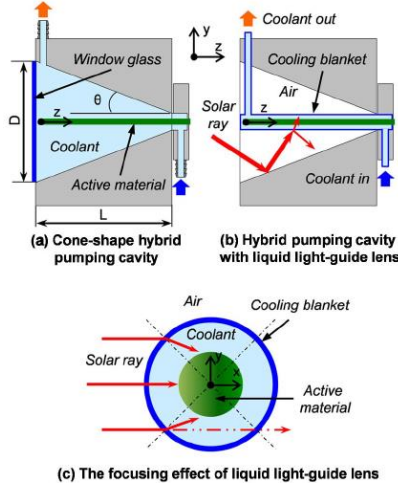


**Figure 3.7** a) cone-shaped hybrid pumping cavity and b) liquid light-guide lens configuration. c) the focusing effect of the liquid light-guide lens.

Also in 2012, Mizuno et al., in Toyota Central Research and Development Laboratories, Japan, demonstrated the realization of a solar-pumped fiber laser operating under natural sunlight using Nd-doped fluoride optical fiber as a laser medium. Their intention was to exploit the very large surface area-to-volume ratio of the fiber media to remove the need for active cooling. 0.57 mW output power was measured [61].

In 2013, a substantial progress in solar laser production with the first TEM<sub>00</sub>-mode solar laser. 2.3 W continuous-wave TEM<sub>00</sub>-mode solar laser power ( $M^2 \leq 1.1$ ) was produced, corresponding to 1.9 W laser beam brightness figure of merit, which was 6.6 times larger than the previous results [62]. In the Fig. 3.8 is presented the Fresnel lens and the solar laser head used.

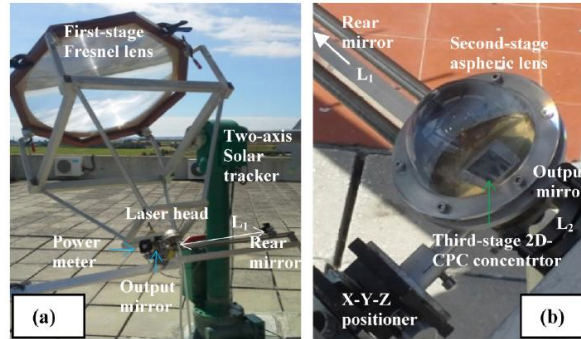


**Figure 3.8** (a) The solar-pumped TEM<sub>00</sub>-mode Nd:YAG laser system (b) The laser head.

The fundamental mode slope efficiency of 0.7% and the collection efficiency of 2.93 W/m<sup>2</sup> were achieved [27].

A Nd:YAG rod with grooved sidewall has been employed for the first time in an end-pumping solar-pumped laser scheme by Xu et al. [24]. 20.3 W cw solar laser output was obtained. The efficiency and beam quality were improved relatively to other unpolished rods. The maximum output power from the grooved rod was more than 50% higher than the maximum output power from the unpolished rod, leading to maximum slope efficiency of 8.34% compared to only 6.13% for unpolished rod.

In 2015, it was reported a large improvement in both collection and slope efficiencies by end-side-pumping a Nd:YAG solar laser through a heliostat – parabolic mirror system in PROMES-CNRS [21]. 56 W cw laser output power was measured, corresponding to 21.1 W/m<sup>2</sup> solar laser collection efficiency. 4.9% slope efficiency was also calculated, corresponding to 170% enhancement over our previous result with same solar facility [22]. Also in 2015, 5.5 W cw TEM<sub>00</sub> mode solar laser was registered, improving the TEM<sub>00</sub>-mode solar laser power [44]. A 4.0 mm diameter, 30-mm-length 1.1 at.% Nd:YAG single-crystal rod was pumped by a light guide with a large rectangular cross section, which also enabled a stable uniform pumping profile along the laser rod, resulting also in an enhanced tracking error compensation capacity. 2.84 W/m<sup>2</sup> TEM<sub>00</sub>-mode collection efficiency and 1.27% slope efficiency were found, representing an enhancement of 150% and 157% respectively over that of the previous TEM<sub>00</sub>-mode solar laser, in 2014.

Still in 2015, in the Massachusetts Institute of Technology, USA, Reusswig et al. presented an architecture for solar pumped lasers that uses a luminescent solar concentrator (LSC) to shift the part of solar spectrum that otherwise could not be absorbed by the active medium, to the frequency range where active medium has strong absorption bands, thereby increasing the pumping efficiency of the laser. In this case, a 750-μm-thick Nd<sup>3+</sup> doped YAG planar waveguide was sensitized by a luminescent CdSe/CdZnS (core/shell) colloidal nanocrystal, yielding a peak cascade energy transfer of 14% and an equivalent quasi-CW solar lasing threshold of 23 W/cm<sup>2</sup>, approximately 230 suns [63].

Quatermann et al. in 2014 proposed a new solar laser architecture with a solar-pumped vertical external cavity surface emitting laser (SP-VECSEL), known as semiconductor disk laser, as a logical continuation of the proven mode-converting capabilities of diode-pumped VECSELs. In experiments using VECSEL gain samples pumped using sunlight, it was demonstrated that no major drop in efficiency is observed beyond that associated with the quantum defect of the pump light, allowing us to predict that SP-VECSEL performance can substantially surpass that of existing solar lasers [64].

In 2016, through the same solar facility of PROMES-CNRS, TEM<sub>00</sub>-mode laser collection efficiency of 4.0 W/m<sup>2</sup> was obtained by side-pumping a 4.0 mm diameter, 34 mm length grooved Nd:YAG rod with an ellipsoid-shaped fused silica secondary concentrator and a 2V-shaped pumping cavity. TEM<sub>00</sub>-mode laser slope efficiency of 2.36% was also achieved [46].

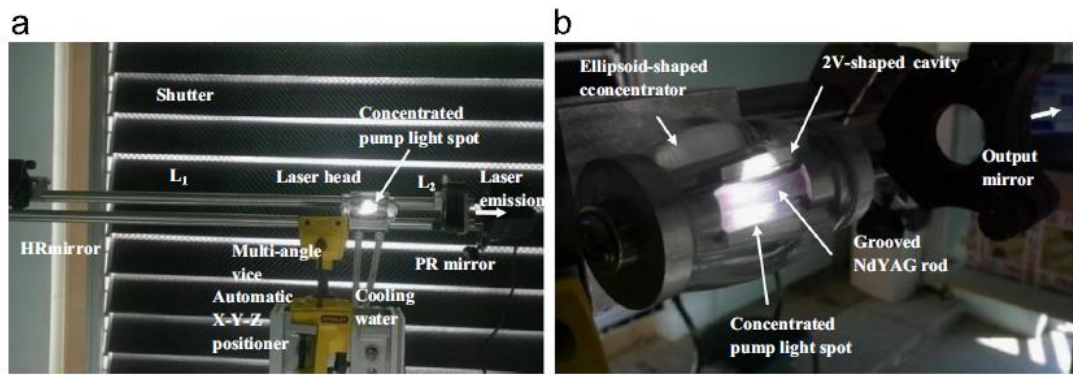


**Figure 3.9** The solar laser head is composed of the ellipsoid-shaped fused silica concentrator and a 2V-shaped pumping cavity within which the grooved Nd:YAG rod is efficiently pumped. (b) The grooved laser rod is cooled by water along 26 mm of its longitudinal surface.

Also in 2016, a new progress in solar laser collection efficiency was reported, by using the NOVA heliostat-parabolic solar energy collection and concentration system. A large aspheric fused silica lens was used to couple efficiently the concentrated solar radiation from the focal zone of a 1.5 m diameter primary concentrator into a 4.0 mm diameter, 35 mm length Nd:YAG single-crystal rod. 29.3 W continuous-wave laser power was measured, attaining 25.0 W/m<sup>2</sup> solar laser collection efficiency, corresponding to 19% increase over the previous results with parabolic mirror. 5.1% result slope efficiency was also measured [65].

Very stable TEM<sub>00</sub>-mode solar laser operation was achieved by using a twisted fused silica light-guide to uniformly side-pumping a thin and long Nd:YAG rod in PROMES-CNRS in 2017 [66, 67]. Excellent TEM<sub>00</sub>-mode laser beam profile at  $M^2 \leq 1.05$  and very good output power stability of less than 1.6% were achieved. Heliostat orientation error dependent laser power variation was considerably less than previous solar laser pumping schemes.

In 2017, by end-side-pumping the 4.0 mm diameter 35 mm length Nd:YAG single-crystal rod with PROMES-CNRS heliostat-parabolic mirror solar energy concentration system, significant progresses in both multimode and fundamental mode regimes were reported [17].

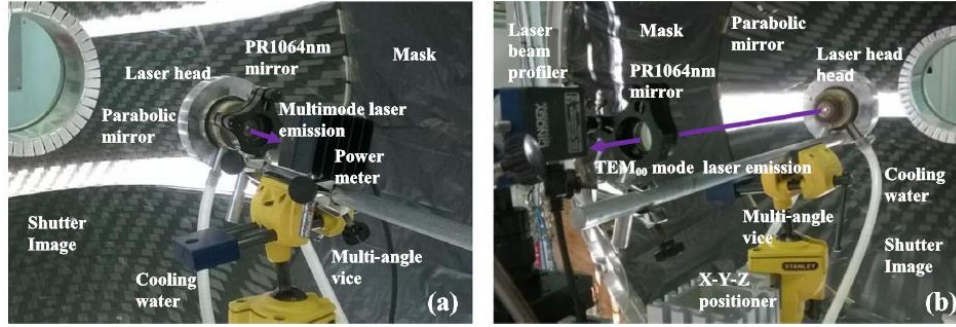


**Figure 3.10** (a) Laser head and output coupler were separated by 11 mm for producing the maximum multimode laser power (b) Laser head and output coupler were separated by 430 mm for the generation of TEM<sub>00</sub>-mode laser power.

Maximum multimode solar laser power of 37.2 W was registered, corresponding to a collection efficiency of 31.5 W/m<sup>2</sup> and 8.9% slope efficiency. By adopting the asymmetric large-mode resonator cavity, 9.3 W cw TEM<sub>00</sub>-mode ( $M^2 \leq 1.2$ ) solar laser power and consequently 7.9 W/m<sup>2</sup> fundamental mode laser collection efficiency was registered, doubling the previous result with parabolic mirror [46].

# Chapter 4 Solar energy collection and concentration systems for solar–pumped lasers

## 4.1 Parabolic mirrors

A parabolic reflector, shown schematically in Figure 1 is a point-focus collector, concentrating solar energy onto a receiver located at the focal point of the parabolic mirror. Its structure must fully track the sun to reflect the beam into the receiver.

A parabola can be defined by an equation with a vertex at  $(x, y) = (0, 0)$  given by:

$$y = ax^2 \quad (3.1)$$

where  $a$  is the aperture of the parabola and it is related to the focal length  $f$  through:

$$f = \frac{1}{4a} \quad (3.2)$$

The shape of the parabola as a function of its focal length can be obtained by:

$$x^2 = 4yf \quad (3.3)$$

A parabolic mirror is able to concentrate solar rays, and this property is schematically represented in Fig. 4.1.

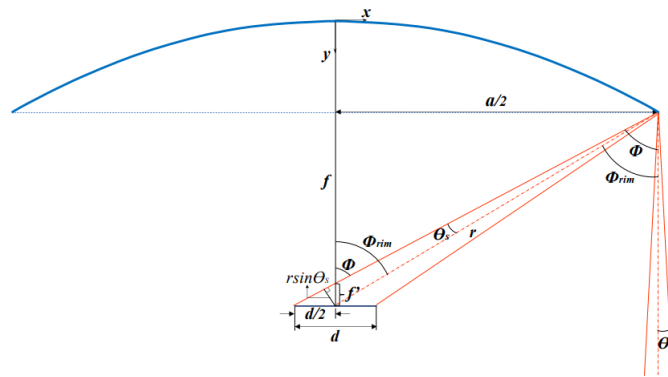


**Figure 4.1** Solar concentration by a parabolic mirror.

The rays parallel to the axis of the parabola are focused into its focal point. However, the Sun rays are not parallel, producing an apparent half-angle  $\theta_s$  of  $0.27^\circ$  in relation to the Earth. In this case the focal width becomes a range defined by  $d$ . Since the parabolic mirror has rotational symmetry about its axis,  $d$  also represents the diameter of the formed image at its focal spot. The width of the focal spot  $d$  is given by:



$$d = 2f' \tan \phi = 2f' \frac{\sin \phi}{\cos \phi} \quad (3.4)$$

where  $\phi = \phi_{\text{rim}} + \theta_S$  is the angle between the y-axis and the reflected light ray with angle  $\theta_S$ .  $\phi_{\text{rim}}$  is the rim half angle. Since

$$f' = \frac{r \sin(\theta_S)}{\cos(\phi)} \quad (3.5)$$

d can be expressed

$$d = \frac{2r \sin(\theta_S)}{\cos(\phi)} \quad (3.6)$$

The aperture of the parabolic mirror  $a$  can be written as

$$a = 2r \sin(\phi_{\text{rim}}) \quad (3.7)$$

We can write the width of the focus  $d$  as a function of the aperture of the parabolic mirror  $a$  as:

$$d = \frac{a \sin(\theta_S)}{\sin(\phi_{\text{rim}}) \cos(\phi_{\text{rim}} + \theta_S)} \quad (3.8)$$

With this equation and as it is shown in Fig. 1, we can observe that for the same focal length  $f$  the width of the focus increases as increases the aperture of the parabolic mirror and, consequently, with the increasing rim angle.

## 4.2 NOVA Heliostat-parabolic mirrors system

NOVA stationary heliostat–parabolic solar system in Fig. 4.2 is composed of a large plane mirror, composed of 2 flat segments, mounted on a two-axis heliostat (Dezhou Gaokeli hydraulic Co. Ltd., China), which redirected the incoming solar radiation towards a stationary parabolic mirror with 1.5 m diameter,  $60^\circ$  rim angle and 660 mm focal length within the laboratory. An effective collection area of  $1.77 \text{ m}^2$  is hence calculated. The plane mirror segments were provided by FLABEG Solar GmbH & Co KG, Germany. Their glass substrate was 4 mm thick, with low iron content, which allowed 93.5% reflectance of the incoming radiation. There is a small shadow area of around  $0.25 \text{ m}^2$  for the solar laser head and its supporting and positioning structure.



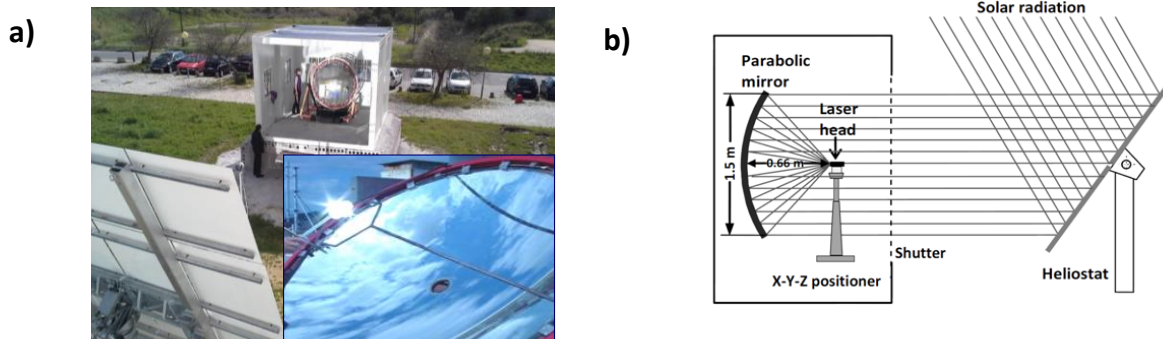


**Figure 4.2** NOVA parabolic-heliostat mirror solar energy collection and concentration system.

The parabolic mirror is back-surface silver coated and 80% reflectivity is assumed for this primary concentrator. The total combined reflectance of both the heliostat and the parabolic mirrors is considered of 75%. For clear sunny days in Lisbon, maximum terrestrial solar irradiance can reach about  $900 \text{ W/m}^2$ . In this case, more than 1.1 kW solar power can be focused into an 8.0 mm full width at half maximum diameter (FWHM) light spot, with near-Gaussian distribution, reaching the peak flux of  $12.6 \text{ W/mm}^2$ .

### 4.3 PROMES Heliostat-parabolic mirror system

The PROMES energy collection and concentration system is composed of a large plane mirror with 36 small flat segments ( $0.5 \text{ m} \times 0.5 \text{ m}$  each), mounted on an automatic two-axis heliostat tracking system, and redirects the incoming solar radiation toward the horizontal axis primary parabolic mirror with 2.0 m diameter,  $60^\circ$  rim angle and 850 mm focal length, as shown in Fig. 4.3. Direct solar irradiance is measured simultaneously during lasing with a Kipp & Zonen CH1 pyrheliumeter on a Kipp & Zonen 2AP solar tracker. All the mirrors are back-surface silver-coated. Due to iron impurities within the glass substrates of plane and parabolic mirrors (with 5 and 10 mm thickness, respectively), along with more than 70-year usage, only 59% of incoming solar radiation is effectively focused to the focal zone. Two sliding doors and a shutter with motorized blades regulate the incoming solar power from the heliostat.

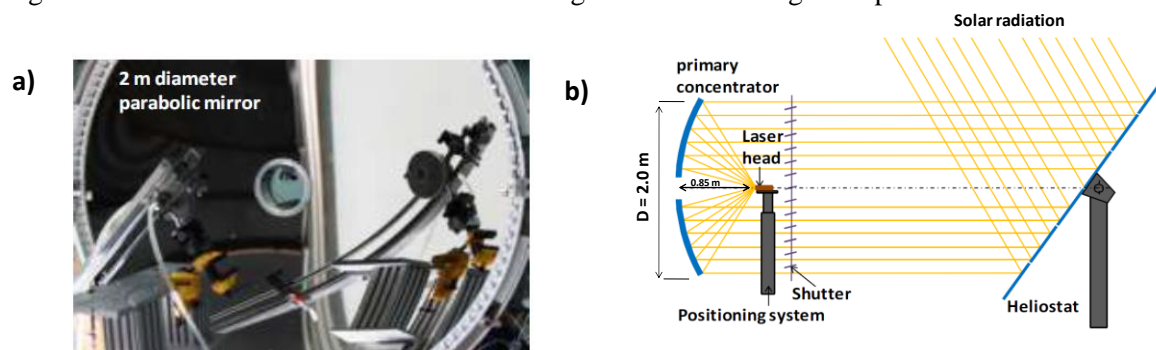


**Figure 4.3** PROMES parabolic-heliostat mirror solar energy collection and concentration system.

On high solar irradiance days, more than 1.8 kW solar powers can be focused into a 15 mm diameter wide light spot, reaching the peak flux of 16 W/mm<sup>2</sup>.

## 4.4 Numerical ring-array concentrator

Ring-array concentrators, introduced by Vasylyev et al [68], consist of a set of concentric reflective rings mounted coaxially to prevent shadowing effect from either incoming or reflected light among the parabolic rings, forming its focal spot in the rear side by superposition of rays from the reflective rings. This configuration permits an efficient integration of components, reducing the shadow areas between the incoming solar light and the laser head, as compared with heliostat-parabolic mirrors. The RAC also avoids the dispersion of the full solar spectrum radiation along its focal zone and can provide higher solar concentration efficiencies compared to Fresnel lenses. In the Fig. 4.4 is shown the modeled RAC used along the thesis.

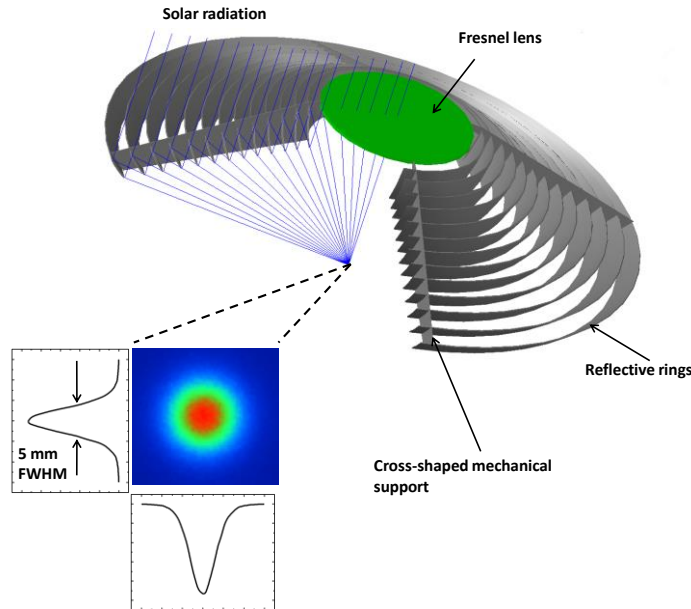


**Figure 4.4** Schematics of the RAC solar energy collection and concentration system. Inset picture with the pump light distribution at its focal zone.

RAC systems were already numerically investigated to produce multimode solar laser using single-rod schemes with end-side-pumping configurations [32, 69], as well as a 3D solar furnace [70]. The RAC used in this thesis is shown in Fig. 4.4, and its parameters were optimized using ZEMAX<sup>®</sup> software.

The RAC consisted of 13 rings, each one with off-axis parabolic profile, 0.6 mm thickness and protective silver coating with 95% reflectivity. In the central region of the RAC, a small Fresnel lens with 12.50 cm diameter was added, due to a cost-efficiency relationship compared to the reflective rings. The Fresnel lens was made of polymethyl methacrylate (PMMA) material, transparent at visible and near-infrared wavelengths while absorbing radiation beyond 2200 nm and cutting UV undesirable solar radiation below 350 nm. Table 4.1 shows the key parameters of each reflective ring, from the largest to the smallest, and of the Fresnel lens.

Table 4.1. Key parameters of the reflective rings and the Fresnel lens of the RAC.

| Element<br>(from the<br>largest to<br>the<br>smallest) | Maximum<br>aperture (m) | Minimum<br>aperture (m) | Radius of<br>curvature<br>(mm) | Vertical<br>position (mm) |
|--|-------------------------|-------------------------|--------------------------------|---------------------------|
| Ring 1   | 0.75                    | 0.70                    | 402                            | 410                       |
| Ring 2   | 0.70                    | 0.65                    | 347                            | 439                       |
| Ring 3   | 0.65                    | 0.60                    | 296                            | 465                       |
| Ring 4   | 0.60                    | 0.55                    | 250                            | 488                       |
| Ring 5   | 0.55                    | 0.50                    | 208                            | 510                       |
| Ring 6   | 0.50                    | 0.45                    | 169                            | 530                       |
| Ring 7   | 0.45                    | 0.40                    | 135                            | 546                       |
| Ring 8   | 0.40                    | 0.35                    | 104                            | 561                       |
| Ring 9   | 0.35                    | 0.30                    | 78                             | 576                       |
| Ring 10  | 0.30                    | 0.25                    | 56                             | 588                       |
| Ring 11  | 0.25                    | 0.21                    | 37                             | 597                       |
| Ring 12  | 0.21                    | 0.16                    | 24                             | 607                       |
| Ring 13  | 0.16                    | 0.13                    | 15                             | 614                       |
| Fresnel<br>lens  | 0.06                    | 0.00                    | 430                            | 890                       |

A cross-shaped mechanical structure, which connects and supports all the 13 rings and the small Fresnel lens, as well as the thickness of each one of the rings, were taken into account. 3% extra loss was hence considered. The parameters given are the maximum and the minimum apertures, the radius of curvature and the vertical position in relation to the focal plane. The RAC solar energy primary collector had 1.50 m diameter, providing an effective solar radiation collection area of 1.76 m<sup>2</sup>. Compared with the heliostat-parabolic mirror systems, the RAC system presented no shadowing area due to the laser head positioning. An average solar irradiance of 950 W/m<sup>2</sup> was considered. 1624 W solar power can hence be focused into a 5.0 mm full-width at half maximum (FWHM) diameter Gaussian solar light spot, 890 mm away from the center of the small Fresnel lens, as shown in Fig. 1.

## 4.5 Aspheric lens secondary concentrator

In this section it will be briefly presented the type of fused silica secondary concentrator studied along this thesis: the aspherical lens. The secondary concentrators are used in solar-pumped lasers to further concentrate the solar radiation onto the laser medium, which is to say a second step of the concentration process to achieve the highest solar concentration factor possible, enabling an efficient solar light pumping. The fused silica lens were chosen because of its transparency over the Nd:YAG absorption spectrum, low coefficient of thermal expansion and resistance to thermal shock.

Fused silica aspherical lens are used to correct spherical aberration. Aspheric lenses have been used for many years to reduce spherical aberration and improve the performance of optical systems. In Fig. 4.5 is shown the spherical lens with the spherical aberration compared to an aspheric lens with no spherical aberration. It is also shown the aspherical lens used for the solar laser experiments fixed by the lens supporter.

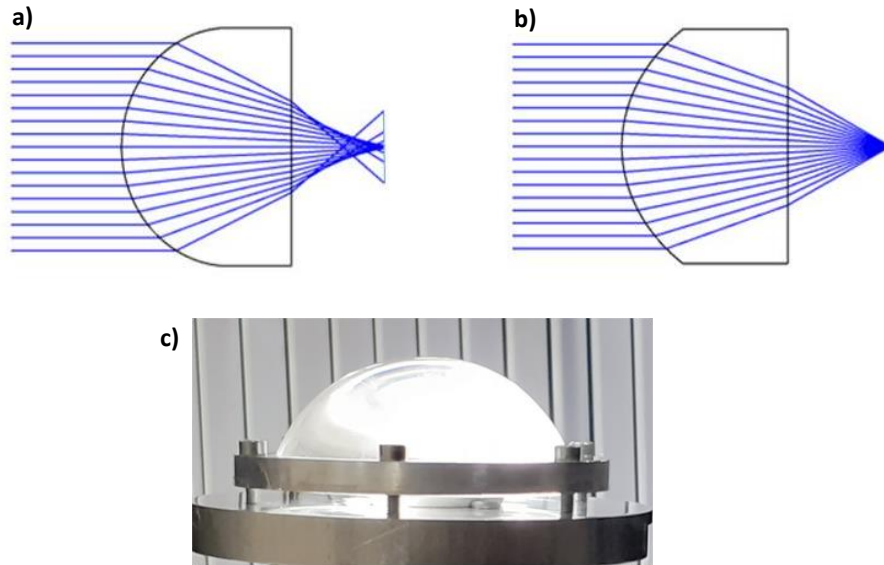


**Figure 4.5** Concentration properties and the: a) spherical lens with spherical aberration and b) aspheric lens (adapted from Shanghai Optics); c) the aspherical lens used for the solar laser experiments fixed by the lens supporter.

Aspheric lenses have been traditionally defined with the surface profile (sag) given by Equation 4.1:

$$Z(s) = \frac{Cs^2}{1 + \sqrt{1 - (1 + k)C^2s^2}} + A_4s^4 + A_6s^6 + A_8s^8 + \dots \quad (4.1)$$

Where  $Z$  is the sag of surface parallel to the optical axis,  $s$  the radial distance from the optical axis,  $C$  the curvature, inverse of radius,  $k$  the conic constant and  $A_4s^4 + A_6s^6 + A_8s^8$  are the order aspheric coefficients.

**Table 4.2** Conic constants and the conic surfaces for aspherical surfaces.

| Conic constant | Conic surface |
|----------------|---------------|
| $k = 0$        | Sphere        |
| $k > -1$       | Ellipse       |
| $k = -1$       | Parabola      |
| $k < -1$       | Hyperbola     |

When the aspheric coefficients are equal to zero they are considered to be a conic. Table 4.2 shows how the actual conic surface generated depends on the magnitude and sign of the conic constant.



# Chapter 5 Modeling tools for solar pumped lasers

In this chapter it will be described the tools for design, modeling and optimization of the solar-pumped lasers. The design parameters of all the solar pumping systems were firstly optimized through ZEMAX<sup>®</sup> non-sequential ray-tracing software. Laser resonator parameters were then modeled by Laser Cavity Analysis and Design (LASCAD<sup>®</sup>) codes to optimize the laser output power and beam quality. After the optimization of the solar laser system design, AUTOCAD<sup>®</sup> software was used to design the mechanical components of the solar laser head for its final machining.

## 5.1 ZEMAX<sup>®</sup> software for modeling and analysis of solar laser systems

ZEMAX<sup>®</sup> is a program used to model and analyze in the design of optical systems. In the solar-pumping system modeling, the Non-Sequential mode is utilized, making the operation of the program easier for systems which are non-imaging. In this method, the rays are traced only along a physically realizable path until they intercept an object. The ray then refracts, reflects, or it is absorbed, depending upon the properties of the object hit. The ray then continues its new path. In non-sequential ray tracing, depending upon the geometry and properties of the objects, rays may strike any group of objects in any order, or may strike the same object repeatedly. For this reason, the non-sequential simulations usually require longer time to obtain accurate results. All the non-sequential objects can be divided into three types: Sources, geometric optical elements and detectors.

Sources are software objects utilized to emit the rays of the simulation, thus representing the solar pumping sources. The geometric optical elements determine the optical components in which the emitted rays are absorbed, refracted, reflected or diffracted. These objects represent in this case the components of the solar energy collection and concentration system and the solar laser head. The detectors objects define the qualitative and/or quantified information of the light rays. With these objects it is possible to design and parameterize the whole optical system, which transfer the pump energy into the active medium of the solar laser.

### Solar pumping source

There are several different types of source objects in ZEMAX<sup>®</sup>, but for solar pumping source we use the “source ellipse”, as shown in the Fig. 5.1.

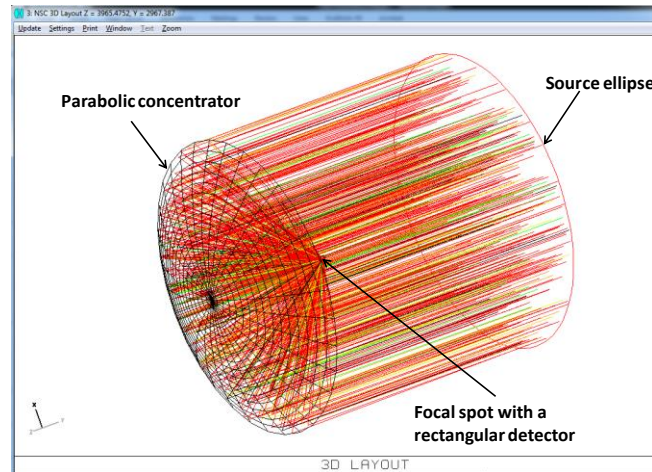


**Figure 5.1** Non-sequential objects of ZEMAX® software to model and analyze a parabolic concentrator solar system.

We can select the source ellipse as shown in the Fig. 5.2.

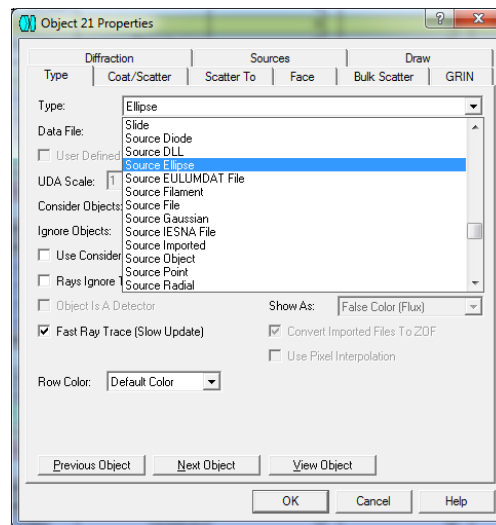


**Figure 5.2** Selection of the source ellipse in the source objects of ZEMAX®.

In all objects there are parameters to place our solar system in space, such as the position and angle x, y and z axes and the direction, tilting about x, y and z. Also, we have some parameters to define our solar source.

*Layout* and *analysis rays*: give how many random light rays will be launch from the source when performing the analysis. In order to accurately compute the energy distributions on the detectors, it generally requires a larger number of rays in the *analysis rays*, differently from the *layout rays*, just for visualization. The number of rays used in the simulation process is a critical parameter throughout the process of modeling the system. On one hand, a reduced number of analysis rays in the simulations reduce the computing time but the accuracy of the results is low. On the other hand, a high number can give more accurate results, but the time spent in each simulation is also increased.



*Power*: the total power used by the source. Here we consider the terrestrial solar irradiance, but also define an effective pump power of the light source, taking into account the overlap between the absorption spectrum of the active medium and the solar emission spectrum, which is considered as 16% [38] for the Nd:YAG laser material. Thus, for the modeling of the Nd:YAG solar laser system, the source power is calculated by the product of the source area ( $\pi \times 0.45 \text{ m}^2 = 0.636 \text{ m}^2$ ) with the terrestrial irradiance considered (for this case we will assume  $850 \text{ W/m}^2$ ) and the overlap between the Nd:YAG absorption spectrum and the solar emission spectrum:  $P_{\text{source}} = 0.636 \text{ m}^2 \times 850 \text{ W/m}^2 \times 0.16 \approx 86.5 \text{ W}$ . Other parameters have specific meanings, such as: *X-Half Width* and *Y-Half Width*, defined in millimeters (mm). The Source Ellipse is a flat elliptical surface. Thus, since the amount of radiation collected is relative to the collection area of the primary concentrator, which is usually circular, the dimensions of the solar pumping source are similarly defined to those of the primary concentrator, in order to simplify the parameterization of the solar system, as observed in FIG. 4.3. By defining the same X, Y *Half-Width* of 450 mm, as shown in FIG. 5.3, it means that the solar radiation is collected by a circular primary concentrator with 900 mm diameter. *Source distance* is the distance from the source to the object.

The figure shows three screenshots of the 'Non-Sequential Component Editor' window, each displaying a table of parameters for a source ellipse.

**Table 1 (Top Screenshot):**

| Object Type  | Comment | Ref Object | Inside Of | X Position | Y Position | Z Position | Tilt About X | Tilt About Y |
|--------------|---------|------------|-----------|------------|------------|------------|--------------|--------------|
| 1 Source El. |         | 0          | 0         | 0.000      | 150.000    | 0.000      | 90.000       | 0.000        |

**Table 2 (Middle Screenshot):**

| Object Type  | # Analysis Rays | Power(Watts) | Wavenumber | Color # | X Half Width | Y Half Width | Source Distance | Cosine Exponent |
|--------------|-----------------|--------------|------------|---------|--------------|--------------|-----------------|-----------------|
| 1 Source El. | 250000          | 86.500       | 0          | 0       | 750.000      | 750.000      | 0.000           | 4.000E+004      |

**Table 3 (Bottom Screenshot):**

| Object Type  | # Layout Rays | # Analysis Rays | Power(Watts) | Wavenumber | Color # | X Half Width | Y Half Width | Source Distance |
|--------------|---------------|-----------------|--------------|------------|---------|--------------|--------------|-----------------|
| 1 Source El. | 500           | 1000000         | 86.500       | 0          | 0       | 750.000      | 750.000      | 0.000           |

**Figure 5.3** List of parameters of the source ellipse used for solar-pumped lasers in the Non-sequential component editor.

*Cosine exponent*, the origin of each ray launched by the source lies on the surface of the ellipse with a uniform distribution, but the distribution of the rays may emit in a cosine distribution of the form

$$I(\theta) = I_0(\cos(\theta))^n \quad (4.1)$$

where  $n$  is the cosine exponent, which may be any value greater than or equal to unity. When using  $n$  different from zero, the source acts like a diffuse cosine source.

The figure shows a 'Wavelength Data' dialog box with two columns of data. The left column contains 12 entries, and the right column contains 12 entries. Each entry consists of a checked checkbox, a wavelength value in micrometers, and a weight value.

| Use                                    | Wavelength (micrometers) | Weight | Use                                    | Wavelength (micrometers) | Weight |
|--|--------------------------|--------|--|--------------------------|--------|
| <input checked="" type="checkbox"/> 1  | 0.52700000               | 65     | <input checked="" type="checkbox"/> 13 | 0.79000000               | 67     |
| <input checked="" type="checkbox"/> 2  | 0.53100000               | 70     | <input checked="" type="checkbox"/> 14 | 0.79300000               | 66     |
| <input checked="" type="checkbox"/> 3  | 0.56800000               | 82     | <input checked="" type="checkbox"/> 15 | 0.80300000               | 65     |
| <input checked="" type="checkbox"/> 4  | 0.57800000               | 87     | <input checked="" type="checkbox"/> 16 | 0.80500000               | 64     |
| <input checked="" type="checkbox"/> 5  | 0.58600000               | 88     | <input checked="" type="checkbox"/> 17 | 0.80800000               | 63     |
| <input checked="" type="checkbox"/> 6  | 0.59200000               | 88     | <input checked="" type="checkbox"/> 18 | 0.81100000               | 62     |
| <input checked="" type="checkbox"/> 7  | 0.73200000               | 81     | <input checked="" type="checkbox"/> 19 | 0.81500000               | 61     |
| <input checked="" type="checkbox"/> 8  | 0.73600000               | 80     | <input checked="" type="checkbox"/> 20 | 0.82000000               | 60     |
| <input checked="" type="checkbox"/> 9  | 0.74300000               | 80     | <input checked="" type="checkbox"/> 21 | 0.86500000               | 49     |
| <input checked="" type="checkbox"/> 10 | 0.74600000               | 78     | <input checked="" type="checkbox"/> 22 | 0.88000000               | 46     |
| <input checked="" type="checkbox"/> 11 | 0.75300000               | 77     | <input type="checkbox"/> 23            | 0.55000000               | 1      |
| <input checked="" type="checkbox"/> 12 | 0.75800000               | 76     | <input type="checkbox"/> 24            | 0.55000000               | 1      |

At the bottom, there is a 'Select ->' dropdown menu set to 'F, d, C (Visible)', a 'Primary:' dropdown menu set to '17', and buttons for 'OK', 'Cancel', 'Help', 'Save', and 'Load'.

**Figure 5.4** Solar source wavelength data, for solar-pumping of a Nd:YAG laser.

The larger  $n$ , the narrower the distribution becomes. The apparent half angle of  $\pm 0.27^\circ$  subtended by the Sun has to be considered in the analysis of any solar laser system, which is defined to be among 30000 to 80000.

For the laser medium Nd:YAG, 22 absorption peaks can be defined in the numerical data [17, 43, 45, 46]. The central wavelengths of these peaks were 527 nm, 531 nm, 568 nm, 578 nm, 586 nm, 592 nm, 732 nm, 736 nm, 743 nm, 746 nm, 753 nm, 758 nm, 790 nm, 793 nm, 803 nm, 805 nm, 808 nm, 811 nm, 815 nm, 820 nm, 865 nm, 880 nm. All the above peaks and their respective absorption coefficients are added to the glass catalogue for the Nd:YAG material. Spectral irradiance ( $\text{W}/\text{m}^2/\text{nm}$ ) values corresponding to the above mentioned 22 peak absorption wavelengths could be consulted from the standard solar spectrum for one-and-a-half air mass (AM1.5) [39]. The absorption spectrum and the wavelength dependent refractive indexes of fused silica and water are also included in the numerical data.

### Solar energy collection and concentration systems and solar laser head in ZEMAX®

Parabolic mirrors and RACs' systems, as well as the laser head components, are modeling using the different non-sequential geometrical optical components, as observed in FIG. 5.5.

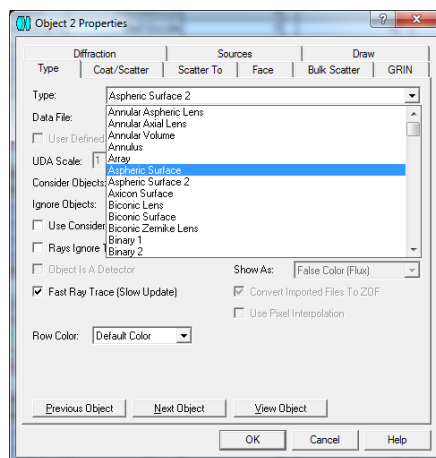


**Figure 5.5** Geometrical objects in ZEMAX®. *Aspheric Surface* represent the object selected to model the Parabolic mirror system.

The ZEMAX® has an extensive list of objects with geometric shapes that can be used to absorb, reflect refract the rays emitted by the source object, depending on the function for which it is intended to function, being also able to import objects from AUTOCAD®.

The properties of reflection, absorption or refraction of the objects are parameterized according to the selected material in the editor menu of non-sequential components.

If the object has the function of only absorbing the *absorb* function is selected in material box. If the object has the properties of only reflecting, such as the Aspheric Surface for the modeling of the parabolic mirror, the *mirror* function is selected. However, in the case of a refractor material, such as the laser rod, all the characteristics must be defined through the *Glass Catalog* menu, as shown in Fig. 5.6, within which it is possible to change the values or create new materials. One of the parameters that can be changed is the absorption/transmission spectrum of the material, which depends on the wavelength,

doping material, absorption coefficient, the temperature and the distance traveled by the radiation inside the material.

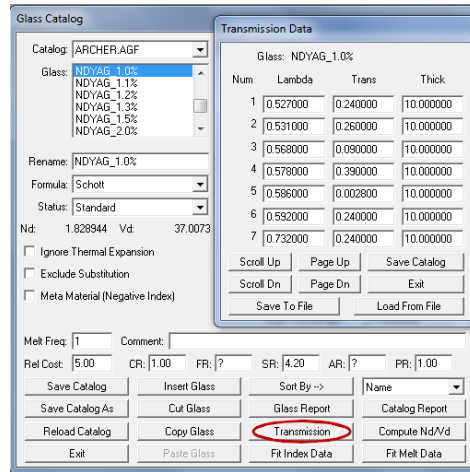


Figure 5.6 Transmission data of the Nd:YAG laser material.

### Detectors for the absorbed pump power analysis

In order to produce information about the incident or absorbed pump power it is necessary to use the detector objects in ZEMAX®. A *detector rectangular* is usually used because permits us to record the data, such as the incident power and angle, the bidimensional power distribution and the profile of incident/absorbed power in the area defined by the detector. This type of detector can be placed either inside or outside of an object and have the function of absorbing, reflecting or not have any effect on the incident radiation. The shape of the detector is limited to a rectangular surface defined by the user. The image resolution can be adjusted by the number of pixels of the detector, taking into account the influence on the total time of computation required for each simulation. If we aim to produce an analysis of the incident or absorbed pump power within a laser material, or to obtain the pump profiles presented along this thesis, a *detector volume* is used. Similar to the rectangular detector, the detector volume is limited to the shape of a rectangle. However, with this detector it is possible to add a new dimension to obtain the power information, since it has a 3D shape, whose dimensions are defined by the user, as well as the number of voxels, the pixels of volume. The resolution of the volume detector has also a great influence on the computing time of each simulation. The path length in each voxel is then found. With this value and the effective absorption coefficient of the Nd:YAG material, its absorbed solar pump power within the laser medium can be numerically calculated by summing up the absorbed pump radiation of all zones. The absorbed pump flux data from the ZEMAX® analysis was then processed by LASCAD® software for optimization of the laser resonator parameters.

## 5.2 LASCAD<sup>®</sup> software for modeling of the solar laser resonant cavity

LASCAD<sup>®</sup> software can combine several simulation tools to optimize the laser resonator design: *The Thermal and Structural Finite Element Analysis (FEA)*; the *ABCD Gaussian Beam Propagation Code*; and the propagation algorithm of non-Gaussian beams – the *Beam Propagation Method (BPM)*. Thus, it is possible to model resonant cavities through the analysis of the thermal lensing effects, which is one of the key problems in solid-state lasers, multimode and TEM<sub>00</sub>-mode output power, laser beam quality and profile, as well as laser beam propagation outside the laser cavity, taking into account several laser parameters, such as reflectivity, radius of curvature and distance between cavity components, diffraction losses, gain saturation, etc.

### Finite element analysis (FEA)

The Finite Element Analysis (FEA) calculates the heat, temperature and stress induced factors in the laser medium, taking into account the laser material parameters, pump configuration and cooling geometry. LASCAD<sup>®</sup> provides some pre-defined models of typical configurations, as shown in FIG. 5.7(a).

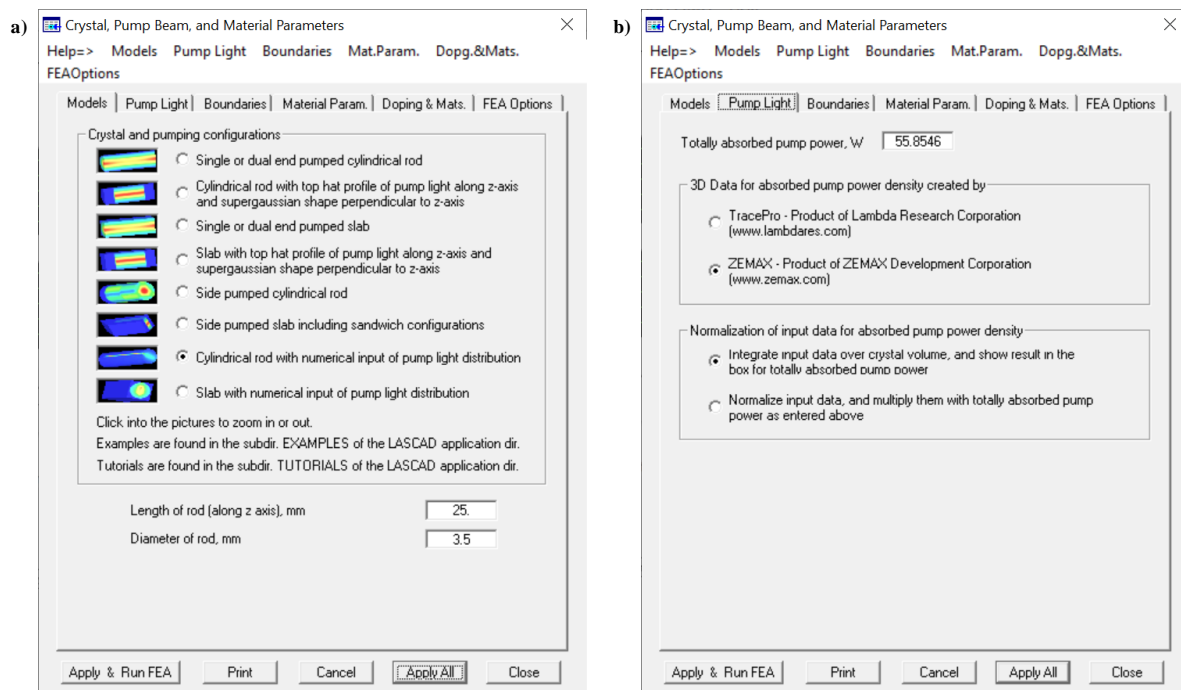


**Figure 5.7** a) Active medium and pump configuration models of LASCAD<sup>®</sup>; b) importation of data files from ZEMAX<sup>®</sup>.

However, the pumping scheme may have very particular characteristics, which are not defined in the pre-defined models of LASCAD<sup>®</sup>, as in the case of solar-pumped lasers. Thus, to accurately model the solar laser systems, it is possible to import files from ZEMAX<sup>®</sup> ray-tracing software, as indicated in Fig. 5.7b, whose content is the three-dimensional distribution of the absorbed pump power by the active medium defined in ZEMAX<sup>®</sup>. The parameters of the active medium, and the material properties can be defined in the *boundaries* and *material parameter* menus, as shown in the Fig. 5.8.

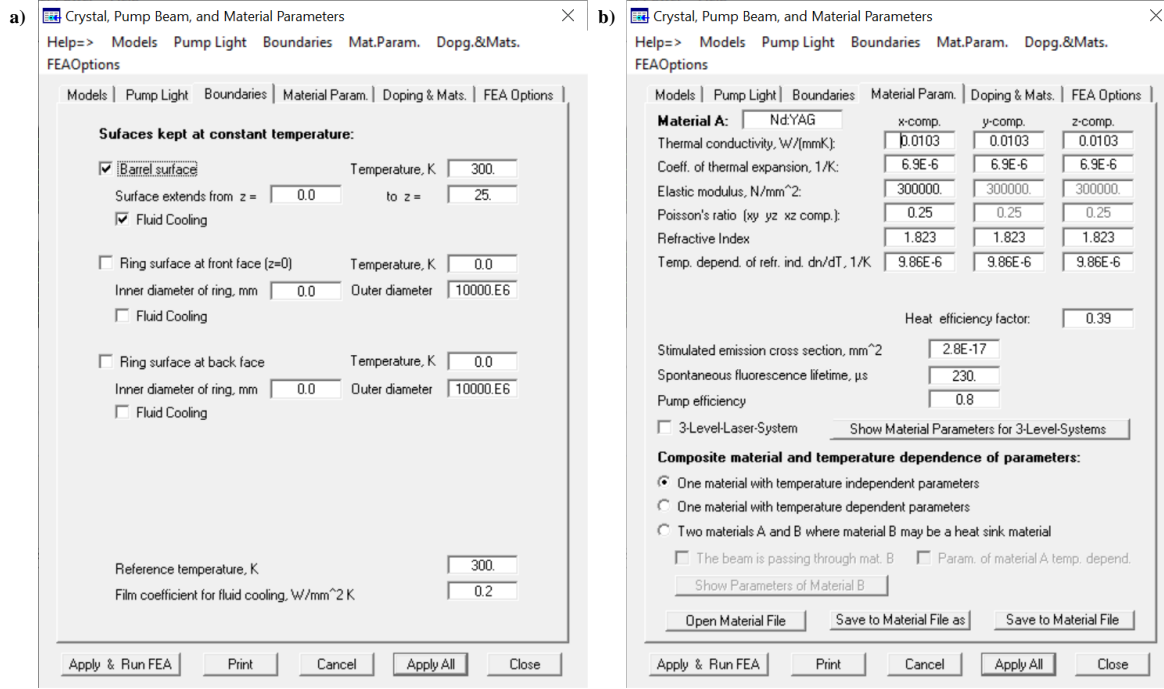


**Figure 5.8** a) The cooling parameters of a side-pumping scheme solar laser; b) Nd:YAG laser material parameter.

The simulation conditions, such as the resolution and the number of iterations are defined in Tab *FEA options*. After defining all the parameters related to pumping, active medium and cooling, the thermal and structural analysis by finite elements (FEA) can be started. The thermal analysis is carried out through the determination of the heat load distribution, the 3D differential equations of the heat conduction and the differential equation of structural deformation [71]. The differential equations of heat conduction are given by:

$$-\text{div}[k(T)\nabla(T)] = Q(x, y, z) \quad (4.2)$$

with  $k$  the coefficient of thermal conductivity,  $T$  the constant temperature of the active medium surface,  $Q$  the heat load distribution in the active medium. The differential equations of structural deformation are given by the strain-stress relation:

$$(\varepsilon_{ij}) = (\alpha_x, \alpha_y, \alpha_z)(T - T_0) + \frac{1}{E} C^{-1} (\sigma_{ij}) \quad (4.3)$$

where  $\varepsilon_{ij}$  is the strain tensor given by:

$$(\varepsilon_{ij}) = \frac{1}{2} \left( \frac{\partial u_i}{\partial x_j} + \frac{\partial u_j}{\partial x_i} \right) \quad (4.4)$$

$\alpha_i$  is the coefficient of thermal expansion,  $E$  the elastic modulus,  $\sigma_{ij}$  the stress tensor and  $u_i$  the displacement. To solve the differential equations, the LASCAD<sup>®</sup> FEA code discretizes the laser crystal into a tri-dimensional grid, whose resolution is defined by the user, and produces the iterations through an amount of times. The accuracy of the results depends directly on the grid resolution, as well as on the

simulation time. Running the FEA generates the data used for simulating thermal lensing within the laser cavity. It also produces three dimensional representations of the crystal heat load, temperature and stress, relying on the above equations which describe heat conduction, structural deformation and absorption [71]. The remaining results of the algorithms within LASCAD® depend on the results from the FEA.

## GAUSSIAN ABCD MATRIX APPROACH

By using the *FEA mesh* results, the thermal lensing element can be defined by parabolic approximation. In the same way, a fit of the deformed end faces of the crystal is accomplished. With the obtained parabolic coefficients, it is possible to model the resonant cavity through the Gaussian beam propagation matrix algorithm (*ABCD code*). In the results of the ABCD matrix approach, fundamental mode spot sizes, as well as multimode, are visualized along the resonator axis, as shown in Fig. 5.9.

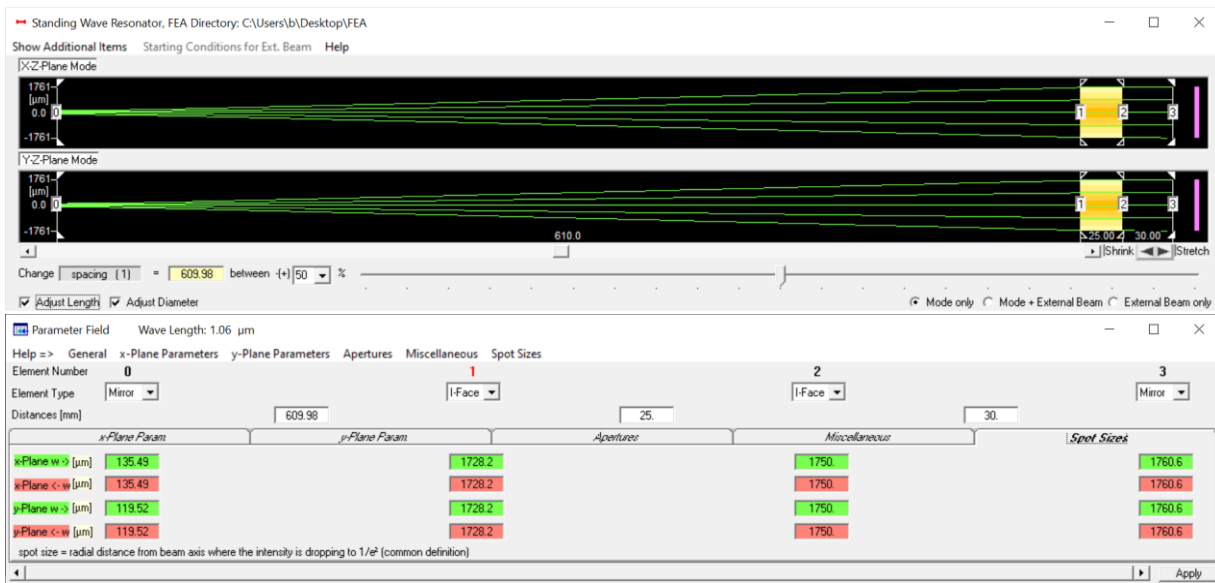


**Figure 5.9** The resonant cavity and the laser beam represented in the propagation planes of X-Z and Y-Z for the TEM<sub>00</sub>-mode solar laser emission.

With the Gaussian modes distribution and absorbed pump power distribution we can calculate the multimode or TEM<sub>00</sub>-mode laser power in continuous - wave (cw) or pulsed operation mode using the *Laser Rate Equations* [72]. The laser emission curve as a function of either the power absorbed or the reflectivity of the output coupler can be displayed, as shown in FIG. 5.10(a) and FIG. 5.10(b), respectively. In addition, it is possible to optimize the laser resonator by changing its length, angle between the various components, applying mirrors or lenses, changing the focal length of the components, etc.

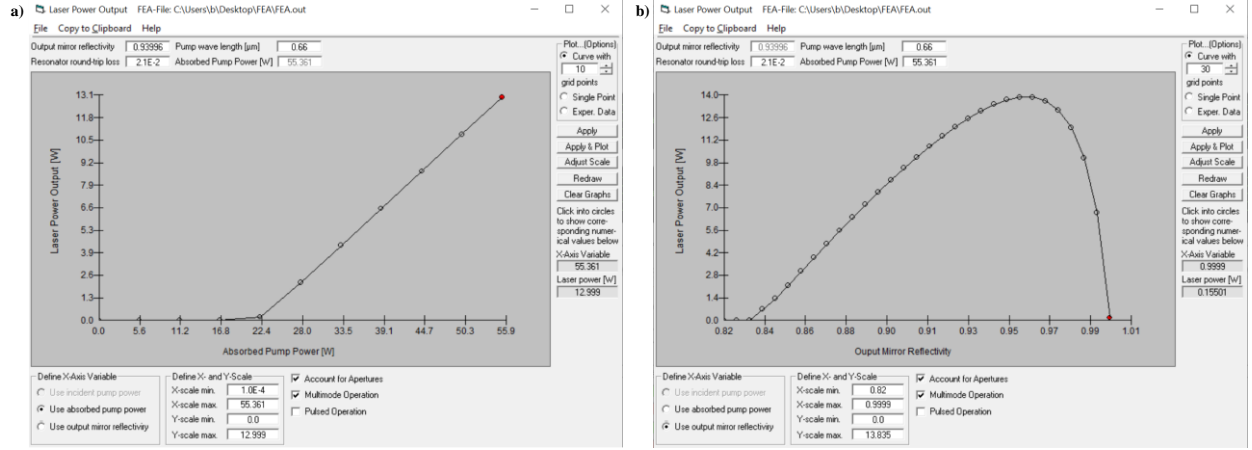


**Figure 5.10** Calculated laser output power as a function of a) the absorbed pump power and b) the reflectivity of the output coupler used.

The laser output power,  $P_{out}$ , is obtained in LASCAD<sup>®</sup> analysis by computing the number of laser photons passing the output coupler per unit of time through the power output relation:

$$P_{out} = h\sigma_L S_L \frac{c(-\ln(R_{out}))}{2L} \quad (4.5)$$

where  $h$  is the Planck's constant,  $\sigma_L$  the frequency of laser light,  $S_L$  the number of photons passing through the output coupler,  $c$  the vacuum speed of light ( $3 \times 10^8$  m/s),  $R_{out}$  the reflectivity of the output mirror, and  $L$  the optical path length of the resonant cavity, which is given by:

$$L = L_{cavity} + nL_A - L_A \quad (4.6)$$

where  $L_{cavity}$  is the total cavity length,  $L_A$  the active medium length and  $n$  is the refractive index of the laser material. The number of photons in the laser resonant cavity can be obtained by the equation:

$$S_L = \tau_c \eta_p S_p \iiint \frac{P_0(x, y, z)}{1 + \frac{n}{c\sigma\tau S_L S_0(x, y, z)}} dV \quad (4.7)$$

This equation can be solved by iterative integration, where the integral extends over the volume of the active medium.  $\tau_c$  is the mean life time of laser photons in the laser resonant cavity;  $\eta_p$  is the pump efficiency;  $S_p$  is the total number of pump photons absorbed in the crystal per unit of time;  $P_0(x, y, z)$  is the absorbed pump power density distribution normalized over the crystal volume;  $\sigma$  the stimulated emission cross section;  $\tau$  is the spontaneous fluorescence life time of upper laser level; and  $S_0(x, y, z)$  the normalized distribution of the laser photons.

## LASER BEAM PROPAGATION METHOD (BPM)

FEA results can be used as input for a Fast Fourier Transform (FFT) split-step Beam Propagation Method (BPM) [73]. This code is able to give a full 3D simulation of the interaction of the wave-front propagating through the thermally deformed laser crystal. Based on the principle of Fox and Li [74] a series of round-trips through the resonator is computed, which finally converges to the fundamental mode, or to a superposition of higher-order transverse modes. The intensity profile at the output mirror, as it is computed with the increasing number of iterations, is also shown as the computation is running. The BPM code also takes into account the gain dynamics and diffraction effects, due to the finite extension of apertures and mirrors.

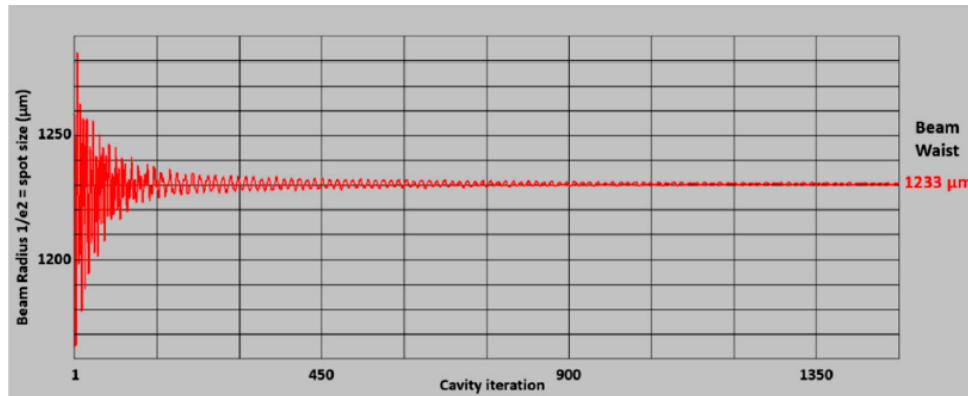


**Figure 5.11** Laser beam waist at the output mirror calculation by BPM cavity iterations function of LASCAD<sup>®</sup> software.

The numerical optimization of the solar laser systems is based in both ZEMAX<sup>®</sup> and LASCAD<sup>®</sup>, which give the key parameters and dimensions of the experimental work to be developed.



# Chapter 6 Recent advancements in solar-pumped laser technology

## 6.1 Solar-pumped lasers in multimode regime

Usually, solar-pumped lasers can operate in two major different regimes: multimode and single-mode regimes and the numerical and experimental research on solar lasers have focused on the improvement of its efficiency parameters, such as collection efficiency, beam brightness and slope efficiency. In the last four years, many advances have been made in the frame of this thesis in collaboration with the colleagues and Professor, not only on solar laser efficiency issues, but also on its versatility, for example in the study of the solar laser production with other solar concentrators with different forms and sizes, and in order to develop other shapes of solar laser radiation, such as doughnut shapes, and to investigate stable laser emission, with solar laser heads specially designed to have large tracking error tolerances. In this chapter it will be described the advancements and developments in solar-pumped lasers in multimode regime technology.

### 6.1.1 Improving solar-pumped laser efficiency by a ring-array concentrator

In the beginning of 2017, my first solar laser model was developed using a numerically modeled ring-array concentrator (RAC) as primary concentrator, described in Chapter 4, using an effective collection area of  $1.76 \text{ m}^2$  and a solar irradiance  $950 \text{ W/m}^2$ , by the first time used to pump a solar laser. The configuration chosen was the end-side-pumped, desiring to reach high collection efficiencies with this generally more efficient arrangement. A large fused aspherical lens was implemented to further concentrate the solar radiation, allowing a tight focused pump flux radiation to couple the thick  $5.5 \text{ mm}$  diameter laser rod [32].

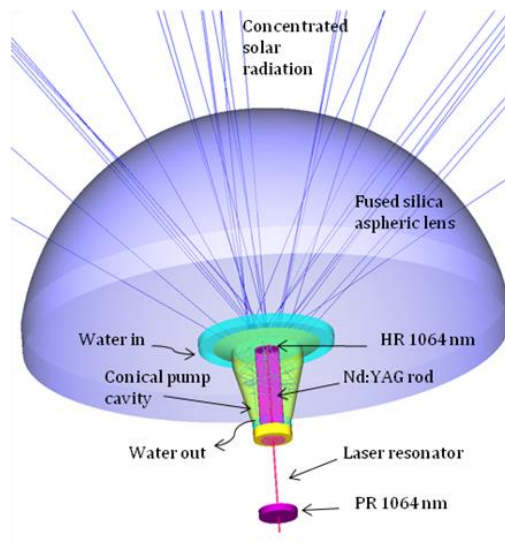


**Figure 6.1** Design of the Nd:YAG rod solar laser head, composed of a large fused silica aspheric lens, conical pump cavity and the Nd:YAG rod.

The solar laser head studied is shown in Fig. 6.1, and it was composed by the aspherical lens and a conical-shaped pump cavity, within which the Nd:YAG rod is mounted. The aspheric lens is 100 mm in diameter, 47 mm in height, 60 mm in front surface radius of curvature and -0.003 in rear  $r^2$  parameter. It allows an efficient coupling of the solar radiation from the focal spot to the Nd:YAG rod. The zigzag passage of the rays within the conical cavity ensures a multi-pass process to side pump the rod [22]. The inner wall of the pumping cavity is bonded with a protected silver-coated aluminum foil with 98% reflectivity. The hollow pump cavity, the Nd:YAG rod and the end face of the aspheric silica lens are all cooled by water. The direct cooling of the rod is essential for an efficient and rapid removal of the generated heat, preventing UV solarization and IR heating.

The analytical calculations used the equations already described in Chapter 2. For this work it was determined  $\eta_T = 0.85$  and  $\eta_A = 0.82$ . In Table 6.1 is shown the analytically calculated laser output power, slope efficiency and threshold pump power for 90%, 94% and 98% reflectivity. Since the above mentioned equations do not rely upon the detailed absorbed pump distribution within the laser rod, only approximate values are presented in Table 6.1. More accurate laser output power is calculated by both ZEMAX<sup>®</sup> and LASCAD<sup>®</sup> software in the next section since they involve the detailed absorbed pump power distribution and its associated thermal effects within the laser rod.

**Table 6.1** Analytically calculated laser output power, slope efficiency and threshold pump power for R = 90%, 94% and 98%.

| Reflectivity, R (%)                  | 90    | 94    | 98    |
|--------------------------------------|-------|-------|-------|
| Laser output power, $P_{out}$ (W)    | 52.8  | 59.6  | 52.1  |
| Slope efficiency, $\eta_{slope}$ (%) | 5.3   | 5.0   | 3.7   |
| Threshold pump power, $P_{th}$ (W)   | 559.0 | 351.9 | 153.4 |

In Fig. 6.2 is shown the absorbed pump flux distributions along one longitudinal and five transversal central cross-sections of the 5.0 mm diameter, 20 mm length Nd:YAG rod. The red color means maximum pump absorption, whereas blue means little or no absorption. The main contribution to the absorbed pump power comes from end pumping, which produces a more intense pump flux within the upper-end region of the laser rod. Different RAC focal lengths were numerically investigated, ranging from 50 mm to 650 mm, in order to maximize the pumping flux into the Nd:YAG crystal rod. The absorbed pump flux data from the ZEMAX<sup>®</sup> analysis was then processed by LASCAD<sup>®</sup> software for optimization of the laser resonator parameters.

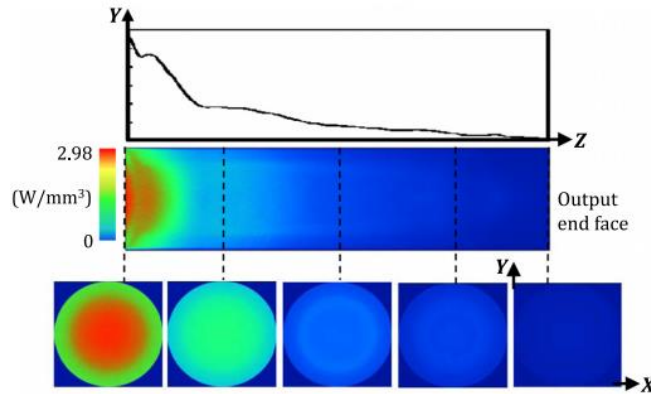


**Figure 6.2** Absorbed pump flux distributions along the 5 mm diameter, 20 mm length Nd:YAG rod, at the focal distance of 410 mm.

Laser resonant cavity analysis and optimization of the laser output power were carried out using LASCAD<sup>®</sup> software, described in a previous section of this thesis. The effective pump power of the light source took into account about 16% overlap between the absorption spectrum of the 1.0 at% Nd:YAG laser medium and the solar spectrum [38]. The stimulated emission cross-section of  $2.8 \times 10^{-19} \text{ cm}^2$ , a fluorescence life time of 230  $\mu\text{s}$  [40], and an absorption and scattering loss of  $0.003 \text{ cm}^{-1}$  for the 1.0 at% Nd:YAG medium were adopted in the LASCAD<sup>®</sup> analysis. The mean absorbed and intensity-weighted solar pump wavelength of 660 nm [26] was also assumed in the calculations. Imperfect optical coating losses were assumed for the laser rods and the high reflection (HR 1064 nm) end mirror, respectively. The diffraction losses depend strongly on rod diameter, resonator length and radius of curvature (RoC) of the resonator. LASCAD<sup>®</sup> beam propagation method predicts the diffraction losses for the specific rod diameter and lengths.

The optical laser resonator is formed by both HR 1064 nm reflector and PR 1064 nm output coupler, in a resonator cavity with 11 mm length and -1 m radius of curvature (RoC). The laser output power as function of the RAC focal lengths, for 15, 20, 25 and 30 mm rod lengths (L) and 5 mm diameter (D) is shown in Fig. 6.3. At the focal length of 410 mm, the maximum laser output power was gradually obtained by reducing the rod length from 30 to 20 mm. Further reduction in rod length to 15 mm finally decreased the laser power. The best value of 67.3 W was found for  $L = 20 \text{ mm}$ .

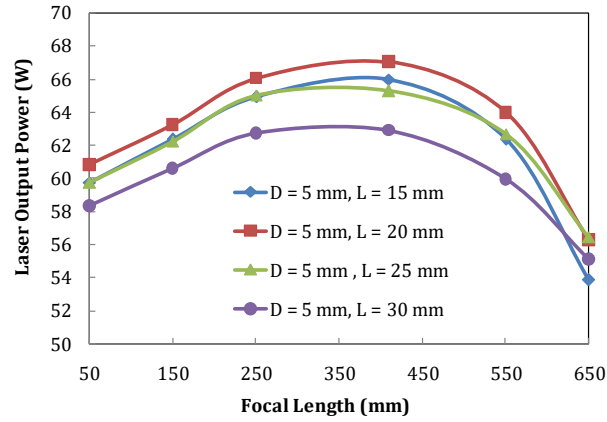


**Figure 6.3** Numerically calculated laser output power as function of the RAC focal length. The laser resonator cavity has 11 mm length.

The solar laser output power is also dependent on the laser rod diameter, as shown in Fig. 6.4.

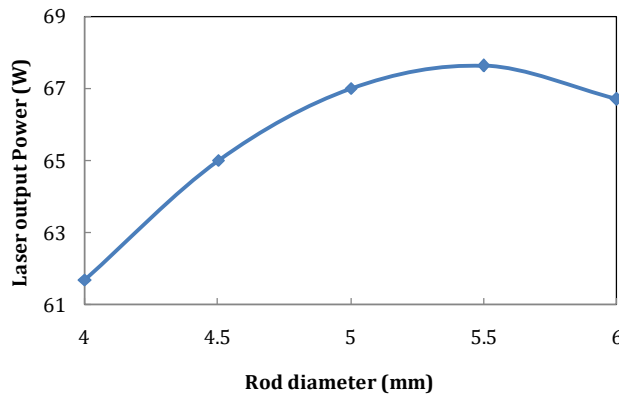


**Figure 6.4** Numerically calculated laser output power as function of the Nd:YAG rod diameter, for 20 mm length.

For 410 mm focal length, 20 mm rod length, 5.5 mm rod diameter resulted in the maximum solar power of 67.6 W. In the present work, a conversion efficiency (defined as laser output power divided by the incoming solar radiation onto the concentrator) of 4.0% was achieved for the 5.0 mm diameter rod.

The slope efficiency was numerically calculated, for each output reflectivity, as shown in Fig. 6.5. The highest slope efficiency of 5.8% was obtained for  $R = 90\%$  with threshold pump power of 587.2 W. For  $R = 94\%$ , 5.4% slope efficiency was found with 419.4 W threshold pump power. The lowest threshold pump power of 167.8 W was found for  $R = 98\%$ , with only 3.5% slope efficiency.

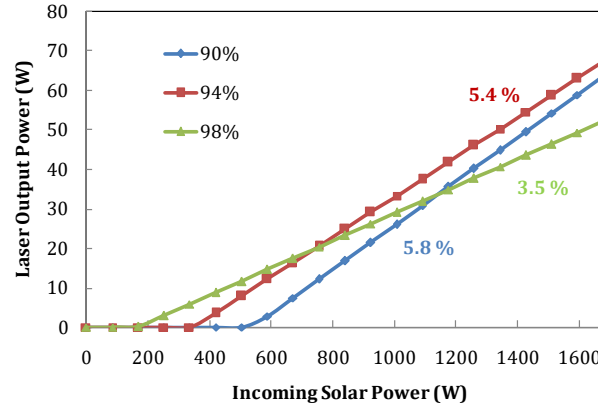


**Figure 6.5** Laser output power as function of the incoming solar power for 5.0 mm diameter, 20 mm length rod, with three different reflectivities: 90%, 94% and 98%.

The laser beam quality factors,  $M^2$  factors, were also numerically calculated with LASCAD<sup>®</sup> software, analyzing the evolution of the beam radius at  $1/e^2$ , along the propagation direction and fitted to the generalized Gaussian beam propagation equation. The calculated  $M^2$  factors were  $M_x^2 = M_y^2 = 56$ , which leads to a brightness figure of merit (defined as the laser output power divided by the product of the  $M^2$  factors) of 0.021 W [15].

In LASCAD<sup>®</sup> numerical analysis, the absorbed pump flux data from ZEMAX<sup>®</sup> software is integrated over the Nd:YAG rod volume. The thermally induced effects – heat load, temperature and stress intensity – in the 5.0 mm diameter 20 mm length Nd:YAG rod, are shown in Fig. 6.6.

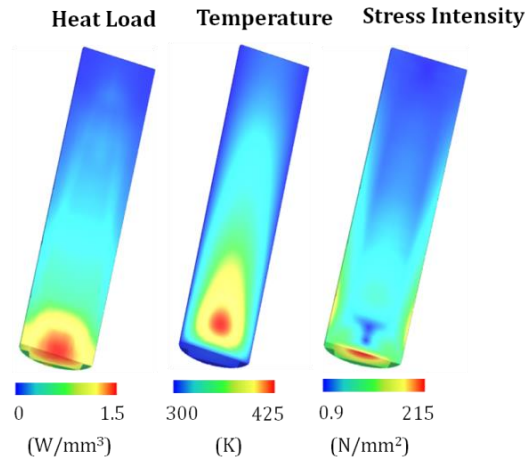


**Figure 6.6** Numerically calculated heat load, temperature and stress intensity distributions for the 5 mm diameter 20 mm length Nd:YAG rod.

The major thermal problems occurred at the upper-end side of the rod, due to the non-uniform absorbed pump flux distribution. The temperature from the surface to the center of the laser rod increased from 300 K to 425 K. Maximum stress intensity of 215 N/mm<sup>2</sup> was also numerically attained, which is slightly above the stress fracture

limit of 200 N/mm<sup>2</sup> for Nd:YAG medium [40]. The small overlap of only 16%, between the absorption spectrum of the Nd:YAG material and the solar emission spectrum [38], 84% of unabsorbed solar radiation, ranging between 0.25 and 2.5  $\mu$ m, contributes to the heating of the laser rod.

In Table 6.2 is presented the thermal analysis of both 5.0 and 5.5 mm diameter laser rods. The latter has only 0.36 W more laser power, but suffers from more severe thermal conditions in terms of temperature and stress intensity. 5.0 mm diameter rod was therefore chosen to alleviate the thermal problem of the laser medium.

**Table 6.2** Thermal performances of 5.0 and 5.5 mm Nd:YAG rod.

| Rod diameter (mm)              | 5.0   | 5.5   |
|--------------------------------|-------|-------|
| Absorbed pump power (W)        | 225.5 | 236.4 |
| Heat load (W/mm <sup>3</sup> ) | 1.51  | 1.48  |
| Temperature (K)                | 425.0 | 431.0 |
| Stress (N/mm <sup>2</sup> )    | 215.0 | 242.9 |
| Laser power (W)                | 67.3  | 67.6  |

Upward or downward shift of the laser rod can offer a very effective solution to the above mentioned problem. The upward shift of 4.0 mm of the crystal alleviated its stress intensity to less than 150 N/mm<sup>2</sup>, consequently decreasing the laser output power, as observed in Fig. 6.7. The downward shift of –4.0 mm of the crystal aggravated not only its stress intensity to 260 N/mm<sup>2</sup>, but also reduced its laser output power.

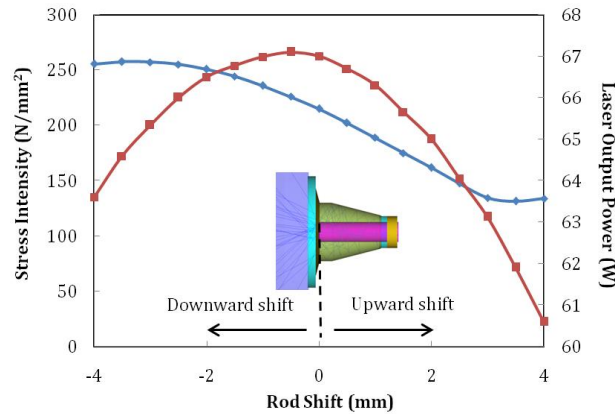


**Figure 6.7** Numerically calculated laser output power and stress intensity as function of the shift of the 5 mm diameter, 20 mm length rod.

The heat load, the temperature and the stress intensity for the 5 mm diameter, 20 mm length Nd:YAG rod, shifted 1.5 mm upward, is presented in Fig. 10. The changes in the distribution of the absorbed pump profile inside the laser rod are clearly visible, where the contribution of the side-pumping portion of the absorbed power was more pronounced. With only 1.6 W less laser output power, the stress intensity of  $D = 5.0$  mm rod shifted 1.5 mm upward was significantly reduced to 175 N/m<sup>2</sup>, below the fracture limit.

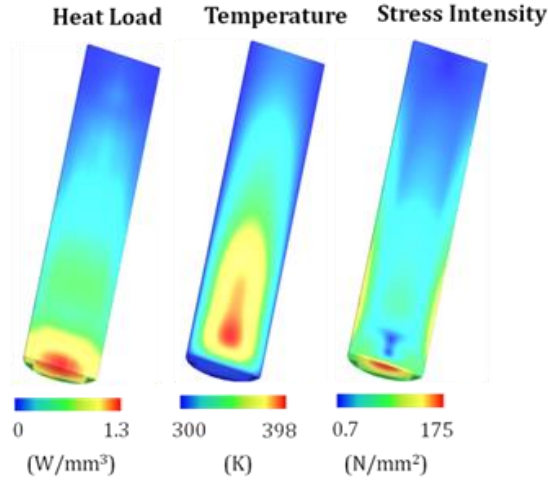


**Figure 6.8** Numerically calculated heat load, temperature and stress intensity distributions for the 5 mm diameter, 20 mm length Nd:YAG rod, shifted 1.5 mm upward.

Significant enhancements in collection, conversion and brightness figure of merit were numerically achieved. The numerical results obtained in this work are summarized in Table 6.3 and compared with the previous experimental results with both Fresnel lens [16] and heliostat-parabolic mirror schemes [17].

**Table 6.3** The numerical results in this work compared with the experimental results of Dinh *et al* [16] and Liang *et al* [17].

| Parameters  | [16]   | [17]  | Present work | Improvement in relation to [16] and [17] (Times) |      |
|---|--------|-------|--------------|--|------|
| Collection area(m <sup>2</sup> )  | 4      | 1.18  | 1.76         | -  | -    |
| Collection efficiency (W/m <sup>2</sup> )   | 30     | 31.5  | 38.2         | 1.27   | 1.22 |
| Conversion efficiency (%)   | 3.2    | 3.1   | 4.0          | 1.25   | 1.29 |
| Laser output (W)  | 120    | 37.2  | 67.3         | -  | -    |
| Slope efficiency (%)  | 4.3    | 5.15  | 5.4          | 1.26   | 1.05 |
| M <sup>2</sup> factor(M <sub>x</sub> <sup>2</sup> = M <sub>y</sub> <sup>2</sup> ) | 137.0  | 53.4  | 56.0         | -  | -    |
| Figure of merit (W)   | 0.0064 | 0.013 | 0.021        | 3.28   | 1.62 |

By comparing these parameters, it is clear that the present work represents an interesting alternative for enhancing solar laser efficiencies. It is also worth noting that the proposed RAC solar laser pumping scheme is also valid for many other solar laser materials. The collection efficiency obtained with this work was 38.2 W/m<sup>2</sup> multimode solar laser power, the highest numerical result obtained in solar-pumped lasers by end-side-pumping configuration.

### 6.1.2 Single-rod side-pumped solar laser

By using a two-dimensional semi-cylindrical pump cavity and a large fused silica aspherical lens, it was reported another improvement in slope efficiency and side-pumping collection efficiency [18].

The primary system used was the NOVA heliostat-parabolic mirror, with an effective collection area of  $0.9 \text{ m}^2$  and a solar irradiance of  $700 \text{ W/m}^2$ . The solar laser head is given in the Fig. 6.9, with its water cooling system and insets of the prototype. The solar laser head was composed of the fused silica aspheric lens and the 2D semi-cylindrical pump cavity within which the 3.0 mm diameter, 30 mm length Nd:YAG single-crystal rod was mounted. The water cooling scheme is indicated by Fig. 6.9.

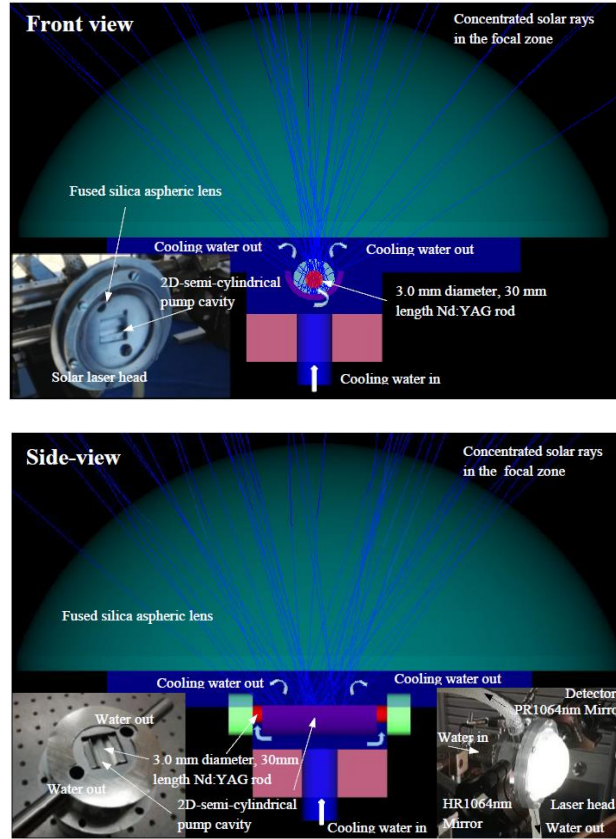


**Figure 6.9** Front and side views of the solar laser head, showing water cooling scheme for the laser rod through the space between the fused silica aspheric lens and the two-dimensional semi-cylindrical pump cavity. Inset photos on the left show the mechanical design details of the solar laser head. Inset photo on the right shows the external resonant laser cavity and solar laser head being pumped at the focus of the parabolic mirror.

In Fig. 6.10 is given the multimode solar laser output power obtained. As a conclusion, 15.3 W cw 1064 nm solar laser power was measured, corresponding to  $17.0 \text{ W/m}^2$  collection efficiency, 5.4% slope efficiency and 2.43% solar-to-laser power conversion efficiency, being 1.45, 2.3, and 2.15 times, respectively, more than the previous highest results in side-pumping configuration [27]. The measured system slope efficiency is already 1.08 times higher than end-side-pumped solar laser with Nd:YAG single-crystal rod [17], being 2.08 and 2.30 times, respectively, more than the previous results by side-pumping configuration.



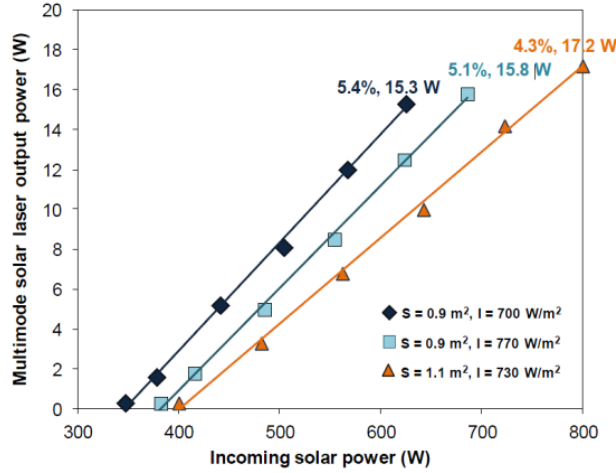


**Figure 6.10** Solar laser output power versus incoming solar power.

### 6.1.3 Highly efficient and stable dual-rod side-pumped solar laser

A new work was developed to increase the solar laser efficiency, which led to a publication in January 2020. Still with the NOVA heliostat-parabolic mirror system, a novel pump cavity was designed to optimize the solar rays coupling with the laser rods, being this time a hybrid pump cavity, with an individual semicylindrical part to pump each one of the rods individually, and other being common to both rods, differently from the former one CPC-pump cavity to each one of the rods from previous works already published. Relatively to the secondary concentrator a small fused silica aspherical lens was chosen to further increase the pump efficiency onto the crystals. The description of the multimode solar laser emission is given below [30].

The primary concentrator used in this work was the NOVA heliostat-parabolic mirror, using an effective collection area of  $1.56 \text{ m}^2$  and assuming a solar irradiance of  $890 \text{ W/m}^2$ . As shown in Fig. 6.11, the solar laser head of the single-rod pumping scheme was composed of a fused silica aspherical lens and a 2D-shaped-semicylindrical pump cavity within which a 5.5 mm diameter and 25 mm length Nd:YAG rod was mounted and efficiently pumped. The laser rod was cooled by water in its longitudinal surface along 17 mm length and the remaining 8.0 mm was used for mechanical fixation by two rod holders. Both aspherical lens and the pump cavity were all actively cooled by water. The fused silica aspherical lens had an input face with 15 mm radius of curvature, 26 mm diameter, 0.002 conic factor and a plane output face. The 2D-shaped pump cavity had  $11 \text{ mm} \times 14 \text{ mm}$  rectangular input aperture and  $8.0 \text{ mm} \times 14 \text{ mm}$  rectangular output aperture and a semicylindrical pump cavity with 5.0 mm radius, 14 mm length and 3.0 mm height. This pump cavity ensured one-pass, double-pass and even multi-pass absorption of the radiation by the laser material. 95% reflectivity was assumed for the inner wall of the reflectors of the pump cavity.



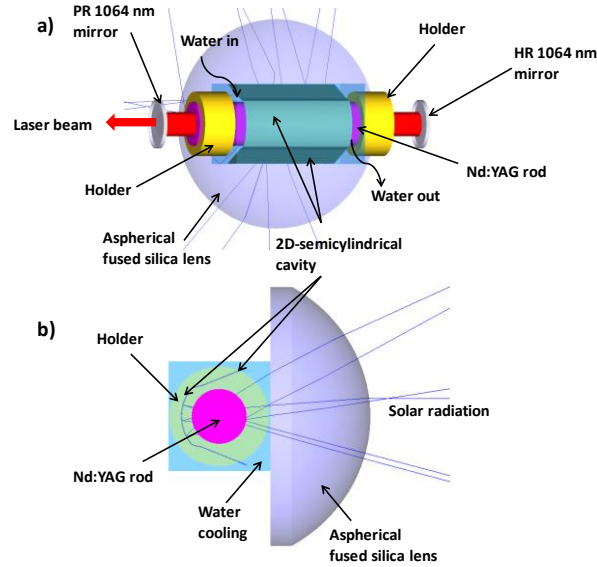


**Figure 6.11** Nd:YAG rod solar laser head design in its traditional side-pumped single-rod scheme: a) 3-D view and b) front view. It is composed of the fused silica aspherical lens, the 2D-shaped-semicylindrical pump cavity and the Nd:YAG rod, fixed by two holders.

The laser cavity was formed by one HR 1064 nm mirror with 99.9% reflectivity and another PR 1064 nm mirror with 94% reflectivity (Fig. 6.11a).

For the dual-rod pumping scheme approach, as shown in Fig. 6.12, the same fused silica aspherical lens was used to pump the laser rod through the cooling water.

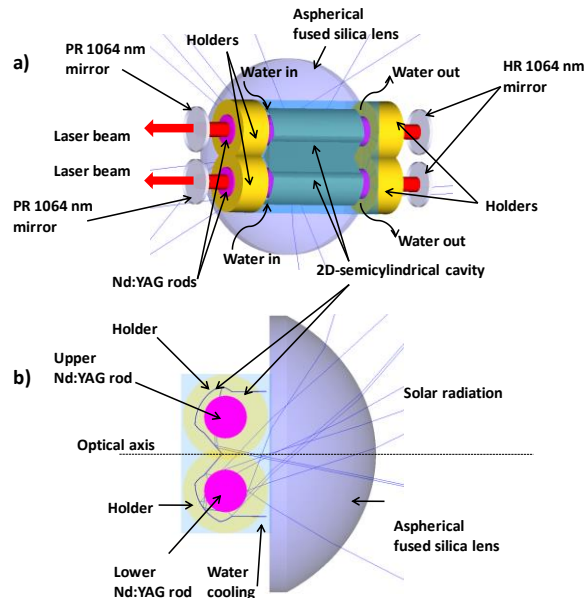


**Figure 6.12** Solar laser head design with two Nd:YAG laser rods: a) 3-D view and b) front view. It is composed of the fused silica aspherical lens, the two 2D-shaped-semicylindrical pump cavities and the two thick Nd:YAG rods, fixed by holders. The HR 1064 nm mirrors and the PR 1064 nm mirrors form the laser resonant cavities, along with the two laser rods.

The solar radiation was equally distributed from the output face of the fused silica lens into the apertures of the two 2D-shaped-semicylindrical cavities, mounted together with an angle of  $33^\circ$  in relation to the optical axis.

Each 2D-shaped pump cavity had  $12\text{ mm} \times 14\text{ mm}$  rectangular input aperture and  $11\text{ mm} \times 14\text{ mm}$  output aperture. Solar pump radiation emitted from the 2D-shaped cavity output ends could be efficiently coupled to the Nd:YAG rods through the semicylindrical pump cavities with 8.0 mm radius, 14 mm length and 3.0 mm height, producing one-pass, double-pass and even multi-pass absorption of the radiation by the laser material. 95% reflectivity was assumed for the inner wall of the pump cavity. The laser resonant cavity was formed by one HR 1064 nm mirror with 99.9% reflectivity and another PR 1064 nm mirror with 95% reflectivity.

The simulations were carried out similarly to previous numerical analysis on solar lasers and already mentioned in this thesis [19, 23, 27].

The absorbed pump flux distributions are shown in Fig. 6.13. The main contribution of the absorbed pump power comes from the center of the laser rod, especially in the case of the single-rod pumping scheme. In the case of the proposed dual-rod pumping scheme, a reduced peak intensity of about 52% was found in relation to that of the single-rod scheme.

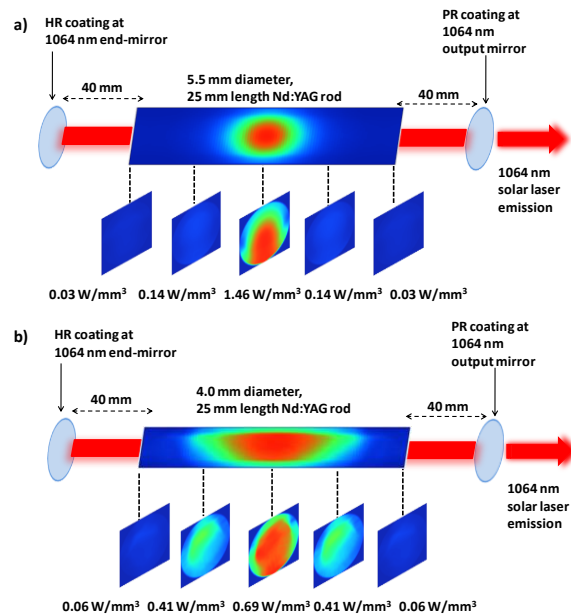


**Figure 6.13** Absorbed pump flux distributions along a) the 5.5 mm diameter, 25 mm length Nd:YAG rod of the single-rod scheme and b) the 4.0 mm diameter, 25 mm length rod of the dual-rod scheme.

The laser resonant cavity analysis and optimization of the laser output power were carried out using LASCAD<sup>®</sup> software similarly to other previous simulations. 0.2% and 0.1% imperfect optical coating losses were assumed for the laser rods and the HR 1064 nm end mirror, respectively. The diffraction losses depend strongly on rod diameter, resonator length and RoC of the resonator. LASCAD<sup>®</sup> beam propagation method predicted 0.02% and 0.03% diffraction losses for the 5.5 mm diameter single-rod and for the 4.0 mm diameter dual-rod schemes, respectively.

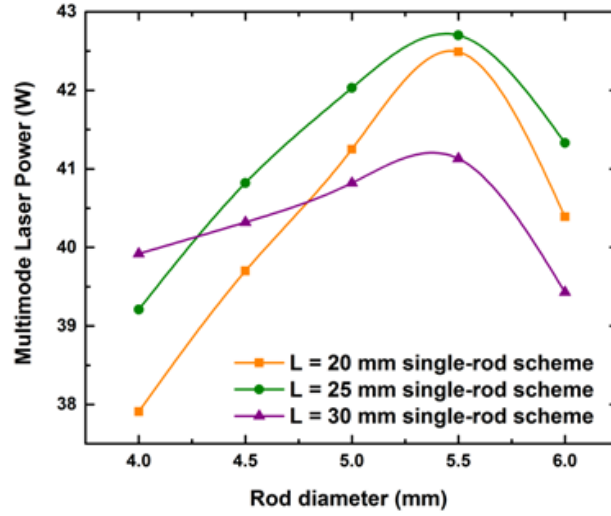


**Figure 6.14** Numerically calculated multimode laser output power as a function of both rod diameter and length for the single-rod scheme.

The maximized numerical multimode laser output power for the single-rod scheme was achieved with a 105 mm length resonant cavity, and  $\text{RoC} = -10$  m for both end-mirrors. For the dual-rod scheme, the same parameters were found for achieving the maximum multimode laser output power.

The multimode laser output power for the single-rod scheme as a function of the laser rod diameter and length is shown in Fig. 6.14. With 5.5 mm diameter and 25 mm rod length, the maximum multimode laser output power of 42.70 W was obtained.

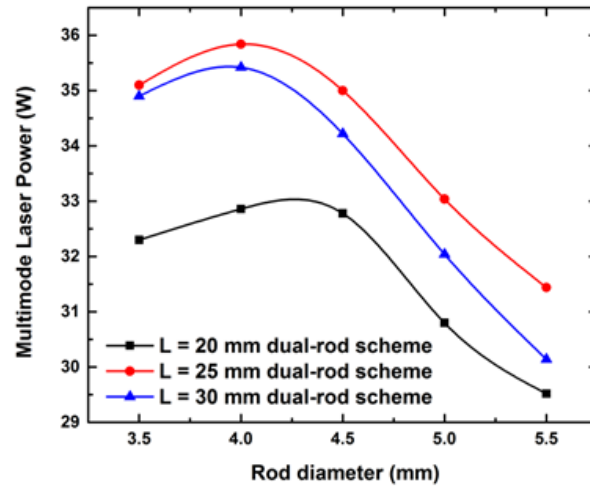


**Figure 6.15** Numerically calculated multimode laser output power as a function of both rod diameter and length for the dual-rod scheme with combined laser power.

The multimode laser output power as a function of the rod diameter and length for the dual-rod scheme is shown in Fig. 6.15. The total maximum laser output power of 35.84 W was obtained from the combined laser output power of 17.63 W from each of the 4.0 mm diameter and 25 mm length rods.

Using a U-shaped resonant cavity, such as in diode-pumped rod lasers, through a single folded laser cavity [75], one laser beam can be obtained from the two laser rods, as shown in Fig. 6.16. The laser resonant cavity was formed by one HR 1064 nm end mirror with 99.9% reflectivity (0.1% loss), two HR 1064 nm folding mirrors with 99.9%

reflectivity (0.1% loss each) and one PR 1064 nm output mirror with 95% reflectivity. 0.4% total imperfect optical coating losses for the two laser rods were assumed. LASCAD<sup>®</sup> beam propagation method predicted 0.03% diffraction losses for the 4.0 mm diameter dual-rod scheme, resulting in the total round-trip loss of 3.73%, as explained in section 3.3.

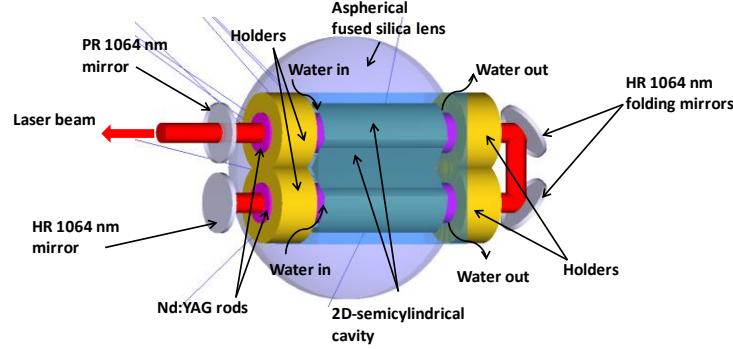


**Figure 6.16** Proposed design of the solar laser head with two Nd:YAG rods to obtain one single laser beam from the two rods. Two HR 1064 nm folding mirrors, one HR 1064 nm mirror and one PR 1064 nm mirror compose the U-shaped laser resonant cavity, along with the two laser rods.

The multimode laser output power as a function of the incoming solar power reaching the input face of the primary solar concentrator was also numerically calculated for all the schemes, as shown in Fig. 6.17. The laser power of each individual rod (both upper and lower rod), as well as its combined laser power, is also represented.

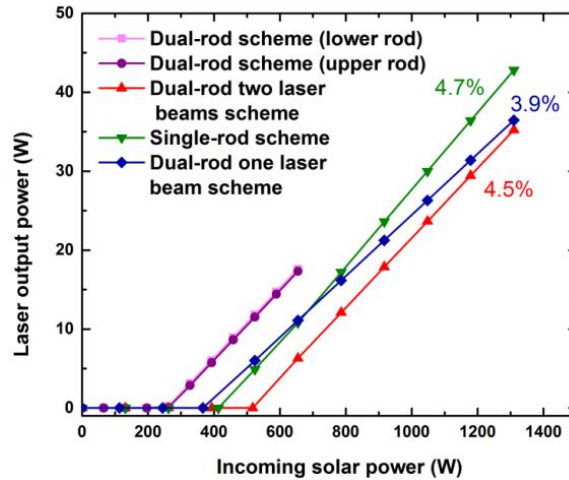


**Figure 6.17** Numerically calculated multimode laser output power as a function of the incoming solar power, for both the single-rod and the dual-rod schemes. The latter in two configurations, two laser beams and one laser beam schemes. The solar laser slope efficiencies are also represented.

The multimode laser slope efficiency, the  $M^2$  factors and the brightness figure of merit [15] were also numerically calculated for all the schemes. The numerical performance of the single-rod, the dual-rod two laser beams and the dual-rod one laser beam schemes are summarized in Table 6.4.

**Table 6.4** Numerically calculated multimode laser output power, collection efficiency, solar-to-laser power conversion efficiency, slope efficiency, threshold pump power,  $M^2$  factors and brightness figure of merit for the single-rod scheme, the dual-rod two laser beams and the dual-rod one laser beam schemes.

| Parameter                                      | Schemes    |                          |                         |
|--|------------|--------------------------|-------------------------|
|  | Single-rod | Dual-rod two laser beams | Dual-rod one laser beam |
| Laser output power (W)                         | 42.70      | 35.84                    | 37.72                   |
| Collection efficiency (W/m <sup>2</sup> )      | 27.37      | 22.97                    | 24.18                   |
| Solar-to-laser power conversion efficiency (%) | 3.26       | 2.74                     | 2.88                    |
| Slope efficiency (%)                           | 4.70       | 4.50                     | 3.90                    |
| Threshold pump power (W)                       | 413        | 517                      | 366                     |
| $M^2$ factor ( $M^2_X$ ; $M^2_Y$ )             | 95.0; 95.0 | 39.0; 39.0               | 36.3; 36.3              |
| Brightness figure of merit (W)                 | 0.005      | 0.024                    | 0.029                   |

The single-rod scheme offered the highest laser output power and laser slope efficiency, but the lowest brightness figure of merit. The dual-rod one laser beam scheme presented the highest brightness figure of merit amongst the studied schemes.

The analytical calculation of the solar laser output power followed the described in Chapter 2. Using ZEMAX<sup>®</sup> analysis,  $\eta_T = 0.78$  and  $\eta_A = 0.87$  were obtained for the single-rod scheme and  $\eta_T = 0.74$  and  $\eta_A = 0.82$  for the dual-rod scheme. For the dual-rod one laser beam scheme with folding mirrors,  $\delta_M = 0.007$  and  $\delta_D = 0.0004$  were assumed. The numerical and analytical calculations of the laser output power, slope efficiency and threshold pump power for the single-rod scheme and the dual-rod scheme with two laser beams and one laser beam are summarized in Table 6.5.

**Table 6.5** Numerically and analytically calculated laser output power, slope efficiency and threshold pump power, for the single-rod scheme and the dual-rod scheme with two laser beams and one laser beam.

|                          | Parameters             |                      |                          |
|--------------------------|------------------------|----------------------|--------------------------|
|                          | Laser output power (W) | Slope efficiency (%) | Threshold pump power (W) |
| Analytical calculation   |                        |                      |                          |
| Single-rod               | 34.70                  | 4.00                 | 445                      |
| Dual-rod two laser beams | 28.50                  | 3.67                 | 535                      |
| Dual-rod one laser beam  | 30.81                  | 3.31                 | 381                      |
| Numerical calculations   |                        |                      |                          |
| Single-rod               | 42.70                  | 4.70                 | 413                      |
| Dual-rod two laser beams | 35.84                  | 4.50                 | 517                      |
| Dual-rod one laser beam  | 37.72                  | 3.90                 | 366                      |

Regarding the thermal conditions of the Nd:YAG rods, the results are shown in Fig. 6.18, as well as the reduction in prejudicial thermal induced effects.

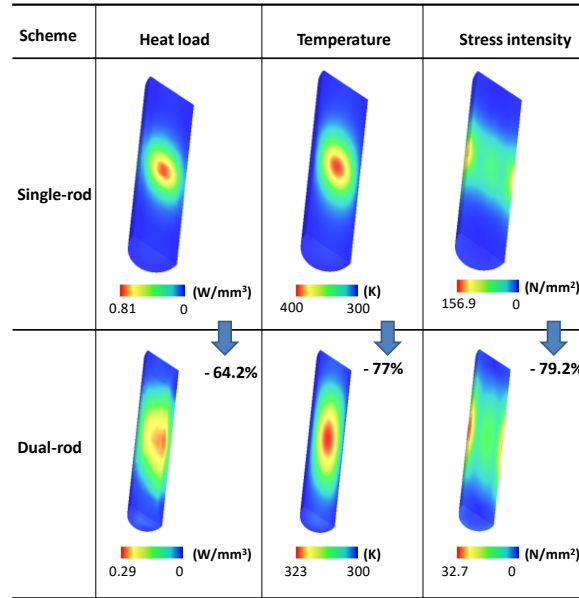


**Figure 6.18** Numerically calculated heat load, temperature and stress intensity distributions of the 5.5 mm diameter 25 mm length Nd:YAG rod from the single-rod scheme, and the 4.0 mm diameter 25 mm length Nd:YAG rod from the dual-rod scheme.

Comparing the thermal conditions, the thermal performance of the dual-rod scheme was significantly improved in relation to the single-rod scheme. The obtained results are shown in Table 6.6.

**Table 6.6** Numerically calculated laser output power, collection efficiency and solar-to-laser power conversion efficiency for the single-rod and the dual-rod schemes, and its comparison with the most efficient experimental side-pumped solar laser of Liang *et al* [76]. It is also shown the collection areas and the solar irradiance.

| Parameters                                     | [76] | Present numerical work |                 | Improvements (times)      |                         |
|--|------|------------------------|-----------------|---------------------------|-------------------------|
|  |      | Single-rod scheme      | Dual-rod scheme | Single-rod scheme to [76] | Dual-rod scheme to [76] |
| Collection area (m <sup>2</sup> )              | 0.9  | 1.56                   | 1.56            | -                         | -                       |
| Solar irradiance (W/m <sup>2</sup> )           | 770  | 890                    | 890             | -                         | -                       |
| Laser output power (W)                         | 15.8 | 42.70                  | 37.72           | -                         | -                       |
| Collection efficiency (W/m <sup>2</sup> )      | 17.6 | 27.37                  | 24.18           | 1.55                      | 1.37                    |
| Solar-to-laser power conversion efficiency (%) | 2.43 | 3.26                   | 2.88            | 1.34                      | 1.19                    |

The single-rod scheme obtained 42.70 W solar laser power, corresponding to 27.37 W/m<sup>2</sup> collection efficiency and 3.26% solar-to-laser power conversion efficiency, being 1.55 and 1.34 times, respectively, more than the previous experimental records in side-pumping solar laser configurations [76]. The dual-rod scheme achieved a lower value, 37.72 W solar laser power, but still corresponding to 24.20 W/m<sup>2</sup> collection efficiency and 2.88% solar-to-laser power conversion efficiency, being 1.34 and 1.19 times, respectively, more than the previous highest results in side-pumping configurations [76]. On the other hand, the dual-rod with two laser beams and one laser beam schemes

presented a largely reduced  $M^2$  factors, obtaining 4.8 and 5.8 times more brightness figure of merit, respectively, than that of the single-rod scheme.

The thermal performance of the dual-rod configurations also showed a large enhancement in relation to the single-rod scheme, achieving a decrease in heat load, temperature and stress intensity of about 64.2%, 77% and 79%, respectively.

#### 6.1.4 Simultaneous solar laser emissions from three Nd:YAG rods

Within the concept of multi-rod approach for solar-pumped lasers, it was experimentally tested and reported the first simultaneous emission of three continuous-wave solar laser beams in end-side-pumped configuration [20].

The primary concentrator used was the PROMES heliostat-parabolic mirror system, using an effective collection area of  $1.0 \text{ m}^2$  and a solar irradiance of  $830 \text{ W/m}^2$ . Fig. 6.19a) presents the front image of the solar laser head composed of the large fused silica aspheric lens and the three 3.0 mm diameter, 25 mm length Nd:YAG rods within the single conical pump cavity. By optically aligning three small PR 1064 nm output mirrors with their corresponding laser rods, as show in Fig. 6.19b), simultaneous cw 1064 nm solar laser emissions were produced. Accurate resonant cavity alignments were ensured by adjusting the output couplers individually through the three positioners. The laser head was fixed on the X-Y-Z axes positioning system, ensuring its optical alignment in the focal zone.

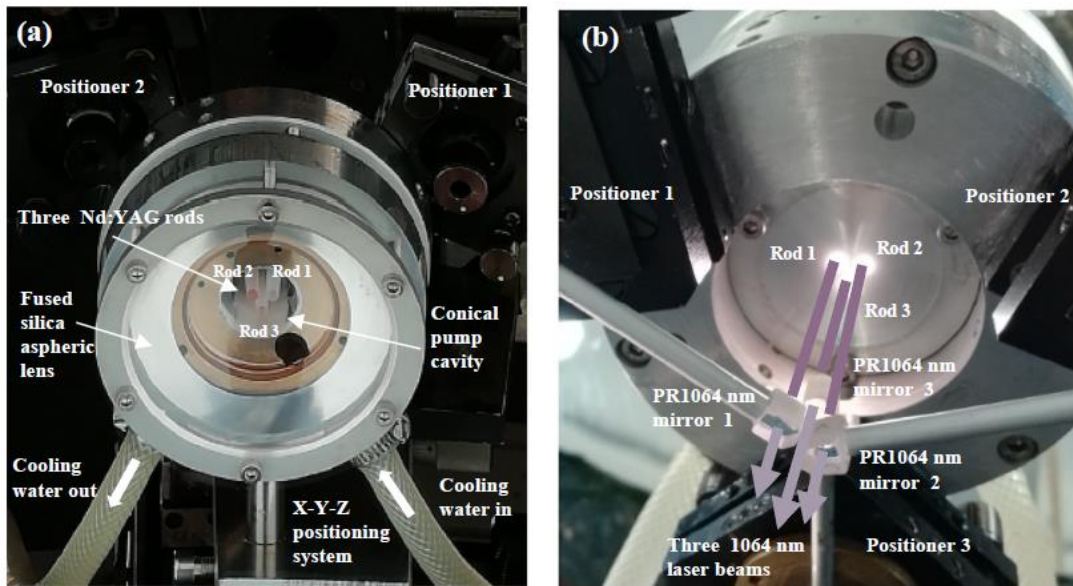


**Figure 6.19** (a) Front image showing the three-rod solar laser head actively cooled by water. (b) Back image of the solar laser head with three positioners for accurate adjustments of the three small output couplers in relation to the three rods.

In Fig. 6.20 is shown the solar laser output power and the slope efficiency obtained.



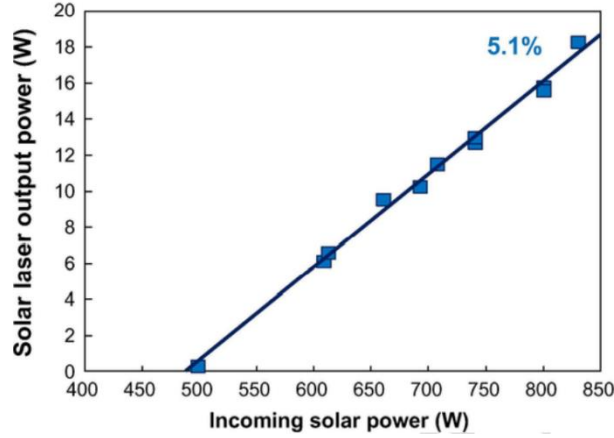


**Figure 6.20** Total solar laser output power from the three rods versus incoming solar power for  $R = 95\%$ ,  $RoC = \infty$  and  $L_1 = L_2 = L_3 = 50$  mm.

By end-side-pumping three 3.0 mm diameter, 25 mm length Nd:YAG single-crystal rods within a single conical pump cavity, 18.3 W multimode solar laser power was measured, resulting in 5.1% laser slope efficiency.

### 6.1.5 Ce:Nd:YAG side-pumped solar laser

Continuing a previous work with the solar pumping of Ce:Nd:YAG rods, searching for more improvements in solar laser efficiency with this promising laser material, a significant advancement in solar laser performance using a side-pumping configuration and a Ce:Nd:YAG laser rod was reported [77].

The primary system used in this work was the NOVA heliostat-parabolic mirror system, using an effective collection area of  $0.7 \text{ m}^2$  and measuring a solar irradiance of  $860 \text{ W/m}^2$ . The solar laser head is shown in Fig. 6.21 and was composed of a double-stage semispherical lens and a trapezoidal-shaped pumping cavity, which coupled and redistributed the concentrated solar radiation from the focal zone of a parabolic mirror into a laser rod. The laser output performance of a 4.0 mm diameter, 35 mm length Ce:Nd:YAG laser rod was tested and compared with that from a Nd:YAG rod with the same dimensions.

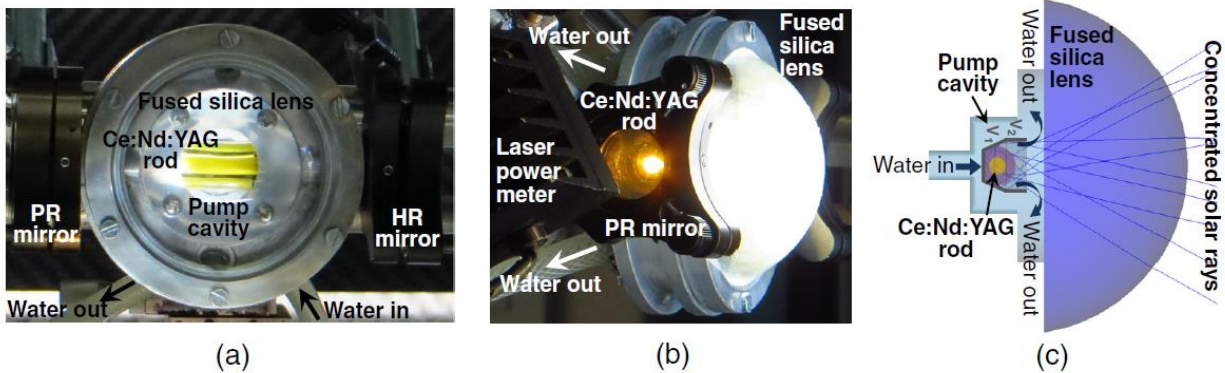


**Figure 6.21** (a) Front view; (b), (c) side view of the Ce:Nd:YAG solar laser head. PR, partial reflection; HR, high reflection.

The Nd:YAG laser rod was also tested at the same incoming solar power. A solar laser cw power of 10.5 W was obtained from the Nd:YAG laser rod, corresponding to a collection efficiency of  $15.0 \text{ W/m}^2$  and solar-



to-laser power conversion efficiency of 1.8%. A threshold pump power of 255 W was measured, resulting in 3.0% solar laser slope efficiency.

At an incoming solar power of 600 W, the Ce:Nd:YAG solar laser achieved 23.6 W/m<sup>2</sup> collection efficiency, 4.4% slope efficiency, and 2.8% solar-to-laser power conversion efficiency. The Ce:Nd:YAG rod used in a side-pumping configuration proved to be a potential material for solar-pumped lasers.

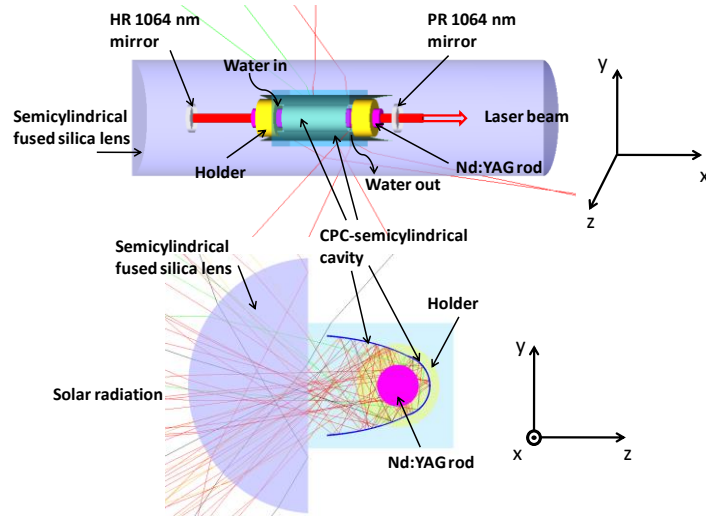
## 6.2 Solar-pumped lasers in TEM<sub>00</sub>-mode regime

In this section it will be described the advancements and developments during the time of my thesis in solar-pumped laser in TEM<sub>00</sub>-mode regime and other laser beam shapes, such as the useful doughnut shapes, laser beams highly demanded by industry and scientific technological research. Not only medium solar energy collection and concentration systems were often used to develop and explore the laser emission of TEM<sub>00</sub>-mode regime, but also large solar energy facilities.

### 6.2.1 Dual-rod pumping concept for TEM<sub>00</sub>-mode solar lasers

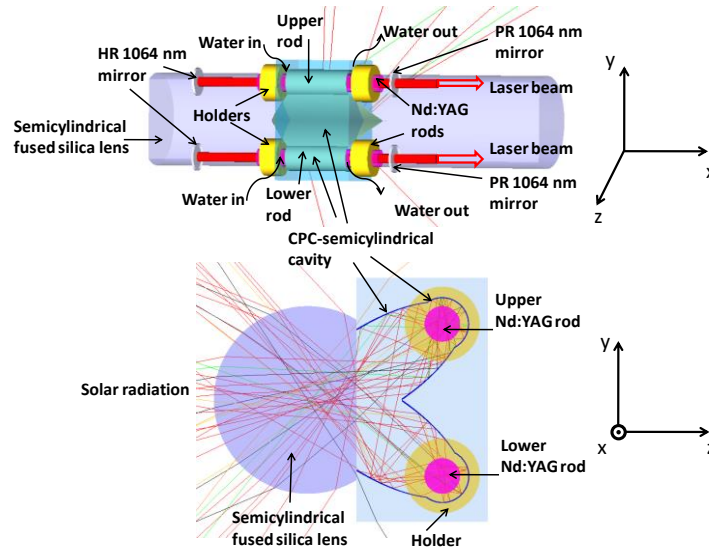
Aiming to improve of TEM<sub>00</sub>-mode solar laser efficiency, a first model was introduced and developed by me with the dual-rod concept, using a fused silica semicylindrical lens and a CPC-pump cavity to each one of the rods. The same numerical model was also studied to produce multimode solar laser with enhanced tracking error compensation capacity. The detailed description of this scheme producing TEM<sub>00</sub>-mode solar laser, which led to a publication in February 2019, will be given below. The proposed dual-rod schemes investigated were always compared to a single-rod configuration with similar secondary concentrator and pump cavity. The dimensions of the crystals were also studied in the optimization process for both schemes [29].

The primary concentrator used in this work was the NOVA heliostat-parabolic mirror using an effective collection area of 1.56 m<sup>2</sup> and assuming a solar irradiance of 890 W/m<sup>2</sup>. The laser head of a traditional side-pumped solar laser is composed of a small semicylindrical fused silica lens with a CPC-semicylindrical pump cavity, within which a 4.0 mm diameter and 25 mm length Nd:YAG rod is mounted. The laser rod is cooled along 17 mm of its longitudinal surface while the remaining 8.0 mm length, 4.0 mm on each side, is used for mechanical fixation by two rod holders. The semicylindrical fused silica lens with 25 mm diameter, 90 mm length, and 11 mm height, was responsible for collecting and concentrating the solar radiation to the CPC pump cavity with 9.7 mm×13 mm rectangular large input aperture, 5.7 mm×13 mm small output aperture, and 8.0 mm height. The CPC was used to convert the rays from the large input aperture emitting into a small angle to the small output aperture emitting into a large angle, thus the source étendue is preserved, leading to a net concentration of the pump radiation. This radiation from the CPC output could efficiently pump the laser rod with the help of the semi-cylindrical pump cavity with 5.9 mm diameter, 2.0 mm height, and 13 mm length. The inner wall of the pump cavity is considered to have 95% reflectivity. The laser cavity is formed by one high reflection (HR) at 1064 nm mirror with 99.8% reflectivity and another partial reflection (PR) at 1064 nm mirror with 94% reflectivity at the output, as shown in Fig. 6.22.



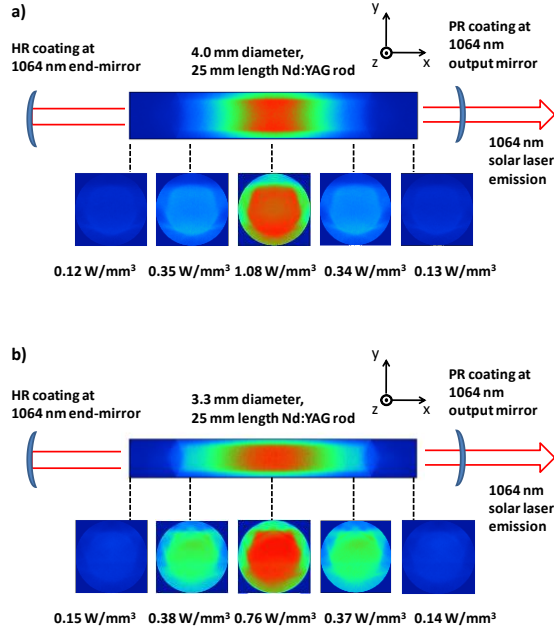
**Figure 6.22** Design of the Nd:YAG rod solar laser head in its traditional side-pumped single-rod scheme, composed of a fused silica semicylindrical lens, CPC-semicylindrical pump cavity and the Nd:YAG rod, fixed by two holders.

The proposed dual-rod scheme is shown in Fig. 6.23. In the proposed dual-rod scheme, the semicylindrical fused silica lens is 20 mm in diameter, 90 mm in length, and 15 mm in height. The solar radiation is equally distributed at the output of the fused silica lens into the CPC input aperture. The CPC pump cavity has 8.0 mm  $\times$  13 mm rectangular large input aperture, 5.5 mm  $\times$  13 mm small output aperture, and is 7.8 mm in height. The radiation emitted from the CPC output end could be efficiently coupled to each Nd:YAG rod through the semicylindrical pump cavity with 5.3 mm diameter, 2.6 mm height, and 13 mm length.



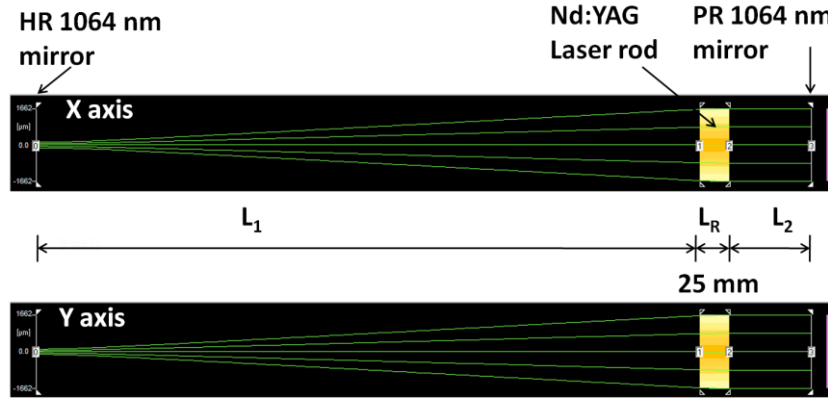
**Figure 6.23** Design of the solar laser head with two Nd:YAG laser rods, composed of a fused silica semicylindrical lens, CPC-semicylindrical pump cavities and the two thin rods, fixed by holders. The HR 1064 nm mirrors and the PR 1064 nm mirrors form the laser resonant cavity, along with the two laser rods.

Figure 6.24 shows the absorbed pump flux distributions along one longitudinal and five transversal central cross-sections of the Nd:YAG crystal rods: a) the 4.0 mm diameter 25 mm length Nd:YAG rod for the single-rod pumping scheme and b) 3.3 mm diameter 25 mm length rod for the dual-rod pumping scheme.



**Figure 6.24** a) Absorbed pump flux distributions along the 4.0 mm diameter, 25 mm length Nd:YAG rod single-rod scheme. b) Absorbed pump flux distributions along the 3.3 mm diameter, 25 mm length Nd:YAG dual-rod scheme.

By adopting the proposed dual-rod scheme, a more uniform pump profile is observed with a reduced peak intensity of about 30%. It is shown in Fig. 6.25, the asymmetric laser resonant cavity used for an efficient extraction of  $\text{TEM}_{00}$ -mode solar laser output power from the laser rod.



**Figure 6.25** Asymmetric laser resonant cavity for the efficient production of fundamental  $\text{TEM}_{00}$ -mode solar laser power.  $L_1$  and  $L_2$  represent the separation length of the high reflection (HR) mirror and partial (PR) mirror, respectively, to the end face of the laser rod with length  $L_R$ . For the dual-rod scheme were used  $L_1=563$  mm and  $L_2=70$  mm. For the single-rod scheme were used  $L_1=477$  mm and  $L_2=70$  mm.

The highest numerical  $\text{TEM}_{00}$ -mode laser output power for the dual-rod scheme was achieved with  $\text{RoC} = -2$  m at  $L_1 = 563$  mm and  $\text{RoC} = -10$  m at  $L_2 = 70$  mm. For the single-rod scheme,  $\text{RoC} = -5$  m at  $L_1 = 477$  mm and  $\text{RoC} = -10$  m at  $L_2 = 70$  mm were numerically used for achieving the maximum  $\text{TEM}_{00}$ -mode laser output power.  $L_1$  was a key parameter for maximizing solar pump mode and laser mode overlap. If  $L_1$  increased, the fundamental mode size within the rod also increased. Higher amount of pump radiation for the single-rod scheme resulted in strong thermal lensing and consequently short  $L_1$ . Since each single laser rod of the dual-rod scheme was pumped by only a half of the solar pump power of the single-rod scheme, larger  $L_1$  was achieved, enabling therefore an enhanced solar pump mode–laser mode matching and consequently higher  $\text{TEM}_{00}$ -mode solar laser power and efficiency.

The 3-D TEM<sub>00</sub>-mode laser beam pattern numerically attained on the output mirror of the asymmetric laser resonant cavity is shown in Fig. 6.26, for a) the 3.3 mm diameter 25 mm length rod and b) the 4.0 mm diameter 25 mm length Nd:YAG rod. It has a near diffraction-limited Gaussian distribution with spot-size  $1/e^2$  width,  $\omega$ , of approximately 1.1 mm on the output mirror for the former and 2.1 mm for the latter.

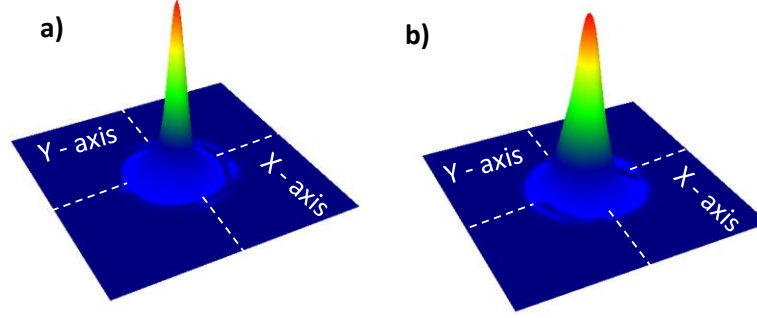


**Figure 6.26** Numerically simulated 3-D TEM<sub>00</sub>-mode laser output beam pattern on the output mirror of the asymmetric laser resonant cavity for a) 3.3 mm diameter 25 mm length Nd:YAG rod and b) 4.0 mm diameter 25 mm length Nd:YAG rod. The spot size  $1/e^2$  width is approximately  $\omega = 1.1$  mm for the former and 2.1 mm for the latter.

Figure 6.27 shows the strong dependency of the TEM<sub>00</sub>-mode laser output power on the rod diameter for both the single and dual-rod schemes.

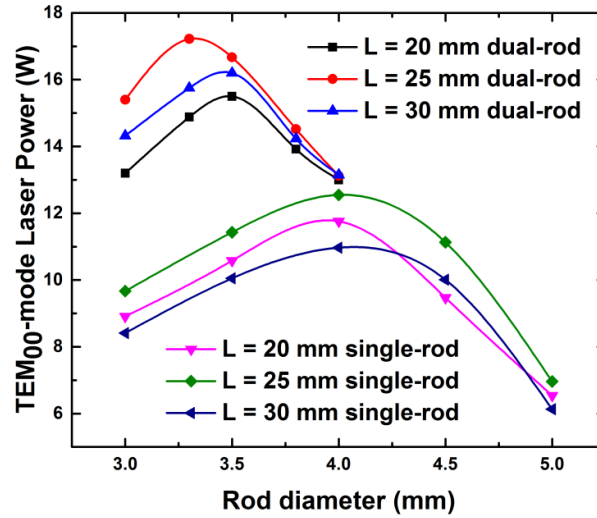


**Figure 6.27** Numerically calculated TEM<sub>00</sub>-mode laser output power as a function of the rod diameter with 20, 25 and 30 mm length for combined dual-rod and single-rod schemes.

The dual-rod scheme with combined TEM<sub>00</sub>-mode laser power from two rods offers 1.38 times more output power than that with single-rod scheme.

The  $M^2$  factors were also numerically calculated and led to a brightness figure of merit of the TEM<sub>00</sub>-mode laser output [15]. Figure 6.28 presents the numerically calculated brightness figure of merit of both the single and dual-rod schemes, as a function of both the rod diameter and length.

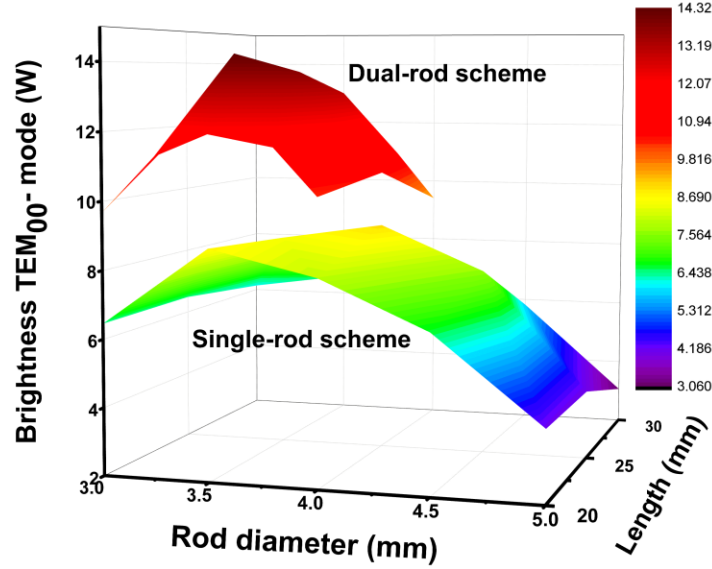


**Figure 6.28** Numerically calculated brightness figure of merit as a function of the rod diameter and length, for both the dual-rod and the single-rod schemes.

The numerical TEM<sub>00</sub>-mode output power as a function of the incoming solar power was also numerically determined and is shown in Fig. 6.29.

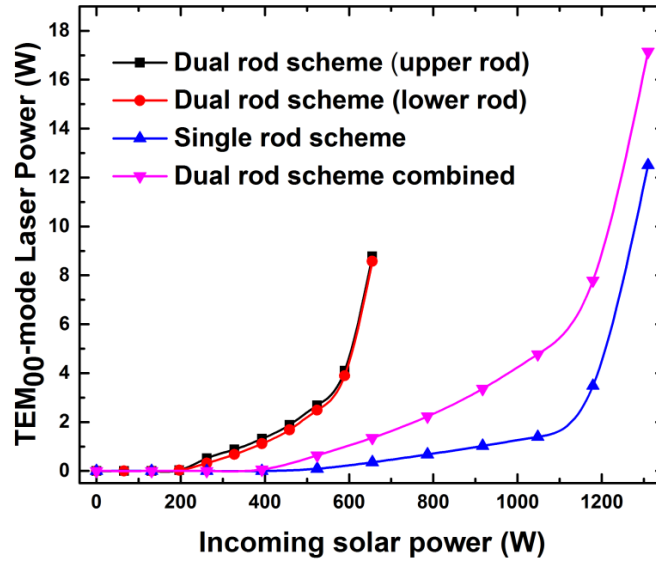


**Figure 6.29** Numerical TEM<sub>00</sub>-mode laser output power as a function of the incoming solar power for the dual-rod scheme with 3.3 mm diameter and 25 mm length rod, and the single-rod scheme with 4.0 mm diameter and 25 mm length rod.

The laser output power, the threshold pump power, the absorbed solar pump power, the absorbed solar pump power-to-TEM<sub>00</sub>-mode laser power efficiency, solar-to-TEM<sub>00</sub>-mode laser power conversion efficiency and the brightness conversion efficiency were determined, as shown in Table 6.7.

**Table 6.7** Solar-to-TEM<sub>00</sub>-mode laser power efficiencies comparison between the single-rod and dual-rod schemes.

| Parameter   | Schemes    |          |
|---|------------|----------|
|   | Single rod | Dual rod |
| Laser output power (W)  | 12.47      | 17.2     |
| Threshold pump power (W)  | 655        | 524      |
| Absorbed solar pump power (W)   | 99         | 108      |
| Absorbed solar pump power-to-TEM <sub>00</sub> -mode laser power efficiency (%) | 12         | 16       |
| Solar-to-TEM <sub>00</sub> -mode laser power conversion efficiency (%)          | 0.95       | 1.31     |
| Brightness conversion efficiency (%)  | 0.67       | 1.09     |

Each individual rod, upper and lower rod (Fig. 6.29), as well as its combined laser power was also represented. Both upper and lower rods had, individually, numerical threshold pump power around 262 W, resulting in the combined threshold pump power of 524 W. The single-rod scheme had numerical threshold pump power around 655 W, being 1.25 times higher than the combined threshold power of the dual-rod scheme.

The thermal performances of the two schemes are summarized in Table 6.8, as well as the decrease in the thermal effects obtained with the proposed dual-rod scheme.

**Table 6.8** Numerical thermal performances of 4.0 mm diameter 25 mm length of the single-rod scheme and 3.3 mm diameter 25 mm length of the dual-rod scheme.

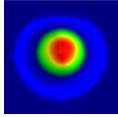
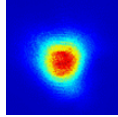
| Thermal effect                        | 4.0 mm rod | 3.3 mm rod | Decrease from 4.0 mm to 3.3 mm rod (%) |
|---------------------------------------|------------|------------|--|
| Heat load (W/mm <sup>3</sup> )        | 0.49       | 0.31       | 37                                     |
| Temperature (K)                       | 341        | 318        | 56.1                                   |
| Stress intensity (N/mm <sup>2</sup> ) | 57.3       | 24.2       | 57.8                                   |

The dual-rod concept is an effective approach to attain higher power from solar-pumped lasers, being possible to extract more laser output power from two thin rods with the same solar collection area. The significant improvement in the thermal conditions of the laser medium helps to increase the laser emission [78].

Table 6.9 shows the comparison between the LASCAD<sup>®</sup> numerical results and the experimental results of the most recent solar laser experiment using the same primary concentrator [18]. A 3.0 mm diameter, 30 mm length 1.0 at% Nd:YAG rod was side-pumped, which is very similar to the single-rod scheme used in this work. A large fused silica aspheric lens allowed an efficient focusing of the concentrated solar power from the focal zone of the parabolic mirror into the laser rod within a two-dimensional semi-cylindrical pump cavity. An asymmetric laser resonator was adopted to achieve maximum extraction of TEM<sub>00</sub>-mode laser power. For 2.87 W numerical TEM<sub>00</sub>-mode solar

laser power, 2.5% difference was found. The LASCAD<sup>®</sup> software also presented good agreement in the calculated and measured output laser beam profiles, as shown in Table 6.9.

**Table 6.9** Comparison between the LASCAD<sup>®</sup> numerical results and the experimental results of the most recent solar laser experiment [18].

| Side-pumped solar laser experiment [30] | LASCAD <sup>®</sup> numerical results   | Experimental results  |
|---|---|---|
| Solar irradiance                        | 770 W/m <sup>2</sup>  | 770 W/m <sup>2</sup>  |
| Effective collection area               | 0.9 m <sup>2</sup>  | 0.9 m <sup>2</sup>  |
| Thermal length                          | 406 mm  | 400 mm  |
| TEM <sub>00</sub> -mode laser power     | 2.87 W  | 2.80 W  |
| TEM <sub>00</sub> -mode beam profile    | <br>Calculated | <br>Measured |

For 770 W/m<sup>2</sup> solar irradiance and 0.9 m<sup>2</sup> effective collection area, 400 mm thermal length and 2.80 W TEM<sub>00</sub>-mode solar laser power with very good TEM<sub>00</sub>-mode laser beam profile were measured. The LASCAD<sup>®</sup> numerical analysis method was used to analyze the TEM<sub>00</sub>-mode solar laser output performance [18], revealing its accuracy in determining the thermal length of 406 mm with only 1.5% difference.

Significant enhancements in collection, conversion efficiencies and brightness figure of merit were numerically achieved. Due to the lower pumping intensity on each rod of the dual-rod scheme, considerable alleviation of thermal induced effects, such as heat load, temperature and stress intensity was achieved by using thin rods, when compared to the single-rod scheme. Besides, 1.25 times lower threshold pump power was also numerically calculated. The results are summarized in the Table 6.10.

**Table 6.10** The numerical results in this work compared with the experimental results in side-pumped TEM<sub>00</sub>-mode laser production of Vistas et al [45], Liang et al [46] and Liang et al [17].

| Parameters  | [45] | [46] | [17] | Present numerical work | Improvement in relation to<br>(Times) |      |      |
|---|------|------|------|------------------------|---------------------------------------|------|------|
|   |      |      |      |                        | [45]                                  | [46] | [17] |
| Collection area (m <sup>2</sup> )                       | 1.1  | 1.13 | 1.18 | 1.56                   | -                                     | -    | -    |
| Collection efficiency (W/m <sup>2</sup> )               | 3.6  | 3.98 | 7.9  | 11.0                   | 3.06                                  | 2.76 | 1.39 |
| Laser output (W)  | 4.0  | 4.5  | 9.3  | 17.2                   | 4.3                                   | 3.82 | 1.85 |
| Solar-to-TEM <sub>00</sub> -mode laser power conversion | 0.44 | 0.55 | 1.06 | 1.31                   | 2.98                                  | 2.38 | 1.23 |

|  |          |          |          |               |      |      |      |
|--|----------|----------|----------|---------------|------|------|------|
| efficiency (%)   |          |          |          |               |      |      |      |
| Solar irradiance (W/m <sup>2</sup> )   | 900      | 900      | 1000     | 890           | -    | -    | -    |
| M <sup>2</sup> factor (M <sub>x</sub> <sup>2</sup> ; M <sub>y</sub> <sup>2</sup> ) | 1.2; 1.1 | 1.1; 1.1 | 1.2; 1.2 | 1.1; 1.1      | -    | -    | -    |
| Brightness figure of merit (W)   | 3.0      | 3.72     | 6.46     | 7.15+<br>7.15 | 4.76 | 3.84 | 2.21 |
| Brightness conversion efficiency (%)   | 0.34     | 0.52     | 0.76     | 1.10          | 3.23 | 2.11 | 1.44 |

Significant advances in TEM<sub>00</sub>-mode output performances were numerically calculated, attaining 11.0 W/m<sup>2</sup> TEM<sub>00</sub>-mode collection efficiency, 1.31% solar-to-TEM<sub>00</sub>-mode laser power conversion efficiency, 14.3 W (7.15 W+7.15 W) brightness figure of merit and 1.09% brightness conversion efficiency, being 1.39, 1.23, 2.21 and 1.44 times, respectively, more than the previous experimental results.

### 6.2.2 Seven-rod pumping approach for TEM<sub>00</sub>-mode solar laser

A seven-rod concept for simultaneous emission of seven TEM<sub>00</sub>-mode solar laser was proposed following the multi-rod studies [79]. In present-day single-rod/single-beam solar laser systems, the thermal lens effect is a serious issue which limits its ability for a scale-up to higher powers and improved beam quality. Aiming at resolving this shortcoming, the concept of a seven-rod/seven-beam solar pumping scheme was developed.

The primary system used was NOVA heliostat-parabolic mirror, using an effective collection area of 1.77 m<sup>2</sup> and assuming a solar irradiance of 950 W/m<sup>2</sup>. The large laser head, presented in Fig. 6.30 consisted of seven fused silica compound parabolic concentrators, which transmitted and focused the concentrated solar radiation to each single laser rod of small diameter, within a conical cavity. Consequently, each laser rod was pumped by only one-seventh of the total concentrated solar power, ensuring a significant reduction of the thermal induced effects in the laser rods.

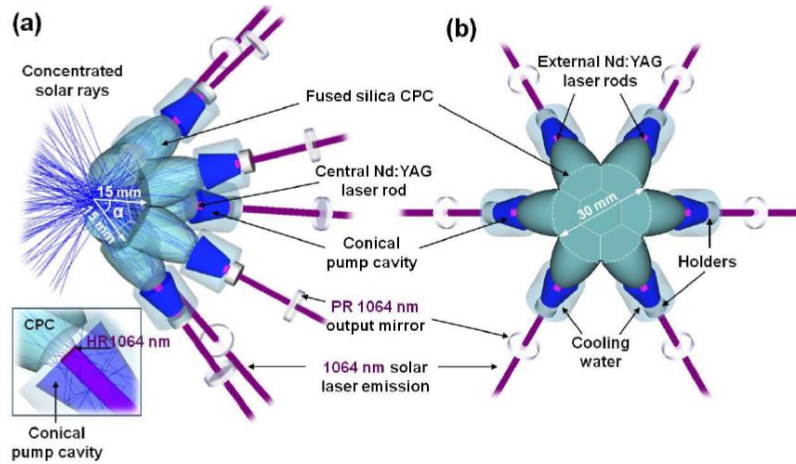


**Figure 6.30** (a) 3D and (b) 2D view of the single large laser head near the focal zone, with their respective resonators.  $\alpha$  represents the spatial angle between the optical axes of the external CPCs and the optical axis of the parabolic mirror.

TEM<sub>00</sub>-mode laser power of 23.43 W (3.51 W + 6×3.32 W) was calculated, as given in Fig. 6.31.



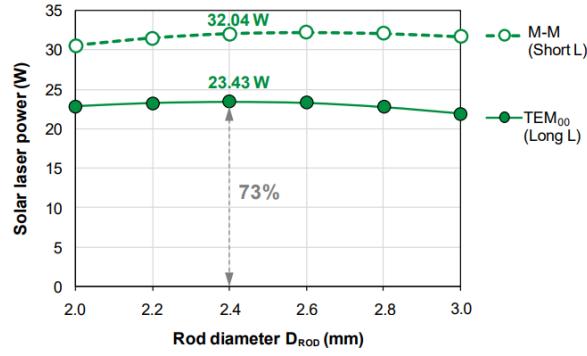


**Figure 6.31** Total TEM<sub>00</sub>-mode-to-multimode (M-M) laser power ratio as a function of the laser rod diameter (DROD) from the seven-rod scheme.

An alternative seven-rod solar pumping scheme is proposed to significantly improve the TEM<sub>00</sub>-mode solar laser performance. 13.3 W/m<sup>2</sup> TEM<sub>00</sub>-mode solar laser collection efficiency was numerically achieved, representing an enhancement of 1.68 times over the experimental result from a single-rod prototype. 1.80 times improvement in solar-to-TEM<sub>00</sub>-mode laser power conversion efficiency was also registered in relation to the previous experimental results.

### 6.2.3 Doughnut-shaped solar laser beams numerical analysis

A doughnut-shaped and a top-hat solar laser beam numerical analysis was also developed during these years [80]. The top hat laser beam profile is well-known for uniformly irradiating the target material, significantly reducing the heat-affected zones, typical of Gaussian laser irradiation, whereas the doughnut-shaped laser beam has attracted much interest for its use in trapping particles at the nanoscale and improving mechanical performance during laser-based 3D metal printing. Solar-pumped lasers can be a cost-effective and more sustainable alternative to accomplish these useful laser beam distributions.

The proposed side-pumping solar laser approach (Fig. 6.32) was composed of six circular Fresnel lenses ( $F_1 - F_6$ ), for collection and concentration of the incoming solar radiation, aligned with six plane folding mirrors ( $M_1 - M_6$ ), which redirected the concentrated solar radiation from the Fresnel lenses onto the laser head. The total collection area used was of 4.0 m<sup>2</sup>. The plane folding mirrors had an inclination angle of 45° in relation to their common optical axis and were located below their respective Fresnel lenses.

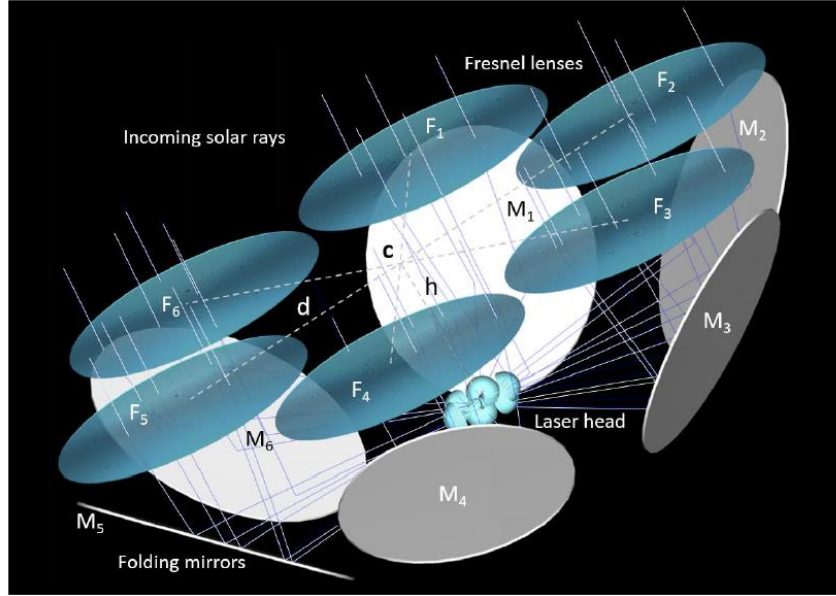


**Figure 6.32** Six Fresnel lens solar laser side-pumping concept with 4.0 m<sup>2</sup> total collection area. F<sub>1</sub> – F<sub>6</sub> and M<sub>1</sub> – M<sub>6</sub> indicates the six Fresnel lenses and the six folding mirrors, respectively.

For a high focusing of the solar radiation into the Nd:YAG laser rod, six fused silica aspheric concentrators and six twisted fused silica light guides were designed, as presented in Fig 6.33.

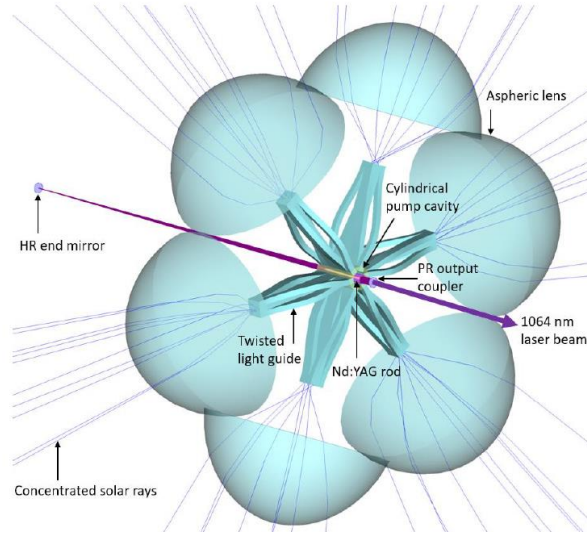


**Figure 6.33** 3D view of the six secondary aspheric lenses, the six twisted light guides, the cylindrical pump cavity and the Nd:YAG rod, and the HR end mirror and the PR output coupler, which compose the resonant cavity.

Fig. 6.34a presents the 3D view of the top hat laser beam profile obtained from the 5.5 mm diameter laser rod with beam quality factors of  $M_x^2 = 1.25$ ,  $M_y^2 = 1.00$  and TEM<sub>00</sub>-mode laser power of 37.5 W. For the doughnut-shaped laser beam profile obtained from the 5.8 mm laser rod diameter, 39.0 W TEM<sub>00</sub>-mode laser power was numerically attained, with beam quality factors of  $M_x^2 = 1.90$ ,  $M_y^2 = 1.00$ , as shown in Fig. 6.34b.

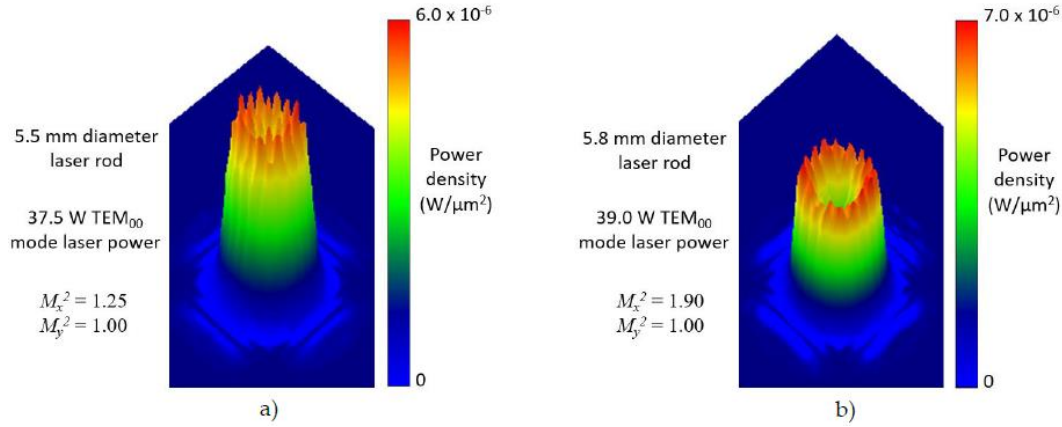


**Figure 6.34** Numerically simulated 3D laser beam profile for (a) the 5.5 mm diameter and (b) the 5.8 mm diameter laser rods.

As far as we know, the first numerical simulation of doughnut-shaped and top hat solar laser beam profiles was reported here, significantly contributing to the understanding of the formation of such beam profiles, what significantly contributes to understand how to generate such beams, particularly the top hat solar laser beam that was not yet demonstrated in practical essays. Future research aims to experimentally validate the results obtained here for both the top hat and doughnut-shaped laser beam profiles. A top hat laser beam profile ( $M_x^2 = 1.25$ ,  $M_y^2 = 1.00$ ) was computed, with  $9.4 \text{ W/m}^2$  TEM<sub>00</sub>-mode laser power collection and 0.99% solar-to-TEM<sub>00</sub>-mode power conversion efficiencies.

#### 6.2.4 A doughnut-shaped Nd:YAG solar laser beam

Solar laser beams with doughnut shapes were already extracted in [81]. This time it was reported a doughnut-shaped solar laser beam from a Nd:YAG rod pumped through a heliostat-parabolic mirror system [82]. The influences of the radius of curvature of the output mirror and laser resonant cavity length on the laser output performance were studied. The primary system used was NOVA heliostat-parabolic mirror, using an effective collection area of  $1.0 \text{ m}^2$  and a solar irradiance of  $850 \text{ W/m}^2$ . The solar laser head used in this experience is shown in the Fig. 6.35.

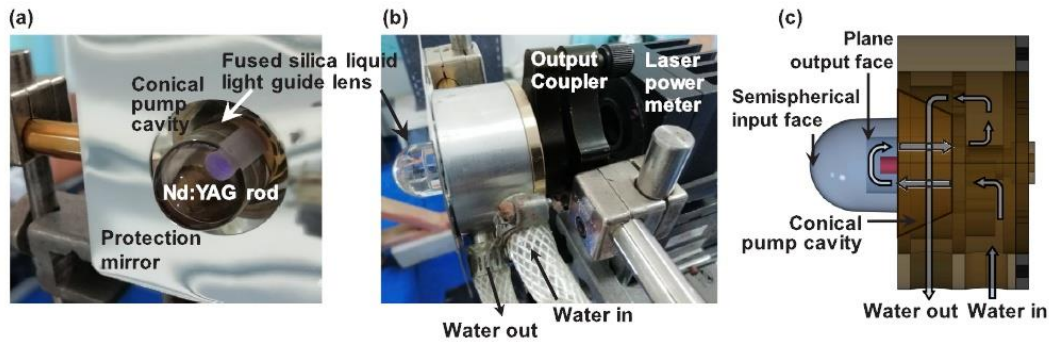


**Figure 6.35** (a, b) Photographs and (c) mechanical design of the Nd:YAG solar laser head.

To obtain efficient extraction of low mode power, the laser should operate close to the edge of the optically stable region, where the fundamental mode size is more sensitive to thermal focus fluctuations. At a resonant cavity length of 600 mm, doughnut-shaped solar laser beam with 4.5 W laser power was registered, corresponding to  $4.5 \text{ W/m}^2$  collection efficiency. The TEM<sub>01</sub>\* doughnut-shaped mode is the second lowest order mode, having approximately

1.5 times the diameter of the fundamental  $TEM_{00}$ -mode [40, 83]. The  $TEM_{00}$ -mode solar laser oscillation was obtained by shifting the output coupler to  $L = 680$  mm, at the limit of thermally stable zone. Maximum  $TEM_{00}$ -mode solar laser power of 3.0 W was measured. The experimental results with the beam shapes are given in the figure 6.36. The intensity distribution of the doughnut-shaped beam and thus the laser power changed with slight angular adjustments in the output mirror (Fig. 6.36b). A doughnut-shaped beam with 18% of the maximum intensity at the center was obtained at the cost of slightly lower laser output power of 4.2 W, as indicated by Fig. 6.36c. To characterize the radial intensity distribution of the doughnut-shaped beams, beam diameters and dark spot sizes [84] are also indicated in Fig. 6.36.

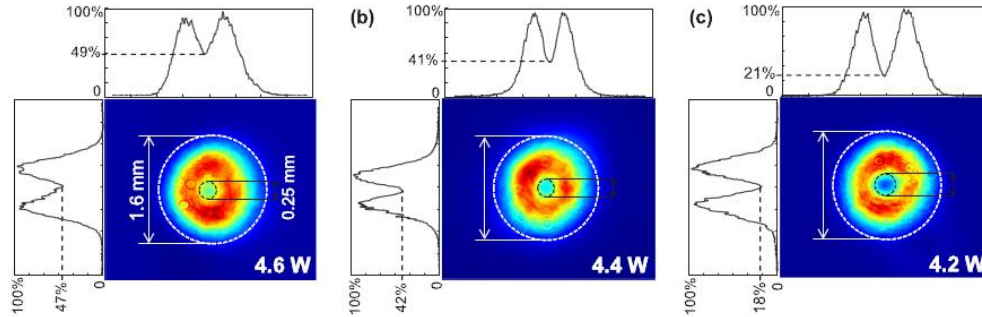


**Figure 6.36** Doughnut-shape solar laser beam profiles at a resonant cavity length of 600 mm. Influenced by the slight angular adjustment of the output mirror.

By operating the laser close to the edge of the optically stable region,  $4.5 \text{ W/m}^2$  doughnut-shaped solar laser collection efficiency was obtained without any extra optical element in the resonator. Non-conventional laser beam shapes, such as doughnut-shaped and petal-like laser beams, open new perspectives for technologically relevant areas such as deep-hole drilling, photopolymerization, nano-patterning, optical manipulation, and so forth.

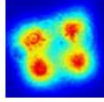
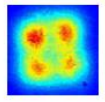
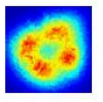
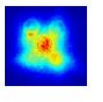
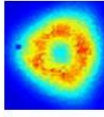
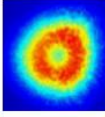
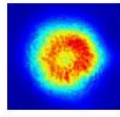
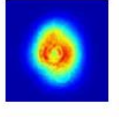
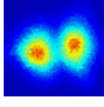
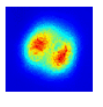
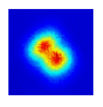
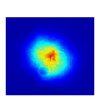
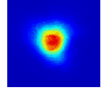
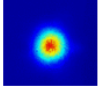
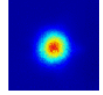
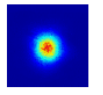
### 6.2.5 Solar laser $TEM_{11}$ , $TEM_{01*}$ , $TEM_{10}$ , $TEM_{00}$ mode profiles

Using the same solar laser experiment producing multimode solar power already described in section 6.1, the novel side-pumping approach also enabled an efficient production of high-quality solar laser beams with very useful  $TEM_{11}$ ,  $TEM_{01*}$ ,  $TEM_{10}$ ,  $TEM_{00}$  mode profiles [18].

The primary system used was NOVA heliostat-parabolic mirror with an effective collection area of  $0.9 \text{ m}^2$  and a solar irradiance of  $700 \text{ W/m}^2$ . The solar laser head was already described in this thesis. By adopting an asymmetric laser resonator, it was obtained the following results:  $TEM_{11}$  (4.0 W),  $TEM_{01*}$  (doughnut-shaped, 2.9 W),  $TEM_{10}$  (3.2 W) or  $TEM_{00}$  (2.8 W) mode profiles. As shown in Table 6.11, when  $L_2$  was fixed at 60 mm, then  $L_1$  played a very important role in controlling the number of lasing modes and power. For  $L_1 = 315$  mm at  $770 \text{ W/m}^2$  solar irradiance, 3.9 W – 4.0 W solar laser power with  $TEM_{11}$  mode profiles were observed. When  $L_1$  was increased to 370 mm, the  $TEM_{11}$  profile was reduced to a quasi- $TEM_{00}$ -mode profile with 3.5 W solar laser power. For  $L_1 = 380$  mm, we took advantage of the variation of solar irradiance, from  $700 \text{ W/m}^2$  to  $810 \text{ W/m}^2$ , during the day, to achieve different  $TEM_{01*}$  mode profile at different laser power level, varying between 2.6 W and 2.9 W. Due to the power-dependent thermal lensing and mode-matching sensitivity of the laser material, different solar irradiance led to different thermal lensing effect, and hence the production of  $TEM_{01*}$  beams with different dimensions, power and contrast. For these reasons, strong thermal lensing at  $810 \text{ W/m}^2$  irradiance had the tendency to change the  $TEM_{01*}$  doughnut-shaped beam into an approximate  $TEM_{01*} + TEM_{00}$  mode beam at 2.7 W laser

power. For  $L_1 = 390$  mm, TEM<sub>01</sub> mode laser beam was obtained. We took again the advantage of the variation of solar irradiance during another day, from 700 W/m<sup>2</sup> to 840 W/m<sup>2</sup>, to achieve different TEM<sub>01</sub> mode profiles at different laser power level, varying between 2.5 W and 3.2 W. In Table 6.11 it is shown the experimental results with different solar laser beam shapes obtained.

**Table 6.11** Summary of TEM<sub>11</sub>, TEM<sub>01</sub><sup>\*</sup>, TEM<sub>10</sub> and TEM<sub>00</sub>-mode laser beam profiles by side-pumping the 3mm diameter 30mm length rod with the two-dimensional semi-cylindrical pump cavity.

|  |   |   |  |   |
|--|---|---|--|---|
| TEM <sub>11</sub><br>Mode              | 4.0W, L <sub>1</sub> 315mm<br>770W/m <sup>2</sup>                                   | 3.9W, L <sub>1</sub> 315mm<br>770W/m <sup>2</sup>                                   | 3.7W, L <sub>1</sub> 360mm<br>770W/m <sup>2</sup>                                    | 3.5W, L <sub>1</sub> 370mm<br>770W/m <sup>2</sup>                                     |
| Constant<br>irradiance                 |    |    |    |    |
| TEM <sub>01</sub> <sup>*</sup><br>Mode | 2.9W, L <sub>1</sub> 380mm<br>700W/m <sup>2</sup>                                   | 2.7W, L <sub>1</sub> 380mm<br>720W/m <sup>2</sup>                                   | 2.6W, L <sub>1</sub> 380mm<br>760W/m <sup>2</sup>                                    | 2.7W, L <sub>1</sub> 380mm<br>810W/m <sup>2</sup>                                     |
| Variable<br>irradiance                 |    |    |    |    |
| TEM <sub>01</sub><br>Mode              | 3.2W, L <sub>1</sub> 390mm<br>700W/m <sup>2</sup>                                   | 2.8W, L <sub>1</sub> 390mm<br>760W/m <sup>2</sup>                                   | 2.6W, L <sub>1</sub> 390mm<br>800W/m <sup>2</sup>                                    | 2.5W, L <sub>1</sub> 390mm<br>840W/m <sup>2</sup>                                     |
| Variable<br>irradiance                 |   |   |   |   |
| TEM <sub>00</sub><br>Mode              | 2.8W, L <sub>1</sub> 400mm<br>770W/m <sup>2</sup>                                   | 2.5W, L <sub>1</sub> 400mm<br>790W/m <sup>2</sup>                                   | 2.4W, L <sub>1</sub> 400mm<br>820W/m <sup>2</sup>                                    | 2.3W, L <sub>1</sub> 400mm<br>830W/m <sup>2</sup>                                     |
| Variable<br>irradiance                 |  |  |  |  |

TEM<sub>00</sub>-mode solar laser emissions with excellent beam profiles, at 2.5 W, 2.4 W, and 2.3 W power were respectively measured for the solar irradiance varying between 790 W/m<sup>2</sup> and 830 W/m<sup>2</sup>.

### 6.3 Laser beam merging technique

In this section it will be described what we name as solar laser beam merging technique, a novel technology developed to obtain a single laser beam from various laser rods emitting from the multi-rod approaches investigated along these years. The term is related to the resonant laser cavity configuration composed of several output mirrors, in which several laser beams are merged to one single laser beam with improved M<sup>2</sup> factors and brightness, simplifying its operation and the delivering of the solar laser beam.



### 6.3.1 Dual-rod multimode solar laser beam merging technique

In 2019, the laser beam merging technique was implemented for the first time with the dual-rod scheme described in section 6.2.1 with a semi-cylindrical fused silica lens and CPC-semicylindrical pump cavities [28]. Instead of combining the two laser beams using extra optical mirrors (dual-rod two laser beams scheme, with two separate laser cavities), there is an interesting alternative laser cavity design to obtain a single laser beam from the two rods (dual-rod one laser beam scheme) through a single folded laser cavity such as in diode-pumped lasers, as shown in Fig. 6.37. This constitutes an effective solution to reduce the  $M^2$  factors and consequently improve the beam quality of solar lasers.

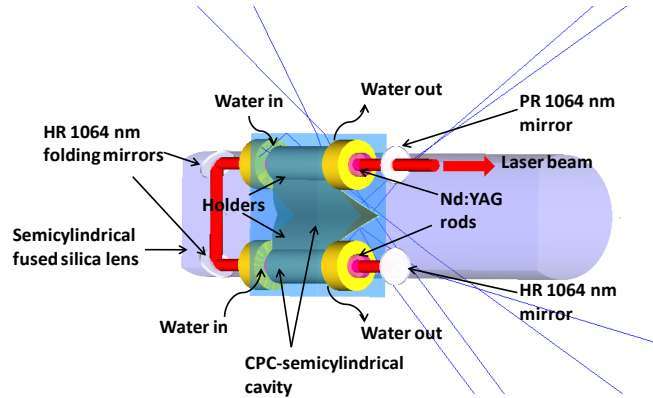


**Figure 6.37** Alternative dual-rod laser cavity design to extract one single laser beam from the two Nd:YAG rods. One HR 1064 nm end mirror, two HR 1064 nm folding mirrors, one PR 1064 nm output mirror and two laser rods form the laser resonant cavity in the dual-rod single laser beam approach.

The multimode laser output power as a function of the incoming solar power reaching the primary solar concentrator was also numerically calculated, as shown in Fig. 6.38, for the single-rod scheme and the dual-rod scheme with two laser beams and one laser beam.

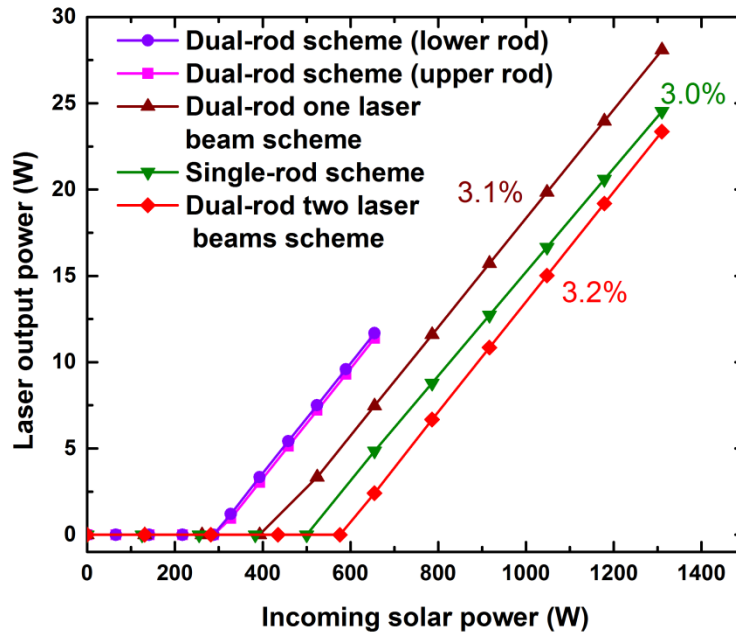


**Figure 6.38** Multimode laser output power as a function of the incoming solar power for the single-rod scheme with the 4.5 mm diameter, 25 mm length rod and the dual-rod scheme, with two 3.5 mm diameter, 25 mm length rods.

For the single-rod scheme, the threshold pump power of 500 W was numerically calculated. For the dual-rod scheme, 288 W threshold pump power was calculated for either the upper or the lower rod, resulting in a combined threshold pump power of 576 W for the dual-rod two laser beams scheme. However, with the dual-rod one laser beam scheme, the threshold pump power was significantly reduced to 400 W. The multimode laser slope efficiency – the slope of the curve obtained by plotting the laser output versus the incoming solar power – was also calculated for both schemes. The  $M^2$  factors and the brightness figure of merit of the single and dual-rod schemes were also numerically calculated. The results are summarized in Table 6.12.

**Table 6.12** Numerically calculated multimode laser output power, slope efficiency, threshold pump power,  $M^2$  factors and brightness figure of merit for the single-rod scheme and the dual-rod two laser beams and one laser beam schemes.

| Parameter                          | Schemes    |                          |                         |
|------------------------------------|------------|--------------------------|-------------------------|
|                                    | Single-rod | Dual-rod two laser beams | Dual-rod one laser beam |
| Laser output power (W)             | 24.9       | 23.1                     | 28.1                    |
| Slope efficiency (%)               | 3.0        | 3.2                      | 3.1                     |
| Threshold pump power (W)           | 500        | 576                      | 400                     |
| $M^2$ factor ( $M_x^2$ ; $M_y^2$ ) | 39.4; 39.4 | 40.2; 40.2               | 37.0; 37.0              |
| Brightness figure of merit (W)     | 0.016      | 0.014                    | 0.018                   |

As shown in Table 6.12, the dual-rod one laser beam scheme offers the best laser power and the lowest threshold pump power, as compared to both the single-rod and dual-rod two laser beams schemes. In terms of laser beam quality  $M^2$  factor, the dual-rod one laser beam scheme also provides a slightly reduced  $M^2$  factor of  $M_x^2 = M_y^2 = 37.0$ , resulting in the highest laser beam figure of merits of 0.018W among the three schemes.

### 6.3.2 Dual-rod multimode solar laser with ring-array concentrators and beam merging

At the end of 2020, the dual-rod model that demonstrated the better solar laser performance, pumped by the RAC as a primary concentrator, was introduced and simulated, using a fused silica aspherical lens and the semicylindrical pump cavity with some differences from other publications, due to the rim angle of the solar rays coming from the primary concentrator to pump the laser rods. The same numerical model was also studied to produce TEM<sub>00</sub>-mode solar laser, and the results were very good. The detailed description of this dual-rod side-pumping solar laser pumped by a RAC, will be given below, which led to a publication in 2021. A three-folding beam merging technique was also introduced, this time in order to analyze the influence of the non-uniformities of the solar pumping onto the laser rods and their laser emission [31].

The primary concentrator used in this work was the RAC with an effective collection area of 1.71 m<sup>2</sup> and considering a solar irradiance of 950 W/m<sup>2</sup>. The solar laser head of the single-rod pumping scheme was composed of a fused silica aspherical lens and a 2D-shaped-semicylindrical pump cavity, within which a 5.5 mm diameter, 25 mm length Nd:YAG laser rod was mounted, as shown in Fig. 6.39.

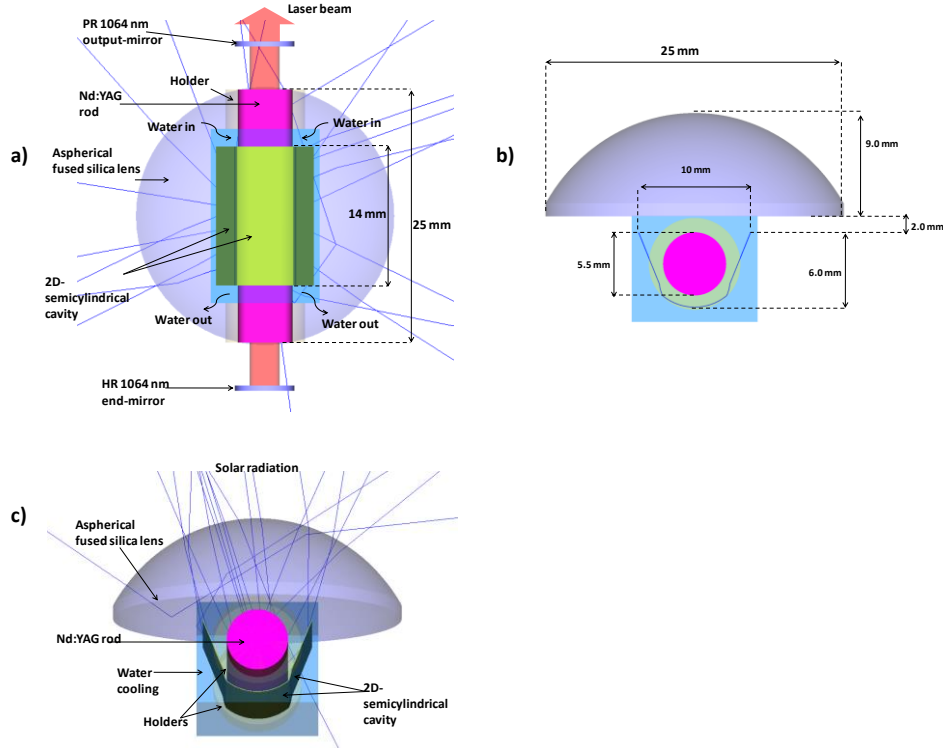


**Figure 6.39** Solar laser head design for the Nd:YAG side-pumped single-rod scheme: a) top view, b) cross-sectional view with the key dimensions indicated and c) 3D view. It consisted of the fused silica aspherical lens, the 2D-shaped-semicylindrical pump cavity and the Nd:YAG laser rod, fixed by two holders. The resonant laser cavity is also represented in a).

A multi-pass absorption of the radiation by the laser rod was ensured by the 2D-shaped-semicylindrical pump cavity, with  $10 \text{ mm} \times 14 \text{ mm}$  rectangular input aperture,  $6.0 \text{ mm} \times 14 \text{ mm}$  rectangular output aperture, and a semicylindrical pump cavity at its end with 5.5 mm radius, 14 mm length and 3.0 mm height. 95% reflectivity was assumed for the inner walls of the pump cavity reflectors. The single-rod scheme resonant laser cavity consisted of one HR 1064 nm end-mirror at 99.9% reflectivity and one PR 1064 nm end-mirror at 96% reflectivity.

In Fig. 6.40a), b) and c) is presented the dual-rod side-pumping scheme configuration, composed of a small fused silica aspherical lens and a 2D-shaped-semicylindrical pump cavity, within which a 4.0 mm diameter, 25 mm length Nd:YAG laser rod was mounted. The 2D-shaped pump cavity had  $7.2 \text{ mm} \times 14 \text{ mm}$  rectangular input aperture and  $4.5 \text{ mm} \times 14 \text{ mm}$  output aperture, efficiently coupling the solar rays to the laser crystals through the semicylindrical pump cavities with 8.0 mm radius, 14 mm length and 3.0 mm height. 95% reflectivity was assumed for the inner walls of both pump cavity reflectors. The dual-rod side-pumping scheme had a laser resonant cavity for each one of the rods, which consisted of one HR 1064 nm end-mirror at 99.9% reflectivity and one PR 1064 nm end-mirror at 94% reflectivity. In Fig. 6.40d) is shown the laser head built for future solar laser experiments. All the key dimensions were based on both the numerical simulations and experimental design feedbacks acquired from building this solar laser head. Technical issues such as water cooling, the mechanical fixation of the two Nd:YAG rods, the HR 1064 nm end-mirror, the PR 1064 nm output mirror and the three HR 1064 nm folding mirrors have been considered in the present numerical scheme, providing more reliability to the numerical modeling by ZEMAX<sup>®</sup> and LASCAD<sup>®</sup> analysis, as compared to the previous published numerical results [30].



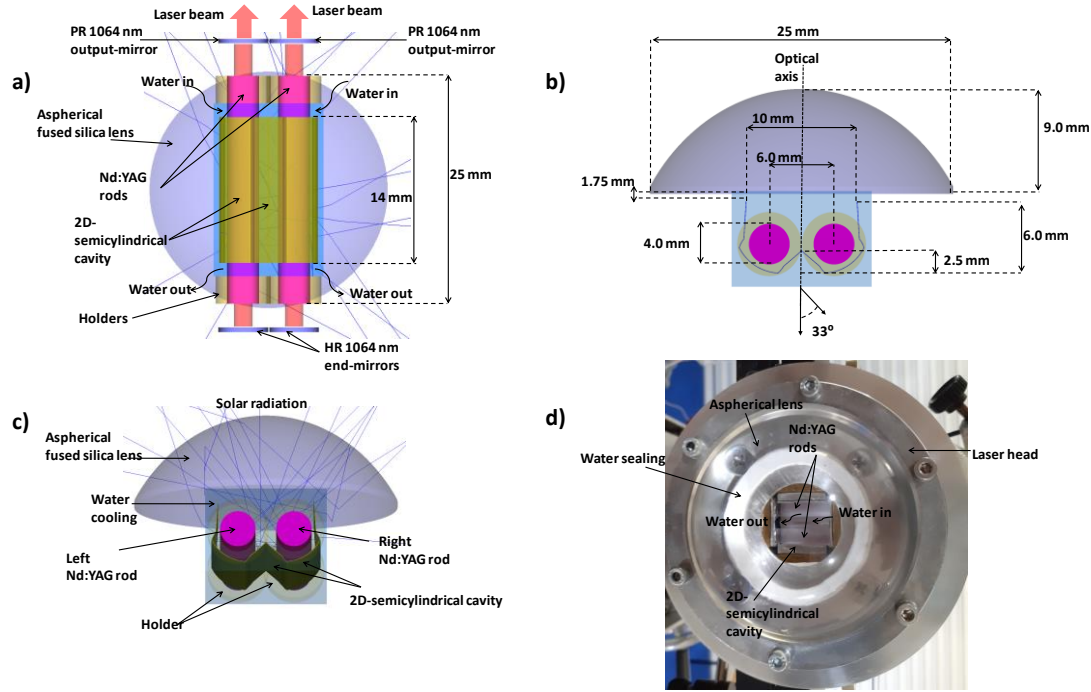


**Figure 6.40** Solar laser head design for the Nd:YAG side-pumped dual-rod scheme: a) top view, b) cross-sectional view with the key dimensions indicated, c) 3D view and d) laser head built for future solar laser experiments.

The simulations in ZEMAX<sup>®</sup> were done in a similar way as the previous ones already described before in this thesis. The dual-rod side-pumping scheme showed a reduction in the peak intensity of about 47.3% at the center of the laser rods, where the main contribution of the absorbed pump power comes from, relatively to the single-rod side-pumping scheme, reducing the creation of hotspots in the laser rod.

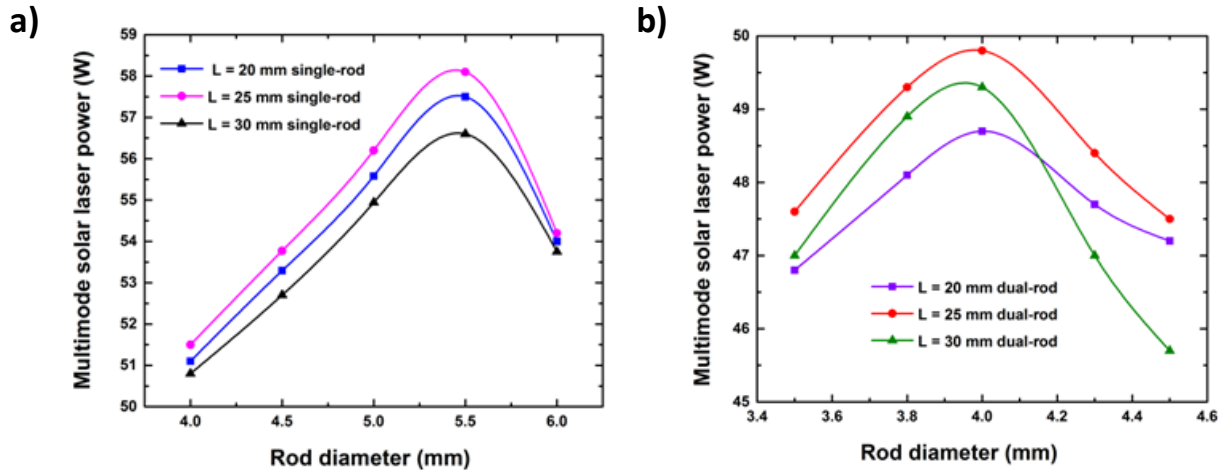


**Figure 6.41** Numerically calculated multimode solar laser output power as a function of the rod diameter and length (L), for the single-rod and the dual-rod side-pumping schemes.

For the single-rod side-pumping scheme, the maximum numerical multimode laser output power was achieved with an 85 mm length resonant cavity and  $\text{RoC} = -10$  m for both end-mirrors. For the dual-rod side-pumping scheme, the same parameters were found for the maximum multimode laser output power. In Fig. 6.41a) is shown the multimode laser output power for the single-rod side-pumping scheme, as a function of the laser rod diameter and length. The maximum multimode solar laser power obtained was 58.30 W. In Fig. 6.41b) is shown the multimode

laser output power for the dual-rod side-pumping scheme, as a function of the laser rod diameter and length. The maximum multimode solar laser power obtained was 49.70 W, calculated from the sum of the laser output power of 24.85 W from each one of the rods.

The laser output power is directly proportional to the transfer efficiency from the solar pump source onto the laser rod and its absorption efficiency by the rod. The rod diameter affects the optimum beam waist radius and the maximum output laser power greatly. Too small rod diameter means that the crystal could not absorb the pump power adequately and the laser output is low. Nevertheless, too large rod diameter is not good for the laser output, too, due to the low pump intensity in the rod center. The result implies that there is the optimum rod diameter to maximize the output laser power [85]. For the proper design of a solar-pumped laser, another key parameter that determines the laser efficiency and output power is the spatial overlap between the solar pump mode and the laser mode in the active material. Since the laser mode is mainly determined by laser resonator parameters, the optimization of laser rod diameter and consequently, approaching the solar pump mode size to that of the laser mode is fundamental for efficient solar laser emission. In order to extract one single laser beam from the two laser crystals, a single folding laser resonant cavity can be set, forming an U-shaped cavity, such as in diode-pumped lasers [75], as shown in Fig. 6.42.

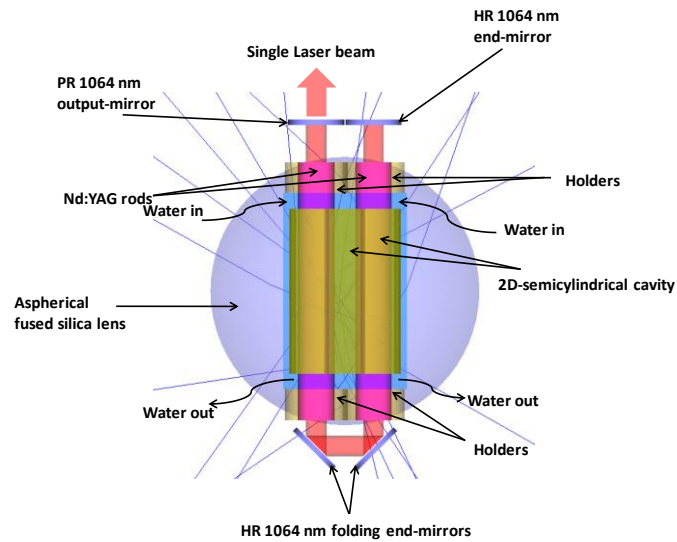


**Figure 6.42** Design of the solar laser head with two Nd:YAG crystals in order to obtain one single laser beam from the two rods. Two HR 1064 nm folding end-mirrors, one HR 1064 nm end-mirror and one PR 1064 nm output-mirror compose the folding laser resonant cavity, along with the two laser rods.

The single laser beam cavity from the dual-rod scheme consisted of one HR 1064 nm end-mirror with 99.9% reflectivity and 0.1% loss, two HR 1064 nm folding end-mirrors with 99.9% reflectivity and 0.1% loss each, and one PR 1064 nm output-mirror with 94% reflectivity were used. The beam propagation method was used to calculate 0.03% diffraction losses for the dual-rod scheme with 4.0 mm diameter, 25 mm length laser rods, resulting in a total round-trip loss of 3.73%.

The numerical multimode solar laser output power as a function of the incoming solar power was also determined, as shown in Fig. 6.43. Each individual laser rod, both left and right, and their total solar laser power are also represented.

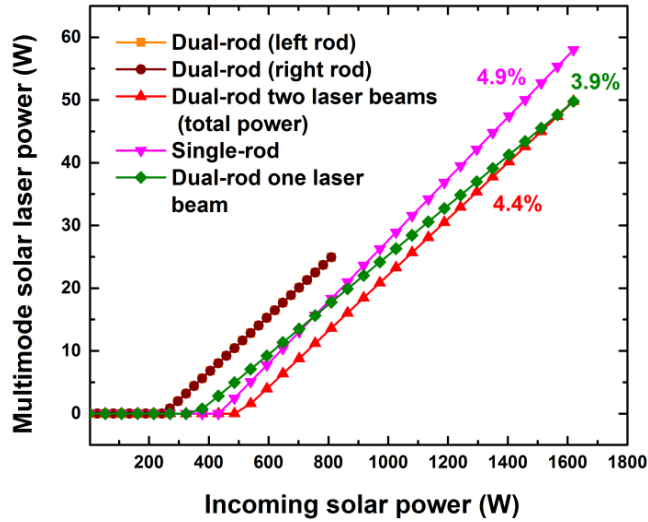


**Figure 6.43** Multimode solar laser output power as a function of the incoming solar power, for both the single-rod and the dual-rod side-pumping-schemes: the latter in two configurations, two laser beams with its total power and single laser beam. The laser slope efficiencies are also represented.

The numerical slope efficiency was also calculated. The threshold pump power, the  $M^2$  factors and the brightness figure of merit [15] were determined for all the schemes. The numerical results of the single-rod, the dual-rod two laser beams and the dual-rod single laser beam side-pumping schemes are summarized in Table 6.13.

**Table 6.13** Multimode solar laser output power, collection efficiency, threshold pump power, laser slope efficiency, solar-to-laser power conversion efficiency,  $M^2$  factors and brightness figure of merit for the single-rod scheme, the dual-rod two laser beams and the dual-rod single laser beam schemes.

| Parameter                                      | Schemes    |                          |                            |
|--|------------|--------------------------|----------------------------|
|  | Single-rod | Dual-rod two laser beams | Dual-rod single laser beam |
| Solar laser output power (W)                   | 58.30      | 49.70                    | 49.89                      |
| Collection efficiency (W/m <sup>2</sup> )      | 34.09      | 29.06                    | 29.18                      |
| Threshold pump power (W)                       | 432        | 486                      | 243                        |
| Laser slope efficiency (%)                     | 4.91       | 4.38                     | 3.85                       |
| Solar-to-laser power conversion efficiency (%) | 3.59       | 3.06                     | 3.07                       |
| $M^2$ factor ( $M^2_x$ ; $M^2_y$ )             | 92.0; 92.0 | 36.0; 36.0               | 33.0; 33.0                 |
| Brightness figure of merit (W)                 | 0.007      | 0.038                    | 0.046                      |

In the solar laser configurations studied in this work, the laser resonant cavities used for the solar laser extraction were short (85 mm), hindering the clear observation of the effect of the non-uniform solar absorption pumping profiles of the laser rods on the laser beam profile and, hence, on the laser beam quality factors. However, this effect on the solar laser beam profile is more evident when longer resonant cavities are used, as shown in Fig. 6.44, since

they only allow the oscillation of low-order laser modes. For easy understanding, each laser rod of the dual-rod scheme was divided in two regions, one representing the section with higher pump flux absorption (A and B for the right and the left rods, respectively) and the other representing the section with lower pump flux absorption (A' and B' for the right and the left rods, respectively). Analogously, the representation of the laser beam, passing back and forth through those sections of the laser rod between the HR 1064 nm and the PR 1064 nm mirrors, were also divided in two in order to represent the contributions of each one of these pumped regions to the total solar laser emission. A compensation of the laser beam profile was obtained with the arrangement of the three HR 1064 nm folding end-mirrors  $M_1$ ,  $M_2$  and  $M_3$ , as shown in Fig. 6.44a), where the part of the laser beam passing through the region of the right laser rod with higher pump flux absorption (A) is folded to the region of the left laser rod with lower pump flux absorption (B'); while the part of the laser beam passing through the region of the left laser rod with higher pump flux absorption (B) is folded towards the region of the right laser rod with lower pump flux absorption (A'). In this way, the uniformity of the pump flux absorption by the laser rods was achieved, resulting in a quasi-symmetric beam profile for this dual-rod single laser beam and, consequently, an improved beam quality. This is not the case with the dual-rod single laser beam scheme with just two HR 1064 nm folding end-mirrors, as shown in Fig. 6.44b), where the laser beam passing through the region of the right (left) laser rod, with higher pump flux absorption A (B) is folded to the region of the left (right) laser rod with also higher pump flux absorption B (A), leading to an asymmetric single laser beam profile.

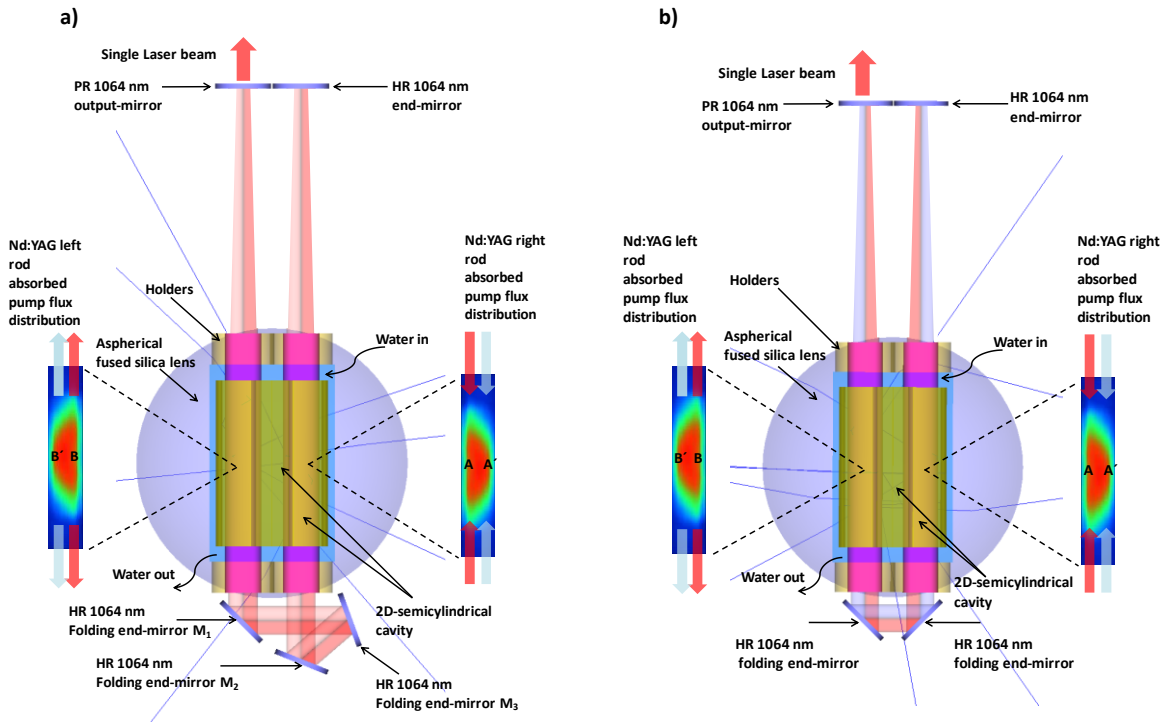


**Figure 6.44** Designs of the dual-rod solar laser heads with longer resonant cavities in order to obtain one single laser beam from the two Nd:YAG rods: a) dual-rod single laser beam with quasi-symmetric beam profile, b) the dual-rod single laser beam, with only two HR 1064 nm folding end-mirrors to compose the folding resonant cavity, along with the PR 1064 nm output mirror.

The three-folding-scheme arrangement used in Fig. 6.44 a), designed to compensate the laser beam profile, was also studied in a short resonant cavity, but the  $M^2$  beam quality factors obtained were similar to that of the dual-rod single laser beam, since short laser cavity allows the oscillation of higher-order modes inside the resonant cavity [17, 78]. The single-rod and the dual-rod two laser beams schemes were also investigated with longer resonant cavities. The

numerically calculated solar laser  $M^2$  factors with their respective longer resonant cavity lengths are summarized in Table 6.14.

**Table 6.14** Numerically calculated solar laser  $M^2$  factors and resonant cavity lengths for the single-rod scheme and the dual-rod scheme for two laser beams, single laser beam and single laser beam with quasi-symmetric beam profile.

| Scheme  | $M_x^2$ | $M_y^2$ | Resonant cavity length (mm) |
|---|---------|---------|-----------------------------|
| Single-rod scheme   | 1.00    | 12.98   | 1325.3                      |
| Dual-rod scheme two laser beams                                     | 1.00    | 4.06    | 1981.6                      |
| Dual-rod scheme single laser beam                                   | 1.00    | 7.74    | 1022.2                      |
| Dual-rod scheme single laser beam with quasi-symmetric beam profile | 1.00    | 1.41    | 1073.6                      |

The obtained numerical results from this work and their comparison with the most efficient experimental side-pumped Nd:YAG solar laser are provided in Table 6.15.

**Table 6.15** Numerically calculated laser output power, collection efficiency and solar-to-laser power conversion efficiency for the single-rod and the dual-rod schemes presented in this work, and their comparison with the most efficient experimental side-pumped solar laser of Liang *et al* [76] and the most efficient numerical single-rod and dual-rod solar laser [30]. It is also shown the collection areas and the solar irradiance. The collection areas of the solar concentrators are also shown.

| Parameters                                     | Experimental results from [76] | Single-rod scheme from [30] | Dual-rod scheme from [30] | Present numerical work |                 | Improvements (times)      |                         |                           |                         |
|--|--------------------------------|-----------------------------|---------------------------|------------------------|-----------------|---------------------------|-------------------------|---------------------------|-------------------------|
|  |                                |                             |                           | Single-rod scheme      | Dual-rod scheme | Single-rod scheme to [76] | Dual-rod scheme to [76] | Single-rod scheme to [30] | Dual-rod scheme to [30] |
| Collection area (m <sup>2</sup> )              | 0.9                            | 1.56                        | 1.56                      | 1.71                   | 1.71            | -                         | -                       | -                         | -                       |
| Laser output power (W)                         | 15.8                           | 42.70                       | 35.84                     | 58.30                  | 49.70           | -                         | -                       | -                         | -                       |
| Collection efficiency (W/m <sup>2</sup> )      | 17.6                           | 27.37                       | 22.97                     | 34.10                  | 29.06           | 1.94                      | 1.65                    | 1.25                      | 1.26                    |
| Solar-to-laser power conversion efficiency (%) | 2.43                           | 3.26                        | 2.74                      | 3.59                   | 3.06            | 1.48                      | 1.26                    | 1.10                      | 1.12                    |

By considering important issues such as water cooling and the mechanical fixation of the two Nd:YAG rods, the HR and PR resonator mirrors, numerical designs were accomplished by ZEMAX<sup>®</sup> and LASCAD<sup>®</sup> software and an experimental side-pumped dual-rod solar laser head was built to improve these designs.

Significant enhancements were numerically achieved with the proposed side-pumping schemes being pumped by the RAC. For the single-rod scheme, 58.30 W solar laser output power was obtained, corresponding to 34.10 W/m<sup>2</sup> collection efficiency and 3.59% solar-to-laser power conversion efficiency, being 1.94 and 1.47 times, respectively, more than the previous experimental results in side-pumping solar laser configurations [76]. The dual-rod scheme attained 49.70 W solar laser output power, but still corresponding to 29.06 W/m<sup>2</sup> collection efficiency and 3.06% solar-to-laser power conversion efficiency, being 1.65 and 1.26 times, respectively, more than the previous experimental result in side-pumping configuration [76].

Relatively to the numerical results of the previous single-rod and dual-rod side-pumping schemes [30], the numerical achievements obtained in this work by the single-rod scheme presented 1.25 and 1.10 times more collection efficiency and solar-to-laser power conversion efficiency, respectively, than the previous single-rod side-pumping scheme [30], while the dual-rod scheme showed 1.26 and 1.12 times more collection efficiency and solar-to-laser power conversion efficiency, respectively, than the previous dual-rod side-pumping scheme. The dual-rod with two laser beams and single laser beam schemes of the present work also achieved reduced  $M^2$  factors, obtaining 1.58 and 1.59 times more brightness figure of merit in relation to the previous dual-rod side-pumping schemes [30].

A three-folding-scheme single laser beam technique was presented for the first time for the dual-rod pumping scheme. With an arrangement of three HR 1064 nm folding mirrors, significantly enhanced laser beam quality factors were obtained. In this way, the non-uniformity of the pump flux absorption on the two laser rods as described in [30] could now be successfully compensated, resulting in a quasi-symmetric beam profile for the final single laser beam with beam quality factors of  $M_x^2 = 1.00$  and  $M_y^2 = 1.44$ , as compared to the asymmetric beam profile with  $M_x^2 = 1.00$  and  $M_y^2 = 7.74$ .

### 6.3.2 Multi-rod for TEM<sub>00</sub>-mode solar laser from a megawatt solar furnace and its beam merging

Based on the megawatt solar furnace in France, it was presented an alternative multi-rod solar laser end-side-pumping concept, proposed to significantly improve the TEM<sub>00</sub>-mode solar laser output power level and its beam brightness through a novel zigzag beam merging technique [86].

The MWSF of the PROMES-CNRS laboratory (Figure 6.45), in Odeillo, France, was the primary concentrator of this work. This installation is comprised of a 63-heliostat field with a total surface area of 2835 m<sup>2</sup> and a 1830 m<sup>2</sup> faceted truncated parabolic mirror with 18 m focal length, mounted on the north face of an eight story building [87]. The 63 heliostats are distributed among eight flat terraces at different heights, placed in staggered rows (Figure 6.45c). Each heliostat tracks the Sun, collects the solar rays and redirects them horizontally towards the parabolic mirror. It then focuses 1 MW of solar power into an 80 cm diameter Gaussian spot, reaching a peak flux value beyond 10 W/mm<sup>2</sup> [88].

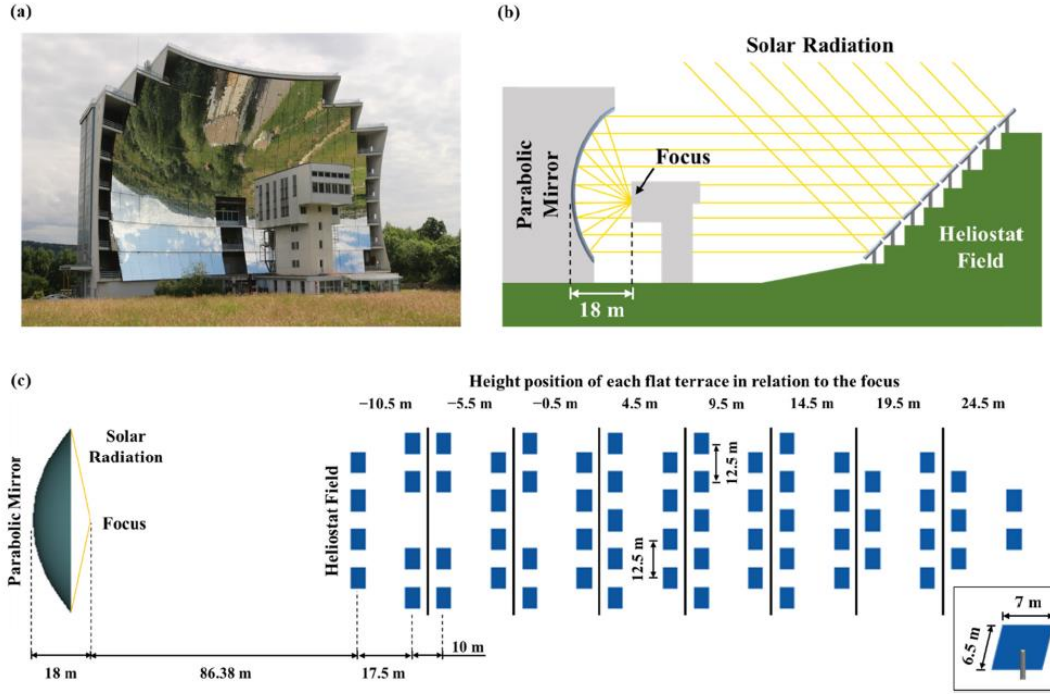


**Figure 6.45** (a) Photograph and (b) simplified schematic of the MWSF facility in Odeillo, France. (c) Top-view of the solar energy collection and concentration system (based on [47]). The dimensions of a heliostat are presented in the inset of (c).

As depicted in Figure 6.46a, at the homogenizer's input face, the concentrated solar radiation presented a Gaussian distribution with a  $10.21 \text{ W/mm}^2$  peak flux.

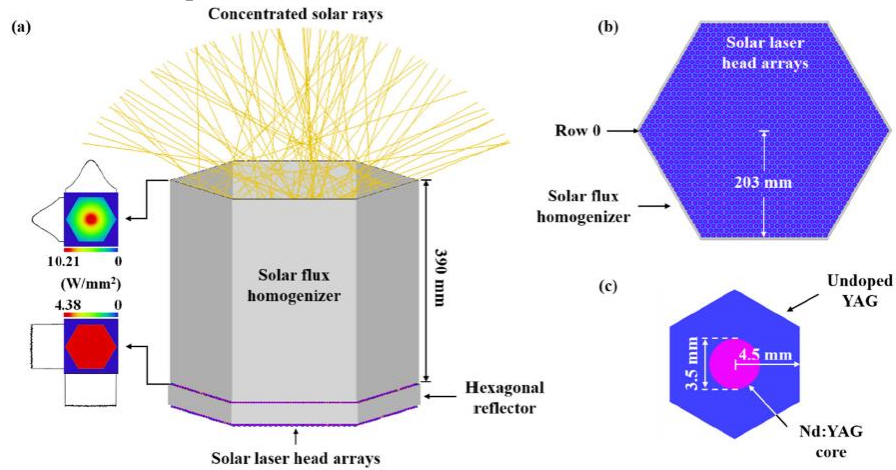


**Figure 6.46** (a) 3D and (b) top view of the solar flux homogenizer, 1657 laser rods and the hexagonal reflector. The concentrated light distribution at the input and output faces of the homogenizer is also presented in (a). (c) Top view of a core-doped Nd:YAG rod.

The beam merging technique was implemented by inclining each rod and positioning them at a certain distance from the fused silica window. A zigzag beam merging technique can be implemented to enable the extraction of brighter  $\text{TEM}_{00}$ -mode laser beams, despite having to reduce the number of rods. The angle of inclination of the rods should not be too low to avoid high laser beam transmission losses in the cooling water, since they would have to be positioned at a large distance from the fused silica window. By mounting 399 rods at a  $30^\circ$  angle of inclination and



employing the beam merging technique (Fig. 6.47), a maximum of 5.2 kW total TEM<sub>00</sub>-mode laser power was numerically extracted from 37 laser beams, averaging 141 W from each merged beam.

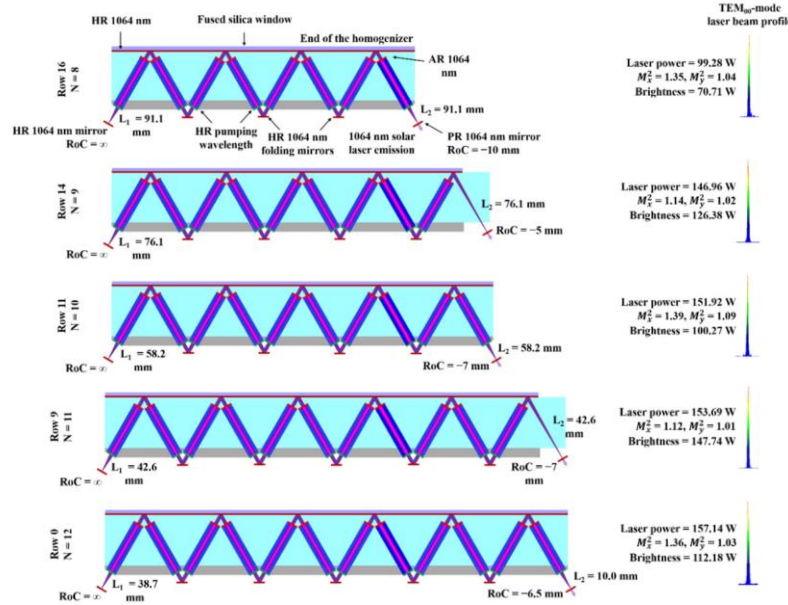


**Figure 6.47** Illustration of the zigzag laser beam merging technique and TEM<sub>00</sub>-mode laser performance for arrays of different N rods.

The rod tilting and distance from the fused silica window may allow the possibility of employing a novel zigzag laser beam merging technique to boost the total TEM<sub>00</sub>-mode solar laser output power and the beam brightness even further, despite having to reduce the number of rods from 1657 to 399. Not only was the TEM<sub>00</sub>-mode power improved by three times, to 5.2 kW, from 37 merged laser beams, but the highest solar laser beam brightness figure of merit of about 148 W was also numerically determined.

### 6.3.3 TEM<sub>00</sub>-mode solar laser with beam merging and ring-array concentrator

The model using a dual-rod scheme with a small fused silica aspherical lens already developed and demonstrated with the better solar laser performance, was introduced and simulated pumped by the RAC as a primary concentrator and using the same fused silica aspherical lens and the semicylindrical pump cavity, slightly different from the other publications, due to the rim angle of the solar rays coming from the primary concentrator to illuminate the rods. The same numerical model was also studied to produce multimode solar laser, and the results in TEM<sub>00</sub>-mode were very encouraging and led to a submission currently in minor review. A three-folding beam merging technique was also introduced for the first time, as seen in previous sections of this thesis, this time in order to improve the TEM<sub>00</sub>-mode solar laser emission. The dual-rod schemes investigated were always compared to a single-rod configuration with the same conditions of secondary concentrator and pump cavity, and also regarding the dimensions of the crystals that were studied in the optimization process.

The primary concentrator used in this work was the RAC using an effective collection area of 1.71 m<sup>2</sup> and considering a solar irradiance of 950 W/m<sup>2</sup>. Water was used as a coolant along the 17 mm length longitudinal surface of the single-rod (Fig. 6.48), and also for the aspherical lens and the pump cavity. The fused silica aspherical lens had an input face with 15 mm radius of curvature, 26 mm diameter, and was able to pump the concentrated



solar radiation from the focus of the RAC to the input aperture of the pump cavity. The 2D-shaped pump cavity designed for this work ensured multiple passages of the solar rays into the laser rod. It had 11 mm  $\times$  14 mm rectangular input aperture and 8.0 mm  $\times$  14 mm rectangular output aperture and a semi-cylindrical pump cavity with 5.0 mm radius, 14 mm length and 3.0 mm height. It was assumed 95% reflectivity for the inner walls of the pump cavity reflectors.

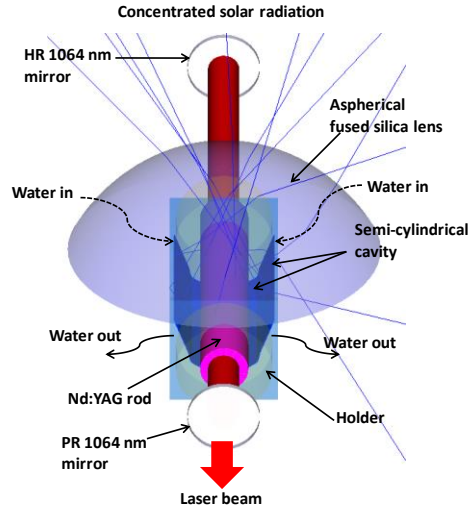


**Figure 6.48** Design for the side-pumped single-rod configuration. It was composed of the fused silica aspherical lens, the semi-cylindrical pump cavity and the Nd:YAG rod.

The resonant laser cavity of the single-rod configuration consisted of one high reflection (HR) 1064 nm mirror with 99.9% reflectivity and another partial reflection (PR) 1064 nm mirror with 96% reflectivity.

The dual-rod pumping configuration is described in Fig. 6.49. It consisted of a fused silica aspherical lens and two semi-cylindrical pump cavities, where the two 3.5 mm diameter and 25 mm length rods were mounted.

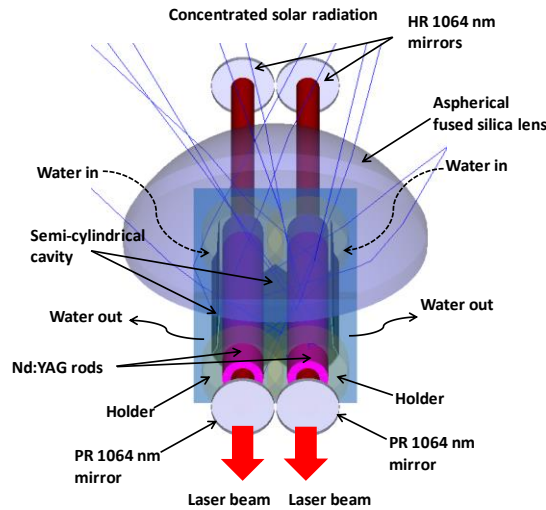


**Figure 6.49** Design for the side-pumped dual-rod configuration, consisting in an aspherical lens, two semi-cylindrical pump cavities and two Nd:YAG rods.

Water was also used as a coolant for the aspheric lens output-face, pump cavity and the laser rods, as for the single-rod configuration, with the remaining 8.0 mm of longitudinal surface of each one of the rods for mechanical fixation by two holders. The dual-rod configuration had a laser resonator for each one of the rods and consisted of one HR 1064 nm mirror with 99.9% reflectivity and another PR 1064 nm mirror with 95% reflectivity. The solar irradiance

of  $950 \text{ W/m}^2$  was assumed in the calculations. Fig. 6.50 shows the absorbed pump flux distributions along five transversal and the longitudinal central cross-sections of both the configurations.

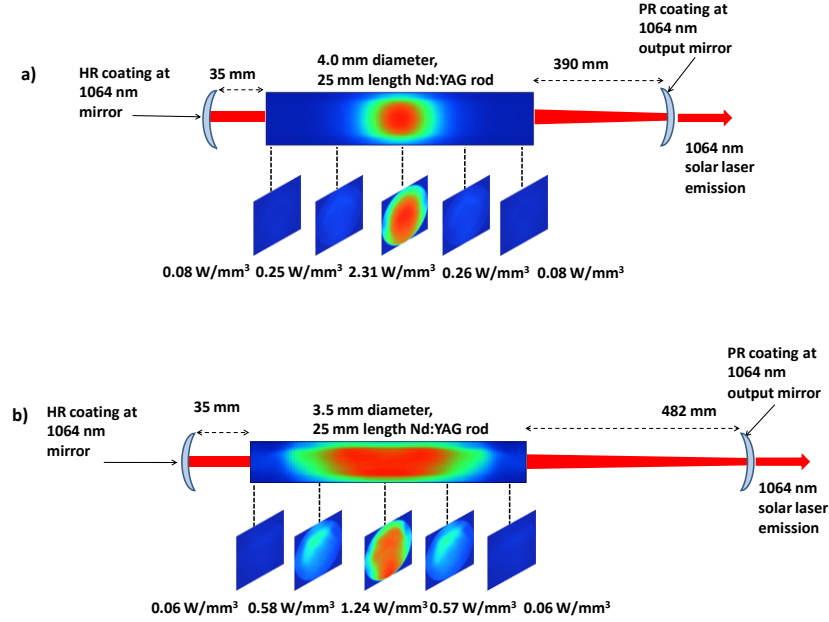


**Figure 6.50** The absorbed pump flux distributions along five transversal and the longitudinal central cross-sections. a) the single-rod and b) one of the rods of the dual-rod configuration.

The dual-rod configuration presented a lower intensity peak of about 54% at the centre of the laser rods in relation to the single-rod configuration.

The losses due to imperfections in the optical coatings on both the mirrors and the laser rods, 0.2% and 0.1%, respectively, were accounted in the LASCAD<sup>®</sup> calculations. The losses due to imperfections in the optical coatings on both the mirrors and the laser rods, 0.2% and 0.1%, respectively, were accounted in the LASCAD<sup>®</sup> calculations. The beam propagation method of LASCAD<sup>®</sup> software calculated 0.2% and 0.3% diffraction losses for the single-rod and the dual-rod configurations, respectively. An asymmetrical laser cavity was once more chosen for an efficient solar laser emission.

The maximum TEM<sub>00</sub>-mode solar laser output power was attained for the single-rod configuration with  $L_1 = 390 \text{ mm}$  and  $L_2 = 35 \text{ mm}$  (450 mm resonant cavity total length), using  $\text{RoC} = 2.0 \text{ m}$  for the HR 1064 nm mirror and  $\text{RoC} = 10 \text{ m}$  for the PR 1064 nm mirror. For the dual-rod configuration, the maximum TEM<sub>00</sub>-mode solar laser output power was achieved with  $L_1 = 482 \text{ mm}$  and  $L_2 = 35 \text{ mm}$  (542 mm resonant cavity total length),  $\text{RoC} = 5.0 \text{ m}$  for the HR 1064 nm mirror and  $\text{RoC} = 10 \text{ m}$  for the PR 1064 nm mirror. The 3D laser beam pattern is shown in Fig. 6.51. A near-diffraction-limited Gaussian distribution was found, with  $1/e^2$  width,  $\omega$ , of approximately 1.15 mm for the single-rod configuration and 1.10 mm for the dual-rod configuration.

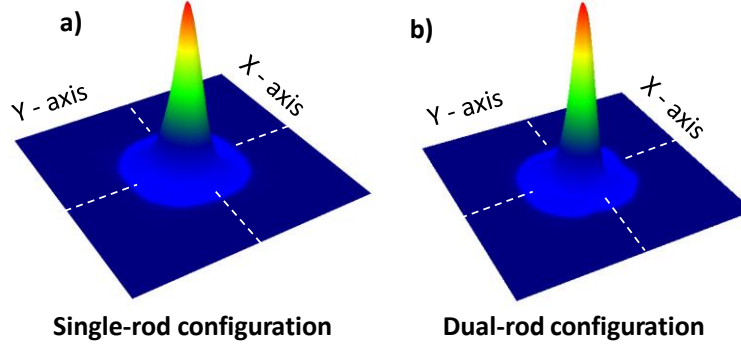


**Figure 6.51** 3D laser beam pattern on the output mirror of the laser resonator for a) 4.0 mm, 25 mm length laser rod of the single-rod configuration and b) the 3.5 mm diameter, 25 mm length laser rods of the dual-rod configuration.

In Fig. 6.52 is shown the  $TEM_{00}$ -mode solar laser output power as a function of the laser rod diameter and length for the single and the dual rod configuration. Using 4.0 mm diameter, 25 mm length Nd:YAG rod, the maximum 22.50 W solar laser output was numerically found. A combined laser output of 26.80 W was obtained from two 3.5 mm diameter, 25 mm length rods, by summing up the output power of the two laser crystals.

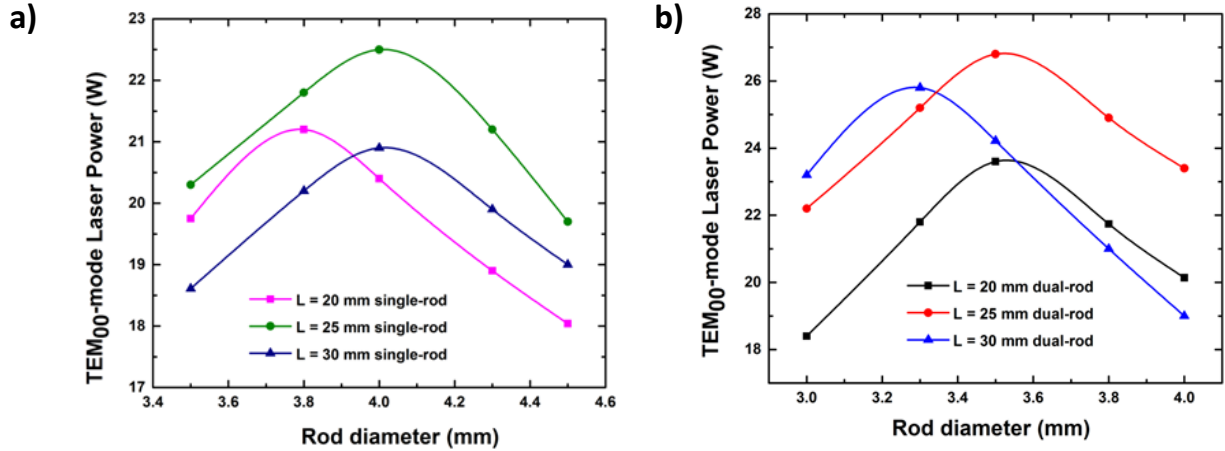


**Figure 6.52**  $TEM_{00}$ -mode laser output power as a function of the rod diameter and length for a) the single-rod and b) the dual-rod configurations.

We followed the possibility of extracting one single  $TEM_{00}$ -mode solar laser beam from the two laser crystals of the dual-rod configuration, as in diode-pumped rod lasers [75], and it can be an interesting approach to enhance  $M^2$  factors and consequently the brightness figure-of-merit of  $TEM_{00}$ -mode solar-pumped lasers. A three-folding-mirror laser beam merging technique was implemented in order to attain a single laser beam from the dual-rod with enhanced laser beam quality, as shown in Fig. 6.53.

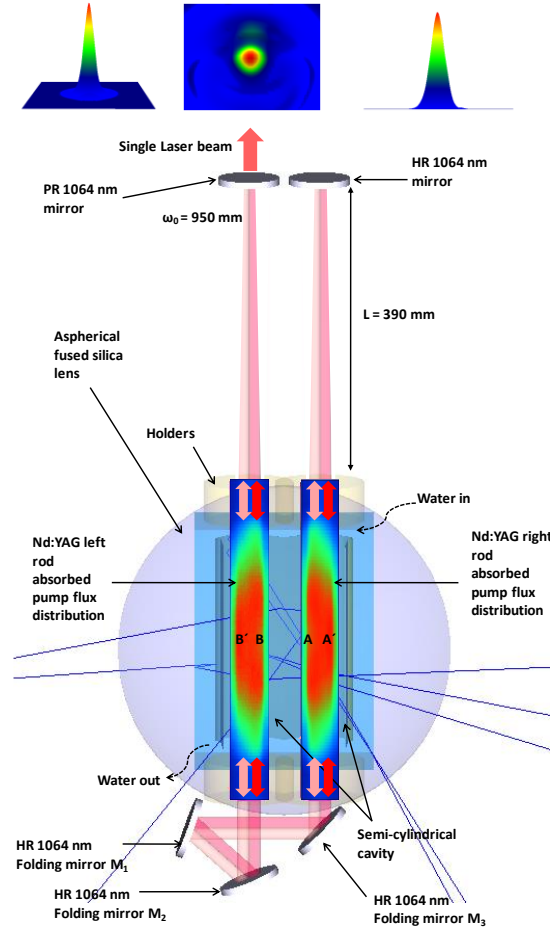


**Figure 6.53** Schematics of the dual-rod single laser beam from the two Nd:YAG crystals. A compensation of the laser beam profile was achieved, by using the arrangement of three HR 1064 nm folding mirrors ( $M_1$ ,  $M_2$  and  $M_3$ ) to compose the folding resonant cavity, along with the mirrors of the laser cavities.

To obtain the single emission with this three-folding-mirror scheme, an asymmetrical resonant cavity was used. As shown in Fig. 6.53,  $L$  indicates the distance between the PR, the HR mirrors and the nearest face of the left, right rods face, respectively. For the dual-rod beam merging scheme, the highest  $TEM_{00}$ -mode solar laser output of 27.5 W was achieved with  $L = 390$  mm,  $RoC = -5.0$  m for the HR 1064 nm mirror and  $RoC = -10$  m for the PR 1064 nm mirror. The 3D  $TEM_{00}$ -mode solar laser beam pattern was also numerically. 950 mm was found for the beam waist radius  $\omega_0$ .

The previous dual-rod configuration, intended for  $TEM_{00}$ -mode laser production, was composed of a small semi-cylindrical fused silica lens with two CPC-semi-cylindrical pump cavities for each one of the laser rods, within which two 3.3 mm diameter, 25 mm length Nd:YAG laser rods were respectively mounted [29]. In the dual-rod configuration of the present work, the laser rods were placed much closer to the output end-face of the aspheric lens and mounted within a common pump cavity, enabling a more efficient pump light absorption, in comparison with the previous configuration [29]. A three-folding-mirror single laser beam technique was also presented for the dual-rod in order to extract  $TEM_{00}$ -mode power in one single laser beam, differently from previous schemes [29]. With an arrangement of three HR 1064 nm folding mirrors, significantly enhanced laser beam quality factors were obtained. The numerical results are summarized in Table 6.16.

**Table 6.16** Laser output power, collection efficiency, solar-to-laser power conversion efficiency, brightness figure-of-merit and brightness conversion efficiency for the single-rod and the dual-rod configurations, and its comparison with the most efficient numerical side-pumped TEM<sub>00</sub>-mode solar laser [29]. The respective collection areas are also shown.

| Parameters  | Dual-rod<br>[29] | Present numerical work |                                |                                  | Improvements (times)  |   |   |
|---|------------------|------------------------|--------------------------------|----------------------------------|-----------------------|---|---|
|   |                  | Single-rod             | Dual-rod<br>two laser<br>beams | Dual-rod<br>single laser<br>beam | Single-rod to<br>[29] | Dual-rod<br>two laser<br>beams to<br>[29] | Dual-rod<br>single laser<br>beam to<br>[29] |
| Collection area (m <sup>2</sup> )                                 | 1.56             | 1.71                   | 1.71                           | 1.71                             | -                     | -   | -   |
| TEM <sub>00</sub> -mode solar laser output power (W)              | 17.20            | 22.50                  | 26.80                          | 27.5                             | 1.31                  | 1.56                                      | 1.60  |
| TEM <sub>00</sub> -mode collection efficiency (W/m <sup>2</sup> ) | 11.00            | 13.15                  | 15.70                          | 16.1                             | 1.20                  | 1.43                                      | 1.46  |
| Solar-to-laser power conversion efficiency (%)                    | 1.31             | 1.38                   | 1.65                           | 1.70                             | 1.05                  | 1.26                                      | 1.30  |
| Brightness figure-of-merit (W)                                    | 14.30            | 17.05                  | 22.15                          | 25.0                             | 1.19                  | 1.70                                      | 1.75  |
| Brightness conversion efficiency (%)                              | 1.10             | 1.05                   | 1.50                           | 1.54                             | 0.95                  | 1.36                                      | 1.40  |

Considerable improvements were numerically attained with the dual-rod configuration being pumped with the RAC, which in its two laser beam configuration attained 15.70 W/m<sup>2</sup> TEM<sub>00</sub>-mode collection efficiency, 1.65% solar-to-laser power conversion efficiency, 22.15 W (11.07 W for each rod) brightness figure-of-merit and 1.37% brightness conversion efficiency.

Regarding the dual-rod single laser beam scheme, with the beam merging technique used to improve its beam quality, it was achieved 16.1 W/m<sup>2</sup> TEM<sub>00</sub>-mode collection efficiency, 1.70 solar-to-laser power conversion efficiency, 25 W brightness figure-of-merit and 1.54% brightness conversion efficiency, being 1.46, 1.30, 1.75 and 1.40 times, respectively, more than the previous numerical records with a dual-rod configuration [29]. The numerical results of the present work in its single laser beam configuration, regarding to collection efficiency, solar-to-laser power conversion efficiency, brightness figure-of-merit and brightness conversion efficiency were also 2.04, 1.60, 3.87 and 2.03 times, respectively, more than the experimental demonstrations of the most efficient solar laser with single-rod [89].

Due to the formation of the focus in the opposite side from where the solar rays reach the primary concentrator, an efficient mounting and integration of the components of the laser head can be attained, avoiding shading areas between the solar rays and the laser head, as compared with the heliostat-parabolic systems. Higher solar laser efficiencies can hence be achieved with the proposed configuration. This alternative dual-rod configuration approach using RAC can also be applied for pumping other laser media [5, 34, 36, 37], composite and grooved laser

rods [35]. Novel schemes for solar lasers [63, 90] can also be used with this configuration to advance the solar laser research.

# Chapter 7 Tracking error in solar energy collection and concentration systems

## 7.1 Sun-Earth relationship

The conceptualization of the apparent movement of the Sun is of paramount importance in the development of solar energy systems and solar tracking error systems.

The discussion that follows is made within the context of orientating a solar tracker with respect to the Sun at any location on the earth and on any given time of the day. In Fig. 7.1 is shown the schematics of the Sun-Earth relationship. As seen from the Earth, the Sun disk forms an angle of 32 minutes of a degree. This is very important in many applications and studies but mainly in solar energy concentration optics, since the Sun cannot be considered as a point source, being significant in the analysis of the optical efficiency of a solar collector.

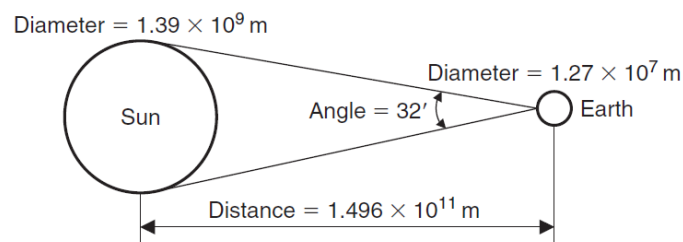


**Figure 7.1** Sun-Earth relationship.

Knowledge of the variation in the Sun's position along the time and through the sky is necessary to calculate the solar radiation falling on a surface. The relative motions of the Sun and Earth are not simple, but they are systematic and thus predictable [91].

The Ptolemaic view of the Sun's motion is used in the analysis for simplicity; since all motion is relative, it is convenient to consider the Earth fixed and to describe the Sun's apparent motion in a coordinate system fixed to the earth with its origin at the site of interest.

Sun tracking systems such as the altitude-azimuth dual axis use a Sun tracking algorithm or ray tracing sensors or software to ensure that the Sun's passage through the sky is predicted and followed with high precision in automated solar tracker applications. A high precision Sun position calculator or Sun position algorithm uses a software program routine to align the solar tracker to the sun and it is an important component in the design and construction of an automatic solar tracking system. Sun position computer software for tracing the sun is available as open source codes.

The Earth makes one rotation about its axis every 24 h and completes a revolution around the Sun in a period of approximately 365.25 days. The eccentricity,  $e$ , of the earth's orbit is very small, equal to 0.01673. Therefore, the orbit of the Earth round the Sun is almost circular. Any location on the surface of the Earth then can be defined by the intersection of a longitude angle and a latitude angle [92].

The Sun is constrained to move with 2 degrees of freedom on the celestial sphere; therefore, its position with respect to an observer on Earth can be fully described by means of two astronomical angles, the solar altitude ( $h$ ) and the solar azimuth ( $\alpha$ ) angles.

The movement of the Earth affects the collected solar radiation on solar systems, and consequently the solar concentration efficiency. The variation of the Sun's position in the sky during the day, or its apparent movement, generates errors in the alignment of the solar energy concentration system with the Sun, which any STS is designed to attenuate with a certain degree of accuracy with its automatic movement. Thus the necessity of a high precision STS become a critical key for the development and implementation of solar concentration systems with the smallest integrated error in the STS.

Before giving the equations of solar altitude and azimuth angles, the solar declination and hour angle need to be defined.

### Declination, $\delta$

The earth axis of rotation (the polar axis) is always inclined at an angle of 23.45 degrees from the ecliptic axis, which is normal to the ecliptic plane. The ecliptic plane is the plane of orbit of the earth around the sun. The solar declination ( $\delta$ ) is the angle between the line joining the centers of the Sun and the Earth and its projection on the equatorial plane, as shown in Fig. 7.2. Declinations North of the Equator (summer in the Northern Hemisphere) are positive, and those South are negative, and is given by:

$$\delta = 23.45 \sin \left[ \frac{360}{365} (284 + N) \right] \quad (1)$$

The declination,  $\delta$ , in degrees for any day of the year ( $N$ ) can be calculated approximately by the above equation [91]:

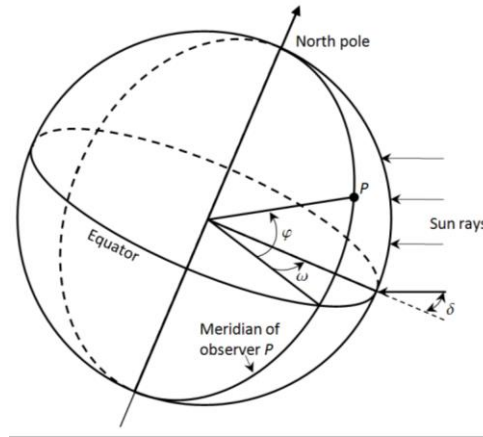


**Figure 7.2** Representative drawing of latitude, solar declination and hour angle, adapted from [93].

The solar declination during any given day can be considered constant in engineering calculations [94, 95]. The variation of the solar declination throughout the year is shown in Fig. 7.3.



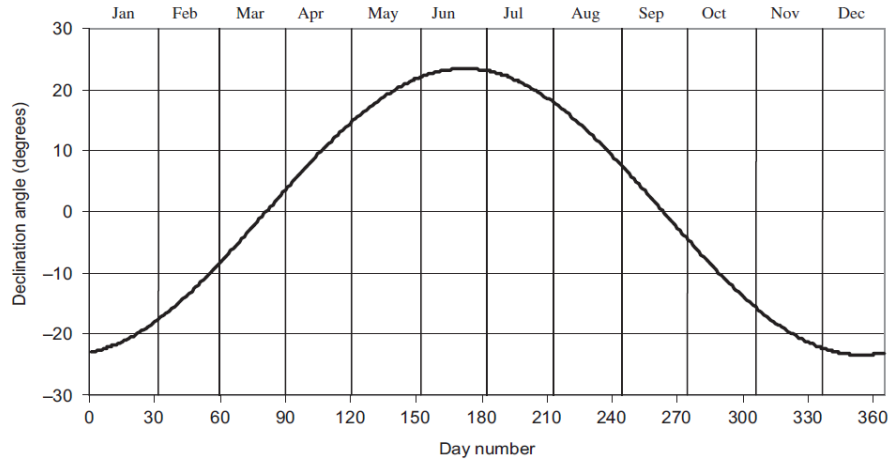


**Figure 7.3** Solar declination angle of the Sun [91].

### Hour angle, $\omega$

The hour angle,  $\omega$ , of a point on the Earth's surface is defined as the angle through which the Earth would turn to bring the meridian of the point directly under the sun. To describe the Earth's rotation about its polar axis the concept of hour angle ( $\omega$ ) is used, which is the angle between the meridian passing through the Sun and the meridian of the observer  $P$ , as shown in Fig. 7.2, and is given by [91]:

$$\omega = \pm 0.25^\circ \times \text{number of minutes from local solar noon} \quad (2)$$

where the plus sign applies to afternoon hours and the minus sign to morning hours. The hour angle at local solar noon is zero, with each  $360/24$  or  $15^\circ$  of longitude equivalent to 1 h. Afternoon hours being designated as positive.

### Solar altitude angle, $h$

The solar rays are characterized by two astronomical angles: solar azimuth angle and the solar altitude angle [91, 96]. The solar altitude angle ( $h$ ) is defined as the vertical angle between the projection of the Sun's rays on the horizontal plane. It is related to the solar zenith angle ( $\theta_z$ ) which is the angle between the Sun's rays and the vertical [91]:

$$\theta_z = 90^\circ - h \quad (3)$$

The solar altitude angle at the time of Sunrise and Sunset is  $0^\circ$ . The solar altitude angle has its maximum value at noon time in all seasons. The elevation angle is related to both the declination angle and the hour angle by the following expression [91].

$$\sin(h) = \cos(\varphi) \cos(\delta) \cos(\omega) + \sin(\varphi) \sin(\delta) \quad (4)$$

where  $\varphi$  is the local latitude ( $38^\circ\text{N}$ ).

### Solar azimuth angle, $\alpha$

The solar azimuth angle,  $\alpha$ , is the angle of the Sun's rays measured in the horizontal plane from due South (true south) for the Northern Hemisphere or due North for the Southern Hemisphere; westward is designated as positive. For a geographical location, the azimuth angle  $\alpha$  is the horizontal angle of the Sun's rays, and is given by the following equation [91]:

$$\sin(\alpha) = \frac{\cos(\delta) \sin(\omega)}{\cos(h)} \quad (5)$$

The output power produced by high-concentration solar systems is directly related to the amount of solar energy collected by the system, and it is necessary to track the Sun's position with a high degree of accuracy, thus decreasing the errors in the alignment of the Sun and the solar concentration system.

Since the first STS, introduced in 1962 [97] using single heliostats, showing very little increased performance over fixed systems, many other researchers have investigated solar trackers in order to improve their solar collection efficiency [98, 99] with the tracking error tolerances varying between 0.5 and 1 degree. Significant improvement on the accuracy of ST was noticed since 1985, after works [100] in which has been demonstrated the influence of the astronomical and constructive parameters on the concentration of solar radiation with plane heliostats on the tracking surfaces of PV systems. Solutions were suggested to correct the heliostat offset errors and the reflected solar radiation images to the receiver using cameras. The system featured a digital camera that captured the real time sun images projected by the heliostats and supplied to a PC via a frame-grabber. These images were then compared to the inbuilt reference images where the solar radiations were perpendicular to the heliostat. The difference between these two images generated a control signal which was used by the control system to activate the servomotors and reorient the collector back to 90° with respect to the solar radiation beam [101]. Chen in 2005 derived the general sun tracking formula for heliostats with arbitrarily oriented axes [102].

Aliman developed novel solar double axis tracker with a higher concentration of solar energy using a tracking master mirror surrounded by several other slave mirrors which reflected the collected solar radiation onto a stationary target. The solar image reflected by the master mirror was used as a reference for all slave mirrors. One was the rotational axis configured pointing to the target and the other one was the elevation axis parallel to the reflector. Encouraging results were reported [103]. Aiuchi in 2006 used two photo-sensors and a heliostat employing an equatorial mount. The system's tracking error was evaluated at 0.002 radians during clear weather [104]. In 2014 a beam characterization system was used to evaluate the tracking error of two heliostats from a central tower solar plant with an estimated accuracy of about 2% for the positioning angle measurement [105].

## 7.2 Solar tracking error in parabolic mirrors

Solar tracking error shifts the focal spot from its optimal alignment, resulting in less solar laser output power. Solar point-focusing concentrators need to employ some form of solar tracking mechanism with sufficient accuracy [106], usually with less than 0.05° [107-109], for enabling the achievement of high concentration ratios, radiation flux and

thus conversion efficiency [91]. Consequently, it becomes necessary to follow the daily apparent motion of the sun in both altitude and azimuth directions, requiring a solar tracking system [91, 110].

Parabolic dish solar concentrators have attracted much interest for many researchers to investigate and develop solar tracking systems for these concentrators, with the goal of reaching high concentration ratios [111-115]. Researchers suggested a control algorithm to track the solar altitude such as that used in satellites with CSP systems [116]. This algorithm used photosensors in a form of a double axis analog module tracking the Sun with respect to their optical axis achieving accurate results with an admissible error of less than  $0.05^\circ$ . Motohiro [117], in order to attain efficient solar energy conversion to laser light utilizing originally designed micro solar-pumped lasers ( $\mu$ SPL), developed a precise solar tracking system with an error smaller than 0.06 degree (1 mrad), required for high concentration ratio:  $1=10626$  of the  $\mu$ SPL collector mirror. Thus, a prototype CST system with precision  $<1$  mrad for an array of 25  $\mu$ SPLs was successfully fabricated in this study (Fig. 7.4).

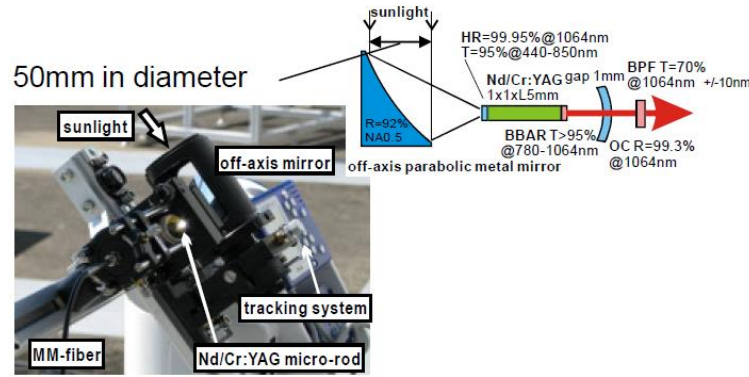


**Figure 7.4** Designed compact solar-pumped laser ( $\mu$ SPL).

Along this thesis we have numerically investigated the tracking error influence in both single-rod and dual-rod solar laser performance using two types of secondary concentrators and pump cavities: cylindrical aspherical lens with CPC pump cavity and aspherical lens with 2D-shaped pump cavity, both configurations at the focus of a parabolic dish, in order to develop a tracking error compensation capacity solar laser scheme. The tracking error width at 10% laser power loss ( $TEW_{10\%}$ ) was chosen to analyze the tracking error compensation capacity of the schemes [28, 30]. At the end of 2018, the idea of pumping two thin laser rods instead of one thick rod, in a side-pumping configuration, had begun to be formed as a concept that could help to decrease the operating temperature of the solar laser emission, and at the same time, able to guarantee a more stable solar laser emission, even with large displacements of the focal spot. With the NOVA heliostat-parabolic mirror system and using the same numerical model studied to improve significantly the production of  $TEM_{00}$ -mode laser emission, but this time optimized and arranged to produce multimode solar power with large tracking error compensation capacity, a new work was simulated, being tested in its tracking error tolerance characteristics aiming to enhance the solar laser stability. In 2019, the tracking error compensation capacity of the optimized dual and single-rod schemes, using semicylindrical CPC pump cavities and semicylindrical fused silica lens, was firstly studied and then was compared to that of the most efficient end-side-pumped laser [17]. All these schemes were pumped by NOVA heliostat-parabolic solar collection and concentration system with the same collection area of  $1.56 \text{ m}^2$  [28].

In Fig 7.5 is shown the influence of the solar tracking error on the dual-rod scheme in altitude ( $\Delta Y$ ) and azimuth ( $\Delta X$ ) directions with cylindrical lens and CPC pump cavity. With the tracking error at  $\Delta Y$ , the focal spot moved upwards (Fig 7.5a), from the lower rod to the upper rod in the dual-rod scheme. With the tracking error at  $\Delta X$ , the focal spot moved in the azimuthal direction of the dual-rod scheme (Fig 7.5b). With the simultaneous tracking error

in  $\Delta Y$  and  $\Delta X$ , the focal spot moved upwards to the upper rod and also to the right in azimuthal directions (Fig 7.5c).

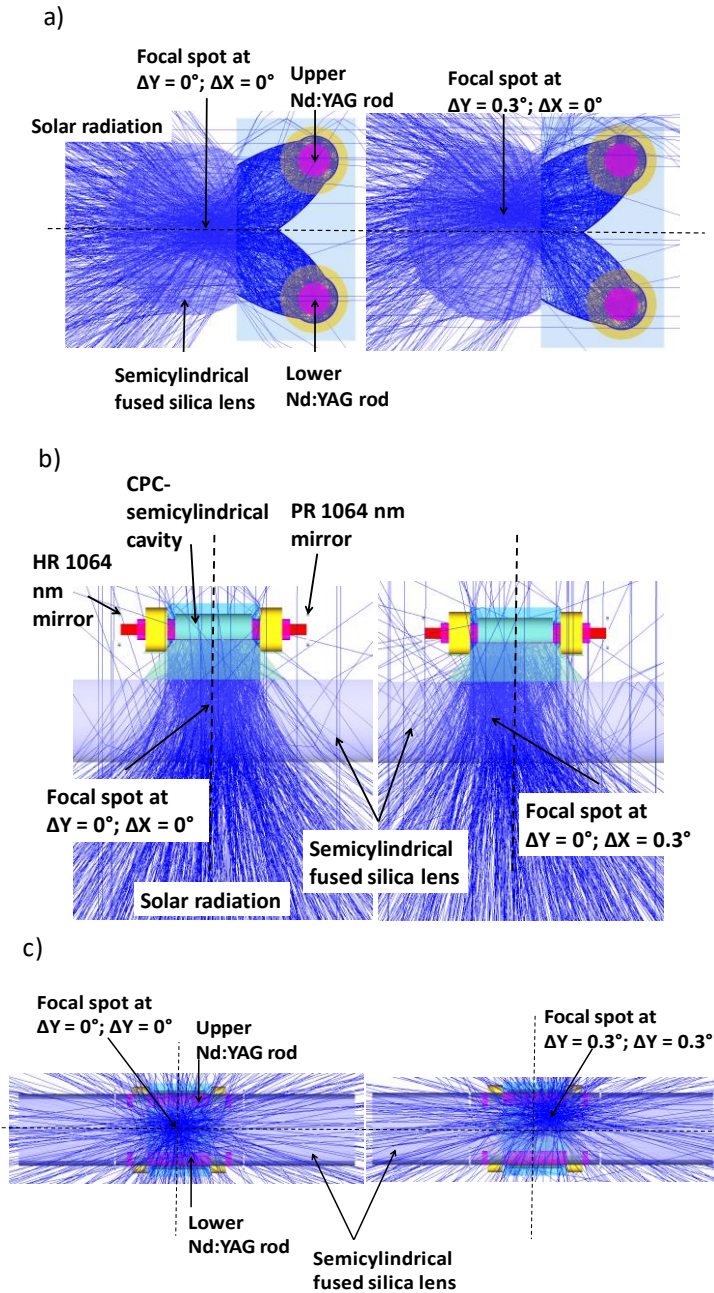


**Figure 7.5** The Influence of the solar tracking error in the focal spot to pump the dual-rod scheme at a)  $\Delta Y$ , moving upwards from the lower rod to the upper rod; b)  $\Delta X$ , moving in azimuthal direction; c)  $\Delta Y$  and  $\Delta X$  simultaneously, moving the focal spot upwards to the upper rod and also to the right in azimuthal direction.

The multimode laser output power of the single-rod scheme, for the rod diameters of 3.0, 3.5, 4.0, 4.5 and 5.0 mm and lengths 20, 25 and 30 mm is shown in Fig. 7.6a). With 4.5 mm diameter and 25 mm rod length, the maximum multimode laser output power of 24.9 W was obtained.

The multimode laser output power as a function of the rod diameters of 3.0, 3.3, 3.5, 3.8 and 4.0 mm and lengths 20, 25 and 30 mm, for the dual-rod scheme is also shown in Fig. 7.6b).

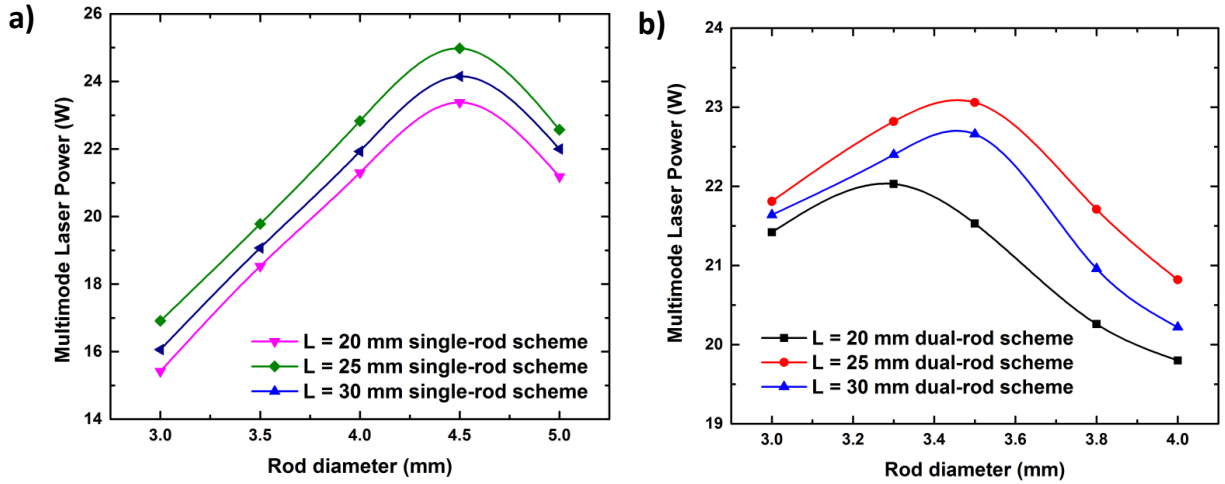


**Figure 7.6** Numerically calculated multimode laser output power as a function of both rod diameter and length for a) the single-rod scheme and b) the dual-rod scheme.

The absorbed pump flux distribution along the longitudinal cross-section of the Nd:YAG crystal rods, pumped with solar tracking error at  $\Delta Y$  and  $\Delta X$ , and the respective laser output powers, for the dual-rod and the single-rod schemes are shown in Fig. 7.7.

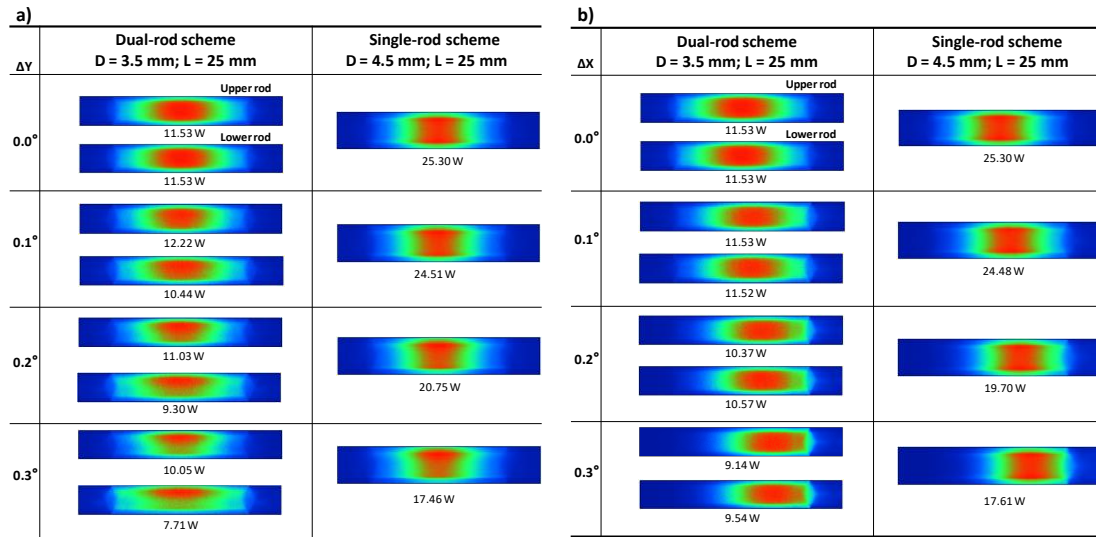


**Figure 7.7** The absorbed pump flux distribution along the longitudinal cross-section of the Nd:YAG crystal rods, for the dual-rod and the single-rod schemes, pumped with solar tracking error at a)  $\Delta Y$  and b)  $\Delta X$ . The laser output powers numerically obtained are also indicated.

The absorbed pump flux distribution was shifted upwards onto the upper rod with the tracking error at  $\Delta Y$  and the laser power of the upper rod of the dual-rod scheme increased, while that of the lower rod decreased (Fig. 7.7a).

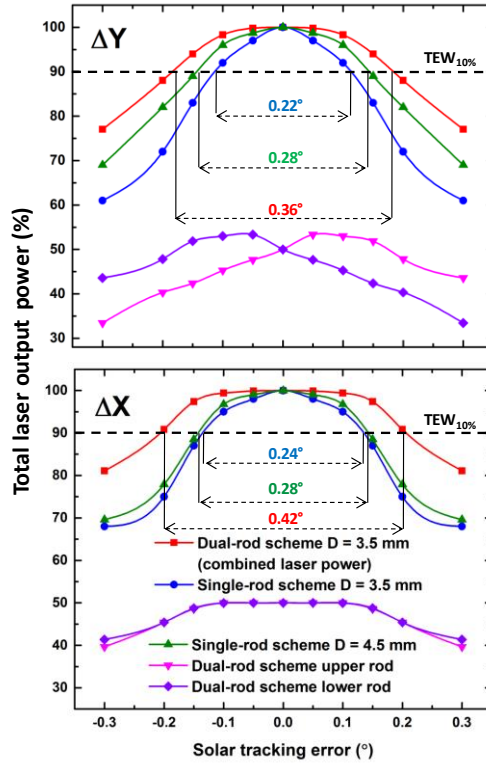


**Figure 7.8** The normalized total multimode laser output power, from the optimal alignment ( $0.0^\circ$ ) of the solar laser head, as a function of the  $\Delta Y$  and  $\Delta X$  solar tracking errors, for the dual and the single-rod schemes.

In Fig. 7.8 is presented the normalized total multimode laser output power as a function of the  $\Delta Y$  and  $\Delta X$  solar tracking errors, for both the single and the dual-rod schemes. The tracking error width at 10% laser power loss is also indicated. However, the total combined laser power from both rods remained more stable than that of the single-rod scheme.  $TEW_{10\%}$  of the dual-rod scheme in  $\Delta Y$  error was improved 1.28 and 1.64 times, in relation to the single-rod scheme with 4.5 mm and 3.5 mm diameter, respectively.

In  $\Delta X$  error,  $TEW_{10\%}$  of the dual-rod scheme was improved 1.50 and 1.75 times, in relation to the single-rod scheme with 4.5 mm and 3.5 mm diameter, respectively.

The absorbed pump flux distribution along the longitudinal cross-section of both the  $D = 3.5$  mm diameter and  $L = 25$  mm length rod of the dual-rod scheme and the 4.0 mm diameter and 35 mm length of the end-side-pumped scheme [17], with  $\Delta Y$  and  $\Delta X$  solar tracking errors, and the laser output powers obtained, are shown in Fig. 7.9. The absorbed pump flux distribution in the end-side pumped scheme [17] shifted upwards with the tracking error at  $\Delta Y$  and also azimuthally with the tracking error at  $\Delta X$ .



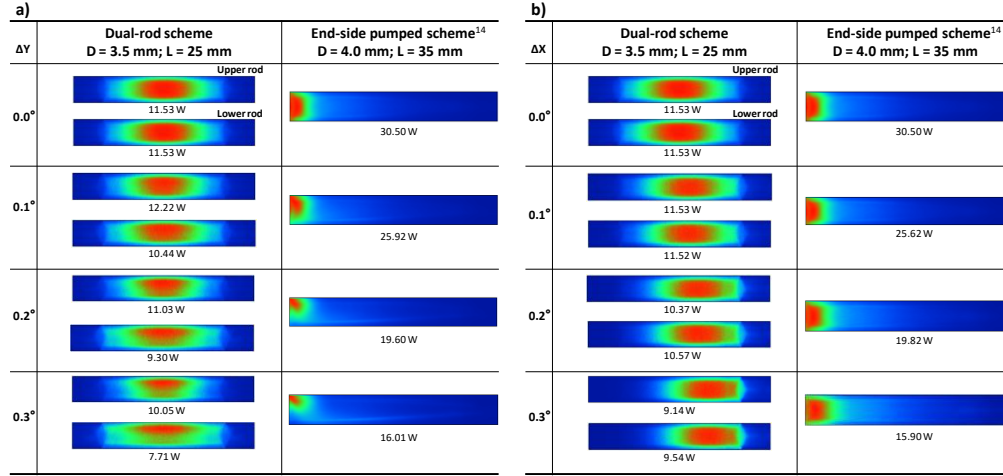


**Figure 7.9** The absorbed pump flux distribution along the longitudinal cross-section of the Nd:YAG crystal rods, pumped with solar tracking error at a)  $\Delta Y$  and b)  $\Delta X$ , for the dual-rod and the end-pumped scheme [17], with the same collection area of NOVA solar system.

In Fig. 7.10 is presented the normalized total multimode laser output power as a function of the  $\Delta Y$  and  $\Delta X$  solar tracking errors, for the dual-rod scheme with D = 3.5 mm diameter and L = 25 mm length and for the end-pumped scheme [17].

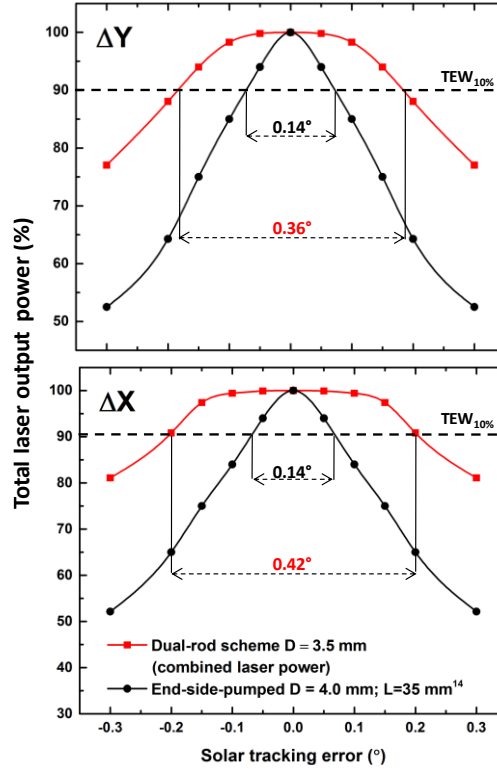


**Figure 7.10** The normalized total multimode laser output power, from the optimal alignment (0.0°) of the solar laser head, as a function of the right and left shift of the  $\Delta Y$  and  $\Delta X$  solar tracking error, for the dual-rod scheme and the end-pumped scheme [17], pumped with the same collection area of NOVA solar system. It is also shown the tracking error width at 10% laser power loss (TEW<sub>10%</sub>).

In the case of the dual-rod scheme in  $\Delta Y$  and  $\Delta X$  errors, the TEW<sub>10%</sub> was improved by 2.57 and 3.00 times, respectively, in relation to the end-side-pumped scheme [17].

The absorbed pump flux distribution along the longitudinal cross-section of the Nd:YAG crystal rods, pumped with  $\Delta Y$  and  $\Delta X$  solar tracking errors simultaneously is shown in Fig. 7.11. The numerically obtained laser output powers are also shown, for the dual-rod scheme and for the end-side-pumped scheme [17]. The absorbed pump flux distribution in the end-side pumped scheme [17] shifted upwards and azimuthally with the tracking error at  $\Delta Y$  and  $\Delta X$ .

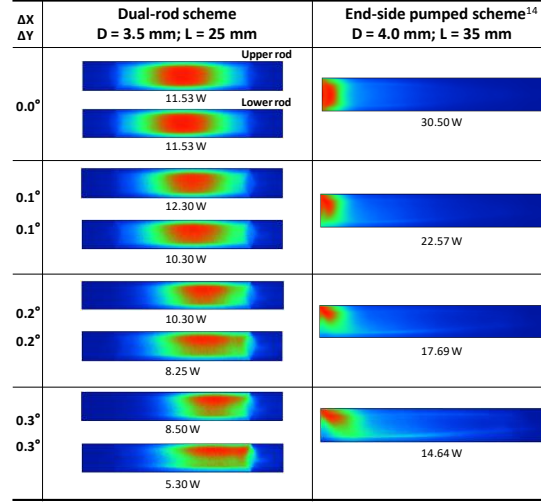


**Figure 7.11** The absorbed pump flux distribution along the longitudinal cross-section of the Nd:YAG crystal rods, pumped with solar tracking error at  $\Delta Y$  and  $\Delta X$  simultaneously, for the dual-rod and the end-side-pumped scheme [17], pumped with the same collection area of NOVA solar system. The laser output powers numerically obtained are also indicated.

In Fig. 7.12 is shown the total normalized multimode laser output power as a function of the simultaneous  $\Delta Y$  and  $\Delta X$  solar tracking errors, for the dual-rod scheme with 3.5 mm diameter and 25 mm length, for the single-rod schemes with 3.5 and 4.5 mm diameter and 25 mm length and for the end-pumped scheme.

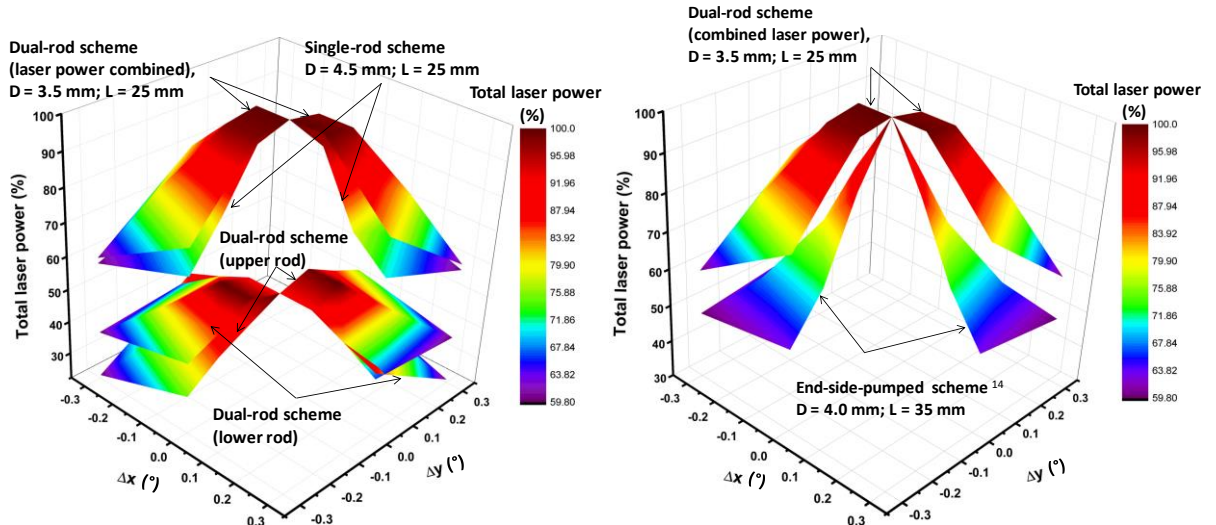


**Figure 7.12** The normalized total multimode laser output power, from the optimal alignment (0.0°) of the solar laser head, as a function of the simultaneous variation in  $\Delta Y$  and  $\Delta X$  solar tracking errors, for the dual-rod and the single-rod schemes and the end-side pumped scheme [17], pumped with the same collection area of NOVA solar system.

The dual-rod scheme demonstrated an enhancement in tracking error compensation capacity comparatively to that of the single-rod scheme not only in the  $\Delta X$  variation, but also in  $\Delta Y$  variation.



It is clear the large enhancement in tracking error compensation capacity of the dual-rod scheme comparatively to that of the end-side pumped scheme [17], not only in the  $\Delta X$  variation but also in  $\Delta Y$  variation.

A substantial enhancement in tracking error compensation capacity was numerically obtained with this novel concept. The improvement in the  $\Delta Y$  and  $\Delta X$  TEW<sub>10%</sub> was 1.28 and 1.50 times, respectively, in relation to the single-rod scheme with a thick rod of 4.5 mm diameter. Relatively to the single-rod scheme with 3.5 mm diameter, the improvement in the  $\Delta Y$  and  $\Delta X$  TEW<sub>10%</sub> was 1.64 and 1.75 times, respectively. The influence of tracking error on the dual-rod pumping approach was also compared with the most efficient Nd:YAG end-side-pumped scheme [17], pumped by NOVA heliostat-parabolic solar collection and concentration system with the same collection area. The numerically obtained improvement in the  $\Delta Y$  and  $\Delta X$  TEW<sub>10%</sub> was 2.57 and 3.00 times, respectively. The obtained results are summarized in the Table 7.1.

**Table 7.1** Numerically calculated tracking error width at 10% laser power loss, for the single-rod and the end-pumped [17] schemes, and the numerically calculated improvement, using the dual-rod pumping scheme.

| Schemes                                  | Tracking error width at 10% laser power loss |            | Improvement by the present numerical simulations (times) |            |
|--|--|------------|--|------------|
|  | $\Delta Y$                                   | $\Delta X$ | $\Delta Y$   | $\Delta X$ |
| Present numerical simulations            | 0.36   | 0.42       |  |            |
| Single-rod<br>(D = 3.5 mm;<br>L = 25)    | 0.22   | 0.24       | 1.75   | 1.64       |
| Single-rod<br>(D = 4.5 mm;<br>L = 25)    | 0.28   | 0.28       | 1.28   | 1.50       |
| End-pumped<br>(D = 4 mm;<br>L = 35) [17] | 0.14   | 0.14       | 2.57   | 3.00       |

In the end of 2019, we numerically studied the dual-rod approach using a small fused silica aspherical lens and a 2D-shaped pump cavity, as already described in this thesis for multimode solar laser emission. Solar tracking error and its influence in the focal spot to pump the dual-rod scheme is shown in Fig. 7.13.

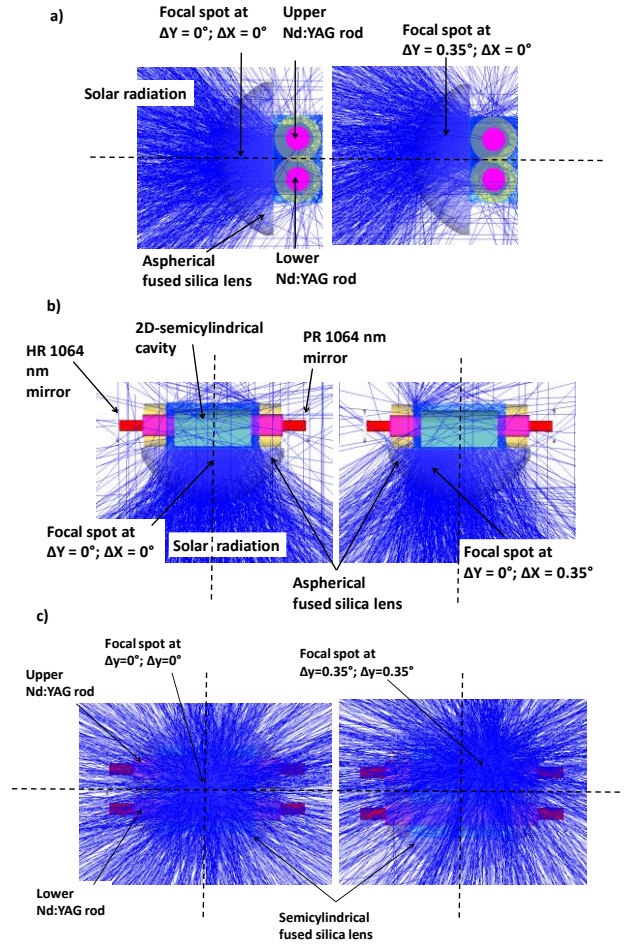


**Figure 7.13** Solar tracking error and its influence in the focal spot to pump the dual-rod scheme at a) altitude direction ( $\Delta Y$ ), b) azimuth direction ( $\Delta X$ ) and c)  $\Delta Y$  and  $\Delta X$  simultaneously.

The single and the dual-rod schemes were also studied regarding to the tracking error capacity. Both schemes were pumped by NOVA heliostat-parabolic solar collection and concentration system with the same collection area of  $1.56 \text{ m}^2$ . In Fig 10 is shown an example of the influence of the solar tracking error on the dual-rod scheme in altitude ( $\Delta Y$ ) and azimuth ( $\Delta X$ ) directions individually, and at  $\Delta Y$  and  $\Delta X$  directions simultaneously.

In Fig. 7.14 is shown the absorbed pump flux distribution along the longitudinal cross-section of the dual-rod and the single-rod pumped with solar tracking error at  $\Delta Y$  and  $\Delta X$ . The laser output powers are also indicated.

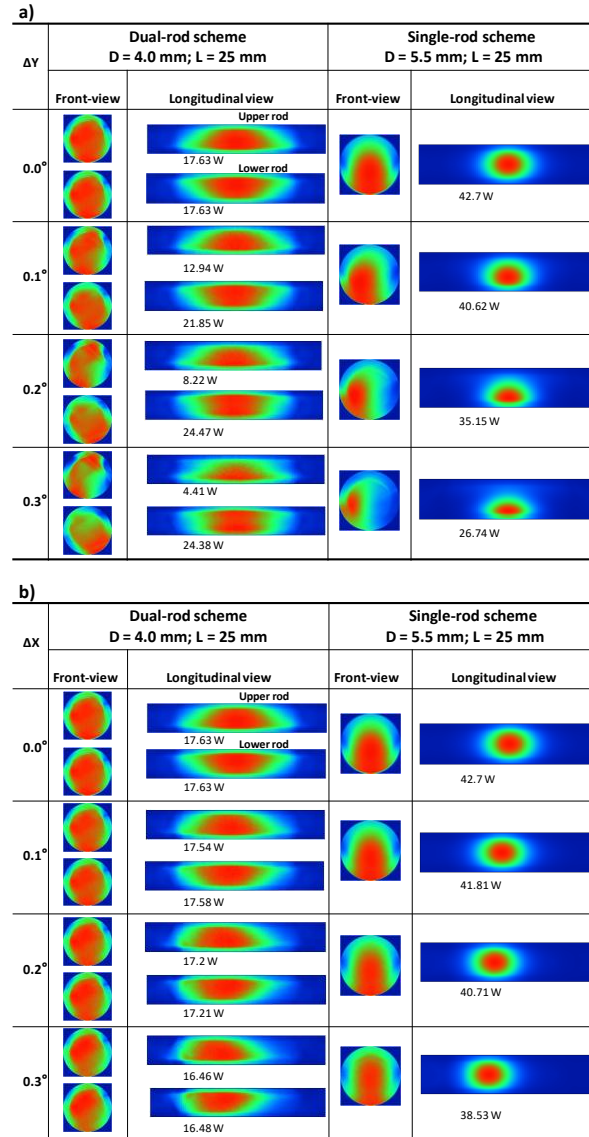


**Figure 7.14** Absorbed pump flux distribution along the longitudinal cross-section of the Nd:YAG crystal rods, for the dual-rod and the single-rod schemes, pumped with solar tracking error at a)  $\Delta X$  and b)  $\Delta Y$ . The laser output powers numerically calculated are also shown.

The normalized total multimode laser output power as a function of the  $\Delta Y$  and  $\Delta X$  solar tracking errors (from the optimal alignment to 0.35° tracking error) for both the single and the dual-rod schemes and also for the 3.5 mm diameter, 25 mm length Nd:YAG from the previous dual-rod scheme [28] are shown in Fig. 7.15.

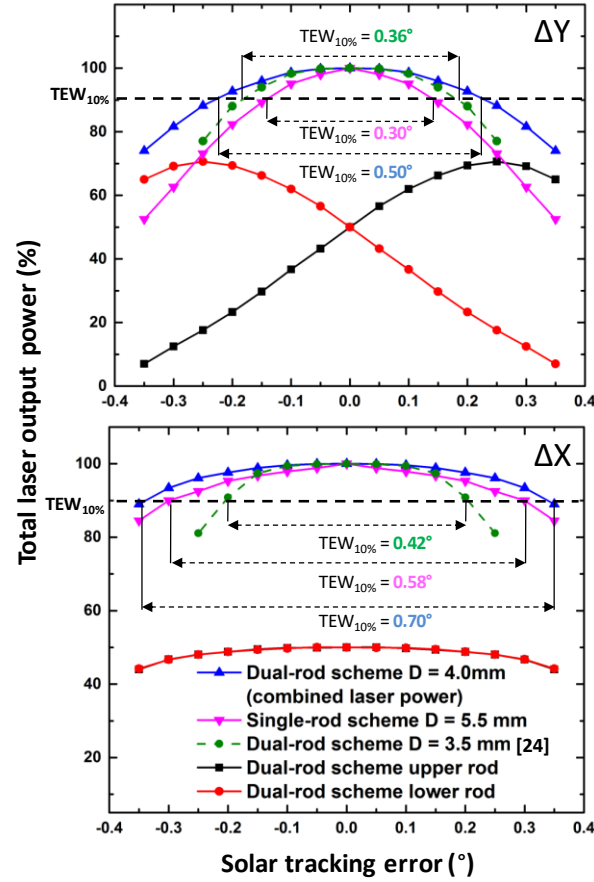


**Figure 7.15** Normalized total multimode laser output power, from the optimal alignment ( $0.0^\circ$ ) of the solar laser head, as a function of the  $\Delta Y$  and  $\Delta X$  solar tracking errors, for the single and the dual-rod schemes and also for the previous dual-rod scheme [28].

It is also represented the tracking error width at 10% laser power loss. The total combined laser power from both rods remained more stable than that of the single-rod scheme. The  $TEW_{10\%}$  of the dual-rod scheme with  $\Delta Y$  error improved 1.66 times in relation to the single-rod scheme with 5.5 mm diameter rod. The  $TEW_{10\%}$  of the dual-rod scheme with  $\Delta X$  error improved 1.21 times in relation to the single-rod scheme.

The absorbed pump flux distribution along the longitudinal cross-section of both the single and the dual Nd:YAG laser rods, pumped with simultaneous  $\Delta Y$  and  $\Delta X$  solar tracking errors, is presented in Fig. 7.16, along with the numerically obtained laser output powers.

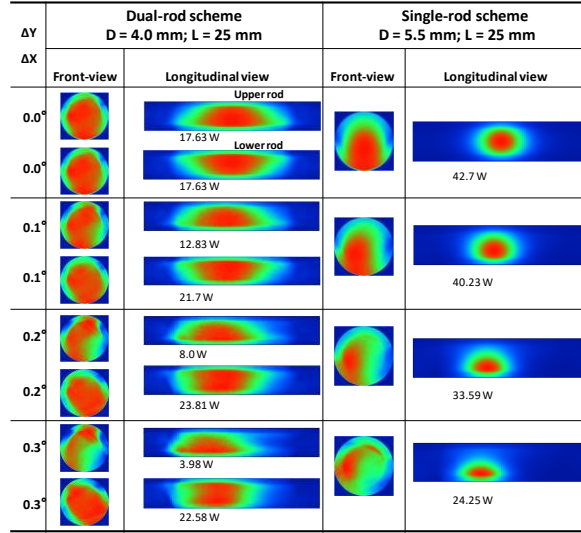


**Figure 7.16** Absorbed pump flux distribution along the longitudinal cross-section of both the single and the dual Nd:YAG crystal rods, pumped with solar tracking error at  $\Delta Y$  and  $\Delta X$  simultaneously. The laser output powers numerically calculated are also shown.

The numerical comparative results obtained are summarized in Table 7.2. It is also shown the previous dual-rod scheme with tracking error capacity [28].

**Table 7.2** Numerically calculated tracking error width at 10% laser power loss, for the single-rod and the dual-rod schemes and the previous dual-rod scheme [28]. The numerically calculated improvement in tracking error capacity using the dual-rod pumping scheme of the present work is also indicated.

| Schemes                               | Tracking error width at 10% laser power loss |            | Improvement of the dual-rod scheme of the present work in relation to the single-rod scheme and [28] (times) |            |
|---------------------------------------|--|------------|--|------------|
|                                       | $\Delta Y$                                   | $\Delta X$ | $\Delta Y$   | $\Delta X$ |
| Dual-rod<br>(D = 4.0 mm;<br>L = 25)   | 0.50   | 0.70       | -  | -          |
| Single-rod<br>(D = 5.5 mm;<br>L = 25) | 0.30   | 0.58       | 1.66   | 1.21       |
| Dual-rod<br>(3.5 mm; L = 25) [28]     | 0.36   | 0.42       | 1.38   | 1.66       |

A large improvement in tracking error compensation capacity was numerically achieved with the dual-rod pumping approach, where the  $TEW_{10\%}$  was improved 1.66 and 1.21 times in altitude ( $\Delta Y$ ) and azimuth ( $\Delta X$ ) errors, respectively, as compared to the numerically simulated side-pumped single-rod scheme with a thick rod.

### 7.3 Solar tracking error in ring-array concentrators

A ring-array solar concentrator, introduced and developed by V. Vasylyev et al. [68] consists of a set of concentric rings disposed in such way that the inner reflective surfaces do not mutually shade, shaping its focal spot through superposition of rays to a common point in the rear side of the collector. This configuration allows efficient integration of components, decreasing the shadow areas between incoming solar rays and the laser head, as compared with heliostat-parabolic mirror.

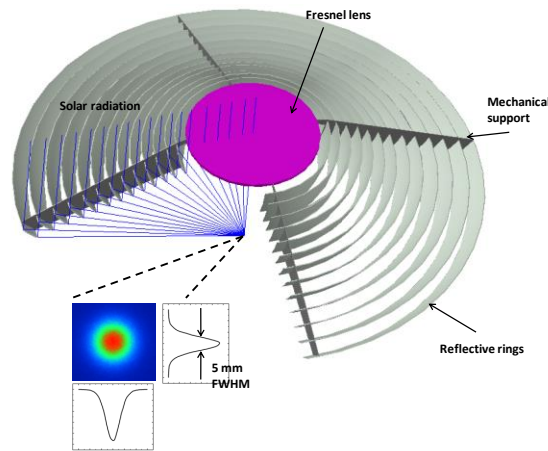


**Figure 7.17** The ring-array concentrator is composed of 13 rings and a small Fresnel lens. Inset picture with the pump light distribution at its focal point.

Using the numerical RAC system described in Chapter 4 (Fig. 7.17), it was studied a typical tracking error from  $0.05^\circ$  to  $0.2^\circ$  in either azimuthal and altitude axes through the laser output power variation. Fig. 7.18 shows the influence of tracking error on the output laser power for the 5.0 mm diameter, 20 mm length Nd:YAG rod. At the maximum tracking error of  $0.2^\circ$  in both azimuth and altitude axes, 48.5 W was attained, corresponding to 28% laser power loss. At the maximum tracking error of  $0.2^\circ$  in only one of the axes, 57.2 W laser power was achieved, corresponding to 15% loss. For a high precision solar tracker with only  $0.05^\circ$  accuracy in both axes [118], only 2% laser power loss was found, resulting in 65.9 W of output laser power, as indicated in Fig. 7.18.

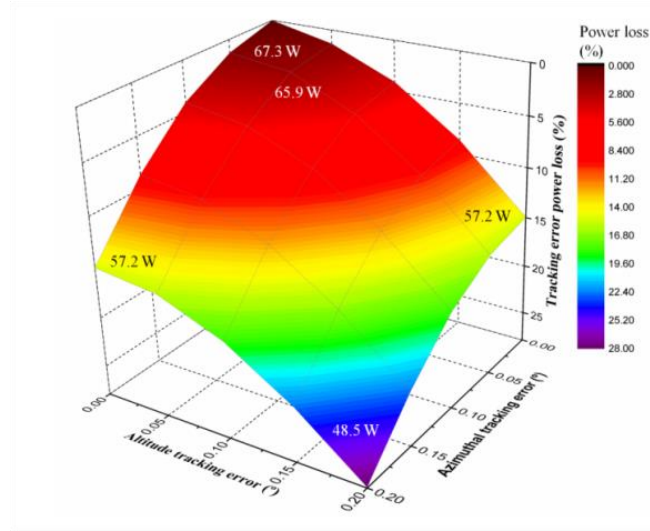


**Figure 7.18** Influence of tracking error on output laser power for the 5 mm diameter, 20 mm length Nd:YAG rod. The solar laser power loss is represented in percentage. Altitude and azimuthal tracking error are represented in degrees.

The influence of the tracking error on solar laser output power was also studied, showing only 2% power loss for a high precision solar tracker with  $0.05^\circ$  accuracy.

A modified RAC concept for solar-pumped lasers [69] was developed achieving very good results and it has also studied on it a typical tracking error from  $0.05^\circ$  to  $0.20^\circ$  in either azimuthal and altitude axes. Fig. 7.19 shows the output laser power for the 5 mm diameter, 20 mm length Nd:YAG rod. At the maximum tracking error of  $0.20^\circ$  in both azimuth and altitude axes, 50.4 W was attained, corresponding to 25.7% laser power loss. To correctly evaluate the tracking error associated laser output power, a 1.5 m diameter Fresnel lens was also designed to pump the same 5.0 mm diameter 20 mm length Nd:YAG rod. Therefore, Fig. 7.19 shows a very clear advantage of the modified ring-array system in both solar laser output power enhancement and tracking error associated laser power reduction.

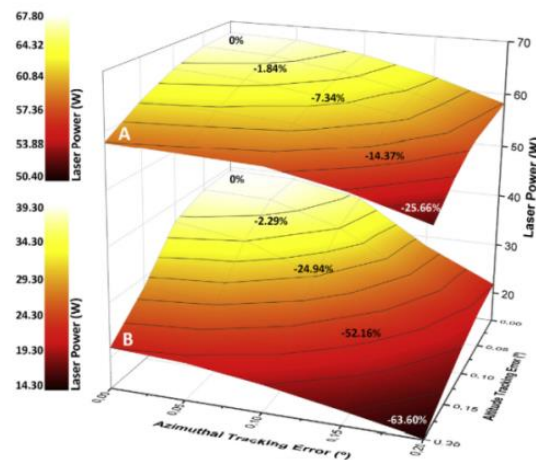


**Figure 7.19** Numerically calculated tracking errors for (A) the ring-array assembly and (B) the Fresnel lens pumping scheme with the same diameter.

In the topic of highly concentrate solar energy by means of innovative solar concentrators, it was analyzed the efficiency loss of the spherical receiver of 15 mm diameter as function of tracking error in altitude and azimuth



directions for MSSF parabolic mirror and 3D RAC solar furnace. In Fig. 7.20 is shown the proposed 3D RAC solar furnace, which consists of five RAC units focusing the incoming solar light into a common focal spot.

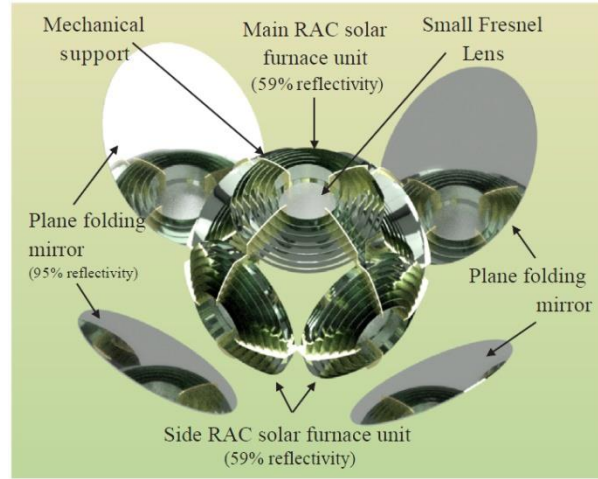


**Figure 7.20** 3D RAC solar furnace composed of five seven-ring RACs and four folding mirrors.

In Fig. 7.21 is shown the tracking error with heat load efficiency distribution at the focal spot by the  $8\text{ mm} \times 8\text{ mm} \times 8\text{ mm}$  detector. For small tracking errors, the 3D RAC produced an enhanced heat load distribution at the center of the detector, as compared to that of the parabolic mirror furnace.

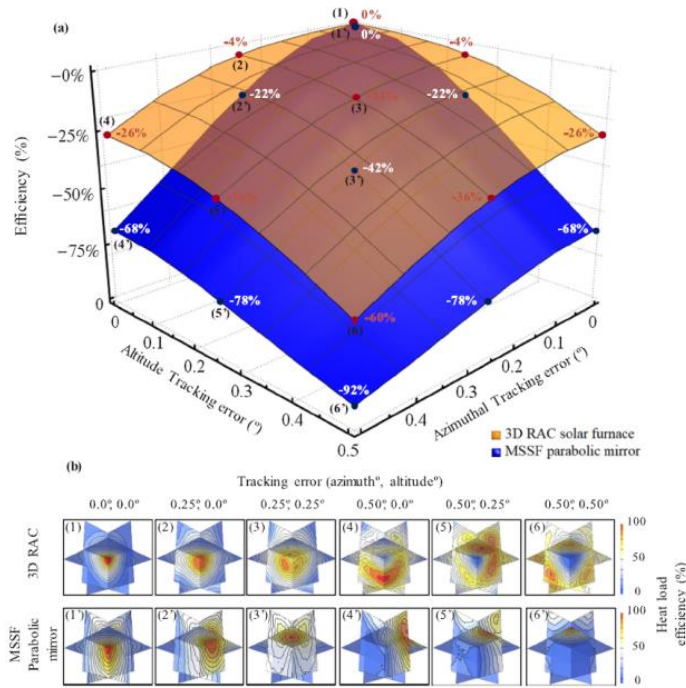


**Figure 7.21** (a) The absorbed energy by black body detector with the tracking error in altitude and azimuth directions. (b) The heat load distributions of the 3D RAC (1)(2)(3)(4)(5) and the MSSF parabolic mirror (1')(2')(3')(4')(5').

At the extreme case of tracking error by  $0.50^\circ$  on both axes, the efficiency was nearly extinguished for the MSSF parabolic mirror and a 60% loss was obtained for 3D RAC. In summary, the 3D RAC furnace had a generally better tracking error performance as compared to the parabolic mirror furnace [70].



The RAC already described in this thesis was further extended to investigate the dual-rod side-pumping concept as an interesting alternative to attain an improved solar laser output power with better beam quality and tracking error compensation capacity [31].

The single and the dual-rod side-pumping schemes were numerically analyzed regarding to the solar tracking error compensation capacity. Both schemes were pumped by the RAC solar energy collection and concentration system. Typical solar tracking error from  $0.05^\circ$  to  $0.30^\circ$  in either azimuthal or altitude directions were numerically investigated. In Fig. 7.22 is shown the normalized total solar laser output power as a function of the altitude and azimuth solar tracking error for both schemes studied in this work. For comparison, an end-side-pumping scheme with a 5.5 mm diameter and 20 mm length Nd:YAG laser rod, pumped by the same RAC solar energy collection and concentration system [32], is also shown. At the maximum tracking error of  $0.30^\circ$  in altitude and azimuth axes, the dual-rod scheme attained only around 10% laser power loss, while the single-rod scheme showed around 22% and 20% laser power loss in altitude and azimuth axes, respectively. The end-side-pumped scheme from [32] achieved around 25% laser power loss in both altitude and azimuth axes. For a high precision solar tracker with  $0.05^\circ$  accuracy, only 0.6% and 0.3% laser power loss was achieved by the dual-rod scheme in altitude and azimuth axes, respectively.

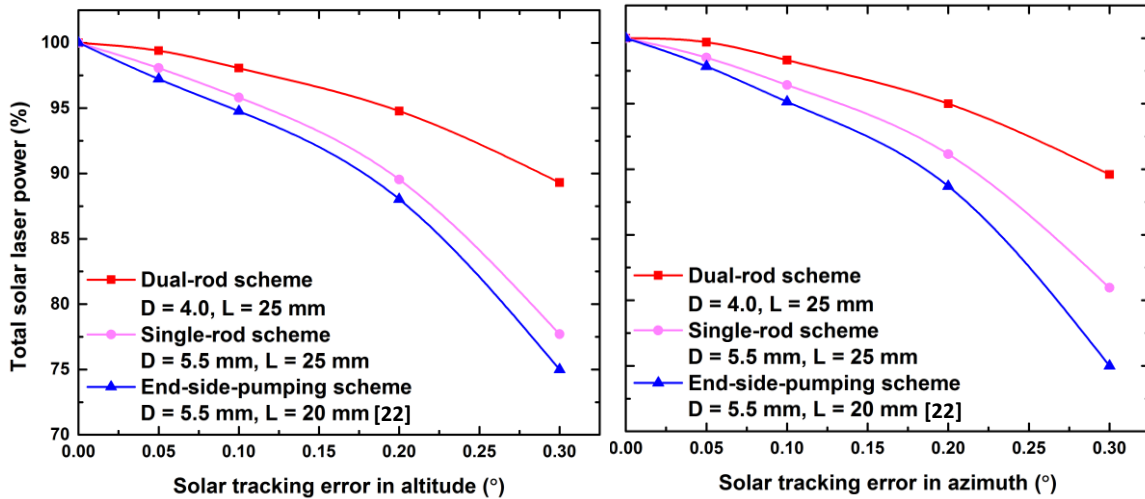


**Figure 7.22** Normalized total solar laser output power for the single and the dual-rod side-pumping schemes and the end-side pumping scheme [32], as a function of the altitude and azimuth solar tracking errors, ranging from the optimal alignment ( $0.0^\circ$ ) to  $0.3^\circ$  using the same RAC solar energy collection and concentration system.

In Fig. 7.23 is shown the 3D normalized solar laser power for both the single and the dual-rod side-pumping schemes from this work and the end-side-pumping scheme from reference [32], as a function of the simultaneous altitude and azimuth solar tracking errors ranging from  $0.0^\circ$  to  $0.3^\circ$ .

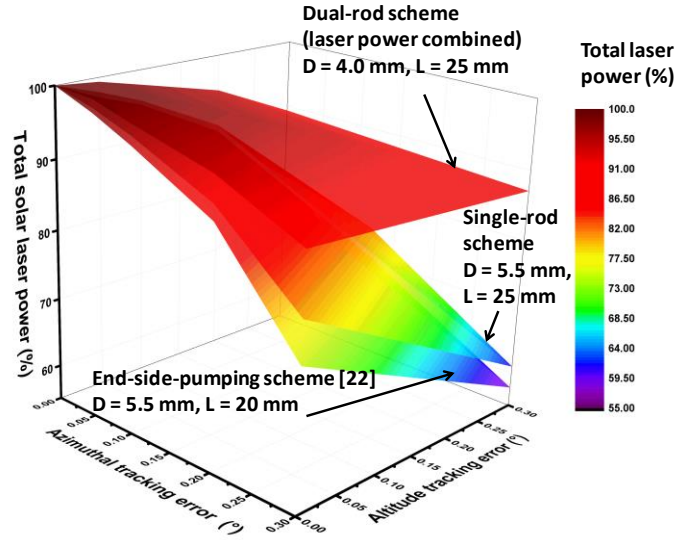


**Figure 7.23** The normalized total solar laser output power in percentage, for both the single and the dual-rod side-pumping schemes, and the end-side pumping scheme [32], as a function of the simultaneous variation in altitude and azimuth solar tracking errors, ranging from the optimal alignment ( $0.0^\circ$ ) to  $0.3^\circ$ , using the same RAC solar energy collection and concentration system.

The dual-rod side-pumping concept is an interesting alternative to attain an improved solar laser output power with better beam quality and tracking error compensation capacity, comparatively not only with the single-rod side-pumping scheme but also with the end-side-pumping scheme from [32]. The significant improvement in the thermal performance of the laser media helps to increase the laser performance and stability.

# Chapter 8 Dual-rod solar laser with tracking error compensation capacity

## 8.1 Dual-rod side-pumping solar-laser

The experimental work started in the summer of 2020, with the designing project of the solar laser head using AUTOCAD®, ZEMAX® and LASCAD®, where the numerical models developed addressed along this thesis had given a very important contribution for building and preparation of the experimental tests. The dual-rod side-pumping simulation model to be built as a prototype was composed of a fused silica aspherical lens and a semicylindrical pump cavity, within which two Nd:YAG laser rods were mounted, one two 3.5 mm diameter and 25 mm length, as shown in Fig. 8.1. The laser rods were cooled by water in their longitudinal surface along 18.4 mm, and 8.0 mm was used for mechanical fixation by two rod-holders. Also the output surface of the fused silica aspherical lens and the semicylindrical pump cavity were all cooled by water.

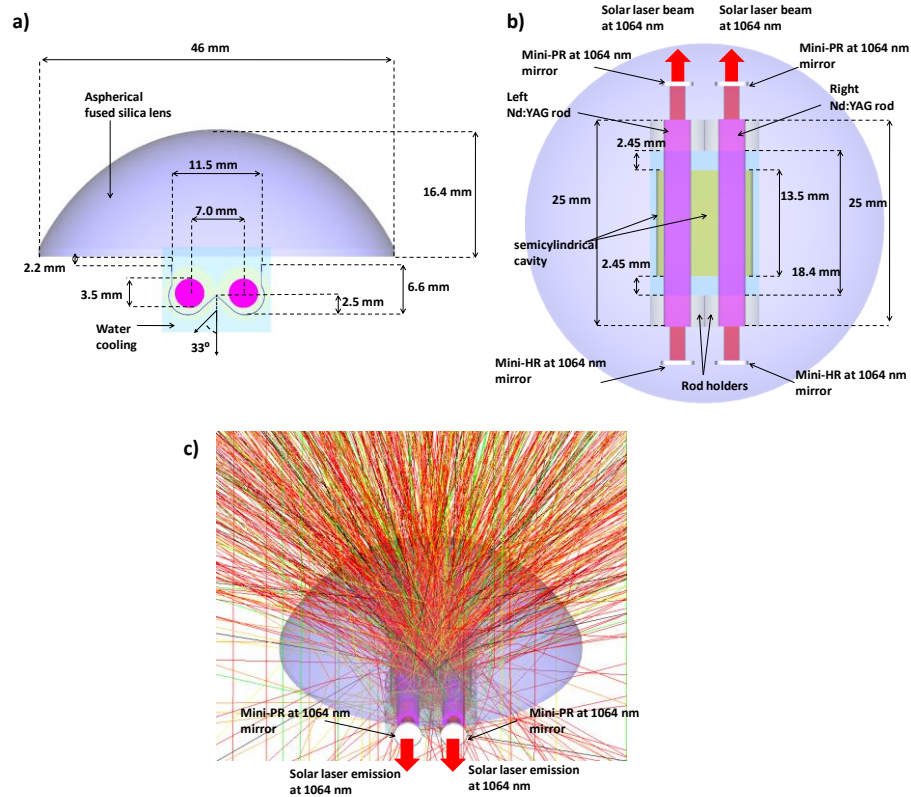


**Figure 8.1** Dual-rod side-pumping solar laser head design with the key dimensions indicated: a) front view, b) top view; 3D view with solar rays from the simulation model. The solar laser head consisted in the fused silica aspherical lens, the semicylindrical pump cavity and two Nd:YAG laser rods, fixed by two rod-holders.

The aspherical lens had an input face with 15 mm radius of curvature, 46 mm diameter, 0.003 conic factor and a plane output face, coupling the concentrated solar radiation from the focal spot to the input aperture of the pump

cavity at the center of the two laser rods. The semicylindrical pump cavity had  $11.5 \text{ mm} \times 13.5 \text{ mm}$  rectangular input aperture and  $11.4 \text{ mm} \times 13.5 \text{ mm}$  rectangular output aperture and a cylindrical segment with 2.5 mm radius, 13.5 mm length and 3.0 mm height. 94% reflectivity was assumed for the inner wall of the pump cavity. In Fig. 8.1 is presented the simulation model and its key dimensions used to numerical optimization and building of the dual-rod side-pumping solar laser head.

Some changes and adaptations were made in the solar laser system project in relation to the simulations, defining a final prototype to be built. Fig. 8.2 presents the AutoCAD drawings showing three different views of the designed laser head. In Fig.8.2a) front view; b) side view; c) top view.

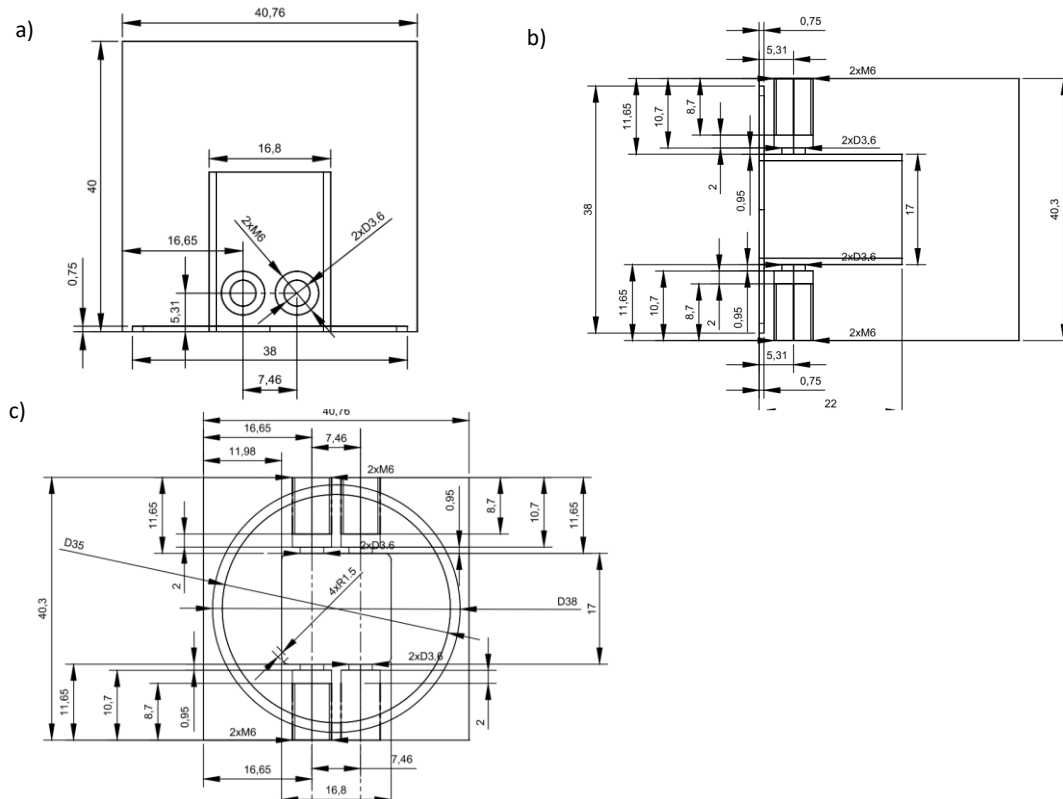


**Figure 8.2** The solar laser head project: a) front view; b) side view; c) top view.

### The solar laser head and the pump cavity

The laser head was partially machined by an outsourcing company, which produced the copper “box” with two parallel drilled rod-holes for the two laser rods. The remaining machining was developed at the Physics Department workshop. After this “box” was finished, two holes were drilled at the sides of the laser head to fit two water tubes of the refrigeration system, being one for the water inlet and the other for the water outlet of the laser rods and the pump cavity. In Fig. 8.3 is given the solar laser head and the aluminum pump cavity built in its first phase of construction of the solar laser head at the workshops of the Physics Department.

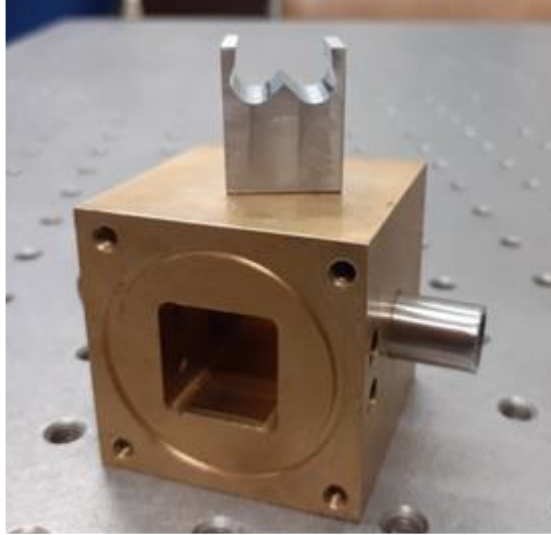


**Figure 8.3** The solar laser head and the pump cavity for the dual-rod solar laser experiments.

For the water sealing mechanism, an o’ring was inserted into the sealing channel on the top of the laser head. The fused silica aspherical lens used for these experimentations was already available in the laboratory. The fused silica aspherical lens used was 46 mm diameter and the solar laser head were arranged with two rods of 3.5 mm diameter and 25 mm length.

### **The pump cavity**

The reflective pump cavity was built in the Physics Department workshop. The aluminum piece was then polished, resized and covered with a 95% reflective surface, following to the setting up of the laser head with the pump cavity. In the figure 8.4a) and b) are shown the aluminum pump cavity with the reflective surface.

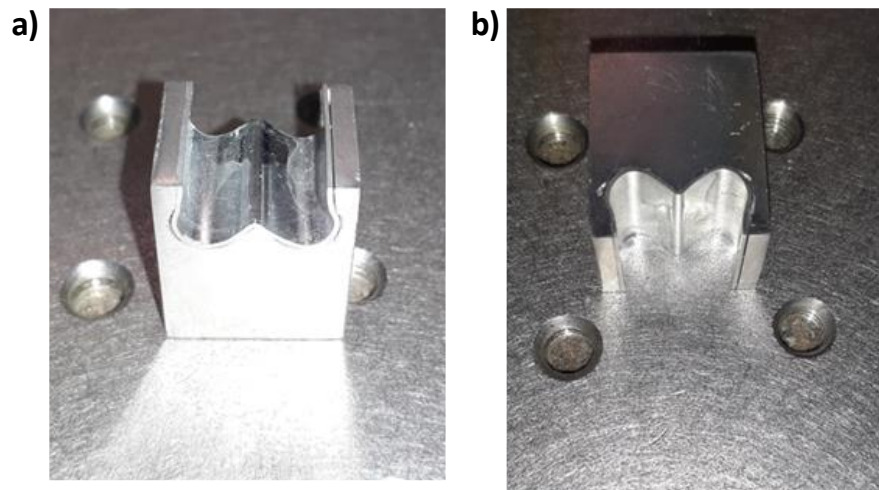


**Figure 8.4** Different views of the pump cavity produced and covered with the reflective surface.

This pump cavity was glued inside the rectangular hole of the laser head, keeping the space designed for the water inlet and outlet.

## Nd:YAG rods mounting

The mounting process of the rods into the laser head is shown in Fig. 8.5, and started by rolling a Teflon tape around their tips to avoid water leakages; in a) special tool built by us to carefully insert the rods and the o'rings inside the rod-hole of the laser head; b) Nd:YAG rods mounted inside the laser head. The o'ring of the aspherical lens was also rolled up with Teflon.

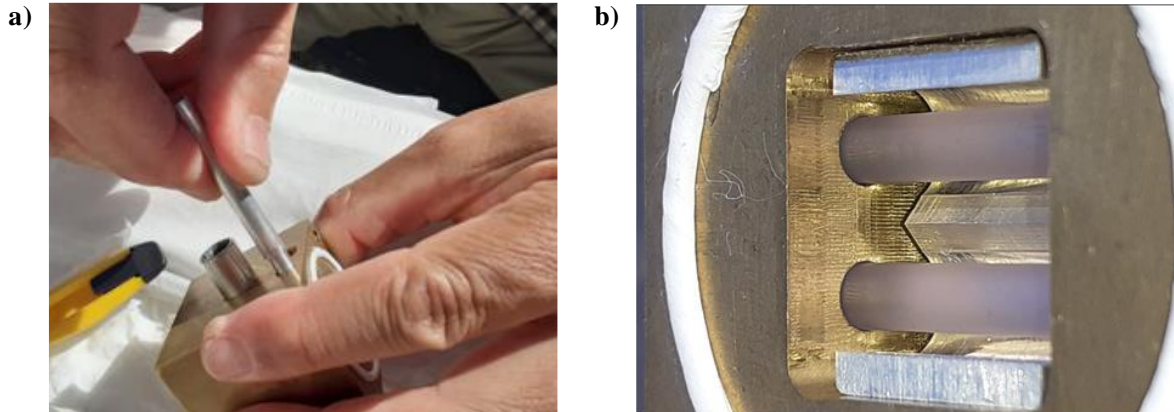


**Figure 8.5** The Nd:YAG rods mounting into the laser head: a) the special tool built by us to carefully insert the rods and the o'rings into the rod-hole of the laser head; b) Nd:YAG rods mounted inside the laser head.

The laser head with the pump cavity fully assembled is presented in the Fig. 8.6, where it can be seen the reflective surfaces on the sides of the laser head, perpendicular to the rods axes, as shown in a) and b).

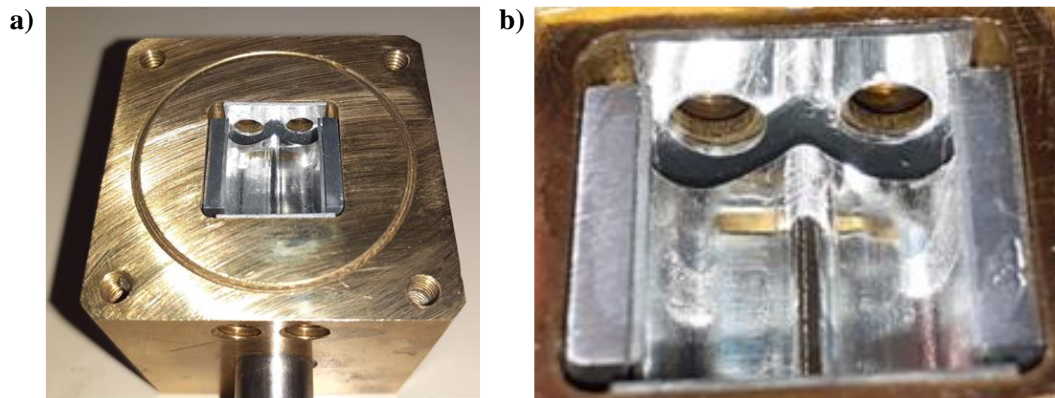


**Figure 8.6** Photographs of the laser head: a) and b) top view of the laser head, with the inserted pump cavity.

## Resonant cavity mirrors

Due to the dimensions of the solar laser head and its accessories, as for example the distance between the two rods, which hamper the installation of a standard commercial output mirror, we built mini-mirrors to act as the PR at 1064 nm and HR at 1064 nm output couplers, with 94% reflectivity and RoC = -10. They were manufactured by cutting a commercial output coupler, as shown in Fig. 8.7a); in b) is shown the supporting structure with positioners and mini-mirrors in place.



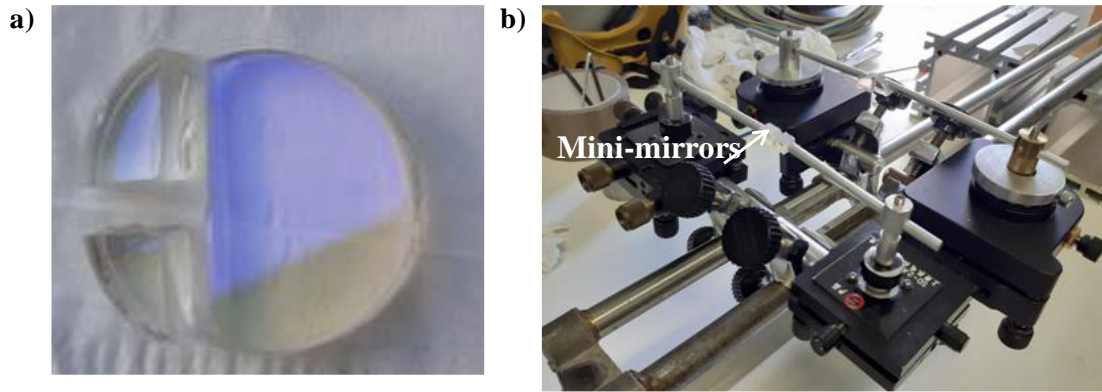


**Figure 8.7** Mini output mirrors fabrication from the large standard commercial output coupler: a) the production of two mini-mirrors for the solar laser experiments; b) The supporting structure for the solar laser head, output couplers and other accessories, where is visible the positioners and the mini-mirrors mounted.

### Water leakage tests

The water-leakage tests were carried out with the fully assembled solar laser head in PROMES-CNRS France. The sealing of the laser rods and the whole laser head is of paramount importance for the experimental procedure, since water-leakage at the rods decrease or even can extinguish the solar laser emission, or disturbs the refrigeration process, what may cause the destruction of the rods or the lens. In Fig. 8.8 is shown the water leakage tests carried out.

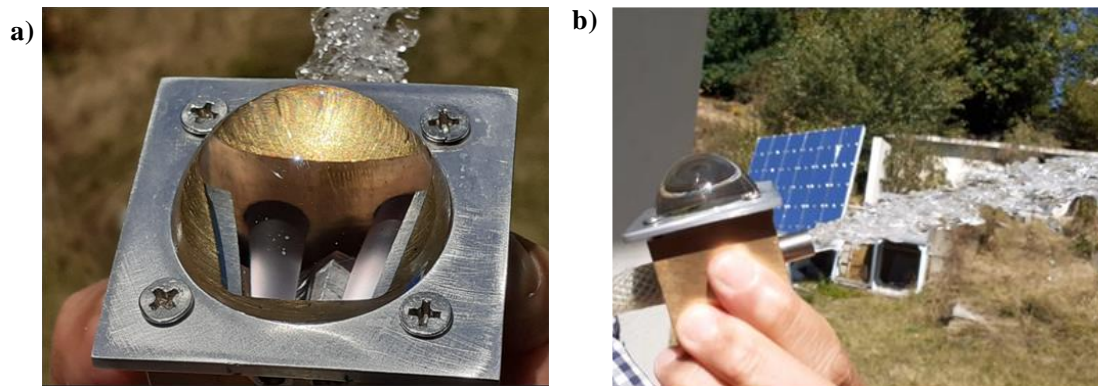


**Figure 8.8** The water-leakage tests: a) and b) show the water test in order to avoid any water leakage;

## 8.2 Experimental tests at PROMES-CNRS heliostat-parabolic mirror system

At the CNRS-PROMES, in France, after finishing the prototype and its accessories we started the first experimental tests of the dual-rod side-pumping scheme.

## Solar laser emission experiments

What follows next is the solar laser setup installed at the solar furnace. In Fig. 8.9 is presented the solar laser head with the water system and the power detector fixed at the supporting structure.

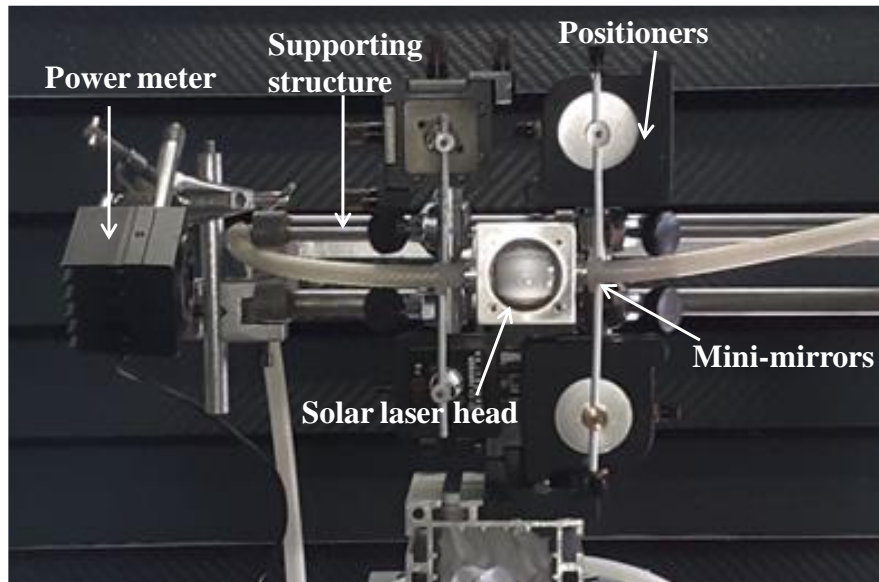


**Figure 8.9** Solar laser head prepared for the experimental tests at the CNRS-PROMES solar furnace, showing the power meter, the supporting structure for the laser head and its accessories.

The solar laser set up prepared for the experimental work is shown in the Fig. 8.10a), where it is possible to observe, from the back of the parabolic mirror, through the hole in its center, the still closed shutter behind the solar laser head, which regulates the light entrance inside the laboratory; b) the alignment of the focal spot at the center of the fused silica aspherical lens; c) the solar pumping, where it is visible the Sun shining at the heliostat outside the laboratory and the solar laser head illuminated.

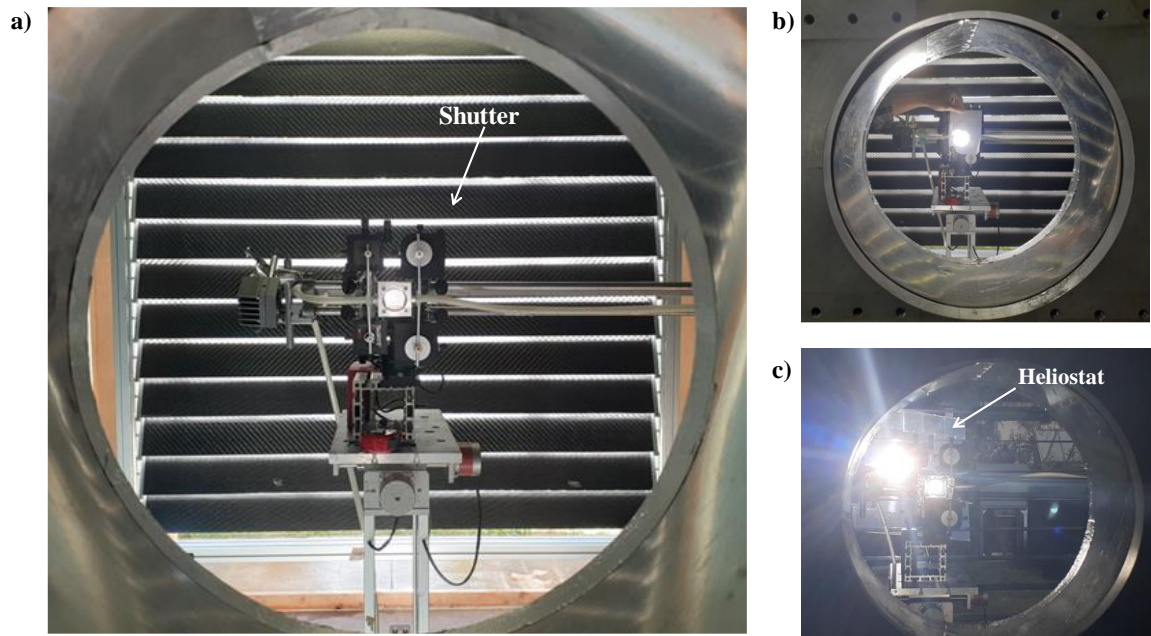




**Figure 8.10** Experimental test at the solar furnace in France: a) the full set up seen from the back of the parabolic mirror, through the hole in its center, from where the shutter is visible behind the solar laser head; b) alignment testing with the focal spot and a piece of paper; c) open shutter for solar pumping, where it can be seen the heliostat outside the laboratory.

## 8.3 Experimental tests at NOVA heliostat-parabolic mirror system

The experimental work at NOVA heliostat-parabolic mirror system started in June 2021, with the installation of the solar laser head at the focus of the parabolic mirror. The dimensions and characteristics of this solar furnace are different from the solar facility CNRS-PROMES in France. A reconfiguration of the solar laser head was necessary to improve the results after the first tests in Portugal with the prototype, and we decided to change the secondary concentration stage and also the dimensions of the laser rods.

### 8.3.1 Improvement of the solar laser prototype

The reconfigured prototype was composed of a larger fused silica aspheric lens, to enhance the secondary stage of the solar rays' concentration into the pump cavity and consequently on the laser rods. The same pump cavity and water cooling system was used. We modified the laser head enlarging the rod-holes to accommodate two larger diameter laser rods, which could be beneficial for the performance of the solar laser system.

The two crystals chosen were available in the laboratory: one with 4.0 mm diameter and 35 mm length and the other with 4.0 mm and 30 mm length, as shown in Fig. 8.11. The aspherical lens had an input face with 46 mm radius of curvature, -0.005 conic factor and a plane output face with 84 mm diameter, coupling the concentrated solar radiation from the focal spot to the input aperture of the pump cavity, with more efficiency than the smaller aspherical lens used before. The final reconfigured model and its key dimensions are shown in Fig. 8.11.

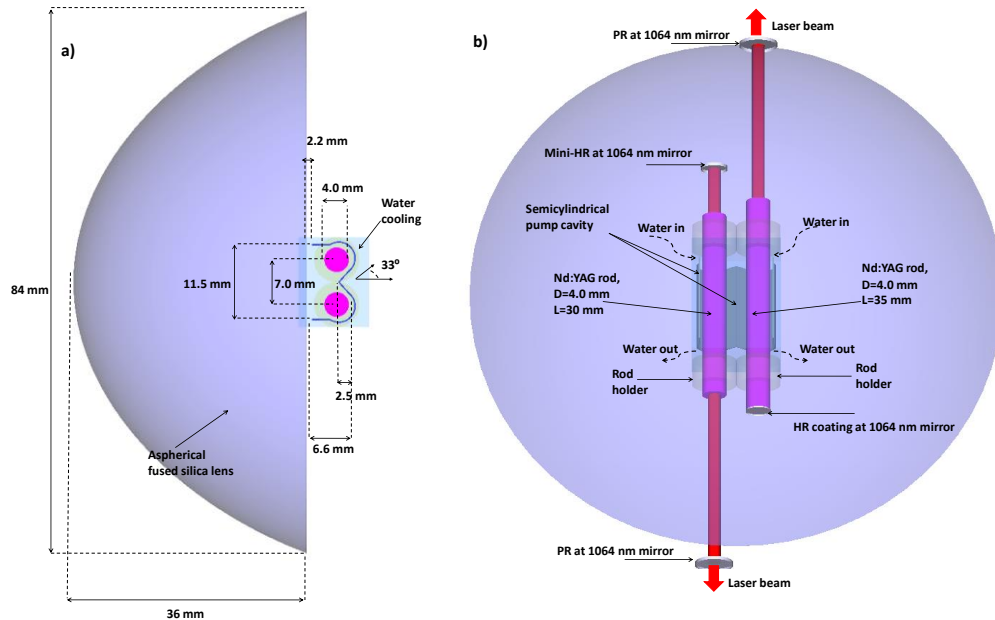


**Figure 8.11** Experimental model for the solar laser head, consisting in the larger fused silica aspherical lens, the same pump cavity as before and the two Nd:YAG laser rods, fixed by two rod-holders: a) side view and the key dimensions; b) top view.

For the 30 mm length rod, the resonant laser cavity was formed by one mini-HR 1064 nm mirror with 99.6% reflectivity and another standard PR 1064 nm mirror with 98% reflectivity, both with  $\text{RoC} = -1 \text{ m}$ .

For the 35 mm length rod, the resonant laser cavity consisted in a HR 1064 nm coating on the rod's end-face and a standard PR 1064 nm mirror with 98% reflectivity and  $\text{RoC} = -1 \text{ m}$ . We also designed and built a new aluminum casing to accommodate the larger lens and the new structure for the laser head. We also designed and built new supporting structures for the mini-output mirrors and their X-Y-Z positioners, bolted in the aluminum casing, as shown in Fig. 8.12a) and b), to diminish the distance from the end-face of the rods to the mini-output mirrors, aiming to simplify the mechanical system and improve the results. We used the standard output couplers X-Y-Z positioners as holders for the mini-output mirrors positioners, as it can be seen in the Fig. 8.12a and 8.12b.

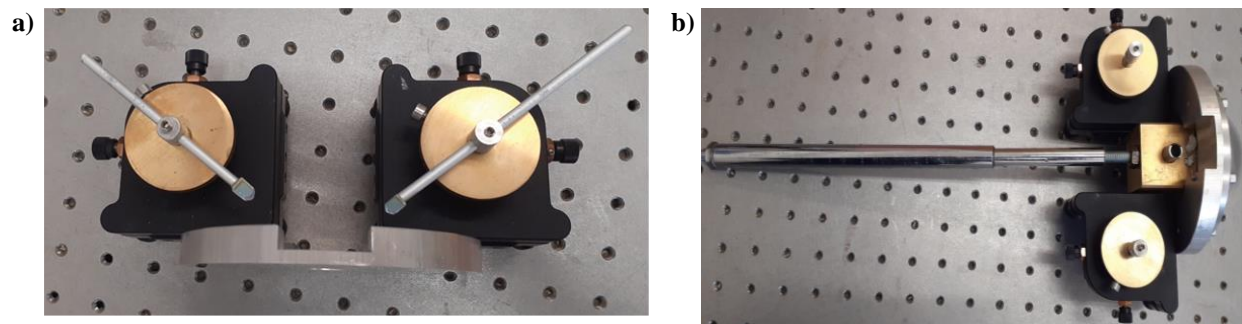


**Figure 8.12** New supporting structures for the mini-output mirrors and their X-Y-Z positioners, bolted in the aluminum casing; a) top view; b) side-view.

At the NOVA solar concentration system, we practiced the alignment of the heliostat and parabolic mirrors, in relation to the solar laser head, with the help of four solar light columns from the entrance door of the laboratory, through four holes specially produced by us for this purpose, as shown in Fig. 8.13, with some alignment tests made to form and optimize the focal spot. It starts in a) and finishes in d), with the formed spherical solar light focus.

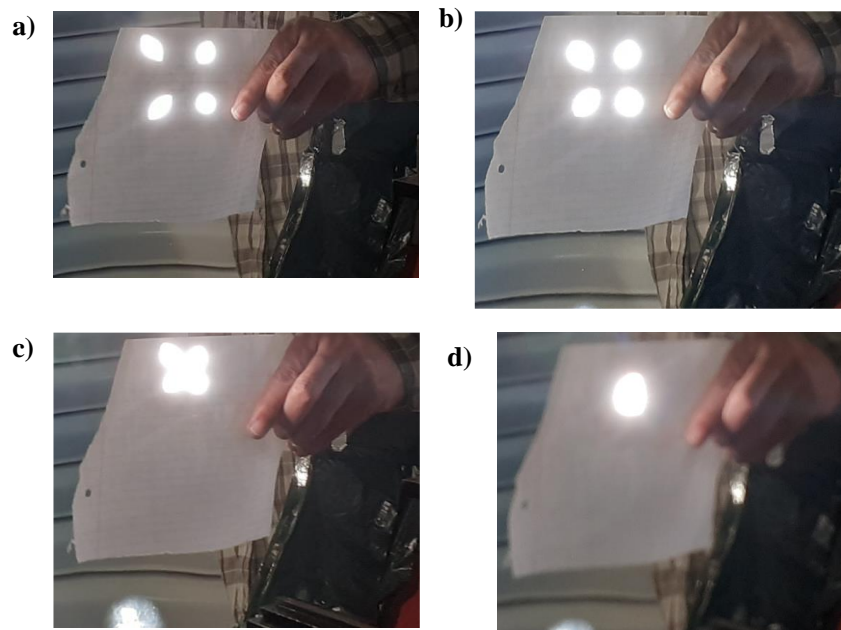


**Figure 8.13** Alignment tests made to form and study the focal spot. It starts in a) and finishes in d), with the formed spherical solar light focus.

In Fig. 8.14 it is presented the solar laser head fully assembled and prepared for the experimental tests at NOVA system; a) the solar laser head set up at the focal area of the parabolic mirror. The power detector, the parabolic mirror, and the mini-mirrors are also indicated. The solar laser head were placed in a horizontal setup at this stage of the experimental work at NOVA, as it can be observed in b).

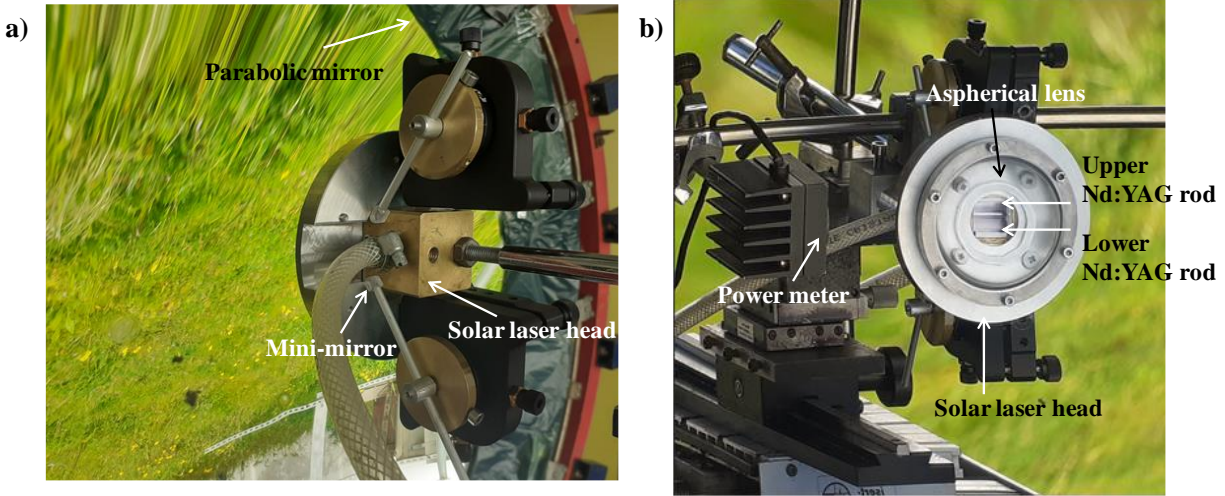


**Figure 8.14** New supporting structures for the mini-mirrors and their X-Y-Z positioners, bolted in the aluminum casing; a) top view; b) side-view; c) perspective d) attached to the laser head and a metal stick for the installation at the solar furnace.

### 8.3.2 Dual-rod solar laser emission with one rod

The dual-rod solar laser experiments at NOVA heliostat-parabolic mirror system started by studying each one of the rods at a time. We used large standard commercial output couplers in order to know which RoC and reflectivity were the most adequate to improve the solar laser emission with the new arrangement of rods and lens, before to cut other mini-mirrors, due to the ones we have already produced, with 95% reflectivity, were not the most adequate ones to extract more laser power. We have investigated both rods with two different setups, a vertical and a horizontal. Different reflectivities and RoC's were tested aiming to reach the higher solar power to be extracted, but also the higher stability in the solar laser emission.

It will be described some of those experiments, with the most interesting results obtained. The procedure followed were the alignment of the focal spot at the center of the pump cavity, between both the laser rods in order to equally distribute the energy of the solar concentrated focal spot between the two crystals in order to attain an equal solar laser emission. After the experimental work with one rod at a time, we followed to the simultaneous solar laser emission by the two laser rods.

#### Vertical set up with one rod (L = 35 mm)

Different input solar powers were measured by the power meter, and consequently different solar powers at the focus were calculated based on the combined reflectance of 75% of both heliostat (93.5%) and the parabolic mirror (80.0%). The solar irradiance measured in the day of the experiment was 827 W/m<sup>2</sup>. The threshold for the solar laser emission was 70% of the solar power at the focus, at 455.9 W.

With the 35 mm length rod, the resonant laser cavity consisted in a HR at 1064 nm coating on the rod's end-face and a standard PR 1064 nm mirror with 98% reflectivity and RoC = -1 m, to be detected by the power meter, as shown in the Fig. 8.15.

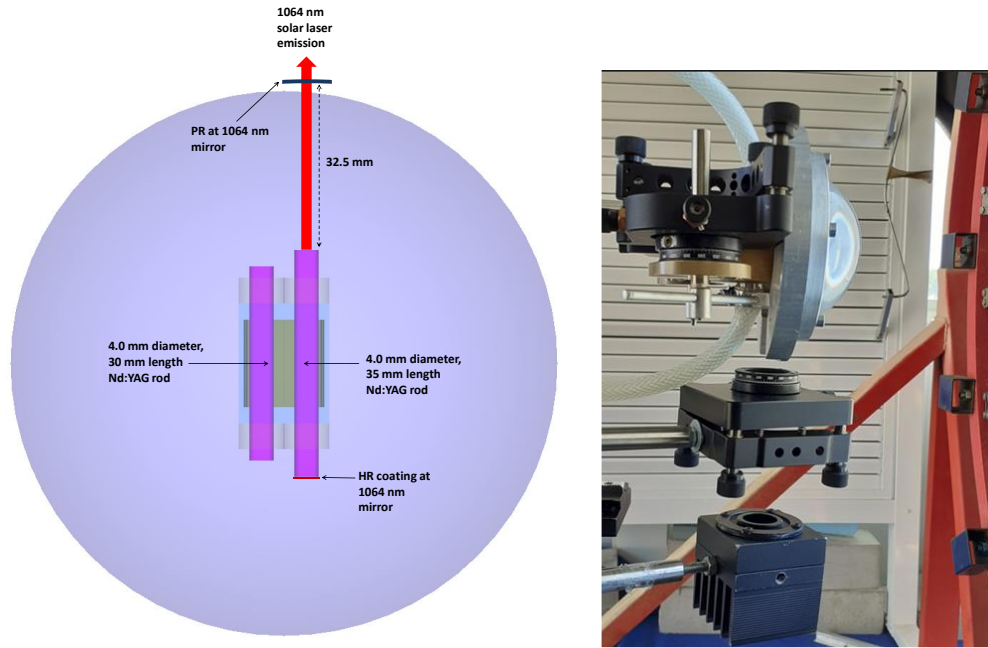


**Figure 8.15** a) The schematics for the solar laser head: a) the output mirrors configuration and the vertical set up for the 35 mm length rod; b) Photograph of the solar laser head showing the aspherical lens, the water cooling system, the output mirror and the power detector.

With this configuration and conditions, the maximum multimode solar laser output power detected by the power meter was of 11.88 W. Using the mini-PR 1064 nm with 95% reflectivity, the maximum multimode laser output power measured was of 8.4 W, showing that the PR 1064 output coupler with 98% reflectivity was the most adequate to extract higher output powers. In Fig. 8.16 is given the solar laser output power versus the solar power at the focus for the one rod experiments of the dual-rod scheme in its vertical setup and the 35 mm length rod. The total solar laser power measured was 11.88 W.

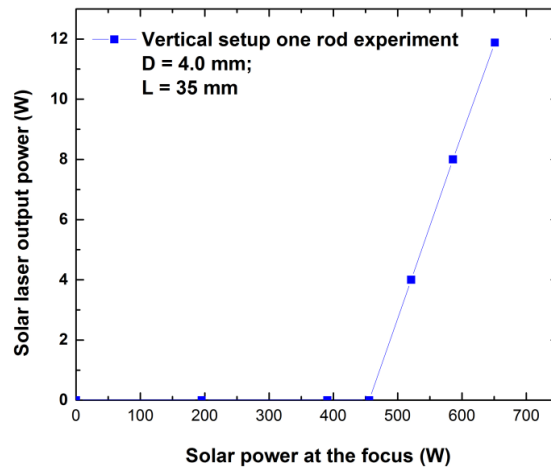


**Figure 8.16** Solar laser output power in its vertical setup in the one rod experiments: solar laser output power as a function of the solar power at the focus.



### Vertical set up with one rod ( $L = 30$ mm)

The 30 mm length rod was also tested in this vertical configuration, with the resonant laser cavity formed by one standard HR 1064 nm mirror with 99.6% reflectivity and another standard PR 1064 nm mirror with 98% reflectivity, both with  $\text{RoC} = -1$  m, to be detected by the power meter, as shown in the Fig. 8.17. The solar irradiance measured in that day was  $843 \text{ W/m}^2$ . The threshold for the solar laser emission was 70% of the solar power at the focus, at 464.7 W.

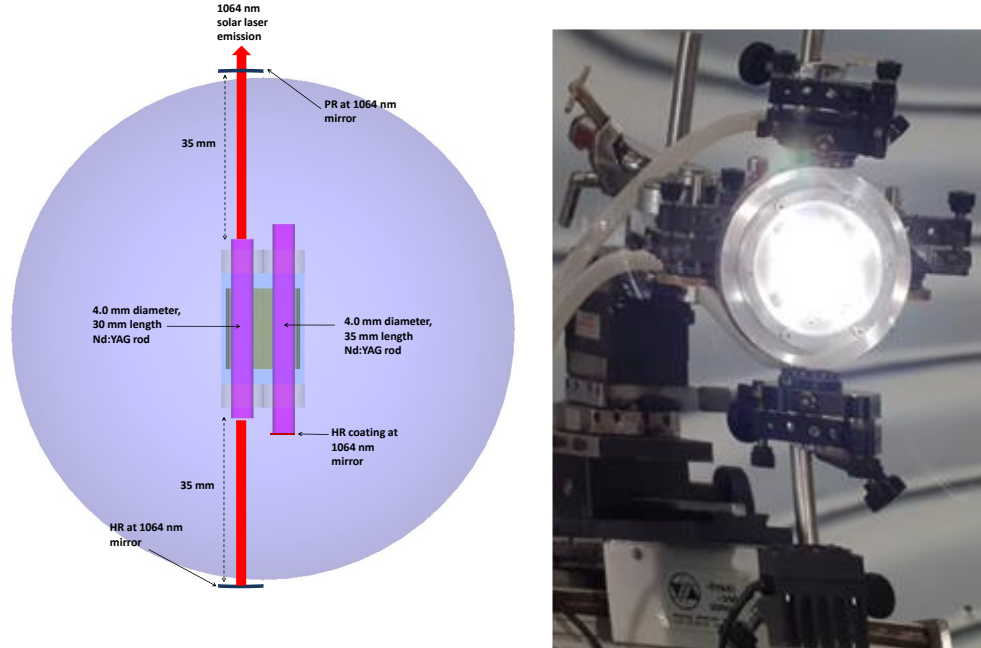


**Figure 8.17** a) The schematics for the solar laser head: a) the output mirrors configuration and the vertical setup for the 30 mm length rod; b) Photograph of the solar laser head showing the aspherical lens illuminated by the solar light, the water cooling system, output mirrors configuration and the power detector.

In Fig. 8.18 is given the solar laser output power versus the solar power at the focus, for the one rod experiments of the dual-rod scheme in its vertical setup and the 30 mm length rod. The total solar laser power measured was 12.86 W.

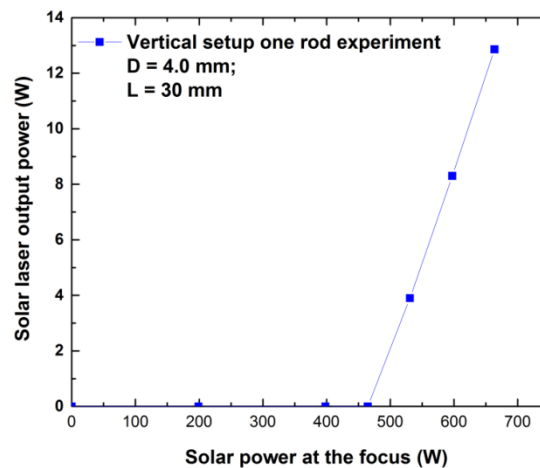


**Figure 8.18** Solar laser output power in its vertical setup in the one rod experiments with the 30 mm length rod: solar laser output power as a function of the solar power at the focus.

### Horizontal setup with one rod ( $L = 35$ mm)

To investigate all possibilities in order to improve the solar laser emission by the two rods to its maximum, a horizontal configuration was also implemented. The 35 mm length rod had, as already mentioned, a resonant laser cavity formed by a HR 1064 nm coating on the rod's end-face and a standard PR 1064 nm mirror with 98% reflectivity and  $\text{RoC} = -1$  m, to be detected by the power meter, as shown in the Fig. 8.19. The solar irradiance measured in that day was  $859.4 \text{ W/m}^2$ . The threshold for the solar laser emission was 70% of the solar power at the focus, at 473.7 W.

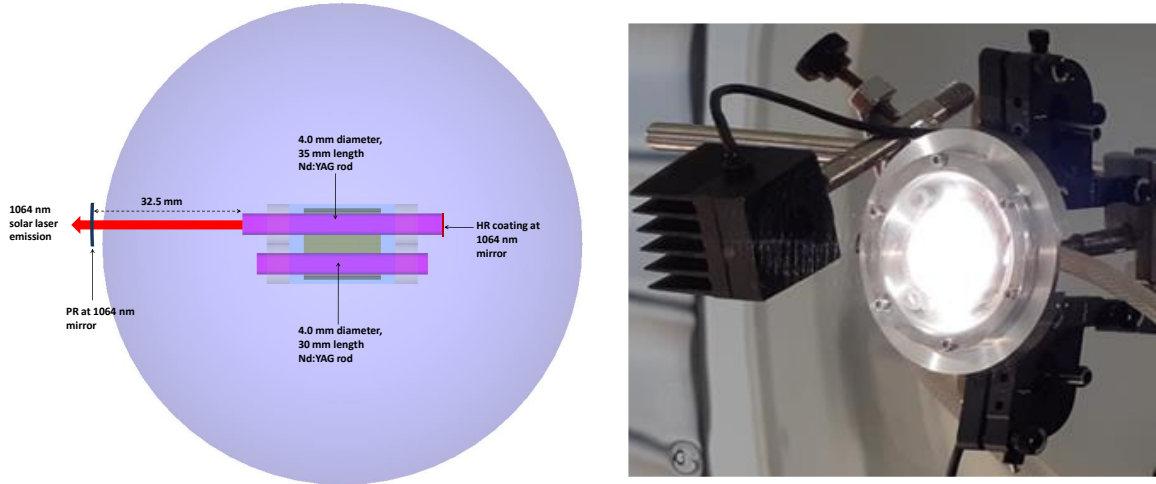


**Figure 8.19** a) The schematics for the solar laser head: a) output mirrors configuration and the horizontal setup for the 35 mm length rod; b) Photograph of the solar laser head showing the aspherical lens illuminated by the solar light, the water cooling system and the power detector.

The  $\text{RoC} = -1$  m and the of 98% for the reflectivity of the standard PR 1064 nm had shown the best performance also for the horizontal setup for the extraction of the maximum solar laser power.

In Fig. 8.20 is given the solar laser output power versus the solar power at the focus for the one rod experiments of the dual-rod scheme in its horizontal setup and the 35 mm length rod. The total solar laser power measured was 15.78 W.

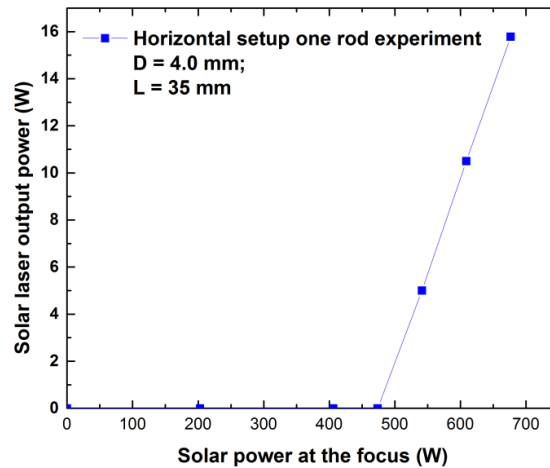


**Figure 8.20** Solar laser in its horizontal setup in the one rod experiments with the 35 mm length rod: solar laser output power as a function of the solar power at the focus.

### Horizontal setup with one rod ( $L = 30$ mm)

The 30 mm length rod was also experimented in the horizontal setup, and the resonant laser cavity was formed by one standard HR 1064 nm mirror with 99.6% reflectivity and another standard PR 1064 nm mirror with 98% reflectivity, both with  $\text{RoC} = -1$  m, to be detected by the power meter, as shown in the Fig. 8.21. The solar irradiance measured in that day was  $891 \text{ W/m}^2$ . The threshold for the solar laser emission was 70% of the solar power at the focus, 491.1 W.

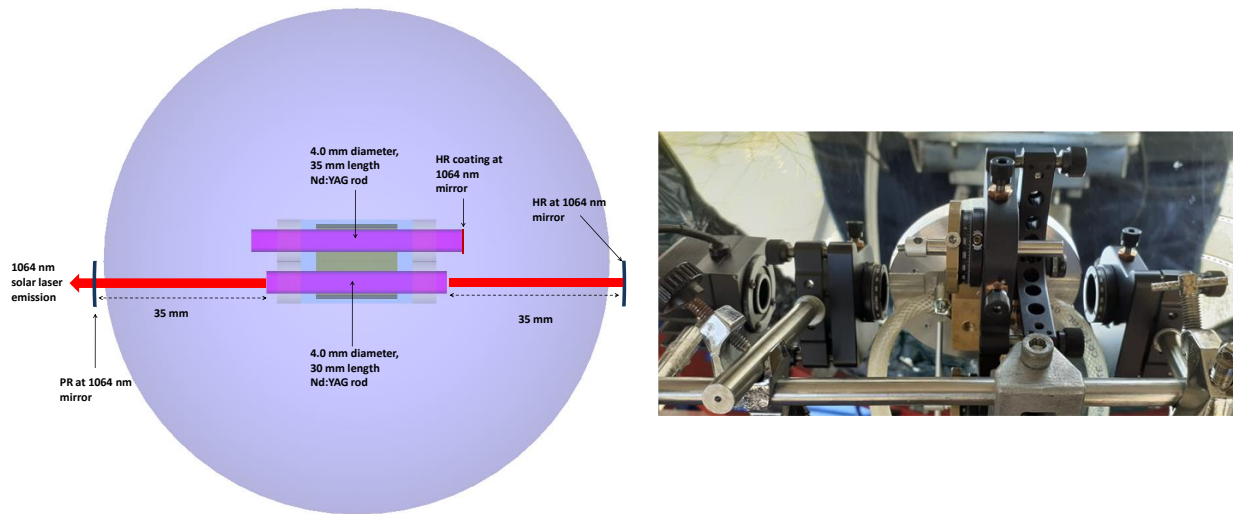


**Figure 8.21** a) The schematics for the solar laser head: a) output mirrors configuration and the horizontal setup for the 30 mm length rod; b) Photograph of the solar laser head showing the aspherical lens illuminated by the solar light, the water cooling system and the power detector.

In Fig. 8.22 is given the solar laser output power versus the incoming solar power for the one rod experiments of the dual-rod scheme in its horizontal setup and the 30 mm length rod. The total solar laser power measured was 11.33 W.

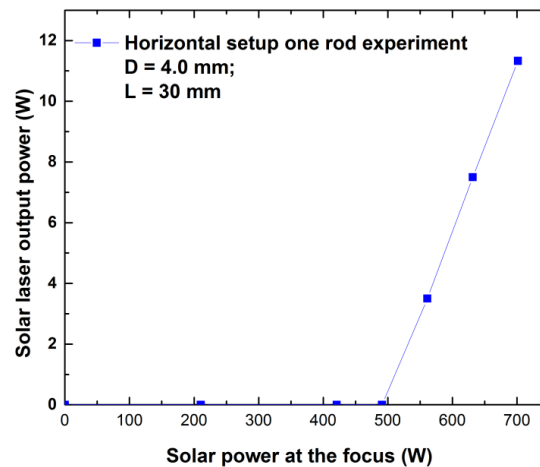


**Figure 8.22** Solar laser output power in its horizontal setup in the one rod experiments with the 30 mm length rod: solar laser output power as a function of the incoming solar power.

In the Fig. 8.23 below is given some readings of the power meter on the solar laser operation, from different solar laser emissions during the experimental work carried out in July 2021.

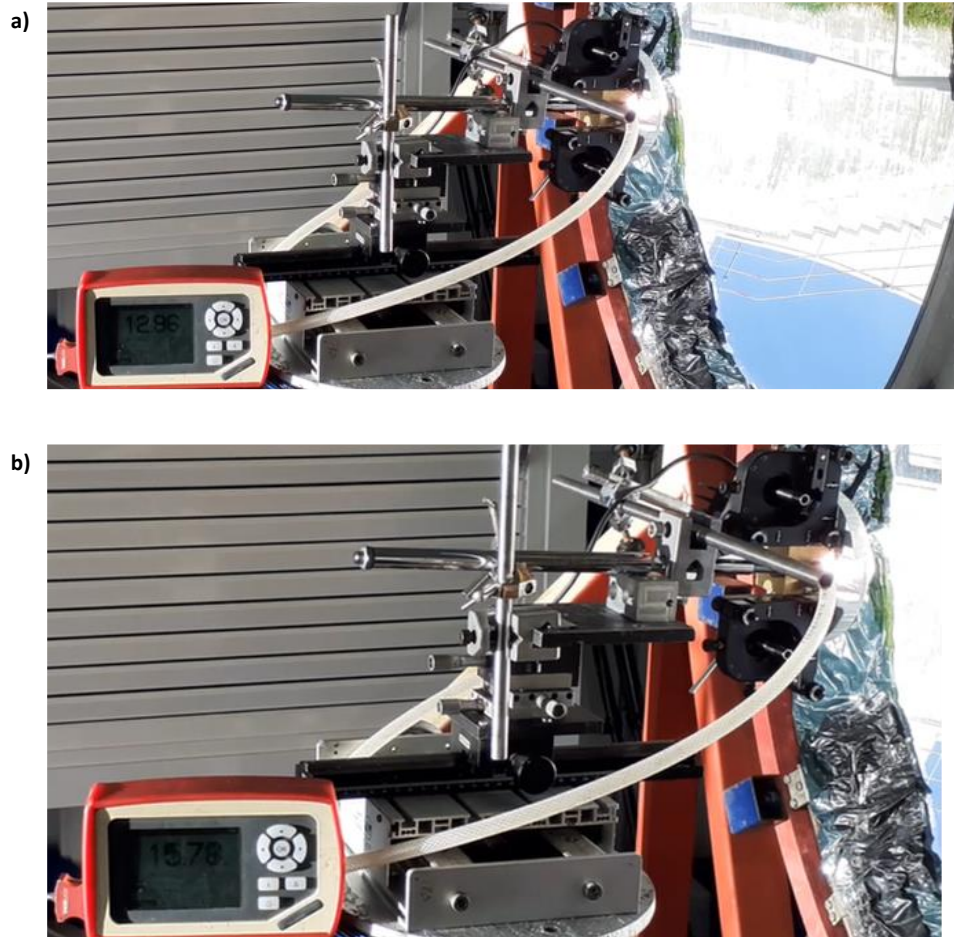


**Figure 8.23** Different solar laser emissions obtained with one rod during the experiments: a) 12.96 W; c) 15.73 W.

### 8.3.3 Dual-rod side-pumping solar laser simultaneous emission

#### **Total solar laser power measurements**

The total solar laser power measurements were carried out to fully develop one of the intentions of this work, which is to obtain two solar laser emissions with the highest output power and stability. We started the work by setting up one power meter and directed the two laser emissions to it in order to detect the maximum solar power obtained by the simultaneous emission.

These experiments were performed during August 2021. Firstly, the two solar laser outputs were pointed towards one direction and were detected by one power meter, in order to measure the maximum solar laser output power from the two laser rods. Different input solar powers were measured by a Thorlabs PM 1100D power meter, and consequently different solar power at the focus were calculated based on the combined reflectance of 75% of both



heliostat (93.5%) and the parabolic mirror (80.0%). In this case, mini output mirrors with RoC = -1 m and 94% reflectivity were chosen. For  $783 \text{ W/m}^2$  solar irradiance, different solar powers at the focus were measured by a Thorlabs PM 1100D power meter as a function of different input solar powers. The solar laser emission started with 70% of the solar power at the focus, 431 W. The total solar laser power measured was 14.81 W. Fig. 8.24 presents the model of the experimental setup used in the dual-rod simultaneous experiments, where both the solar laser emissions were detected by one power meter. The solar pump flux distribution along one longitudinal central cross-section for both the rods is also given in Fig. 8.24, The resonant laser cavity is also represented in the figure.

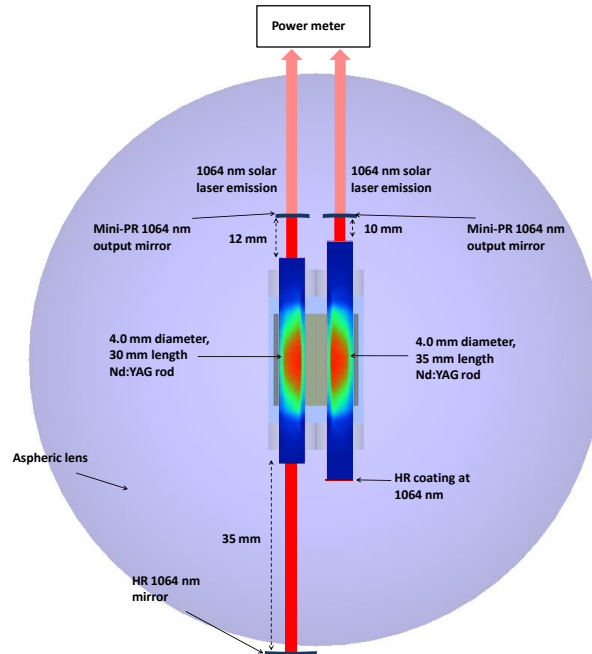


**Figure 8.24** Dual-rod side-pumping solar laser head for the solar laser experiment: The solar laser head consisted in the fused silica aspherical lens, the semicylindrical pump cavity and two Nd:YAG laser rods, fixed by two rod-holders. Both the solar laser emissions were detected by one power meter.

In Fig. 8.25 is given the solar laser output power versus the solar power at the focus. The total solar laser power measured was 14.81 W.

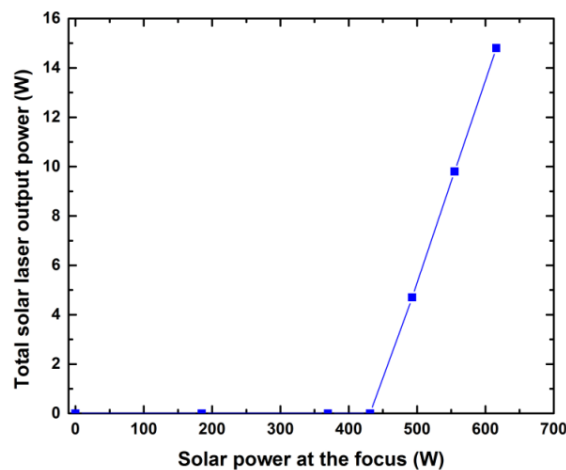


**Figure 8.25** Dual-rod solar laser output power versus incoming solar power.

The limitation of both laser emissions being detected by one power meter is that we cannot know the laser power of each one of the rods individually, so that to evaluate the tracking error stability of the dual-rod prototype. To circumvent this limitation, we decided to turn one of the laser rods in one different direction, so that the solar laser emission from each rod could be detected by two different power meters.

### 8.3.4 Tracking error compensation capacity measurements of the dual-rod solar laser

#### Dual-rod side-pumping vertical setup

In order to implement the tracking error compensation capacity measurements, each one of the solar laser emissions needed to be detected separately, using two power meters. In Fig. 8.26a) is presented the schematics of the laser head used in the dual-rod simultaneous emission experiments to evaluate the tracking error tolerance, measuring the solar laser power of the rods individually. Each one of the laser emissions were pointed to opposite directions, towards to each one of the power meters, so that the output power variation with the tracking error could be detected. In Fig. 8.26b) is presented a photograph of the dual-rod solar laser in its vertical configuration with the aspheric lens illuminated by solar light and in c) the two rods illuminated by solar light during the alignment procedure.

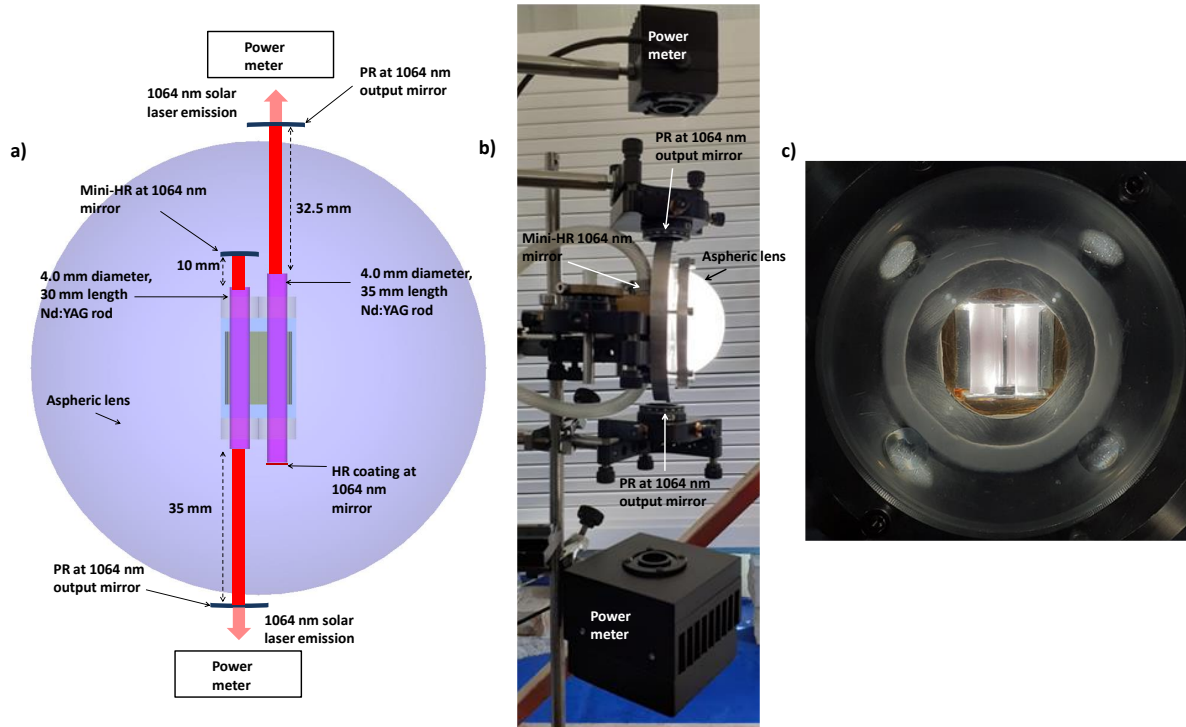


**Figure 8.26** a) Solar laser head design for the Nd:YAG dual-rod side-pumping and its output couplers configuration; b) Photograph of the solar laser head showing the aspherical lens, the water cooling scheme and the power detectors 1 and 2; c) the two rods illuminated by solar light.

The first tracking error compensation capacity measurement was carried out with the vertical setup, as shown in Fig. 8.27. The solar irradiance measured during the experiments was about  $783 \text{ W/m}^2$ . Firstly, the solar laser emission

was tested with accurate Sun tracking in order to attain an equally distributed solar laser emission by the two rods. Secondly, the solar laser emissions were measured with no Sun tracking for 1 minute. The solar heliostat was stopped, but the Sun apparently kept moving and, consequently, the focal spot changed its position, as shown in Fig. 8.27, where the solar laser head and the schematics for two maximum displacements of the focal spot due to the solar tracking error in both altitude and azimuth directions are presented, corresponding to the positions 1 and 3 in Figs. 8.27a) and c), respectively. The optimal alignment is represented by the position 2 in Fig. 8.27b). In Fig. 8.27d) is shown the normalized total solar laser power from the left and the right laser rods, as well as the normalized solar laser power from each rod.

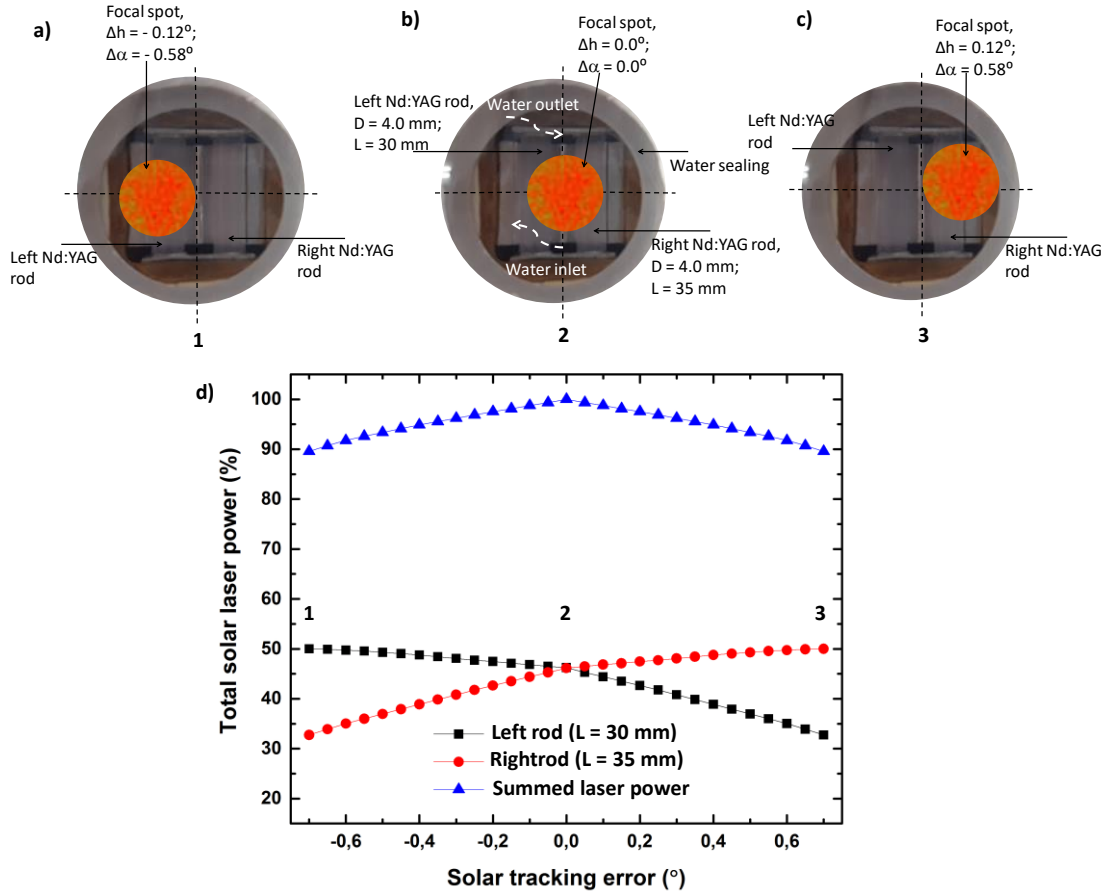


**Figure 8.27** The solar laser head and the schematics for a), c) two maximum displacements of the focal spot due to the solar tracking error in both altitude and azimuth directions in the vertical setup, corresponding to the positions 1 and 3; b) optimal alignment of the focal spot, corresponding to the position 2; d) normalized total solar laser power for the left and the right laser rods.

With the tracking error in altitude, the pump flux distribution moved only slightly along the laser rods of the dual-rod scheme. The largest tracking error occurred in the azimuth direction, which displaced the pump flux distribution from the left rod to the right rod.

### Dual-rod side-pumping solar laser in horizontal setup

The second tracking error compensation capacity measurement was carried out with a horizontal setup. The solar irradiance measured was about  $798 \text{ W/m}^2$ . The same procedure was adopted as in the vertical setup. The solar laser

emission was tested with accurate Sun tracking in order to attain an equally distributed solar laser power by the two rods. Secondly, the solar laser emissions were measured with no Sun tracking for 1 minute.

In the Fig. 8.28a) below is presented the horizontal setup with two detectors for the solar laser measurements of each one of the rods; in b) the two rods illuminated by solar light during the alignment procedure; in c) the size and the shape of the obtained solar laser beam in a piece of paper, where around 2.0 mm was obtained.

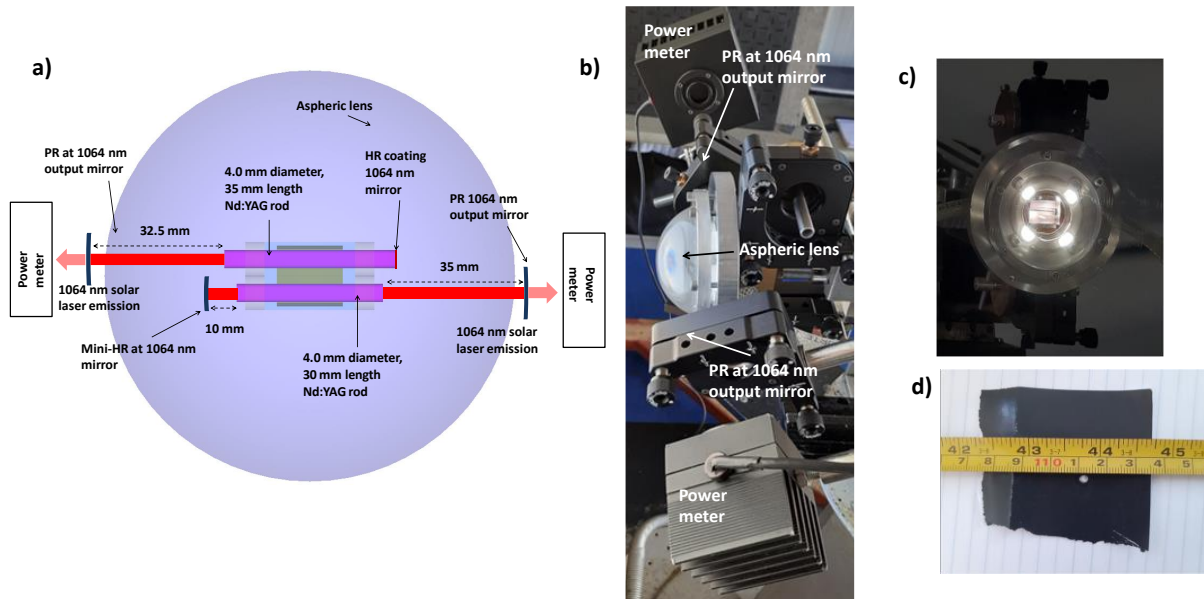


**Figure 8.28** The horizontal setup with two detectors for the solar laser measurements of each one of the rods; in b) the two rods illuminated by solar light during the alignment procedure; in c) The size and the shape of the obtained solar laser beam in a piece of paper, where around 2.0 mm was obtained.

In Fig. 8.29 is presented the solar laser head and the schematics for two maximum displacements of the focal spot due to the solar tracking error in both altitude and azimuth directions in the horizontal setup, corresponding to the positions 1 and 3 in the Figs. 8.29a) and c), respectively.

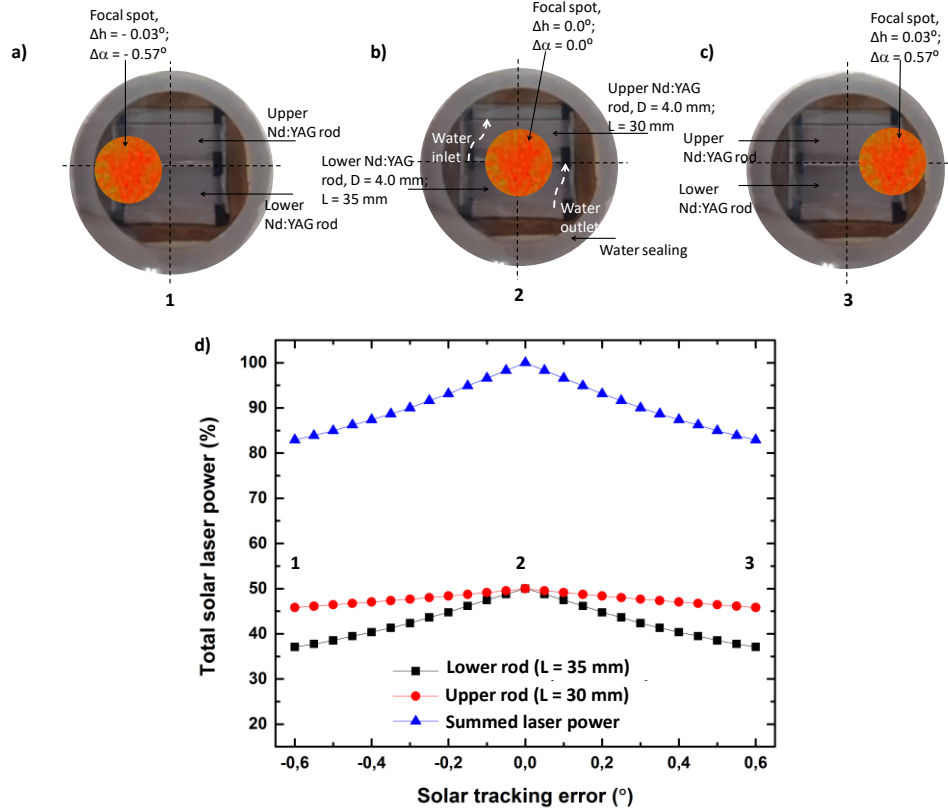


**Figure 8.29** The solar laser head and the schematics for a), c) two maximum displacements of the focal spot due to the solar tracking error in both altitude and azimuth directions in the horizontal setup, corresponding to the positions 1 and 3; b) optimal alignment, corresponding to the position 2; d) normalized total solar laser power for the upper and the lower laser rods, as well as the normalized laser power from each laser rod.

The optimal alignment corresponds to the position 2 in Fig. 8.29b). In Fig. 8.29d) is shown the normalized total solar laser power from the upper and the lower laser rods, as well as the normalized laser power from each laser rod. With the tracking error in altitude, the pump flux distribution moved from the lower rod to the upper rod of the dual-rod scheme. The tracking error in azimuth displaced the pump flux distribution along the rods.

Regarding the previous numerical analysis of dual-rod and single-rod side-pumping configurations with tracking error compensation capacity in horizontal setups using a small aspherical lens [30], the dual-rod side-pumping experiments resulted in a largely enhanced tracking error tolerance, as shown in Fig. 8.30, where the vertical and the horizontal setups presented a  $TEW_{10\%}$  of  $1.4^\circ$  and  $0.6^\circ$ , respectively, and a more stable solar laser emission as compared to the numerical models from the previous publication [30].

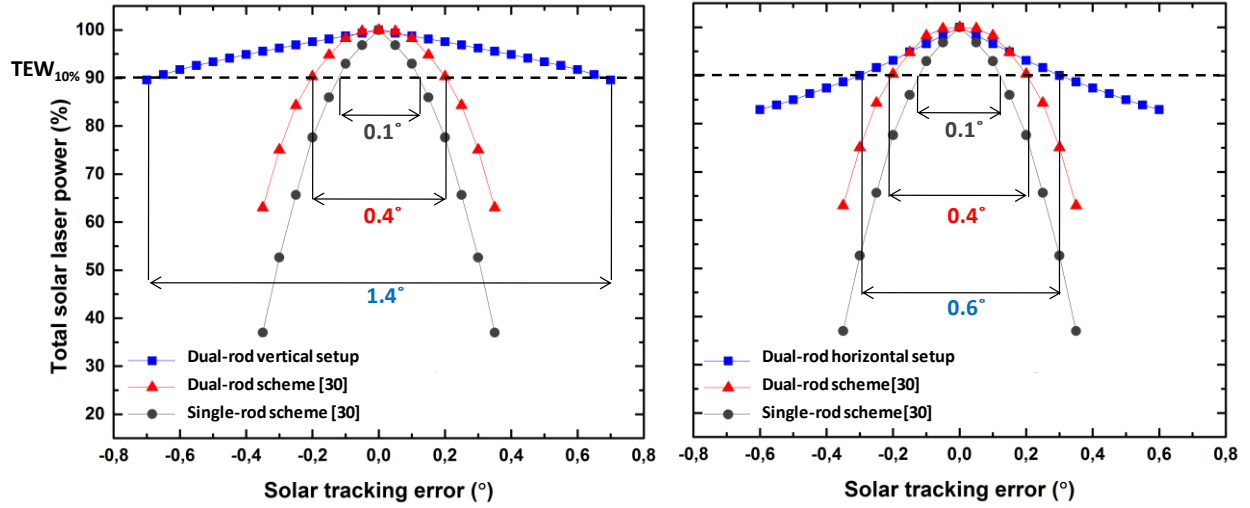


**Figure 8.30** Normalized solar laser output power from the vertical and horizontal setups with no Sun tracking, compared to the previous numerical results of the single-rod and the dual-rod side-pumping using a small aspherical lens as secondary concentrator [30].

In comparison with the other numerical dual-rod side-pumping solar laser with cylindrical lens and one pump cavity to each one of the laser rods [28] in a horizontal setup, the experimental dual-rod side-pumping of the present work had also shown a significantly improved tracking error stability, as given in Fig. 8.31.

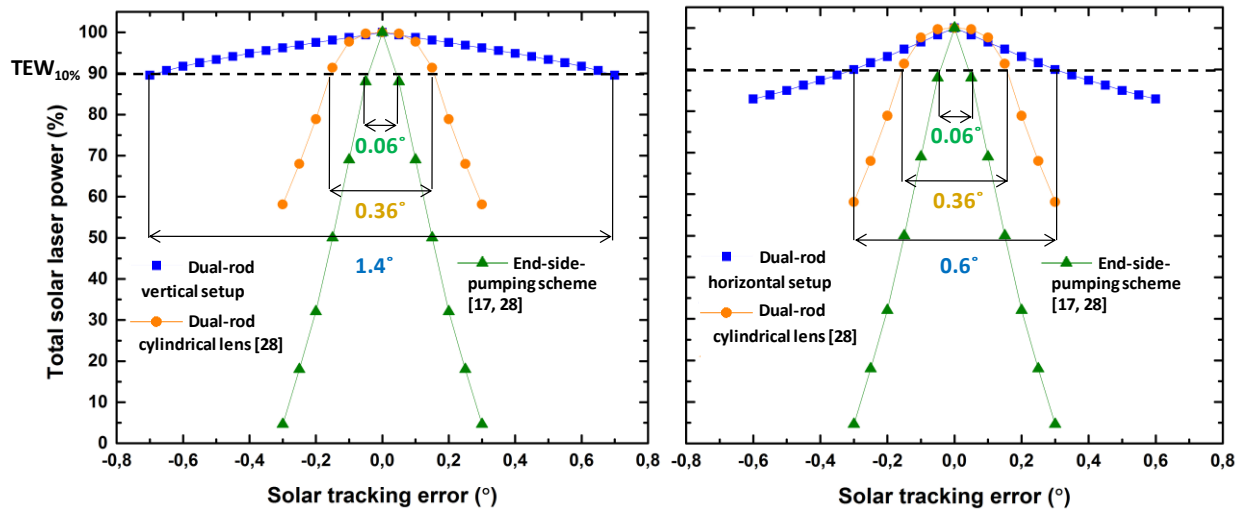


**Figure 8.31** Normalized solar laser output power with vertical and horizontal setups with no Sun tracking, compared to the previous numerical results of the solar laser approach using cylindrical lens as secondary concentrator [28], and that of the most efficient end-side-pumping solar laser [17, 28].

The results and their comparison are summarized in the Table 8.1.

**Table 8.1** Tracking error width at 10% laser power loss comparison for dual-rod scheme experimentally tested in vertical and horizontal setups from this work and the numerically calculated single-rod and dual-rod schemes from [30], and the dual-rod and the end-side-pumped schemes from [17, 28].

| Schemes   | Tracking error<br>width at 10% laser power loss<br>(TEW <sub>10%</sub> ) |                     | Improvement by the present<br>work (times) |                     |
|---|--|---------------------|--|---------------------|
|   | Vertical setup   | Horizontal<br>setup | Vertical<br>setup                          | Horizontal<br>setup |
| <b>Present experimental work</b><br>with dual-rod (D = 4.0 mm;<br>L = 35 mm; L = 30 mm) | 1.4°   | 0.6°                | -  | -                   |
| Single-rod scheme<br>(D = 5.5 mm; L = 25)<br>[30]                                       | 0.1°   |                     | 14.0                                       | 6.0                 |
| Dual-rod scheme<br>(D = 4.0 mm; L = 25)<br>[30]   | 0.4°   |                     | 3.5  | 1.5                 |
| Dual-rod scheme<br>(D = 3.5 mm; L = 25)<br>[17, 28]                                     | 0.36°  |                     | 3.9  | 1.7                 |
| End-side-pumping scheme<br>(D = 4.0 mm; L = 35)<br>[17, 28]                             | 0.06°  |                     | 23.3                                       | 10.0                |

The comparison with the numerical tracking error compensation capacity of the most efficient experimental solar-pumped laser in an end-side-pumping configuration is also represented [17, 28]. Both the vertical and the horizontal setups had shown a substantially improved tracking error tolerance, providing a stable solar laser emission even with large tracking error displacements of the focal spot.





# Chapter 9 Conclusions and future perspectives

During this dissertation, several approaches and strategies have been developed for solar energy harvesting and solar-pumped lasers, aiming to develop and adapt this knowledge to the new challenges of high solar energy concentration systems and industrial decarbonization, proposing new approaches to improve the overall efficiency of solar lasers as an important part of any strategy of reducing the CO<sub>2</sub> emissions into the atmosphere.

The implementation of new materials, such as Ce:Nd:YAG and Cr:Nd:YAG, under high solar concentration conditions, were conducted experimentally producing very encouraging results, adding benefits and robustness to solar laser technology. Also, innovative solar concentrators, such as RAC's were numerically modeled and investigated, helping to increase the solar concentration and the solar-pumped lasers efficiency levels, as well as demonstrating new possibilities towards a sustainable energy generation. Different multi-rod concepts were investigated in order to decrease the operating temperature of the solar laser system with success, enabling the increasing of the solar laser efficiency several times, although at the experimental level more work is to be done to demonstrate the numerically calculated results. The very useful doughnut shapes and other beams profiles were obtained numerically and experimentally, bringing new insights and potentialities about the production of novel renewable laser beam profiles. Large solar installations, such as the megawatt solar furnace in France, were studied and thought as potential primary concentrators for large scale laser production. Experimental advancements, aiming to enhance the efficiency and the stability of solar pumped lasers were also validated, reducing the eventual costs of future solar laser applications.

Several numerical solar laser models were firstly developed and simulated through ZEMAX<sup>®</sup> non-sequential ray-tracing and LASCAD<sup>®</sup> resonant cavity analysis, in order to increase the overall efficiency of solar-pumped lasers based on Nd:YAG laser medium, their collection and conversion efficiency, brightness and solar laser emission with compensation capacity, studies carried out in this work. The laser output for the unit surface area of the primary collector is an important measure for the assessment of solar lasers. A solar laser prototype was designed and built based on the numerical calculations and the optimization of the solar laser system. It was an extensive and difficult task we proposed to ourselves, not only because of the novelty and challenges of the work, with its inherent complexities, but also due to the pandemic situation precisely at the beginning of the construction phase of the solar laser prototype, bringing many obstacles and problems, such as to acquire some indispensable components or to have access to the workshop to build and modify the prototype along the experiments.

Regarding the numerical simulations, in 2018, 38.2 W/m<sup>2</sup> multimode solar laser in an end-side-pumping scheme was achieved by using RAC solar energy primary concentrator. In 2019, enhanced collection and conversion efficiencies of 11 W/m<sup>2</sup> and 1.31%, respectively, in TEM<sub>00</sub>-mode solar laser were attained, using NOVA heliostat-parabolic mirror, with the innovative concept of dual-rod side-pumping with a small semicylindrical lens and compound parabolic concentrator pump cavity. Improved solar tracking error compensation capacity was also achieved in multimode regime with this approach. In 2020, an aspheric lens as a secondary concentrator and a 2D-shaped-semicylindrical pump cavity were investigated with the dual-rod side-pumping scheme, increasing the side-pumping multimode collection efficiency and solar-to-laser power conversion efficiency to 24.18 W/m<sup>2</sup> and 2.88%, respectively, by using the innovative laser beam merging technique. Numerically calculated solar tracking error width at 10% laser power loss was also improved in 1.38 and 1.66 times in altitude and azimuth coordinates, respectively, in comparison to the previous dual-rod scheme with semicylindrical lens. In 2021, through the RAC primary concentrator and the dual-rod scheme, 29.06 W/m<sup>2</sup> in multimode collection efficiency and 3.06% solar-to-laser power conversion efficiency were obtained, besides the novel three-folding-mirror laser beam merging used to

enhance the laser beam quality factors. Also, the TEM<sub>00</sub>-mode solar laser was enhanced with this configuration and the three-folding-mirror laser beam merging in 2022, reaching 16.10 W/m<sup>2</sup> and 1.70% collection and solar-to-laser power conversion efficiencies, respectively.

The concept of dual-rod side-pumping scheme was employed and developed extensively, being pumped by parabolic mirrors to RAC's as primary concentrators, different secondary concentrators and resonant laser cavities. The most simple laser beam merging technique was enhanced to the three-folding-mirror laser beam merging and numerically implemented in order to extract efficiently one single laser beam from the two laser rods, with increased brightness, efficiency and simplicity, avoiding extra optical elements. It was studied in detail two major laser regimes, namely, multimode and TEM<sub>00</sub>-mode, in end-side-pumping and side-pumping configuration, with one and two rods. The dual-rod side-pumping scheme have shown the versatility related to the free access to both rod ends, allowing further optimization of the resonant laser cavity parameters and the enhanced tracking error compensation capacity, allowing a stable solar laser emission not with the maximum or peak power, but during more time with and at reduced costs, alleviating the necessity of high precision solar trackers and enabling longer solar laser emissions with stability, what can bring new opportunities of practical and robust solar laser applications. The tracking error efficiency is an important parameter to characterize a real implementation of a solar laser installation, since it is related to the costs involved in such task.

Regarding the solar tracking error tolerance, a significant enhancement in tracking error compensation capacity was experimentally achieved with the dual-rod approach. The improvement in TEW<sub>10%</sub> was 14.0 and 6.0 times in its vertical and horizontal setups, respectively, in relation to the single-rod scheme from the previous publication [30]. Regarding the dual-rod scheme numerically investigated in [30] using a fused silica aspherical lens as secondary concentrator, the present work attained an enhancement in TEW<sub>10%</sub> of 3.5 times and 1.5 times in its vertical and horizontal setups, respectively. Relatively to the dual-rod scheme numerically investigated using fused silica semicylindrical lens scheme and one CPC-pump cavity to each one of the rods from the previous publication [28], the improvement in TEW<sub>10%</sub> with the vertical and the horizontal setups was 3.9 and 1.7 times, respectively. The tracking error tolerance on the dual-rod experimentally tested was also compared with the numerical simulation of the most efficient experimental Nd:YAG end-side-pumping scheme pumped by NOVA heliostat-parabolic solar collection and concentration system. The enhancement in TEW<sub>10%</sub> attained with the dual-rod scheme of this work in its vertical and horizontal setups was 23.3 and 10.0 times, respectively [17, 28].

As a short term perspective for the dual-rod solar laser is the production of mini-mirrors with the most adequate RoC and reflectivity able to raise the solar laser power output extracted. The proposed schemes and concepts used along this work are also valid for many other solar laser materials, such as Ce:Nd:YAG, composite laser rods YAG-Nd:YAG-YAG undoped-doped-undoped, Nd:YAG grooved rods and Cr:LiCAF to improve their efficiencies.

For the dual-rod side-pumping scheme, the extraction of TEM<sub>00</sub>-mode solar laser is an immediate future perspective, due to the very good results obtained in the numerical simulations. The amplification of both TEM<sub>00</sub>-mode and multimode solar laser beam would be also an interesting possibility to increase efficiency in several parameters. A future vision of the multi-rod solar laser and solar tracking error is that it can be an optical alignment tool for large solar energy concentration systems, for example by using a square-shaped four-rod configuration, in order to extract a solar laser beam from each one, proportional to the solar focus formation and its movement in X- and Y-axes in the alignment procedure. Using Ce:Nd:YAG doped rods as laser medium can significantly improve the efficiency, leading to widespread applications of solar lasers.

# Annexes

Co-principal investigator in the exploratory project financed by FCT 2021: “Production of seven-beam Ce:Nd:YAG solar laser in TEM<sub>00</sub>-mode regime”.

## Publications during the PhD thesis

- I. D. Liang, C.R. Vistas, **B.D. Tibúrcio**, J. Almeida, Solar-pumped Cr:Nd:YAG ceramic laser with 6.7% slope efficiency, *Solar Energy Materials and Solar Cells*, 185, 75-79 (2018).
- II. **B.D. Tibúrcio**, D. Liang, J. Almeida, R. Matos, C.R. Vistas, Improving solar-pumped laser efficiency by a ring-array concentrator, *Journal of Photonics For Energy*, 8 (2018). (4 citations).
- III. R. Matos, D. Liang, J. Almeida, **B.D. Tibúrcio**, C.R. Vistas, High-efficiency solar laser pumping by a modified ring-array concentrator, *Optics Communications*, 420, 6-13 (2018).
- IV. D. Liang, C.R. Vistas, J. Almeida, **B.D. Tibúrcio**, D. Garcia, Side-pumped continuous-wave Nd:YAG solar laser with 5.4% slope efficiency, *Solar Energy Materials and Solar Cells*, 192, 147-153 (2019).
- V. **B.D. Tibúrcio**, D. Liang, J. Almeida, D. Garcia, C.R. Vistas, Dual-rod pumping approach for tracking error compensation in solar-pumped lasers, *Journal of Photonics for Energy*, 9 (2019).
- VI. **B.D. Tibúrcio**, D. Liang, J. Almeida, D. Garcia, C.R. Vistas, Dual-rod pumping concept for TEM<sub>00</sub>-mode solar lasers, *Appl. Opt.*, 58, 3438-3446 (2019). (4 citations).
- VII. J. Almeida, D. Liang, **B.D. Tibúrcio**, D. Garcia, C.R. Vistas, Numerical modeling of a four-rod pumping scheme for improving TEM<sub>00</sub>-mode solar laser performance, *Journal of Photonics for Energy*, 9, 018001 (2019).
- VIII. D. Garcia, D. Liang, **B.D. Tibúrcio**, J. Almeida, C.R. Vistas, A three-dimensional ring-array concentrator solar furnace, *Solar Energy*, 193, 915-928 (2019).
- IX. C.R. Vistas, D. Liang, J. Almeida, **B.D. Tibúrcio**, D. Garcia, A doughnut-shaped Nd:YAG solar laser beam with 4.5 W/m<sup>2</sup> collection efficiency, *Solar Energy*, 182, 42-47 (2019).
- X. D. Liang, J. Almeida, D. Garcia, **B.D. Tibúrcio**, E. Guillot, C.R.J.S.E. Vistas, Simultaneous solar laser emissions from three Nd:YAG rods within a single pump cavity, 199, 192-197 (2020).
- XI. **B.D. Tibúrcio**, D. Liang, J. Almeida, D. Garcia, C.R. Vistas, P.J. Morais, Highly efficient side-pumped solar laser with enhanced tracking-error compensation capacity, *Optics Communications*, 460, 125156 (2020). (3 citations).

- XII. C.R. Vistas, D. Liang, D. Garcia, **B.D. Tibúrcio**, Almeida, 32 W TEM<sub>00</sub>-Mode Side-Pumped Solar Laser Design, *Applied solar energy* 56, 449-457 (2020).
- XIII. J. Almeida, D. Liang, H. Costa, D. Garcia, **B. D. Tibúrcio**, M. Catela, C. R. Vistas, Seven-rod pumping concept for simultaneous emission of seven TEM<sub>00</sub>-mode solar laser beams, *Journal of Photonics for Energy*, 10, 1-14 (2020).
- XIV. M. Catela, D. Liang, C. Vistas, R , D. Garcia, **B. Tibúrcio**, D , H. Costa, J. Almeida, Six-rod/six-beam concept for revitalizing TEM<sub>00</sub>-mode lamp-pumped lasers, *Optical Engineering*, 59, 1-13 (2020).
- XV. C.R. Vistas, D. Liang, D. Garcia, J. Almeida, **B.D. Tibúrcio**, E. Guillot, Ce:Nd:YAG continuous-wave solar-pumped laser, *Optik*, 207, 163795 (2020).
- XVI. H. Costa, J. Almeida, D. Liang, D. Garcia, M. Catela, **B. D. Tibúrcio**, C. R. Vistas, Design of a multibeam solar laser station for a megawatt solar furnace, *Optical Engineering*, 59, 1-12 (2020).
- XVII. C.R. Vistas, D. Liang, J. Almeida, **B.D. Tibúrcio**, D. Garcia, M. Catela, H. Costa, E. Guillot, Ce:Nd:YAG side-pumped solar laser, *Journal of Photonics for Energy*, 11, 1-9 (2021).
- XVIII. D. Garcia, D. Liang, J. Almeida, **B.D. Tibúrcio**, H. Costa, M. Catela, C.R. Vistas, Analytical and numerical analysis of a ring-array concentrator, *International Journal of Energy Research*, 45, 15110-15123 (2021).
- XIX. D. Liang, J. Almeida, **B.D. Tibúrcio**, M. Catela, D. Garcia, H. Costa, C.R. Vistas, Seven-Rod Pumping Approach for the Most Efficient Production of TEM<sub>00</sub>-Mode Solar Laser Power by a Fresnel Lens, *Journal of Solar Energy Engineering*, 143 (2021).
- XX. **B.D. Tibúrcio**, D. Liang, J. Almeida, D. Garcia, M. Catela, H. Costa, C.R. Vistas, Improving side-pumped solar lasers using ring-array concentrators, *International Journal of Sustainable Energy*, 1-21 (2021).
- XXI. M. Catela, D. Liang, C.R. Vistas, D. Garcia, **B.D. Tibúrcio**, H. Costa, J. Almeida, Doughnut-Shaped and Top Hat Solar Laser Beams Numerical Analysis, *Energies*, 14 (2021).
- XXII. M. Catela, D. Liang, C.R. Vistas, D. Garcia, **B.D. Tibúrcio**, H. Costa, J. Almeida, Renovating electrical power-to-TEM<sub>00</sub>-mode laser power conversion efficiency with four-lamp/four-rod pumping scheme, *Journal of Modern Optics*, 68, 895-905 (2021).
- XXIII. H. Costa, J. Almeida, D. Liang, M. Catela, D. Garcia, **B.D. Tibúrcio**, C.R.J.E. Vistas, Zigzag Multirod Laser Beam Merging Approach for Brighter TEM<sub>00</sub>-Mode Solar Laser Emission from a Megawatt Solar Furnace, *Energies*, 14, 5437 (2021).
- XXIV. D. Garcia, D. Liang, J. Almeida, **B.D. Tibúrcio**, H. Costa, M. Catela, C.R. Vistas, Elliptical-Shaped Fresnel Lens design through Gaussian Source Distribution, *Energies*, 15 (2022).
- XXV. **B. D. Tibúrcio**, D. Liang, J. Almeida, D. Garcia, M. Catela, H. Costa and C. R. Vistas, Enhancing TEM<sub>00</sub>-mode solar laser with beam merging technique and ring-array concentrator, submitted to *Journal of Solar Energy Engineering* (in minor revision), (2022).

- XXVI. **B. D. Tibúrcio**, D. Liang, J. Almeida, D. Garcia, M. Catela, H. Costa and C. R. Vistas, Tracking error compensation capacity measurement of a dual-rod side-pumping solar laser, submitted to Renewable Energy (in review), (2022).

## Conferences

J. Almeida, D. Liang, **B. D. Tibúrcio**, D. Garcia, R. Matos, C. R. Vistas, Recent Advances in Renewable Solar-Pumped Lasers, presented in Encontro com a Ciência e Tecnologia em Portugal, 2019.

**B. D. Tibúrcio**, D. Liang, J. Almeida, C. R. Vistas, D. Garcia, R. Matos, M. Catela, Recent Advances in Solar-Pumped Lasers, presented in NOVA Science Day, 2019.

H. Costa, J. Almeida, D. Garcia, **B. D. Tibúrcio**, M. Catela, C. R. Vistas, Novel concepts in solar-pumped lasers, presented in Ciência 2020 – Encontro com a Ciência e Tecnologia em Portugal, 2020.

## Highlights

- I. Featured content in Journal of Photonics for Energy 2019 with “Dual-rod pumping approach for tracking error compensation in solar-pumped lasers”.
- II. Featured content in Journal of Photonics for Energy 2019 with “Numerical modeling of a four-rod pumping scheme for improving TEM<sub>00</sub>-mode solar laser performance”.
- III. Contract for a Chapter in a book publishing contract on “Solar-Pumped Lasers” with Springer Nature 2020.
- IV. Cover page in Journal of Photonics for Energy 2021 with “Seven-rod pumping concept for simultaneous emission of seven TEM<sub>00</sub>-mode solar laser beams”.
- V. Reviewer for *Photonics* and *Materials*.



## REFERENCES

- [1] D. Elliott, Renewable energy and sustainable futures, *Futures*, 32 (2000) 261-274.
- [2] V. Masson, M. Bonhomme, J.-L. Salagnac, X. Briottet, A. Lemonsu, Solar panels reduce both global warming and urban heat island, *Frontiers in Environmental Science*, 2 (2014) 14.
- [3] W.T. Xie, Y.J. Dai, R.Z. Wang, K. Sumathy, Concentrated solar energy applications using Fresnel lenses: A review, *Renewable and Sustainable Energy Reviews*, 15 (2011) 2588-2606.
- [4] G. Overton, NOVEL LASERS: "Solar-pumped Nd:YAG lasers getting brighter ", *Laser Focus World*, 2013.
- [5] M. Lando, Y. Shimony, R.M.J. Benmair, D. Abramovich, V. Krupkin, A. Yogeve, Visible solar-pumped lasers, *Optical Materials*, 13 (1999) 111-115.
- [6] Y. Takashi, O. Tomomasa, D.T. Hung, K. Hiroki, N. Junichi, O. Kouta, Demonstration of Solar-Pumped Laser-Induced Magnesium Production from Magnesium Oxide, *Magnesium Technology 2012*, (2012) 55-58.
- [7] Y. Takashi, O. Tomomasa, D.T. Hung, K. Hiroki, N. Junichi, O. Kouta, Demonstration of Solar-Pumped Laser-Induced Magnesium Production from Magnesium Oxide, in: S.N. Mathaudhu, W.H. Sillekens, N.R. Neelameggham, N. Hort (Eds.) *Magnesium Technology 2012*, Springer International Publishing, Cham, 2016, pp. 55-58.
- [8] D. Graham-Rowe, Solar-powered lasers, *Nature Photonics*, 4 (2010) 64-65.
- [9] M. Lando, J.A. Kagan, Y. Shimony, Y.Y. Kalisky, Y. Noter, A. Yogeve, S.R. Rotman, S. Rosenwaks, Solar-pumped solid state laser program, *SPIE1997*.
- [10] M. Vasile, C. Maddock, Design of a formation of solar pumped lasers for asteroid deflection, *Advances in Space Research*, 50 (2012) 891-905.
- [11] C.G. Young, A Sun-Pumped cw One-Watt Laser, *Appl. Opt.*, 5 (1966) 993-997.
- [12] M. Weksler, J. Shwartz, Solar Pumped Solid State Lasers, *SPIE1987*.
- [13] H. Arashi, Y. Oka, N. Sasahara, A. Kaimai, M. Ishigame, A Solar-Pumped cw 18 W Nd:YAG Laser, *Japanese Journal of Applied Physics*, 23 (1984) 1051-1053.
- [14] R.M.J. Benmair, J. Kagan, Y. Kalisky, Y. Noter, M. Oron, Y. Shimony, A. Yogeve, Solar-pumped Er,Tm,Ho:YAG laser, *Optics letters*, 15 (1990) 36-38.
- [15] M. Lando, J. Kagan, B. Linyekin, V. Dobrusin, A solar-pumped Nd:YAG laser in the high collection efficiency regime, *Optics Communications*, 222 (2003) 371-381.
- [16] T.H. Dinh, T. Ohkubo, T. Yabe, H. Kuboyama, 120 watt continuous wave solar-pumped laser with a liquid light-guide lens and an Nd:YAG rod, *Optics letters*, 37 (2012) 2670-2672.
- [17] D. Liang, J. Almeida, C.R. Vistas, E. Guillot, Solar-pumped Nd:YAG laser with 31.5 W/m<sup>2</sup> multimode and 7.9 W/m<sup>2</sup> TEM<sub>00</sub>-mode collection efficiencies, *Solar Energy Materials and Solar Cells*, 159 (2017) 435-439.
- [18] D. Liang, C.R. Vistas, J. Almeida, B.D. Tiburcio, D. Garcia, Side-pumped continuous-wave Nd:YAG solar laser with 5.4% slope efficiency, *Solar Energy Materials and Solar Cells*, 192 (2019) 147-153.
- [19] D. Liang, C.R. Vistas, B.D. Tiburcio, J. Almeida, Solar-pumped Cr:Nd:YAG ceramic laser with 6.7% slope efficiency, *Solar Energy Materials and Solar Cells*, 185 (2018) 75-79.
- [20] D. Liang, J. Almeida, D. Garcia, B.D. Tiburcio, E. Guillot, C.R.J.S.E. Vistas, Simultaneous solar laser emissions from three Nd:YAG rods within a single pump cavity, *Solar Energy*, 199 (2020) 192-197.
- [21] J. Almeida, D. Liang, C.R. Vistas, E. Guillot, Highly efficient end-side-pumped Nd:YAG solar laser by a heliostat-parabolic mirror system, *Applied Optics*, 54 (2015) 1970-1977.
- [22] J. Almeida, D. Liang, E. Guillot, Y. Abdel-Hadi, A 40 W cw Nd:YAG solar laser pumped through a heliostat: a parabolic mirror system, *Laser Physics*, 23 (2013) 6.
- [23] D. Liang, J. Almeida, Highly efficient solar-pumped Nd:YAG laser, *Optics Express*, 19 (2011) 26399-26405.

- [24] P. Xu, S. Yang, C. Zhao, Z. Guan, H. Wang, Y. Zhang, H. Zhang, T. He, High-efficiency solar-pumped laser with a grooved Nd:YAG rod, *Applied Optics*, 53 (2014) 3941-3944.
- [25] D. Liang, J. Almeida, E. Guillot, Side-pumped continuous-wave Cr:Nd:YAG ceramic solar laser, *Applied Physics B-Lasers and Optics*, 111 (2013) 305-311.
- [26] M. Weksler, J. Schwartz, Solar-pumped solid-state lasers, *IEEE Journal of Quantum Electronics*, 24 (1988) 1222-1228.
- [27] D. Liang, J. Almeida, Solar-Pumped TEM<sub>00</sub>-mode Nd:YAG laser, *Optics Express*, 21 (2013) 25107-25112.
- [28] B.D. Tibúrcio, D. Liang, J. Almeida, D. Garcia, C.R. Vistas, Dual-rod pumping approach for tracking error compensation in solar-pumped lasers, *Journal of Photonics for Energy*, 9 (2019).
- [29] B.D. Tibúrcio, D. Liang, J. Almeida, D. Garcia, C.R. Vistas, Dual-rod pumping concept for TEM<sub>00</sub>-mode solar lasers, *Applied Optics*, 58 (2019) 3438-3446.
- [30] B.D. Tibúrcio, D. Liang, J. Almeida, D. Garcia, C.R. Vistas, P.J. Morais, Highly efficient side-pumped solar laser with enhanced tracking-error compensation capacity, *Optics Communications*, 460 (2020) 125156.
- [31] B.D. Tibúrcio, D. Liang, J. Almeida, D. Garcia, M. Catela, H. Costa, C.R. Vistas, Improving side-pumped solar lasers using ring-array concentrators, *International Journal of Sustainable Energy*, (2021) 1-21.
- [32] B.D. Tiburcio, D. Liang, J. Almeida, R. Matos, C.R. Vistas, Improving solar-pumped laser efficiency by a ring-array concentrator, *Journal of Photonics For Energy*, 8 (2018).
- [33] C.R. Vistas, D. Liang, D. Garcia, J. Almeida, B.D. Tibúrcio, E. Guillot, Ce:Nd:YAG continuous-wave solar-pumped laser, *Optik*, 207 (2020) 163795.
- [34] R.V. Cláudia, L. Dawei, A. Joana, D.T. Bruno, G. Dário, C. Miguel, C. Hugo, G. Emmanuel, Ce:Nd:YAG side-pumped solar laser, *Journal of Photonics for Energy*, 11 (2021) 1-9.
- [35] C. Zhao, Z. Guan, H. Zhang, How to harvest efficient laser from solar light, *SPIE2018*.
- [36] T. Yabe, T. Ohkubo, S. Uchida, K. Yoshida, M. Nakatsuka, T. Funatsu, A. Mabuti, A. Oyama, K. Nakagawa, T. Oishi, K. Daito, B. Behgol, Y. Nakayama, M. Yoshida, S. Motokoshi, Y. Sato, C. Baasandash, High-efficiency and economical solar-energy-pumped laser with Fresnel lens and chromium codoped laser medium, *Applied Physics Letters*, 90 (2007) 261120.
- [37] S. Payziyev, K. Makhmudov, Solar pumped Nd:YAG laser efficiency enhancement using Cr:LiCAF frequency down-shifter, *Optics Communications*, 380 (2016) 57-60.
- [38] C.Z. B. Zhao, J. He, and S. Yang, The study of active medium for solar-pumped solid-state lasers, *Acta Opt. Sin.*, 27 (2007) 1797 - 1801
- [39] Standard Tables for Reference Solar Spectral Irradiances: Direct Normal and Hemispherical on 37° Tilted Surface, ASTM G173-03 International, West Conshohocken, PA, 2012.
- [40] W. Koechner, *Solid-State Laser Engineering*, 6 ed., Springer-Verlag, New York, 2006.
- [41] V. Magni, Resonators for solid-state lasers with large-volume fundamental mode and high alignment stability, *Appl. Opt.*, 25 (1986) 107-117.
- [42] D. Welford, D.M. Rines, B.J. Dinerman, Efficient TEM(00)-mode operation of a laser-diode side-pumped Nd:YAG laser, *Optics letters*, 16 (1991) 1850-1852.
- [43] D. Liang, J. Almeida, C.R. Vistas, E. Guillot, Solar-pumped TEM<sub>00</sub> mode Nd:YAG laser by a heliostat-Parabolic mirror system, *Solar Energy Materials and Solar Cells*, 134 (2015) 305-308.
- [44] J. Almeida, D. Liang, C.R. Vistas, R. Bouadjemine, E. Guillot, 5.5 W continuous-wave TEM<sub>00</sub>-mode Nd:YAG solar laser by a light-guide/2V-shaped pump cavity, *Applied Physics B-Lasers and Optics*, 121 (2015) 473-482.
- [45] C.R. Vistas, D. Liang, J. Almeida, Solar-pumped TEM<sub>00</sub> mode laser simple design with a grooved Nd:YAG rod, *Solar Energy*, 122 (2015) 1325-1333.



- [46] D. Liang, J. Almeida, C.R. Vistas, M. Oliveira, F. Goncalves, E. Guillot, High-efficiency solar-pumped TEM<sub>00</sub>-mode Nd:YAG laser, *Solar Energy Materials and Solar Cells*, 145 (2016) 397-402.
- [47] D. Liang, J. Almeida, C.R. Vistas, Scalable pumping approach for extracting the maximum TEM<sub>00</sub> solar laser power, *Appl. Opt.*, 53 (2014) 7129-7137.
- [48] T. Yabe, S. Uchida, K. Ikuta, K. Yoshida, C. Baasandash, M.S. Mohamed, Y. Sakurai, Y. Ogata, M. Tuji, Y. Mori, Y. Satoh, T. Ohkubo, M. Murahara, A. Ikesue, M. Nakatsuka, T. Saiki, S. Motokoshi, C. Yamanaka, Demonstrated fossil-fuel-free energy cycle using magnesium and laser, *Applied Physics Letters*, 89 (2006) 261107.
- [49] J.X. Meng, J.Q. Li, Z.P. Shi, K.W.J.A.P.L. Cheah, Efficient energy transfer for Ce to Nd in Nd/ Ce codoped yttrium aluminum garnet, *Applied Physics Letters*, 93 (2008) 221908.
- [50] P. Samuel, T. Yanagitani, H. Yagi, H. Nakao, K.I. Ueda, S.M.J.J.o.a. Babu, compounds, Efficient energy transfer between Ce<sup>3+</sup> and Nd<sup>3+</sup> in cerium codoped Nd: YAG laser quality transparent ceramics, *Journal of Alloys Compounds*, 507 (2010) 475-478.
- [51] Y. Li, S. Zhou, H. Lin, X. Hou, W.J.O.M. Li, Intense 1064 nm emission by the efficient energy transfer from Ce<sup>3+</sup> to Nd<sup>3+</sup> in Ce/Nd co-doped YAG transparent ceramics, *Optical Materials*, 32 (2010) 1223-1226.
- [52] V. Bachmann, C. Ronda, A.J.C.o.M. Meijerink, Temperature quenching of yellow Ce<sup>3+</sup> luminescence in YAG: Ce, *Journal of Chemistry of Materials*, 21 (2009) 2077-2084.
- [53] M.R.A. Moghaddam, D. Razzaghi, J.H. Barbaran, M.J.O. Barardaran, Influence of annealing atmosphere on the optical quality and pulsed laser performance of Ce, Nd: YAG single crystal, *Optik*, 181 (2019) 941-947.
- [54] Y. Tai, G. Zheng, H. Wang, J.J.J.o.P. Bai, P.A. Chemistry, Near-infrared quantum cutting of Ce<sup>3+</sup>—Nd<sup>3+</sup> co-doped Y<sub>3</sub>Al<sub>5</sub>O<sub>12</sub> crystal for crystalline silicon solar cells, *Journal of Photochemistry and Photobiology A: Chemistry*, 303 (2015) 80-85.
- [55] S. Payziyev, K. Makhmudov, Y.A.J.O. Abdel-Hadi, Simulation of a new solar Ce: Nd: YAG laser system, *Optik*, 156 (2018) 891-895.
- [56] Z.J. Kiss, H.R. Lewis, R.C. Duncan, SUN PUMPED CONTINUOUS OPTICAL MASER, *Applied Physics Letters*, 2 (1963) 93-94.
- [57] J. Lee, W. Weaver, Solar-pumped gas laser, *Journal of Quantum Electronics*, 17 (1981) 2438-2440.
- [58] R. De Young, Low threshold solar-pumped iodine laser, *Journal of Quantum Electronics* 22 (1986) 1019-1023.
- [59] R.T. Schneider, U.H. Kurzweg, J.D. Cox, N.H. Weinstein, G.J.U.F. NAGI, Gainesville, FL., rep. No. NAG-I-135, Research on solar pumped liquid lasers, (1983).
- [60] D. Jenkins, M. Lando, J. O’Gallagher, R. Winston, A. Lewandowski, C. Bingham, R.J.B.o.I. Pitts, A solar-pumped Nd: YAG laser with a record efficiency of 4.7 watt/m<sup>2</sup> of primary mirror area, 42 (1996) 101.
- [61] S. Mizuno, H. Ito, K. Hasegawa, T. Suzuki, Y.J.O.e. Ohishi, Laser emission from a solar-pumped fiber, *Optics Express*, 20 (2012) 5891-5895.
- [62] J. Almeida, D. Liang, E. Guillot, Improvement in solar-pumped Nd:YAG laser beam brightness, *Optics and Laser Technology*, 44 (2012) 2115-2119.
- [63] P.D. Reusswig, S. Nechayev, J.M. Scherer, G.W. Hwang, M.G. Bawendi, M.A. Baldo, C. Rotschild, A path to practical Solar Pumped Lasers via Radiative Energy Transfer, *Scientific Reports*, 5 (2015) 14758.
- [64] A.H. Quarterman, K.G. Wilcox, Design of a solar-pumped semiconductor laser, *Optica*, 2 (2015) 56-61.
- [65] D. Liang, J. Almeida, C.R. Vistas, 25 W/m<sup>2</sup> collection efficiency solar-pumped Nd:YAG laser by a heliostat-parabolic mirror system, *Applied Optics*, 55 (2016) 7712-7717.

- [66] R. Bouadjemine, D. Liang, J. Almeida, S. Mehellou, C.R. Vistas, A. Kellou, E. Guillot, Stable TEM<sub>00</sub>-mode Nd:YAG solar laser operation by a twisted fused silica light-guide, *Optics and Laser Technology*, 97 (2017) 1-11.
- [67] S. Mehellou, D. Liang, J. Almeida, R. Bouadjemine, C.R. Vistas, E. Guillot, F. Rehouma, Stable solar-pumped TEM<sub>00</sub>-mode 1064 nm laser emission by a monolithic fused silica twisted light guide, *Solar Energy*, 155 (2017) 1059-1071.
- [68] V.P. Vasylyev, O.G. Tovmachenko, S.V. Vasylyev, Expected optical performances of novel type multi-element high-heat solar concentrators, *Proc. ASES Conference*, (2002).
- [69] R. Matos, D. Liang, J. Almeida, B.D. Tiburcio, C.R. Vistas, High-efficiency solar laser pumping by a modified ring-array concentrator, *Optics Communications*, 420 (2018) 6-13.
- [70] D. Garcia, D. Liang, B.D. Tibúrcio, J. Almeida, C.R. Vistas, A three-dimensional ring-array concentrator solar furnace, *Solar Energy*, 193 (2019) 915-928.
- [71] The FEA Code of LASCAD. LAS-CAD GmbH, Brunhildenstrasse 9 D-80639 Munich, Germany.
- [72] LAS-CAD GmbH, Computation of Laser Power Output for CW Operation, Brunhildenstrasse9 D-80639 Munich, Germany
- [73] LASCAD - The Laser Engineering Tool. LAS-CAD GmbH.
- [74] A.G. Fox, T. Li, Resonant modes in a maser interferometer, *Bell System Technical Journal*, 40 (1961) 453-488.
- [75] M. Schelhorn, High Power diode-pumped Tm:YLF Laser, *Applied Physics B, Laser and Optics*, 91 (2008) 71-74
- [76] D. Liang, C.R. Vistas, J. Almeida, B.D. Tibúrcio, D. Garcia, Side-pumped continuous-wave Nd:YAG solar laser with 5.4% slope efficiency, *Solar Energy Materials and Solar Cells*, 192 (2019) 147-153.
- [77] C.R. Vistas, D. Liang, J. Almeida, B.D. Tiburcio, D. Garcia, M. Catela, H. Costa, E. Guillot, Ce:Nd:YAG side-pumped solar laser, *Journal of Photonics for Energy*, 11 (2021) 1-9.
- [78] W. Koechner, Thermal Lensing in a Nd:YAG Laser Rod, *Appl. Opt.*, 9 (1970) 2548-2553.
- [79] J. Almeida, D. Liang, H. Costa, D. Garcia, B. Tibúrcio, D., M. Catela, C. Vistas, R., Seven-rod pumping concept for simultaneous emission of seven TEM<sub>00</sub>-mode solar laser beams, *Journal of Photonics for Energy*, 10 (2020) 1-14.
- [80] M. Catela, D. Liang, C.R. Vistas, D. Garcia, B.D. Tibúrcio, H. Costa, J. Almeida, Doughnut-Shaped and Top Hat Solar Laser Beams Numerical Analysis, *Energies*, 14 (2021).
- [81] J. Almeida, D. Liang, C.R. Vistas, A doughnut-shaped Nd:YAG solar laser beam, *Optics and Laser Technology*, 106 (2018) 1-6.
- [82] C.R. Vistas, D. Liang, J. Almeida, B.D. Tibúrcio, D. Garcia, A doughnut-shaped Nd:YAG solar laser beam with 4.5 W/m<sup>2</sup> collection efficiency, *Solar Energy*, 182 (2019) 42-47.
- [83] M. Okida, Y. Hayashi, T. Omatsu, J. Hamazaki, R. Morita, Characterization of 1.06  $\mu$ m optical vortex laser based on a side-pumped Nd:GdVO<sub>4</sub> bounce oscillator, *Applied Physics B*, 95 (2009) 69-73.
- [84] J. Yin, W. Gao, Y. Zhu, Chapter 3 - Generation of dark hollow beams and their applications, in: E. Wolf (Ed.) *Progress in Optics*, Elsevier2003, pp. 119-204.
- [85] Z. Huang, Theoretical optimization of output power in side pumped Nd<sup>3+</sup>:YAG solar laser, *Optics & Laser Technology*, 111 (2019) 592-596.
- [86] H. Costa, J. Almeida, D. Liang, M. Catela, D. Garcia, B.D. Tibúrcio, C.R.J.E. Vistas, Zigzag Multirod Laser Beam Merging Approach for Brighter TEM<sub>00</sub>-Mode Solar Laser Emission from a Megawatt Solar Furnace, *Energies*, 14 (2021) 5437.
- [87] E. Guillot, R. Rodriguez, N. Boullet, J.-L. Sans, Some details about the third rejuvenation of the 1000 kWth solar furnace in Odeillo: Extreme performance heliostats, *AIP Conference Proceedings*, 2033 (2018) 040016.

- [88] D. Garcia, D. Liang, J. Almeida, B.D. Tibúrcio, H. Costa, M. Catela, C.R. Vistas, Elliptical-Shaped Fresnel Lens Design through Gaussian Source Distribution, *Energies*, 15 (2022).
- [89] D. Liang, J. Almeida, C.R. Vistas, E. Guillot, Solar-pumped Nd:YAG laser with 31.5 W/m<sup>2</sup> multimode and 7.9 W/m<sup>2</sup> TEM<sub>00</sub>-mode collection efficiencies, *Solar Energy Materials and Solar Cells*, 159 (2017) 435-439.
- [90] C.J.C. Smyth, S. Mirkhanov, A.H. Quarterman, K.G. Wilcox, 27.5 W/m<sup>2</sup> collection efficiency solar laser using a diffuse scattering cooling liquid, *Applied Optics*, 57 (2018) 4008-4012.
- [91] S. Kalogirou, *Solar Energy Engineering*, 2nd ed., Academic Press, Massachusetts, 2013.
- [92] H. Mousazadeh, A. Keyhani, A. Javadi, H. Mobli, K. Abrinia, A. Sharifi, A review of principle and sun-tracking methods for maximizing solar systems output, *Renewable and Sustainable Energy Reviews*, 13 (2009) 1800-1818.
- [93] M.T. Hussein, S.N. Albarqouni, Enhanced model of one axis-two positions manual tracking photovoltaic panels for lighting projects in Palestine, *IASTED International Conference on Solar Energy 2010*, pp. 15-17.
- [94] F. Kreith, J.F. Kreider, *Principles of solar engineering*, 1978.
- [95] J.A. Duffie, W.A. Beckman, *Solar engineering of thermal processes*, Wiley New York 1980.
- [96] S. Skouri, A. Ben Haj Ali, S. Bouadila, M. Ben Salah, S. Ben Nasrallah, Design and construction of sun tracking systems for solar parabolic concentrator displacement, *Renewable and Sustainable Energy Reviews*, 60 (2016) 1419-1429.
- [97] C.J.S. Finster, El heliostato de la Universidad santa maria, 119 (1962) 5-20.
- [98] R.H. McFee, Power collection reduction by mirror surface nonflatness and tracking error for a central receiver solar power system, *Applied Optics*, 14 (1975) 1493-1502.
- [99] R.P. Semma, M.S. Imamura, Sun tracking controller for multi-kW photovoltaic concentrator system, 1981, Photovoltaic Solar Energy Conference; Proceedings of the Third International Conference, Cannes, France, October, pp. 375.
- [100] V. Badescu, Influence of certain astronomical and constructive parameters on the concentration of solar radiation with plane heliostats fields, *Rev. Phys. Appl.* (1985).
- [101] M. Berenguel, F.R. Rubio, A. Valverde, P.J. Lara, M.R. Arahal, E.F. Camacho, M. López, An artificial vision-based control system for automatic heliostat positioning offset correction in a central receiver solar power plant, *Solar Energy*, 76 (2004) 563-575.
- [102] Y.T. Chen, B.H. Lim, C.S. Lim, General Sun Tracking Formula for Heliostats With Arbitrarily Oriented Axes, *Journal of Solar Energy Engineering*, 128 (2005) 245-250.
- [103] A. Omar, D. Ismail, I. Muzamir, A. Mohd Rafi, Simplification of Sun Tracking Mode to Gain High Concentration Solar Energy, *American Journal of Applied Sciences*, 4 (2007).
- [104] K. Aiuchi, K. Yoshida, M. Onozaki, Y. Katayama, M. Nakamura, K. Nakamura, Sensor-controlled heliostat with an equatorial mount, *Solar Energy*, 80 (2006) 1089-1097.
- [105] F. Sun, Z. Wang, M. Guo, F. Bai, Z.J.E.P. Xu, Determination of tracking errors with respect to the geometrical errors based on optimization algorithm, *energy procedia*, 49 (2014) 2211-2220.
- [106] D. Chemisana, Building Integrated Concentrating Photovoltaics: A review, *Renewable and Sustainable Energy Reviews*, 15 (2011) 603-611.
- [107] I. Reda, A. Andreas, Solar position algorithm for solar radiation applications, *Solar Energy*, 76 (2004) 577-589.
- [108] K. Aiuchi, K. Yoshida, Y. Katayama, M. Nakamura, K. Nakamura, Sun Tracking Photo-Sensor for Solar Thermal Concentrating System, 2004, pp. 625-631.
- [109] S. Abdallah, S. Nijmeh, Two axes sun tracking system with PLC control, *Energy Conversion and Management*, 45 (2004) 1931-1939.
- [110] A. Rabl, *Active Solar Collectors and Their Applications*, Oxford University Press, New York, 1985.
- [111] P.J. Hession, W.J. Bonwick, Experience with a sun tracker system, *Solar Energy*, 32 (1984) 3-11.

- [112] A.K. Agarwal, Two axis tracking system for solar concentrators, (1992).
- [113] V. Badescu, Different Tracking Error Distributions and their Effects on the Long-Term Performances of Parabolic Dish Solar Power Systems, *International Journal of Solar Energy*, 14 (1994) 203-216.
- [114] U. Jamil, W. Ali, Performance tests and efficiency analysis of Solar Invictus 53S—A parabolic dish solar collector for direct steam generation, *AIP Conference Proceedings*, AIP Publishing LLC2016, pp. 070018.
- [115] J. Yan, Z.-r. Cheng, Y.-d. Peng, Effect of Tracking Error of Double-Axis Tracking Device on the Optical Performance of Solar Dish Concentrator, *International Journal of Photoenergy*, 2018 (2018) 9046127.
- [116] G. Falbel, J. Puig-Suari, A. Peczalski, Sun oriented and powered, 3 axis and spin stabilized CubeSats, *Proceedings, IEEE Aerospace Conference*2002, pp. 1-1.
- [117] T. Motohiro, A. Ichiki, T. Ichikawa, H. Ito, K. Hasegawa, S. Mizuno, T. Ito, T. Kajino, Y. Takeda, K. Higuchi, Consideration of coordinated solar tracking of an array of compact solar-pumped lasers combined with photovoltaic cells for electricity generation, *Japanese Journal of Applied Physics*, 54 (2015) 08KE04.
- [118] C.-D. Lee, H.-C. Huang, H.-Y.J.S. Yeh, The development of sun-tracking system using image processing, 13 (2013) 5448-5459.